Lehrstuhl für Biomedizinische Physik
Technische Universität München

Laboratory-Based X-ray Microscopy

with Staining and Propagation-Based Phase Effects for Contrast Enhancement

Simone Ferstl

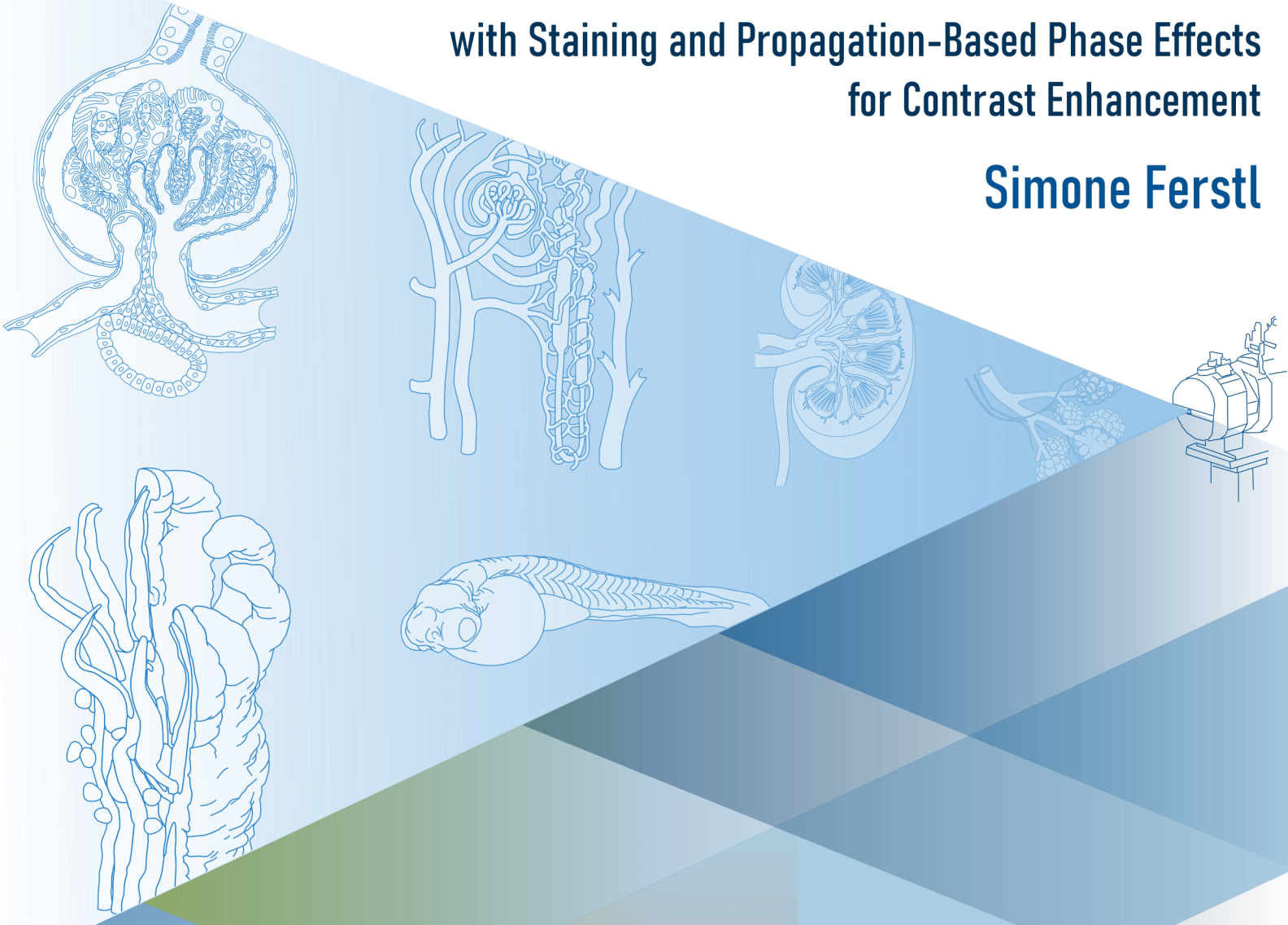

July 2021

Supervisor:
Prof. Dr. Franz Pfeiffer

Technische Universität München

I dedicate this thesis to curiosity and imagination...

Drawing of Myself with my Light Microscope at Age 7.
Colour wax crayons on paper.

Technische Universität München
Fakultät für Physik

Laboratory-Based X-ray Microscopy

with Staining and Propagation-Based Phase Effects for Contrast Enhancement

Simone Ferstl

Vollständiger Abdruck der von der Fakultät für Physik der Technischen Universität München zur Erlangung des akademischen Grades einer

Doktorin der Naturwissenschaften (Dr. rer. nat.)

genehmigten Dissertation.

Vorsitzender:	Prof. Dr. Karen Alim
Prüfer der Dissertation:	1. Prof. Dr. Franz Pfeiffer
	2. Prof. Dr. Wilko Weichert

Die Dissertation wurde am 02.08.2021 bei der Technischen Universität München eingereicht und durch die Fakultät für Physik am 10.11.2021 angenommen.

Abstract

Through complete volume information, 3D microscopy offers new perspectives on the world of cells and on the biological structures they form. In current research, there are numerous techniques devoted to 3D microscopy. Many of these techniques, however, rely on destructive methods, such as sectioning or ablation, struggle with processing artefacts, are limited regarding sample sizes or fail to provide isotropic resolutions in 3D. Microscopy based on X-ray computed tomography is inherently non-destructive, generally more flexible in terms of sample sizes than light or electron microscopy and enables isotropic 3D resolutions.

Only recently, a novel laboratory-based nanotomography setup - the NanoCT - was introduced. It is based on the concept of cone-beam projection imaging. Thereby, the NanoCT enables resolutions in the range of 100 nm and is characterised by an immense versatility regarding the investigation of soft-tissue specimens. The main goal of this work was to further characterise and optimise the NanoCT and to explore novel fields of applications.

For advancing the NanoCT system, the image processing framework was expanded, and experiments were performed to optimise acquisition parameters. Comparative analyses between propagation-based phase contrast and X-ray staining yielded new information to support the development of novel X-ray stains.

Throughout this work, two major areas of application have emerged for the NanoCT: zoology and 3D histology. In the field of zoology, the feasibility was demonstrated to integrate the NanoCT into established routines of correlative microscopy involving transmission electron microscopy. In the pursuit of this goal, various advantages of the NanoCT over sectioning-based light microscopy were discovered and the internal anatomy of a rather unknown tiny sea cucumber and a marine snail was revealed.
In 3D histology, a recently developed technique combining the NanoCT with an eosin-based X-ray stain was translated from investigations on a mouse model to human tissue specimens. In the course of this project, this technique was applied to a large variety of diseased renal tissue specimens, and specimens of healthy skin and lung tissue. In a multiscale investigation, its capability was proven to accurately reproduce characteristic tissue morphologies in 3D.

In conclusion, this work provides valuable insights into imaging principles of the NanoCT and reveals its potential for manifold research applications, in particular for future tissue diagnostics.

Zusammenfassung

Durch umfassende Volumeninformation eröffnet die 3D Mikroskopie neue Einblicke in die Welt der Zellen und in die von ihnen gebildeten biologischen Strukturen. In der aktuellen Forschung gibt es unzählige Techniken, die sich mit 3D Mikroskopie befassen. Viele dieser Techniken greifen jedoch auf destruktive Methoden wie Schnitt- oder Ablationsverfahren zurück. Diese sind daher anfälliger für Prozessierungsartefakte, sind begrenzt hinsichtlich der Probengröße, oder bieten keine isotropen Aufösungen in 3D. Mikroskopie-Methoden, die auf Röntgen-Computertomographie beruhen, sind grundsätzlich zerstörungsfrei, im Allgemeinen flexibler als Licht- oder Elektronenmikroskopie bezüeglich der Probengröße und ermöglichen istrope Auflösungen in 3D.

Erst vor Kurzem wurde ein neuartiger laborbasierter Nanotomographie Aufbau vorgestellt: das NanoCT. Es basiert auf dem Bildgebungskonzept der Kegelstrahlprojektion. Dadurch erreicht das NanoCT Auflösungen in Bereich von 100 nm und zeichnet sich durch eine immense Vielseitigkeit bei der Untersuchung von Weichgewebeproben aus. Das Hauptziel dieser Arbeit bestand darin das NanoCT weiter zu charakterisieren, zu optimieren und neue Anwendungsgebiete zu erschließen.

Zur Weiterentwicklung des NanoCT-Systems wurde die Bildverarbeitungs-Routine durch neue Funktionen erweitert, und es wurden Experimente zur Optimierung von Messparametern durchgeführt. Der Vergleich zwischen propagationsbasiertem Phasenkontrast und Röntgenkontrastmitteln lieferte Ergebnisse, die sich bei der Entwicklung neuer Röntgenkontrastmittel als hilfreich erweisen könnten.

Im Laufe dieser Arbeit haben sich für das NanoCT zwei Hauptanwendungsgebiete herauskristallisiert: Zoologie und 3D-Histologie. Im Bereich der Zoologie wurde gezeigt, dass sich der NanoCT in etablierte Routinen der korrelativen Mikroskopie mit Transmissionselektronenmikroskopie integrieren lässt. Dabei wurden verschiedene Vorteile des NanoCT gegenüber sektionsbasierter Lichtmikroskopie aufgezeigt und die innere Anatomie einer bislang kaum erforschten winzigen Seegurke und einer Meeresschnecke wurde offenbart.
In der 3D-Histologie wurde eine kürzlich entwickelte Technik, die das NanoCT mit einem eosinbasierten Röntgenkontrastmittel kombiniert, von Untersuchungen am Mausmodell auf Anwendungen an menschlichem Gewebe übertragen. Im Verlauf dieses Projekts wurde diese Technik auf eine Vielzahl von erkrankten Nierengewebeproben und Proben von gesundem Haut- und Lungengewebe angewandt. In einer Studie über verschiedene Größenordnungen hinweg wurde nachgewiesen, dass diese Technik fähig ist die charakteristischen 3D Gewebemorphologien genau zu reproduzieren.

Zusammenfassend lässt sich sagen, dass diese Arbeit wertvolle Erkenntnisse über die Bildgebungsprinzipien des NanoCT gewährt und dessen Potenzial für vielfältige Anwendungen in der Forschung verdeutlicht, insbesondere für die moderne Gewebediagnostik.

Contents

1 Introduction

Since the invention of the compound microscope around 1620, the field of microscopy has rapidly evolved and has since then spawned a myriad of highly specialised techniques for diverse applications [vHelden, 2010].
The range of modern microscopy techniques spans from electron microscopy (EM) methods, such as scanning electron microscopy (SEM) or transmission electron microscopy (TEM), over conventional full-field light microscopy (LM) to fluorescence-based microscopy, including super-resolution techniques, like stimulated emission depletion (STED) or stochastic optical reconstruction microscopy (STORM) [Ojeda, 1991; Williams, 1996; Hell, 1994; Garini, 2005].
Particularly in the field of life sciences - including disciplines from zoology to medicine - microscopy has become an essential research tool [Garini, 2005]. In zoological research, the characterisation of an organism's morphology is often performed using LM and EM [Brenzinger, 2013]. Moreover, fluorescence microscopy is a powerful method for targeted analyses of functional, sub-cellular structures, such as mitochondrial matrices or the cytoskeleton [Schwaha, 2012; Garini, 2005; Lloyd, 1987].
In medical research, the standard use case for microscopy is the study of tissue morphologies on a cellular level, generally known as histology [Suvarna, 2013]. Beyond medical research, histology has become an integral part of the clinical routine. Particularly for assessing pathological alterations of human tissue on a cellular level, histology represents the current gold standard. For such histological analyses, a pathologist can choose from a great variety of structure-specific stains and adjust the magnification of the light microscope to meet the respective demands. This provides histology with a high degree of versatility. Apart from these strengths, this method also has its limitations, such as the wavelength-dependent resolution limit [Suvarna, 2013; DAgati, 2005; Als-Nielsen, 2011].
Correlative microscopy combines the strengths of multiple microscopy techniques and thereby enables multi-modal and multi-scale studies [Caplan, 2011]. For instance, multi-modal information can be gained by correlating LM with fluorescence microscopy, which allows for correlating structural with functional information [Giepmans, 2008]. An example for multi-scale investigations is correlative LM and EM (CLEM) [Lucas, 2012; Handschuh, 2013].
Due to the typically small penetration depths of electrons and visible light in matter, however, many of the mentioned microscopy techniques provide only 2D information.

In order to truly gain a precise impression of a sample's structure, 3D information is indispensable [Goldstein, 2018]. TEM tomography, for instance, enables 3D imaging, but only of very small volumes in the range of 1 µm^3 [Bárcena, 2009]. This has motivated many developers and researchers to transform the existing 2D EM- and LM-techniques into 3D imaging techniques by combining multiple 2D images into a 3D data set. For this purpose, ablation or sectioning techniques are employed to obtain a series of 2D images of an entire specimen. Examples for such ablation- or sectioning-based 3D microscopy techniques are focused-ion-beam (FIB) SEM, serial-block-face (SBF) SEM, or serial-sectioning LM/EM (ss-LM/ss-EM) [Knott, 2008; Denk, 2004; Braverman, 1986; Andreasen, 1992; Weninger, 1998; Merchan-Pérez, 2009]. These techniques are, however, destructive, often suffer from sectioning and alignment artefacts and most of them are unable to provide isotropic resolution of an entire volume [McInnes, 2005; Töpperwien, 2018a; Walton, 2015; Bushong, 2014]. In other approaches for generating 3D data with LM or EM, the surrounding tissue is either fully dissolved (corrosion casting with SEM) or it is optically cleared (light-sheet microscopy) to access the relevant internal structures. Thereby, a large amount of tissue information is lost, and it is only possible to retrieve data of the preserved structures [Hossler, 2001; Albers, 2018; Keller, 2012; Wagner, 2011].
Compared to photons in the optical regime, X-ray photons feature significantly smaller absorption cross-sections in materials with small atomic numbers (Z), such as soft tissues. As a result, significantly higher penetration depths are reached in soft tissue. Furthermore, computed tomography (CT) enables the reconstruction of volume information from a set of projection images across an angular range. Nowadays, X-ray CT has established itself as one of the most important methods for non-destructive 3D imaging [Als-Nielsen, 2011; Burnett, 2014].
The weak absorption of X-rays, however, is also associated with poor contrast in soft tissues. To address this matter, there are several approaches: soft X-rays with energies in the water window ($E \in [284; 543]$eV), for instance, provide excellent soft-tissue contrast and have led to brilliant high-resolution results [Schneider, 2012; Chao, 2005; Kirz, 1995]. This technique, however, again entails an immense increase of the general absorption and is consequently flawed by rather limited penetration depths. A more selective absorption enhancement of specific structures can be achieved via X-ray staining with elements of high atomic numbers as contrast agents. Currently widely used X-ray stains are based on iodine, silver, phospho-tungstic acid (PTA) or osmium tetroxide [Jahn, 2018; Sombke, 2015; Metscher, 2009; Handschuh, 2013].
In modern X-ray imaging methods often not only the attenuation of X-rays is used, but also the phase shift experienced by X-ray waves when propagating through a material. Phase-contrast imaging is particularly useful, since the interaction cross-section of the X-ray phase shift can be three orders of magnitude larger than the absorption cross-section [Withers, 2007]. A sufficiently coherent X-ray beam produces phase ef-

fects for large propagation distances in the form of edge enhancement or even complex Fresnel-fringe patterns [Paganin, 2002; Clœtens, 1999]. Analysing these propagation-based phase effects allows for a quantitative phase mapping given proper conditions [Clœtens, 1999]. Most often, these conditions are not easily fulfilled, especially in a laboratory environment, and propagation-based phase-contrast imaging is frequently merely used for enhancing soft-tissue contrast [Paganin, 2002; Töpperwien, 2018b]. For obtaining quantitative phase information, further imaging techniques have been developed, which are less reliant on the coherence of the X-ray source. These techniques include speckle- or grating-based phase-contrast imaging [Zdora, 2020; Pfeiffer, 2006; Umkehrer, 2019; Birnbacher, 2016]. In a laboratory environment, though, these techniques have struggled with reaching resolutions below 1 µm [Zdora, 2020; Umkehrer, 2019; Birnbacher, 2016].

In contrast to that, resolutions below 1 µm are achieved in the field of X-ray nanotomography through a handful of strategies. In this work, the term microCT refers to resolutions down to 1 µm and nanoCT or X-ray nanotomography refers to resolutions well below 1 µm. One major group among X-ray nanotomography techniques is X-ray optics-based systems employing components such as Fresnel Zone Plates (FZP), Kirkpatrick-Baez (KB) optics, Bragg magnifiers or compound lenses. Many X-ray optics-based concepts are hampered by low efficiencies and the focusing properties are strongly dependent on the X-ray energy. Hence, most of these methods require high-flux X-rays of a certain energy, which makes them ideal for synchrotron applications but difficult to implement in the laboratory [Chao, 2005; Kirkpatrick, 1948; Hignette, 2005; Lengeler, 1999; Boettinger, 1979]. An X-ray nanotomography approach which is well suited for laboratory applications is cone-beam projection imaging. It uses geometric magnifications in combination with small X-ray source spots. In these systems, the X-ray spot size of the X-ray tube represents the ultimate limiting factor [Salamon, 2008; Withers, 2007]. Such systems have the major advantage of foregoing any optical components, which require precise alignment and reduce the X-ray flux as well as the field of view (FOV). Furthermore, in cone-beam projection systems, the entire polychromatic X-ray spectrum can be used for imaging and the magnification can be adjusted continuously. A fundamental disadvantage of these systems, however, is the low X-ray flux generated by such fine-focus X-ray tubes. These low X-ray fluxes demand an efficient detection system with minimum noise levels [Withers, 2007].
In order to overcome the aforementioned limitations of the various approaches, we have recently conceived a nanoscopic laboratory-based X-ray CT device, which is based on the concept of cone-beam projection imaging [Müller, 2017]. Throughout this work, it will be referred to as the NanoCT. It is comprised of a nanofocus X-ray tube (NanoTube, Excillum AB, Sweden) and a single-photon counting detector (Pilatus, Dectris, Switzerland). The NanoTube features a maximum acceleration voltage of 60 kV and provides control over the size and shape of the electron focal spot. The Pilatus detector

is equipped with a silicon-sensor and, thus, features high detection efficiencies within the energy spectrum of the NanoTube and achieves minimum noise levels through its single-photon counting mode. The NanoCT reaches resolutions in the range of 100 nm [Müller, 2017]. Adequate soft-tissue contrast is achieved through propagation-based phase contrast and state-of-the-art X-ray staining techniques [Busse, 2018b; Müller, 2018].

Throughout this work, the NanoCT was further characterised and optimised with respect to CT acquisition and image processing. Moreover, applications were explored in the fields of correlative microscopy for zoology [Ferstl, 2018; Ferstl, 2019] and 3D histology [Ferstl, 2020a; Ferstl, 2020b].

Chapter 2-4 lays the theoretical groundwork to promote a better understanding of the methods and the results that follow in the subsequent chapters. Chapter 2 outlines the fundamental physical principles of an X-ray tube, in general, and fine-focus X-ray tubes, in particular. Chapter 3 addresses the theory underlying the image formation principles of the NanoCT: attenuation and propagation-based phase effects. Chapter 4 sets the NanoCT in context to the general research field of X-ray nanotomography. Hence, the basic concepts of CT are explained, followed by a presentation of the most important 3D X-ray microscopy techniques.

In Chapter 5, the methods used and developed in the course of this work are presented. This includes the configuration of the NanoCT and its components, as well as crucial processes for tomography acquisition with the NanoCT and the revised image processing framework.

Insights into further optimising and characterising the performance of the NanoCT are provided in Chapter 6. Thereby, the chapter mostly focuses on the source acceleration voltage and its influence on several indicators for the NanoCT's imaging performance. Afterwards, Chapter 7 investigates the two contrast enhancing mechanisms which are most relevant in the NanoCT: X-ray staining and propagation-based phase contrast. Thereby, the chapter reveals numerous empirical findings which may be particularly useful during the development of novel staining routines for the NanoCT.

In Chapter 8 and 9, two fields of application of the NanoCT are presented. While Chapter 8 performs a feasibility study of integrating the NanoCT into a correlative microscopy work-flow and presents its benefits for the field of zoology, Chapter 9 evaluates the NanoCT's potential for contributing to future tissue diagnostics by examining a multitude of human tissue specimens [Ferstl, 2020a; Ferstl, 2019; Ferstl, 2020b].

Finally, the most important conclusions arising from the previous chapters are summarised and possible future projects and developments of the NanoCT are outlined in Chapter 10.

Basic Concepts of an X-ray Tube 2

The X-ray tube in its original form (Fig. 2.1), as designed by W. D. Coolidge in 1912, is merely comprised of a heated cathode in vacuum emitting electrons which are accelerated towards a metal anode to generate X-rays [Als-Nielsen, 2011]. In modern X-ray tubes the anode is no longer used for X-ray generation, but includes a hole aperture to allow for the electrons to pass through. Behind the anode an electro-optical column focuses and aligns the electron beam onto a separate X-ray target [Als-Nielsen, 2011; Tuohimaa, 2008].

This chapter provides an overview of the underlying physical principles and the functioning of the components and basic concepts of modern X-ray tubes. The chapter closes by conveying the characteristic structure of fine-focus X-ray tubes. A more in-depth description of these subjects can be found in [Goldstein, 2018; Tuohimaa, 2008; Egerton, 2005].

2.1 Cathode and Acceleration Gap

The main task of the cathode in an X-ray tube is to emit electrons, which are subsequently accelerated in an electrostatic field within the acceleration gap. Thereby a defined electron beam is generated. Depending on the application, cathode designs range from simple metal filaments to sophisticated single crystal emitters [Als-Nielsen, 2011; Tuohimaa, 2008]. The main goal determining the design of a cathode is typically to optimise the brightness of the electron beam. The brightness is a central parameter to evaluate the cathode performance. The brightness of an electron beam is defined as the electron current per solid angle and unit area. In a rotationally symmetric system, it can be expressed as:

$$\beta = \frac{I}{\pi r^2 \vartheta_c^2}, \tag{2.1}$$

with I the electron current, r the source radius and ϑ_c the beam divergence angle at the cathode [Goldstein, 2018].

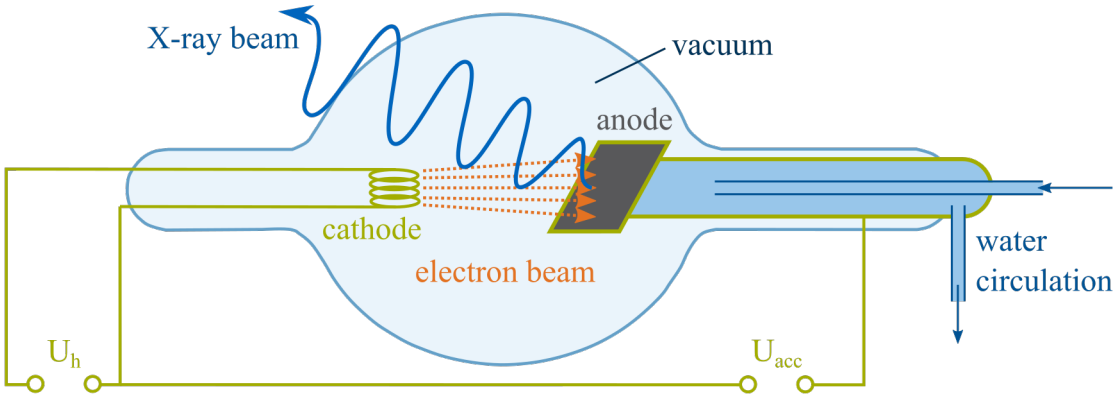

Figure 2.1: **Schematic of a Coolidge Tube.** The X-ray tube consists of an evacuated housing, holding a cathode filament, which is heated with a voltage of U_h. The emitted electrons are accelerated by a voltage U_{acc} towards a water-cooled anode, where they generate X-rays.

2.1.1 Electron Emission

There are three general types of electron emission: thermionic emission, thermal-field emission and cold-field emission. Since thermal-field and cold-field emission require ultra-high vacuum and only provide low beam currents, most fine-focus X-ray tubes are predominantly based on thermionic emission. Thermionic emission can be expressed by the Richardson-Dushman equation:

$$j = AT^2 \exp\left[-\frac{e(\psi_W - \psi_{qt})}{k_B T}\right], \tag{2.2}$$

with j the resulting current density, A a material-specific constant, T the cathode temperature, ψ_W the material-specific work function and ψ_{qt} a correction factor for quantum tunneling. The correction factor ψ_{qt} largely depends on the cathode geometry.
In Fig. 2.2 a, b the fundamental principle explaining thermionic emission is shown. At room temperature ($T \approx 300\,\mathrm{K}$) the Fermi-Dirac distribution lies below the energy threshold E_V which is the minimum energy of an electron required to be emitted from the conduction band. At high temperatures ($T \approx 1500\,\mathrm{K}$) the Fermi-Dirac distribution extends and a proportion of electrons is thermally excited beyond the energy threshold E_V. Thereby, on the cathode surface, an electron cloud is formed with an arbitrary motion orientation and a Maxwellian energy distribution featuring an expectation value of $k_B T$ [Orloff, 2008].
Considering these physical mechanisms, most metal and semiconductor materials qualify for thermionic emission given suitable conditions. Certain criteria (vacuum requirements, operation temperature, surface flatness, achievable levels of emission currents,

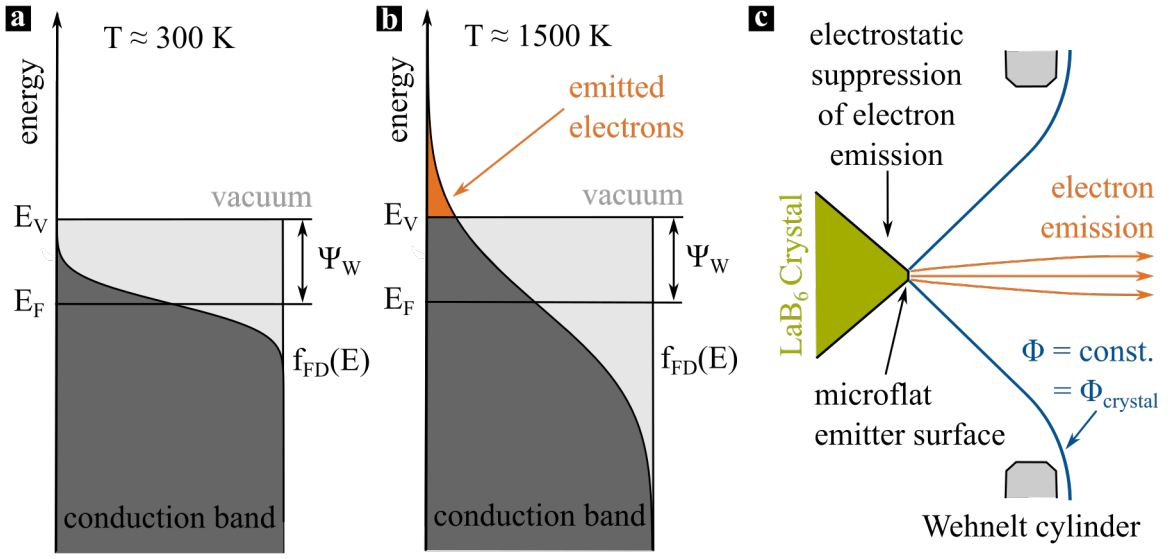

Figure 2.2: **Electron Emission.** (a), (b) The principle of thermionic emission described by the Richardson-Dushman equation. (a) At room temperature, the Fermi-Dirac distribution f_{FD} lies below the vacuum energy E_{V}. (b) For T $\approx$ 1500 K, f_{FD} extends beyond E_{V} to emit electrons. (c) A typical LaB_6 cathode with Wehnelt cylinders creating an equi-potential surface ($\phi = const.$) around the crystal and confining electron emission to a microflat emitter surface. Panels adapted from [Ferstl, 2015].

and cathode lifetime), however, render the single crystal materials LaB_6 and CeB_6 particularly attractive as thermionic emitters. An especially relevant factor is material purity, as slight discrepancies in the work function of an emitter material lead to non-uniform emission and result in increased emission source sizes. Small emission sources, however, are a prerequisite for electron microscopy and fine-focus X-ray tubes. This is why electron microscopes and fine-focus X-ray tubes typically rely on LaB_6 and CeB_6 as emitter materials [Humphries, 1990]. A detailed analysis of emitter materials can be found in [Tuohimaa, 2008].
Figure 2.2 c presents a typical configuration of a thermionic LaB_6-cathode. The figure depicts special electrodes (Wehnelt cylinders), which are used to confine the emission source size to the microflat surface on the crystal via electrostatic suppression of electron emission on the side planes [Orloff, 2008].

2.1.2 Electron Acceleration

In the acceleration gap, the emitted electrons are accelerated in an electrostatic field of an acceleration voltage U_{acc}. The acceleration voltage U_{acc} is applied to provide a constant negative potential on the cathode surface and the ground potential at the anode. Thereby, the diffuse cloud of electrons from the cathode surface is transformed into a well-defined electron beam. Due to high-voltage breakdown, the maximum achievable energy lies around $0.5-1\,\mathrm{MeV}$. Reaching energies beyond this limit demands advanced techniques, such as radio frequency acceleration. Conventional X-ray sources typically feature acceleration voltages in the range of $100\,\mathrm{kV}$ [Sedlacek, 1996].

2.1.3 Emittance

The emittance is one of the central quantities to characterise beam quality. It is defined as the product of a beam spot size and a beam divergence angle. In the following, we will focus on the thermal emittance, which describes the minimum phase space volume that can be reached using a thermionic cathode.
During thermionic emission, electrons are emitted under a random exit angle with a Maxwellian energy distribution featuring an expectation energy value of $k_B T$ (with T the cathode temperature). This introduces a divergence in the emitted electron beam. During acceleration in the electrostatic field of the voltage U_{acc}, a velocity contribution parallel to the electrostatic field is added and the divergence of the electron beam is reduced. In a rotationally symmetric system, the thermal emittance $\epsilon_{thermal}$ can therefore be expressed as follows:

$$\epsilon_{thermal} = r_c \cdot \vartheta_c = r_c \cdot \left[\frac{\pi k_B T}{e U_{acc}}\right]^{1/2}, \tag{2.3}$$

whereby r_c represents the radius of the emission source and ϑ_c the divergence of the beam at the cathode [Worster, 1969].

The emittance is conserved in an optical system. In other words, the emittance at the cathode ϵ_c has the same value as the emittance of the focused electron beam onto the X-ray target ϵ_f:

$$\epsilon_c = r_c \cdot \vartheta_c = r_f \cdot \vartheta_f = \epsilon_f. \tag{2.4}$$

This principle is further illustrated in Fig. 2.3. Moreover, for an isotropic beam the emittance and the brightness are connected via the following relationship:

$$\beta = \frac{I}{\pi \epsilon^2}. \tag{2.5}$$

Thus, the emittance can be interpreted as an indirect measure for the brightness β, but without an electron current contribution I.

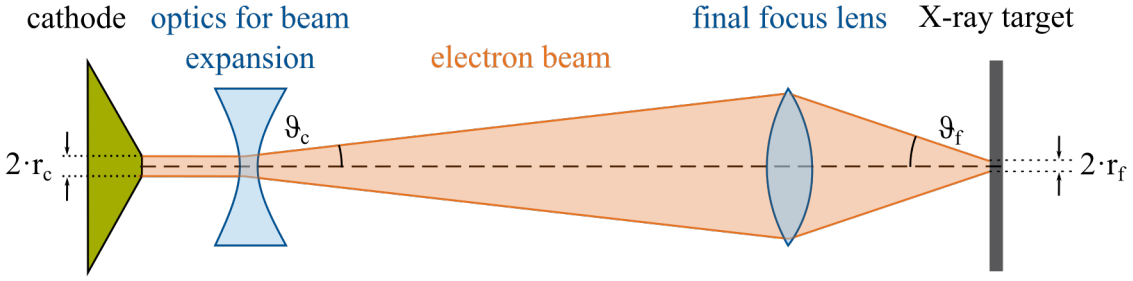

Figure 2.3: **Conservation of Emittance in an Electro-Optical System.** The emittance of the electron beam from the cathode with the opening angle ϑ_c and the emission source radius r_c is equal to the emittance at the X-ray target with the focusing angle ϑ_f and the focal spot radius r_f.

The concept of emittance conservation is particularly powerful for optimising the focal spot size r_f onto the X-ray target. Since the focusing angle ϑ_f is limited, the cathode emittance ϵ_c can be reduced to minimise the focal spot. Reductions in the cathode emittance can be achieved by decreasing either the emission spot size r_c through the use of apertures or by decreasing the divergence ϑ_c. According to Eq. 2.3, this is accomplished by reducing the cathode temperature or by increasing the acceleration voltage. The minimisation of the cathode emittance is, however, limited due to space-charge forces [Humphries, 1990; Hawkes, 2018].

2.2 Electro-Optical Column

The electro-optical column is formed by an array of electron lenses. It is used to further shape and align the electron beam accordingly with either electric or magnetic fields. Therefore, the principle of all electron lenses is based on the Lorentz force law:

$$\frac{d\vec{p}}{dt} = q\left(\vec{E} + \vec{v} \times \vec{B}\right). \tag{2.6}$$

Eq. 2.6 describes the change in relativistic momentum $\vec{p}$ over time of a charge q, which travels through an electrostatic field $\vec{E}$ and a magnetic field $\vec{B}$ with a velocity of $\vec{v}$ [Meschede, 2015].
The geometric shape of an electrostatic or a magnetic electron lens defines its purpose. According to the geometry and their function, electron lenses can be assigned to three different categories: rotationally symmetric, dipole and multipole. Rotationally symmetric lenses are used for focusing and correspond to round lenses in visible-light optics. Dipole lenses are mostly applied for beam deflection and are equivalent to mirrors or cylinder lenses in visible-light optics. Finally, multipole lenses are used for aberration

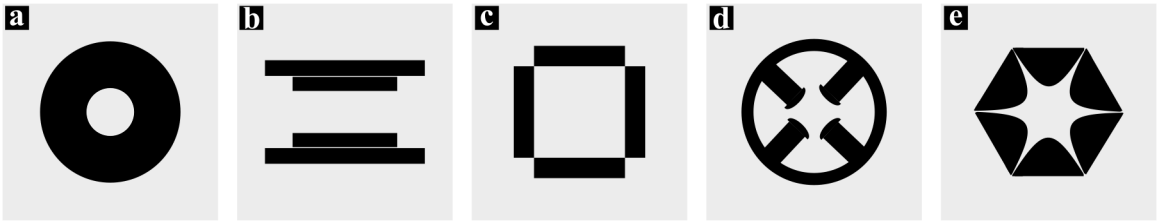

Figure 2.4: **Typical Geometries of Electron Lenses.** (a) rotationally symmetric, (b) dipole (deflection in one direction), (c) double-dipole (deflection in two directions), (d) line focusing quadrupole, (e) sextupole. Figure adapted from [Ferstl, 2015].

corrections, such as quadrupole lenses for astigmatism corrections. In Fig. 2.4, some of the most common electro-optical geometries are displayed [Tuohimaa, 2008].

Just as visible-light optics, electron optics are prone to aberrations. There are field aberrations (field curvature), which result in distortions, off-axis aberrations (such as coma and third-order astigmatism) and axial aberrations (chromatic or spherical aberrations and axial astigmatism). In well-aligned optical systems, field aberrations and off-axis aberrations are negligible. Thus, the most relevant aberrations are axial aberrations [Tuohimaa, 2008].
In electron optics, chromatic aberrations are caused by varying electron energies due to slight voltage deviations from the high-voltage generator and due to the Maxwellian energy distribution from thermionic emission. These energy deviations result in different focusing lengths along the optical axis. A variation in focusing lengths can further originate from imperfections of the focus lens, which are referred to as spherical aberrations. Axial astigmatism describes a deviation in focusing lengths for different orientations perpendicular to the optical axis. All these aberrations contribute to a lower limit of the electron focal spot size. In other words, the electron beam cannot be focused to a point, but to a disk with an increasing radius for increasing aberration severity [Orloff, 2008; Ong, 1998].

2.3 X-ray Target

After manipulating the electron beam into a desired shape, the electrons impinge upon a metal target, and generate among other side-products X-ray photons [Als-Nielsen, 2011].

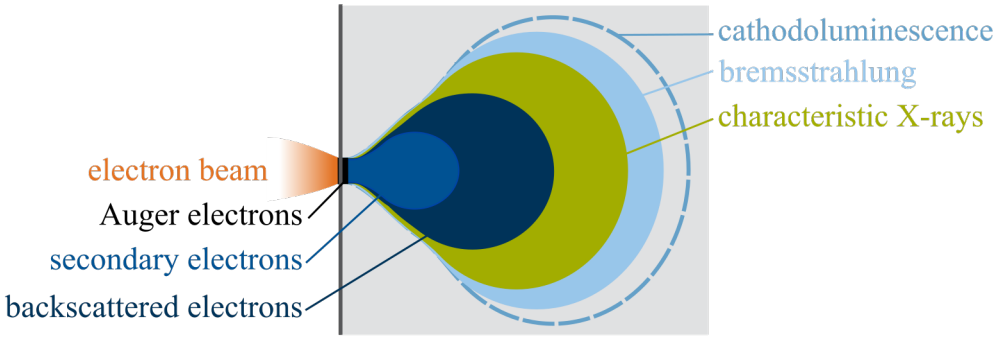

Figure 2.5: **Electron-Matter Interactions.** A typical electron interaction volume inside a material (grey area) with the characteristic zones and the associated dominant physical effect. Characteristic X-rays are only emitted within a region with an electron energy $E \geqslant E_C$, the characteristic energy. Bremsstrahlung is produced down to electron energies of $E = 0\,\mathrm{keV}$. Secondary fluorescence is generated in a larger area than the electron interaction volume. Figure adapted from [Ferstl, 2015].

2.3.1 Electron Matter Interactions

As the electrons travel through the target material, they dispose their energy along their trail. A large proportion of the electron energy in the X-ray target is converted into heat (99.5 % for $U_{acc} = 60\,\mathrm{kV}$) [Hendee, 2003]. The rest of the electron energy triggers a variety of physical processes leading to a number of products: Auger electrons, secondary electrons, backscattered electrons, characteristic X-rays and bremsstrahlung, and secondary X-ray fluorescence. These processes largely depend on the electron energy, and can be assigned to specific zones within the electron interaction volume. Such an interaction volume is depicted in Fig. 2.5.

Secondary electrons appear due to inelastic scattering of an incoming electron with an outer-shell electron. They typically only hold small kinetic energies up to 100 eV. The trajectory of a non-relativistic electron is indirectly proportional to the energy, as shown in Eq. 2.8. Thus, the range of secondary electrons is very limited and secondary electrons are only emitted close to the target surface (Fig. 2.5) [Egerton, 2005; Krieger, 2009].
If an inner shell electron is ejected by an incoming electron, a shell transition of an electron from a higher-energy level occurs and results in a release of energy. This energy can either be emitted as a characteristic X-ray photon with a defined energy or through the ejection of a so-called Auger electron.
Backscattered electrons are elastically scattered electrons, which can leave the target material even from deeper regions given their kinetic energy prior to the scattering

process was still large enough. The amount of backscattered electrons is closely related to the incidence angle of the incoming electron beam and the atomic number of the target material.
These electron signals hold useful information about the target material (Auger electrons, backscattered electrons) or the surface topology (secondary electrons) and are consequently widely used in electron microscopy for image formation or spectroscopy [Egerton, 2005]. For X-ray imaging, however, backscattered electrons can create secondary X-ray sources in the field-of-view (FOV) of the imaging system and, thus, considerably affect the image quality.
While characteristic X-rays are confined to a volume with an electron energy of $E \geqslant E_{\mathrm{C}}$, bremsstrahlung is generated in the entire interaction volume ($E \geqslant 0\,\mathrm{keV}$) (Fig. 2.5). It originates from the electron being deflected from its trajectory by the Coulomb field of the atomic nucleus. This loss in the kinetic energy of the electron is converted into an X-ray photon. This process is stochastic and leads to a continuous X-ray spectrum. The X-ray photons (bremsstrahlung, characteristic X-rays) originating from electron matter interactions can generate a secondary X-ray spectrum, which also consists of characteristic X-rays but with lower energies. This effect is called secondary X-ray fluorescence and occurs over a much larger area than the actual electron interaction volume, as depicted in Fig. 2.5 [Goldstein, 2018].
The total rate of energy loss of along an electron's trajectory in matter can be expressed by the Bethe formula:

$$\frac{dE}{dx} = -7.85 \cdot \left(\frac{Z \cdot \rho}{A \cdot E}\right) \ln\left(1.166 \cdot \frac{E}{J}\right), \tag{2.7}$$

with dE/dx the energy loss per distance, Z the atomic number, ρ the material density, A the nucleon number, E the electron energy, and J the mean ionisation potential ($J = (9.76Z + 58.8Z^{-0.19}) \cdot 10^{-3}$ keV). From Eq. 2.7, the length of the electron trajectory R_{Bethe}, which is also referred to as the Bethe range, can be calculated:

$$R_{\mathrm{Bethe}} = \int_{E_0}^{0} -\left(\frac{dE}{dx}\right)^{-1} dE = \cdots \propto \frac{f_1(E_0)}{f_2(Z,\rho)}, \tag{2.8}$$

with $f_1(E_0)$ a function of the incident electron energy E_0 and $f_2(Z,\rho)$ a material specific function [Krieger, 2009; Tuohimaa, 2008; Goldstein, 2018]. The trajectory followed by the electrons in matter, however, is very complex due to elastic scattering processes. To estimate the size of an electron matter interaction volume considering both inelastic and elastic scattering processes, the Kanaya Okayama range $R_{\mathrm{K-O}}$ is conventionally used. This range, which is defined as the radius of a hemisphere containing 95 % of electron trajectories, is described the following expression:

$$R_{\mathrm{K-O}} = 27.6 \frac{A}{Z^{0.89} \cdot \rho} \cdot E_0^{1.67}, \tag{2.9}$$

whereby A denotes the nucleon number, Z the atomic number, ρ the material density and E_0 the energy of the incoming electron [Goldstein, 2018].
From this it can be deduced, that an increase in electron energy means an increase in the interaction volume, whereas an increase of the atomic number causes smaller interaction volumes. For more precise investigations of the interaction volume, Monte Carlo simulations of the electron trajectories are necessary [Goldstein, 2018]. According to such Monte Carlo simulations, the shape of the interaction volume changes from a pear-like shape for low-Z materials to a hemisphere shape for high-Z materials. In contrast to that, the electron energy E_0 has no influence on the shape of the interaction volume, but significantly affects the size. For instance, in a Cu X-ray target an incident electron beam with $E_0 = 30\,\mathrm{keV}$ creates an interaction volume with an approximate depth of $1.2\,\mu\mathrm{m}$, while electrons with an energy $E_0 = 20\,\mathrm{keV}$ only generate a volume with a depth around $700\,\mathrm{nm}$ [Goldstein, 2018].

2.3.2 X-ray Generation

While the electron signals shown in Fig. 2.5 are extremely valuable to electron microscopy, in X-ray tubes only X-ray generation processes are relevant (Fig. 2.6a). According to Kramers, the intensity distribution of the bremsstrahlung I_{brems} can be estimated with the following expression:

$$I_{\mathrm{brems}}(E) \approx I \cdot Z \frac{E_0 - E}{E}, \tag{2.10}$$

with I the incident electron current onto the X-ray target, E_0 the energy of the incident electrons. Thereby, the electron energy E_0 can be derived from the acceleration voltage ($E_0 = e \cdot \mathrm{U_{acc}}$) and defines the maximum photon energy of the continuous X-ray spectrum [Goldstein, 2018].
The overlay of the continuous energy distribution of bremsstrahlung and the characteristic X-ray peaks results in an X-ray spectrum as shown in Fig. 2.6b. The spectrum in Fig. 2.6 stems from a tungsten target with the characteristic X-ray peaks situated at $E_{\mathrm{K}_\alpha} \approx 59\,\mathrm{keV}$ and $E_{\mathrm{K}_\beta} \approx 67.3\,\mathrm{keV}$. For large electron energies ($E > 100\,\mathrm{keV}$), the X-ray spectrum is emitted in the direction of the incident electron beam. For electron energies below $100\,\mathrm{keV}$, the angular radiation emission distribution is more similar to a dipole, with two emission maximums around 60° from the incident electron beam. This is, however, only the case for very thin material layers. In typical X-ray targets, the diffusion of electrons plays an increasing role, leading to a more homogeneous X-ray emission cone beam with a large divergence angle [Krieger, 2009].

For selecting the optimum X-ray target material, the efficiency for bremsstrahlung and characteristic X-ray emission is an important parameter. The efficiency η for

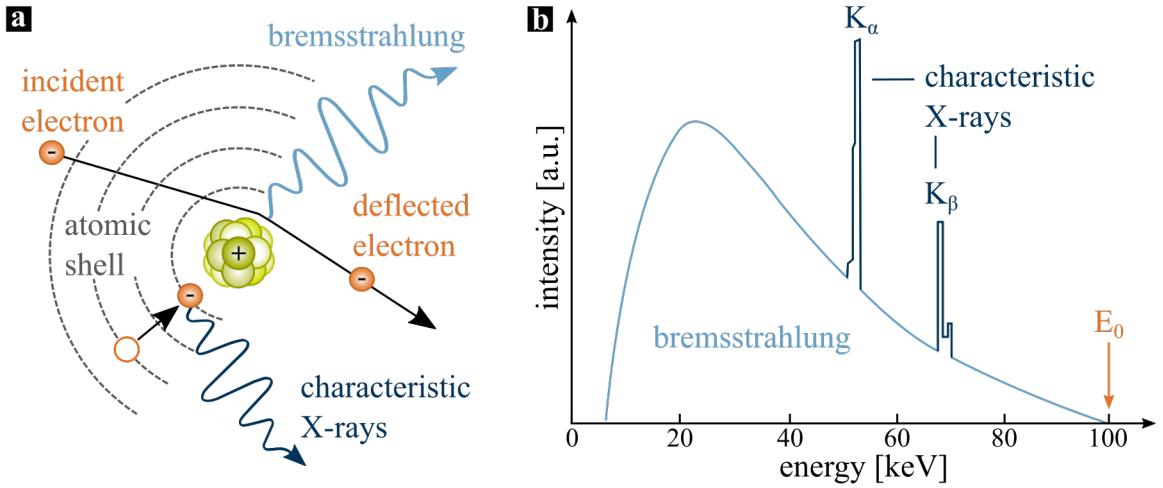

Figure 2.6: **X-ray Generation via Electron-Matter Interactions.** (a) Schematic of the physical processes causing bremsstrahlung and characteristic X-rays. (b) Schematic of a typical X-ray tube spectrum consisting of a continuous energy distribution of bremsstrahlung and the characteristic emission lines K_α and K_β of a tungsten target. The acceleration voltage determines the maximum photon energy of 100 keV. Panels adapted from [Ferstl, 2015].

bremsstrahlung can be calculated as:

$$\eta = K Z \frac{E_0}{e}, \tag{2.11}$$

with a material constant K ($K = 9.2 \cdot 10^{-7}$ kV^{-1}), Z the atomic number, and E_0 the energy of the incident electrons of the X-ray tube. In case of characteristic X-rays, the number of produced K_α photons per electron, can be determined with the following formula:

$$N = N' \left(E_0 - E_{K_\alpha}\right)^{1.63}, \tag{2.12}$$

with a material constant N', the incident electron energy E_0, and E_{K_α} the energy to eject an electron from the K shell of the atom. N' strongly decreases for higher atomic numbers Z [Tuohimaa, 2008]. These two equations imply that higher electron energies are directly associated with a greater yield of X-ray photons. Furthermore, materials with high atomic numbers Z result in more bremsstrahlung, but less emission of characteristic X-rays from the K shell. However, for higher Z materials additional shell transitions are available. Therefore, materials with relatively high atomic numbers such as tungsten ($Z = 74$) and copper ($Z = 29$) are conventionally chosen for X-ray targets [Tuohimaa, 2008; Buzug, 2008].

2.4 Fine-focus X-ray Tubes

There is a wide variety of X-ray tube configurations tailored to specific applications. X-ray tubes which strive for high brightness, mostly struggle with disposing of the large amounts of heat generated inside an X-ray target with high impinging electron currents. There are two approaches to solve this problem: One approach is to use a rotating X-ray target and to distribute the heat over a larger target volume (rotating anode X-ray tube). Another concept uses a liquid metal jet for X-ray generation (liquid metal jet source). Such a liquid metal jet transports the heat away from the electron impact region through a constant material current [Als-Nielsen, 2011; Tuohimaa, 2008]. The main aim of fine-focus X-ray tubes (microfocus, nanofocus) is to minimise X-ray focal spot sizes, and thus enable high resolution X-ray imaging. The ability of an X-ray tube to generate fine focal X-ray spots depends on the cathode emittance, the focusing-ability of the electro-optical column (aberrations), the material and the thickness of the X-ray target (size of the interaction volume). These parameters are all closely connected to the acceleration voltage $\mathrm{U_{acc}}$ [Tuohimaa, 2008].
The total effective electron spot radius can be calculated with the following expression:

$$r_{\mathrm{total}} = \sqrt{r_\beta^2 + r_{\mathrm{Ch}}^2 + r_{\mathrm{S}}^2}. \tag{2.13}$$

Here, the total electron spot radius on the X-ray target r_{total} is defined by the brightness-limited electron spot size r_β and the spot size enlargement due to aberrations (chromatic: r_{Ch}, spherical: r_{S}). The minimum, brightness-limited spot radius r_β is described as follows:

$$r_\beta = \sqrt{\frac{I}{\pi^2 \beta \vartheta_{\mathrm{f}}^2}}, \tag{2.14}$$

with I the target current, β the brightness and ϑ_{f} the focusing angle onto the X-ray target. According to Eq. 2.5, the brightness can be expressed by the emittance. Thereby, we can transform Eq. 2.14 to calculate the emittance-limited spot radius r_ϵ:

$$r_\beta = r_\epsilon \approx \sqrt{\frac{1}{\pi}} \frac{\epsilon_{\mathrm{c}}}{\vartheta_{\mathrm{f}}} = \sqrt{\frac{k_{\mathrm{B}} T}{e \mathrm{U_{acc}}}} \frac{r_{\mathrm{c}}}{\vartheta_{\mathrm{f}}}. \tag{2.15}$$

Since the emittance is conserved in an optical system, we chose to use ϵ_{c} as the relevant parameter.

The electron spot size enlargement due to chromatic aberrations r_{Ch} can be written as follows:

$$r_{\mathrm{Ch}} = \frac{1}{8} C_{\mathrm{Ch}} \frac{\Delta \mathrm{U_{acc}}}{\mathrm{U_{acc}}} \vartheta_{\mathrm{f}}, \tag{2.16}$$

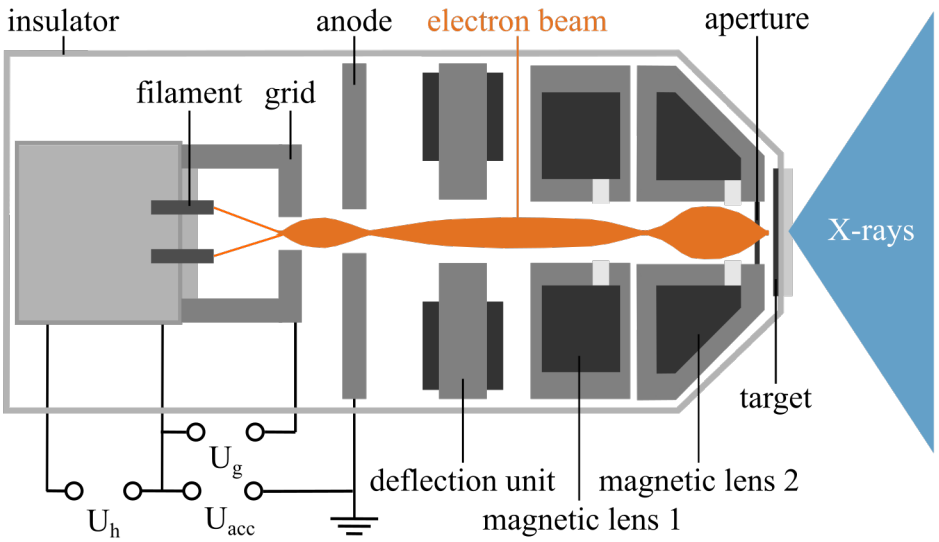

Figure 2.7: **Configuration of a Nanofocus X-ray Tube.** The tube housing provides insulation against outside electro-magnetic influences. The filament and the grid with the grid voltage U_g and the heating voltage U_h form the cathode. The emitted electrons are further accelerated by the acceleration voltage U_{acc}. The resulting electron beam is shaped and aligned in the electro-optical column - deflection unit, magnetic lens 1, magnetic lens 2 - to hit the transmission target to generate an X-ray beam. Figure adapted from [Ferstl, 2015].

with C_{Ch} the chromatic aberration coefficient ($C_{Ch} \propto 1/U_{acc}$) and $\Delta U_{acc}/U_{acc}$ the monochromaticity of the electron beam.
The spherical contributions r_S are described by the following term:

$$r_S = \frac{1}{8} C_S \vartheta_f^3, \tag{2.17}$$

with C_S the spherical aberration coefficient ($C_S \propto 1/{U_{acc}}^2$) [Tuohimaa, 2008]. All contributions to the total electron spot size are proportional to the reciprocal of the acceleration voltage as U_{acc} or ${U_{acc}}^2$. According to these findings, it can be stated that an increase in the acceleration voltage should theoretically result in a decrease of the electron spot size r_{total} onto the X-ray target.

Apart from the electron spot size, the size of the interaction volume inside the X-ray target is crucial for the final X-ray focal spot size. The size of the electron spot and the X-ray spot are not necessarily equal. The expansion of the interaction volume, from which the X-rays are emitted, determine the resulting X-ray focal spot. As the interaction volume even of rather low energy electrons of 30 keV reaches depths around

1.2 µm, thin X-ray targets ($d < 1$ µm) constrain the interaction volume [Withers, 2007]. Thus, the expansion from the electron to the X-ray spot is reduced and adjusting the acceleration voltage U_{acc} has a smaller impact on the expansion. However, by reducing the interaction volume, the efficiency of X-ray generation is significantly reduced [Goldstein, 2018]. By selecting high-Z materials (such as tungsten) for X-ray targets, the linear dimensions of the interaction volume and thereby the X-ray spot size can be decreased.

Taking these considerations into account, the optimum design of a fine-focus X-ray tube minimises cathode emittance, optical aberrations and employs high-Z materials in thin X-ray targets. A configuration of such a fine-focus X-ray tube is illustrated in Fig. 2.7. A small diameter of the hole aperture in the anode (Fig. 2.7) confines the emittance dependent spot radius r_c and the divergence angle ϑ_c and thus leads to a small emittance value ϵ_c. This way, a large amount of electrons is lost and generates small electron currents I. To minimise aberrations, the electro-optical column typically consists of a sophisticated array of electron lenses of at least one focus lens, a deflection and an alignment unit, and in some cases quadrupole lenses for astigmatism correction [Tuohimaa, 2008]. In Fig. 2.7 the electron beam then hits the thin transmission target to emit a fine-focus X-ray cone beam with a large divergence angle.

Fundamentals of X-ray Imaging 3

After a detailed report over the relevant physical processes in fine-focus X-ray tubes in Chapter 2, this chapter will provide deeper insights into the theoretical principles of X-ray imaging. The relevant X-ray matter interactions will be investigated on both a microscopic and a macroscopic scale, according to the wave-particle duality of light. Thereby, attenuation and phase shift as contrast-forming principles will be explained. Subsequently, the chapter will focus on the propagation of X-rays behind a sample, introducing the transport of intensity equation and the concept of coherence. Thus, a fundamental understanding of the underlying principles of attenuation-based and phase-contrast X-ray imaging is provided.

3.1 X-ray Interactions in Matter

X-rays travelling through matter are involved in a number of physical processes. In the following, these processes are first explained on a microscopic scale, considering the incident X-rays as photons. Subsequently, the macroscopic effects caused by these interactions are described, considering the X-rays as waves.

3.1.1 Microscopic Description of X-ray Matter Interactions

To explain the processes on an atomic scale, X-rays are considered as a beam of photons. The energy of these X-ray photons E_i typically lies inside an interval ranging from the binding energy of inner-shell electrons inside an atom and below the energy threshold of pair production 1022 keV. As a consequence, the photons mostly interact with the shell electrons of a material. Fig. 3.1 provides an overview of these interactions: Photoelectric absorption (Fig. 3.1b), elastic scattering or Rayleigh scattering (Fig. 3.1c), inelastic scattering or Compton scattering (Fig. 3.1d).
The probability of each of these processes, can be expressed by the respective cross-section: the photoelectric cross-section σ_ph, the coherent cross-section σ_el and the Compton cross-section σ_inel. The sum of these cross-sections gives the total attenuation cross-section of a material:

$$\sigma_\mathrm{tot} = \sigma_\mathrm{ph} + \sigma_\mathrm{el} + \sigma_\mathrm{inel}. \tag{3.1}$$

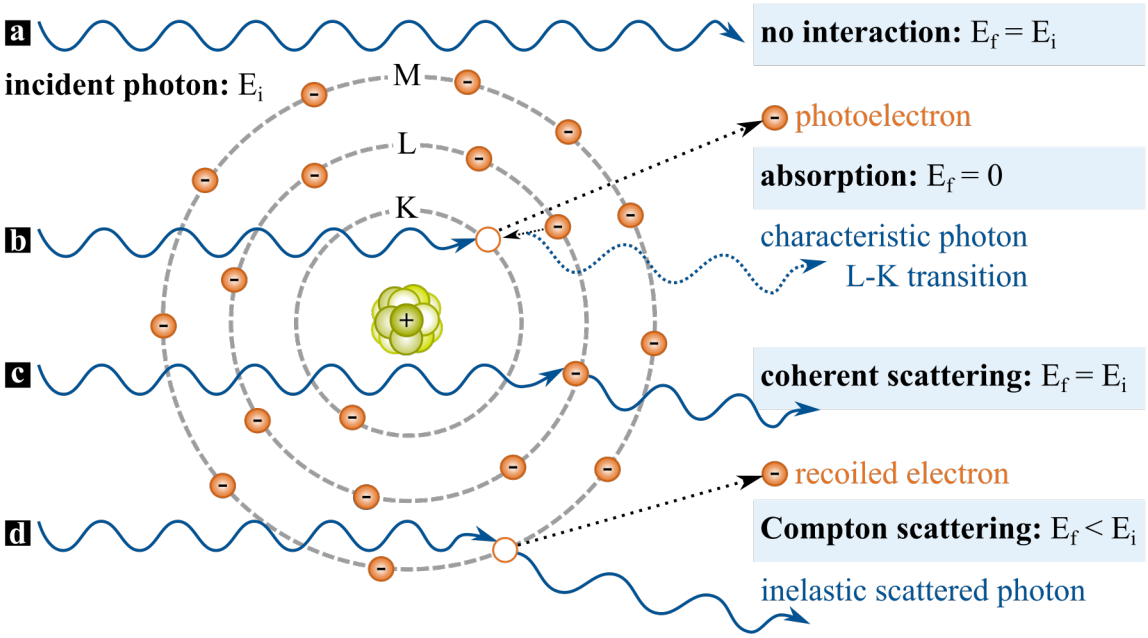

Figure 3.1: **Overview of X-ray Matter Interactions.** E_i is the initial energy of the incident X-ray photon ($E_i < 1\,\text{MeV}$) and E_f is the final photon energy. (a) No interaction: the final and the initial photon energy are equal ($E_f = E_i$). (b) Photoelectric absorption: the X-ray photon is absorbed ($E_f = 0$) and ejects an inner-shell electron. Another electron fills the remaining hole and releases a characteristic X-ray photon. (c) Elastic scattering (coherent): the photon's energy is preserved ($E_f = E_i$). (d) Inelastic scattering (Compton): the X-ray photon transfers part of its energy to the electron ($E_f < E_i$). Figure based on [Seibert, 2005].

The relation of these cross-sections with the energy of the incident X-ray photon E_i is plotted in Fig. 3.2 for the two different materials carbon, and osmium. Carbon is one of the main constituents of soft tissue and osmium is widely used for staining in TEM or X-ray applications [Müller, 2017; Gross, 2019; Handschuh, 2013].

Photoelectric Absorption

As illustrated in Fig. 3.1b, an incident X-ray photon with an energy E_i interacts with an inner-shell electron with a binding energy E_b. During this interaction, the photon transfers its entire energy to the electron, leading to the electron's ejection. The X-ray photon is fully absorbed with a final energy of $E_f = 0$. The excess energy is transferred to the ejected electron in the form of kinetic energy ($E_{kin} = E_i - E_b$). For

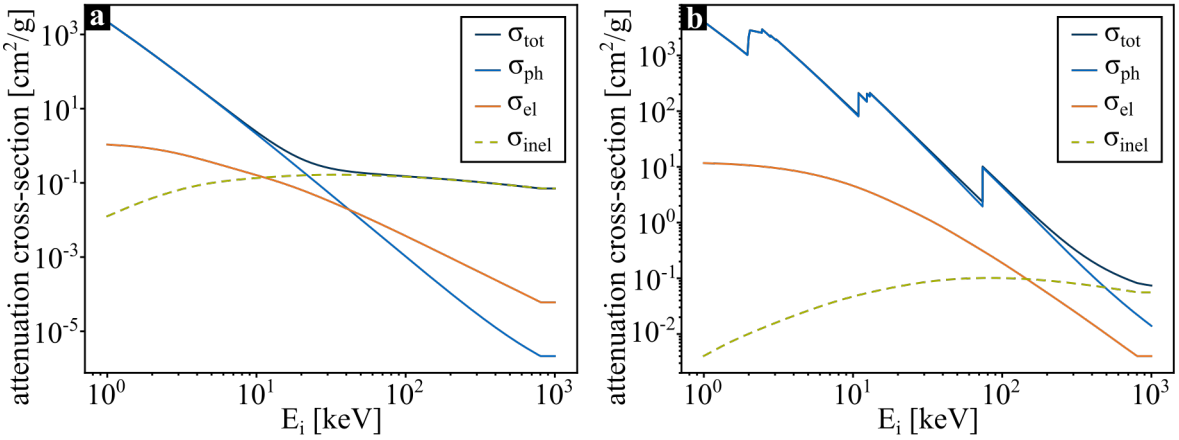

Figure 3.2: **Attenuation Cross Section for Different Energies.** (a), (b) Attenuation cross section of carbon ($Z = 6$, a), osmium ($Z = 76$, b) in cm^2/g. Legend: σ_{tot}: the total attenuation cross-section, $\sigma_{\mathrm{ph}}/\sigma_{\mathrm{el}}/\sigma_{\mathrm{inel}}$: the attenuation cross-section due to photoelectric absorption/elastic scattering/inelastic scattering. E_{i}: the energy of the incident X-ray photon. Cross-section values according to [Schoonjans, 2011].

the photoelectric absorption to happen the initial energy E_{i} of the photon has to be larger than the binding energy E_{b}. The ejected electron leaves a hole in the inner shell, which is then refilled by an electron from a higher energy state releasing the energy difference as a characteristic X-ray photon.
The probability of the occurrence of photoelectric absorption can be expressed by the absorption cross-section σ_{ph}. The value of σ_{ph} exhibits a sudden increase at the specific binding energies E_{b} of the inner-shell electrons of an atom, since photoelectric absorption is most likely to occur for photon energies equal or slightly above the electron binding energy. This can be clearly seen in Fig. 3.2b at multiple energy values for an osmium atom, representing the binding energies of electrons from different inner shells (K, L, M).
Apart from these discontinuities, the behaviour of the photoelectric cross-section can be estimated as:

$$\sigma_{\mathrm{ph}} \propto \frac{Z^4}{E_{\mathrm{i}}^3}, \tag{3.2}$$

with Z being the atomic number and E_{i} the initial energy of the X-ray photon. These dependencies become apparent in Fig. 3.2. At this point it should be noted, that there is no exact dependency known and for other approaches the resulting expression differs from Eq. 3.2 [Krieger, 2009; Als-Nielsen, 2011].

Coherent Scattering

This effect is also known as Rayleigh, Thomson or elastic scattering. The X-ray photon does not transfer any energy to the electron during the scattering process and its final energy is equal to its initial energy ($E_\mathrm{f} = E_\mathrm{i}$). This process is illustrated in Fig. 3.1c. The probability or the cross-section for coherent scattering σ_el increases with higher electron numbers and thus higher atomic numbers and decreases for larger photon energies E_i. For X-ray photons with $E_\mathrm{i} > 10\,\mathrm{keV}$, the following dependency can be used:

$$\sigma_\mathrm{el} \propto \rho \cdot \frac{Z^{2.5}}{A \cdot E_\mathrm{i}^2}, \tag{3.3}$$

with ρ the material density and A the atomic mass [Krieger, 2009]. The declining behavior of σ_el for energies above 10 keV is clearly reproduced in Fig. 3.2 [Russo, 2017].

Compton Scattering

Compton scattering is also often referred to as inelastic or incoherent scattering. In contrast to coherent scattering, in Compton scattering a part of the X-ray photon's energy is transferred to a weakly bound electron. The energy of the scattered X-ray photon E_f depends on the initial photon energy E_i and the scattering angle ψ:

$$E_\mathrm{f} = E_\mathrm{i} \cdot \left[1 + \lambda_\mathrm{c} k \left(1 - \cos\psi\right)\right]^{-1}. \tag{3.4}$$

The constant λ_c is defined as the Compton wavelength:

$$\lambda_\mathrm{c} = \frac{\hbar}{m_\mathrm{e} \cdot c} = 3.86 \cdot 10^{-3}\ \text{Å}, \tag{3.5}$$

with m_e the electron mass at rest [Als-Nielsen, 2011]. The behaviour of the attenuation cross section of Compton scattering is shown in Fig. 3.2. As the probability of the occurrence of Compton scattering increases with the number of electrons and thus with the atomic number Z, the Compton cross-section is proportional to Z. However, there is no simple formalism to describe the dependency of the Compton cross-section σ_inel of the incident photon energy E_i. Klein and Nishina found an empirical expression to describe the scattering cross-section of a single electron:

$$\sigma_\mathrm{KN} = 2\pi r_{\mathrm{e}-}^2 \left(\frac{1+\alpha}{\alpha^2} \left[\frac{2(1+\alpha)}{1+2\alpha} - \frac{1}{\alpha} \ln(1+2\alpha) \right] + \frac{1}{2\alpha} \ln(1+2\alpha) - \frac{1+3\alpha}{(1+2\alpha)^2} \right), \tag{3.6}$$

with $r_{\mathrm{e}-}$ the classical electron radius and with:

$$\alpha = \frac{E_\mathrm{i}}{m_\mathrm{e} c^2}. \tag{3.7}$$

Transferring Eq. 3.6 to an entire atom with Z electrons, we obtain:

$$\sigma_{\text{inel}} = Z \cdot \sigma_{\text{KN}}, \tag{3.8}$$

whereby σ_{inel} represents the Compton cross-section of an atom with atomic number Z [Klein, 1929].

3.1.2 Macroscopic Description of X-ray Matter Interactions

The X-ray matter interactions, which were explained on a microscopic scale in the previous section, can be expressed on a macroscopic scale using the formalism of the complex refractive index η:

$$\eta \equiv 1 - \delta + i\beta. \tag{3.9}$$

In this formalism, the X-rays penetrating the sample are considered as an electromagnetic wave. The wavefield thereby experiences a reduction in the amplitude - attenuation - and an increased wavelength introducing a phase shift compared to an unperturbed wave in vacuum. The attenuation is described by the parameter β and the phase shift by δ. Figure 3.3a depicts the attenuation and phase shift of a plane wave through an object with a refractive index η [Als-Nielsen, 2011].

Considering a monochromatic plane wave with an incident energy of $E_{\text{i}} = \hbar\omega$ and a propagation direction z, we obtain the following expression for the wave in vacuum $E(z,t)_{\text{v}}$:

$$E(z,t)_{\text{v}} = E_0 \cdot e^{i(k_0 z - \omega t)}, \tag{3.10}$$

with $\vec{k}_0 = k_0 \vec{e}_{\text{z}}$ the wave vector, ω the wave frequency and E_0 the wave amplitude. Let's further consider the wave travelling through a homogeneous object with a refractive index of η (Eq. 3.9). We assume no change in the propagation direction and no polarisation inside the material. Thus, we obtain for the wave inside the material $E(z,t)_{\text{m}}$:

$$\begin{aligned} E(z,t)_{\text{m}} &= E_0 \cdot e^{i(\eta k_0 z - \omega t)} \\ &= \underbrace{E_0 \cdot e^{-k_0 \beta z}}_{\text{attenuated amplitude}} \cdot \underbrace{e^{-i(k_0 \delta z)}}_{\text{phase shift}} \cdot \underbrace{e^{i(k_0 z - \omega t)}}_{\text{propagation term}} . \end{aligned} \tag{3.11}$$

X-ray Attenuation

When speaking of attenuation, there are two terms to be distinguished: intensity attenuation and amplitude attenuation. Intensity attenuation is conventionally described by the linear attenuation coefficient μ and amplitude attenuation is determined by β.

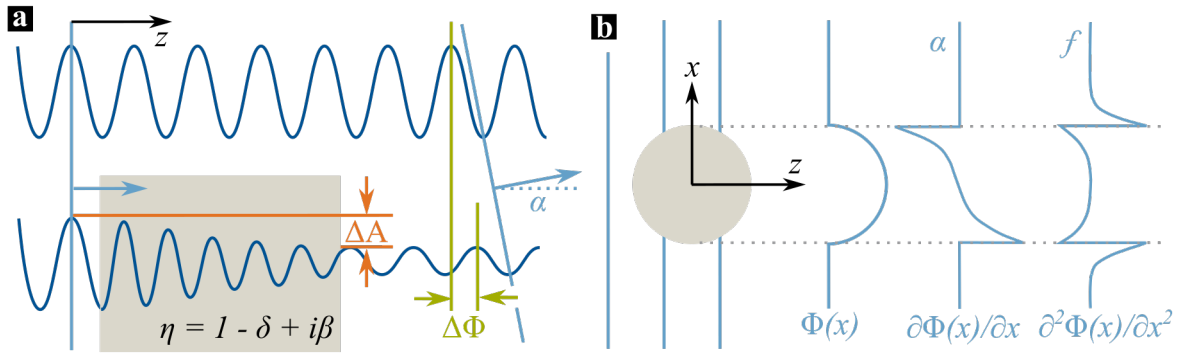

Figure 3.3: **Plane Wave Propagating Through a Sample.** (a) A sample with a refractive index η causes an amplitude reduction ΔA and a phase shift $\Delta\Phi$ in a plane wave. This results in an altered propagation direction of a refraction angle α. (b) A two-dimensional pure phase object in the x-z-plane induces a phase shift $\Phi(x)$. The refraction angle α and the interference fringes f are connected to the derivatives of this phase shift $\Phi(x)$. Figure based on [Wilkins, 1996].

Both variables are closely connected, as the intensity $I(z)$ is proportional to the wavefield amplitude $|E(z,t)|$ squared. Thus, the intensity reduction can be expressed as follows:

$$\frac{I(z)}{I_0} = \frac{|E(z,t)_\mathrm{m}|^2}{|E(z,t)_\mathrm{v}|^2} = e^{-2k_0\beta z}, \tag{3.12}$$

with I_0 the intensity of the incident X-ray wave. Equation 3.12 strongly resembles the Lambert-Beer law, which describes the intensity reduction with the linear attenuation coefficient μ:

$$\frac{I(z)}{I_0} = e^{-\mu z}. \tag{3.13}$$

Investigating the exponents of Eq. 3.12 and Eq. 3.13 reveals a relation between the linear attenuation coefficient μ and the amplitude attenuation coefficient β:

$$\mu = 2k_0\beta. \tag{3.14}$$

The linear attenuation coefficient μ is further defined by the attenuation cross-section per atom σ_tot (Eq. 3.1):

$$\mu = \left(\frac{\rho_\mathrm{m} N_\mathrm{A}}{M}\right) \cdot \sigma_\mathrm{tot}, \tag{3.15}$$

with ρ_m the mass density, N_A Avogadro's number, and M the molar mass [Als-Nielsen, 2011].

As explained in section 3.1.1, many interactions contribute to the total attenuation cross-section. Apart from energies close to the absorption edges, the behaviour of the total atomic attenuation cross-section depends on the incident energy and the material according to the following expression:

$$\sigma_{\mathrm{tot}} \propto \frac{Z^4}{E_{\mathrm{i}}^3}. \tag{3.16}$$

Equation 3.14 and Eq. 3.15 allow for translating this knowledge to obtain the energy and material dependencies of the two attenuation coefficients μ and β:

$$\mu \propto \frac{Z^4}{E_{\mathrm{i}}^3}, \quad \text{and} \quad \beta \propto \frac{Z^4}{E_{\mathrm{i}}^4}. \tag{3.17}$$

This strong variation of μ and β with the atomic number generates the contrast between different materials which is conventionally used in absorption-based X-ray imaging [Als-Nielsen, 2011].

X-ray Phase Shift

As illustrated in Eq. 3.11, an object with a complex refractive index η (Eq. 3.9) causes, apart from a reduced wave amplitude, a certain phase shift. Under the assumption of a homogeneous object, this phase shift $\Delta\Phi$ is determined by the object's thickness z, the wave vector of the incident wave $\vec{k}_0 = k_0\vec{e_{\mathrm{z}}}$ and the real part of the complex refractive index decrements δ:

$$\Delta\Phi = k_0 \delta z. \tag{3.18}$$

While it is rather straight forward to extract the attenuation coefficient β from the intensity distribution of an X-ray projection image (Eq. 3.13), more elaborate techniques have to be used to derive the phase shift and thereby the phase coefficient δ. Figure 3.3b depicts a schematic drawing of the phase shift induced by a pure phase object along with two quantities, which contain information about the phase $\Phi(x)$: the refraction angle α and the interference fringes f.

The refraction of the wavefront arises from the phase shift, as illustrated in 3.3a. The refraction angle α_{x} in x-direction is directly connected to the x-component of the phase gradient of $\Phi(x, y)$ perpendicular to the propagation direction z:

$$\alpha_{\mathrm{x}} = \frac{1}{k_0} \frac{\partial\Phi(x, y)}{\partial x}. \tag{3.19}$$

The refraction angle in y-direction can be calculated in an analogous manner to Eq. 3.19. Techniques based on Talbot-Lau-interferometry allow to determine this refraction angle α. As the refraction angle is used to calculate the phase gradient, such methods are also referred to as differential phase imaging [Pfeiffer, 2006; Als-Nielsen, 2011].

In contrast to that, interference fringes f occur when the refracted wave interferes with the undisturbed wavefront after a certain propagation distance (Fresnel region, see Section 3.2). The interference fringes f along the x-axis can be described by the second derivative of the phase $\Phi(x, y)$ in x-direction:

$$f \propto \frac{\partial^2 \Phi(x, y)}{\partial x^2}. \tag{3.20}$$

Equation 3.20 suggests, that the fringes are most prominent for abrupt changes in the phase coefficient δ or in the sample thickness z, such as occurring at the sample surface or at material interfaces. In an X-ray radiograph behind an object with both phase shifting as well as absorbing properties, the fringes f and the intensity reduction signal due to attenuation are combined. Imaging techniques, which are based on these fringes, are referred to as propagation-based phase-contrast imaging techniques [Clœtens, 1999; Wilkins, 1996].

Beyond that, imaging techniques which derive $\Phi(x, y)$ provide deeper insights into the sample composition. The phase coefficient δ is directly connected to ρ_e the electron number density, $r_{\mathrm{e}-}$ the classical electron radius and k_0 the wave vector ($k_0 = 2\pi/\lambda$):

$$\delta = \frac{2\pi r_{\mathrm{e}-} \rho_\mathrm{e}}{k_0^2}. \tag{3.21}$$

This equation clearly shows that quantitative phase-contrast imaging grants access to the spatial distribution of a material's electron density ρ_e. The wave vector k_0 is directly related to the X-ray wave energy E_i and the electron number density depends on the atomic number Z. Therefore, Eq. 3.21 allows to derive the following formalism about the material and energy dependency of the phase coefficient δ:

$$\delta \propto \frac{Z}{E_\mathrm{i}^2} \tag{3.22}$$

According to Eq. 3.22, the phase coefficient δ decreases less drastically for increasing X-ray energies E_i and decreasing atomic numbers Z, compared to the amplitude attenuation coefficient β. This behaviour can be exploited to achieve adequate contrasts even in low-Z materials, such as soft tissues, at higher X-ray energies with phase-contrast imaging [Born, 1980; Als-Nielsen, 2011; Pfeiffer, 2006]. Therefore, for soft-tissue contrast enhancement, the results presented in this thesis, were generated using propagation-based phase-contrast imaging.

3.2 Free Space Propagation of X-rays

To understand the actual signal received by the detector forming an X-ray image, it is crucial to gain deeper insights into the propagation processes happening after the

X-ray wave has left the sample. Therefore, this section will focus on the basic physics of an X-ray wavefield propagating through free space.

In X-ray imaging the propagation distance R of the wavefield from an object to the detection point defines three regions:

$$\begin{aligned} \text{Fraunhofer region} &: R \gg \frac{a^2}{\lambda} \text{ (far–field)} \\ \text{Fresnel region} &: R \approx \frac{a^2}{\lambda} \text{ (near–field)} \\ \text{Contact region} &: R \ll \frac{a^2}{\lambda}, \end{aligned} \tag{3.23}$$

whereby a denotes the structure size in a sample and λ is the wavelength with $\lambda = 2\pi/k$. The three regions and their implications for the resulting X-ray image are shown in Fig. 3.4.

Figure 3.4a illustrates a coherent plane wave with a wave vector $\vec{k}$ interacting with two objects at the points P and Q. The distance between the two points is defined as the structure size a. Both objects can be interpreted as a point source for a spherical wave.

In the Fraunhofer region, or far-field with distances $R \gg a^2/\lambda$, these spherical waves can be approximated by plane waves with a wave vector $\vec{k}'$. The different propagation distances of the two waves, lead to a well-defined phase difference in the detection point D. Thereby, a diffraction pattern is generated, such as shown in the simulated X-ray image in Fig. 3.4b) on the right. With increasing propagation distances R, the diffraction pattern stays the same except for a decreasing intensity.

In the Fresnel region, or near-field with propagation distances $R \approx a^2/\lambda$, the phase difference is not as well-defined as in the Fraunhofer region (Fig. 3.4b in the centre). With decreasing propagation distances the complex diffraction pattern transforms into edge enhancement (Fig. 3.4b from right to left).

Finally, in the contact region for $R \ll a^2/\lambda$, any phase contributions to the X-ray image have disappeared and only absorption information is reproduced. Thus, in Fig. 3.4b on the left, only the dark blue disks as perfect absorbers are visible, and not the light blue disks as pure phase objects.

It is apparent that the extent of the regions largely depend on the imaged structure size a. For instance, an object with $a = 1\,\text{Å}$ which is illuminated by X-rays with $\lambda = 1\,\text{Å}$, the Fresnel region lies within the scale of $R \approx 1\,\text{Å}$. Thus, all images of this structure are acquired in the Fraunhofer region. In contrast to that, using the same wavelength on a structure size of $a = 1\,\mu\text{m}$ the Fresnel region is in the range of $R \approx 1\,\text{cm}$ and the operator of the X-ray imaging setup can choose the region to acquire the image [Als-Nielsen, 2011].

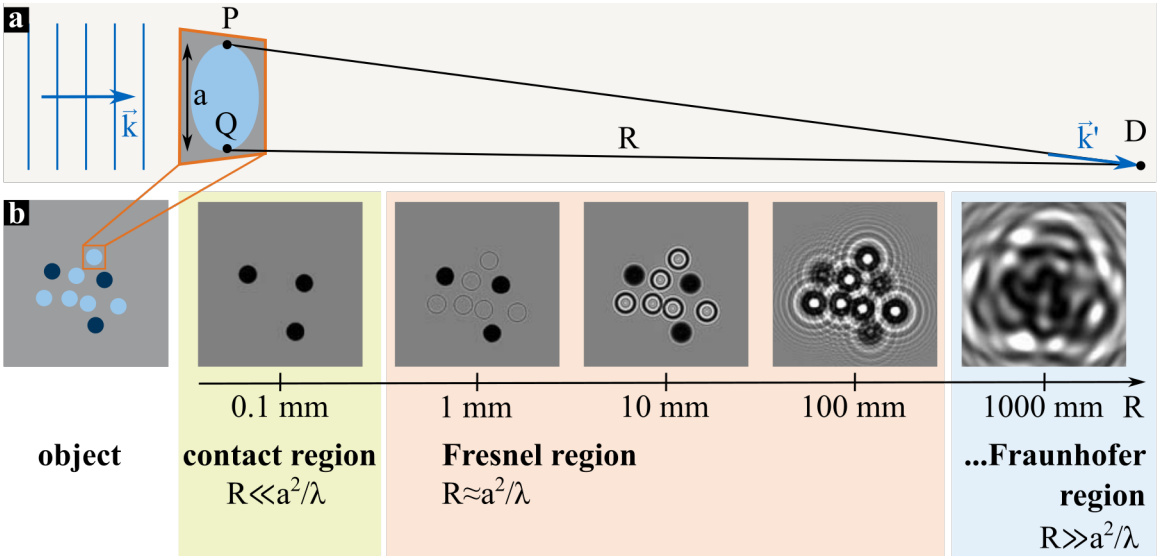

Figure 3.4: **Simulated Imaging Signals for Different Propagation Distances.** (a) A plane wave with a wave vector $\vec{k}$ interacts with two points P and Q and propagates over distance of R to arrive at the detection point D wit a wave vector $\vec{k}'$. (b) A plane wave of monochromatic X-rays with $\lambda = 1\,\text{Å}$ illuminates an object and propagates over a distance R ($R \in [0.1, 1, 10, 100, 1000]\,\text{mm}$) to create a simulated X-ray image. The object consists of two types of idealised disks (dark blue: perfect absorber and zero transmission; light blue: perfect phase object and phase shift π, no absorption) with a structure size of $a = 5\,\mu\text{m}$. Figure based on [Als-Nielsen, 2011]. Simulated images courtesy of [Weitkamp, 2004].

3.2.1 Mathematics of Wavefield Propagation

An X-ray image essentially represents the intensity distribution $I(x, y)$ of the X-ray wave $E(x, y)$ at a certain propagation distance z:

$$I_z(x, y) \propto |E_z(x, y)|^2. \tag{3.24}$$

In order to derive this propagated X-ray wave $E_z(x, y)$, we consider a monochromatic, plane wave propagating in z-direction, as in Eq. 3.10. After passing through an object, the plane wavefront E_0 is distorted and is now a function of the spatial coordinates $E_0(x, y)$ perpendicular to the propagation direction z. We define the z-coordinate, where the wave leaves the object as $z = 0$. Thus, we obtain a wave formalism of $E_0(x, y)$, with

$$E_0(x, y) = \frac{1}{2\pi} \int\int \widetilde{E}_0(k_x, k_y) e^{-i(k_x x + k_y y)} dk_x dk_y. \tag{3.25}$$

Here, $\widetilde{E}_0(k_\mathrm{x}, k_\mathrm{y})$ is the Fourier transform of $E_0(x, y)$. This equation interprets the wave field emerging from the object as a superposition of plane waves with different x- and y-components of the wave vector $\vec{k}$. Under the assumption of small refraction angles α or $k_{\mathrm{x/y}} \ll |\vec{k}|$, an expression can be derived which connects $E_\mathrm{z}(x, y)$ to $E_0(x, y)$:

$$E_\mathrm{z}(x, y) = P_\mathrm{z}(x, y) \star E_0(x, y), \tag{3.26}$$

with the propagator $P_\mathrm{z}(x, y)$ over a certain propagation distance z:

$$P_\mathrm{z}(x, y) = -ik\frac{e^{ikz}}{2\pi z}e^{-ik\frac{x^2+y^2}{2z}}, \tag{3.27}$$

with k the absolute value of the wave vector $\vec{k}$ [Als-Nielsen, 2011]. Equation 3.26 shows that the wavefield after a certain propagation distance $E_\mathrm{z}(x, y)$ can be described by a convolution of the propagator $P_\mathrm{z}(x, y)$ with the exit wavefield $E_0(x, y)$.

3.2.2 Transport of Intensity Equation

As an X-ray image merely contains intensity information (Eq. 3.24), the phase information is not directly accessible. A convenient way to connect the intensity $I(x, y, z)$ with the phase $\Phi(x, y, z)$, and thus retrieve the phase information from the X-ray image, is the transport of intensity equation (TIE). For coherent radiation, the TIE is given as:

$$k\frac{\partial I(x, y, z)}{\partial z} = -\nabla_\mathrm{T} \cdot \left[I(x, y, z)\nabla_\mathrm{T}\Phi(x, y, z)\right], \tag{3.28}$$

whereby ∇_T denotes the transverse gradient to the propagation direction z (in the x-y-plane). For small distances $\Delta z = z - z_0$ (in the Fresnel region), the derivative of the intensity along the z-direction can be estimated as:

$$\frac{\partial I(x, y, z)}{\partial z} \approx \frac{I(x, y, z) - I(x, y, z_0)}{z - z_0}, \tag{3.29}$$

whereby z_0 is conventionally set as the exit surface of the sample. With this approximation Eq. 3.28 can be rewritten as:

$$I(x, y, z) = I(x, y, z_0) - \frac{z - z_0}{k}\left[\nabla_\mathrm{T} I(x, y, z_0) \cdot \nabla_\mathrm{T}\Phi(x, y, z_0) + I(x, y, z_0)\nabla_\mathrm{T}^2\Phi(x, y, z_0)\right] \tag{3.30}$$

In this equation, $I(x, y, z)$ describes the measured intensity at a propagation distance z in the near-field regime (small $\Delta z = z - z_0$). For easier interpretation, we transform Eq. 3.30 and introduce $I_\mathrm{z}(x, y) = I(x, y, z)$, $I_{\mathrm{z}_0}(x, y) = I(x, y, z_0)$ and $\Phi_{\mathrm{z}_0}(x, y) = \Phi(x, y, z_0)$:

$$I_\mathrm{z}(x, y) = \underbrace{I_{\mathrm{z}_0}(x, y)}_{\text{I attenuation}} - \underbrace{\frac{\Delta z}{k}\nabla_\mathrm{T} I_{\mathrm{z}_0}(x, y) \cdot \nabla_\mathrm{T}\Phi_{\mathrm{z}_0}(x, y)}_{\text{II differential phase}} + \underbrace{\frac{\Delta z}{k} I_{\mathrm{z}_0}(x, y)\nabla_\mathrm{T}^2\Phi_{\mathrm{z}_0}(x, y)}_{\text{III propagation−based phase}}. \tag{3.31}$$

In Eq. 3.31, three terms are designated: Term I describes the intensity distribution directly behind the sample and, thus, represents the pure attenuation signal. Term II contains the phase gradient. Differential phase imaging aims to enhance this signal to retrieve the phase information $\Phi_{z_0}(x, y)$. The contribution of this term to the measured intensity $I_z(x, y)$ increases with more prominent intensity gradients. Therefore, differential phase imaging techniques introduce large intensity gradients artificially by adding X-ray optics to the imaging setup. Term III depends on the second derivative of the phase, which is directly related to the fringes f (Eq. 3.20), and increases for larger propagation distances Δz from the sample (as long as they are still in the Fresnel region). The term acts as a modulation of the intensity for abrupt changes in the phase $\Phi_{z_0}(x, y)$. Term III represents the fringe-signal which is used in propagation-based phase imaging. As term III does not depend on an intensity gradient, propagation-based phase imaging techniques do not rely on any X-ray optics for signal enhancement, but larger propagation distances [Russo, 2017].

3.2.3 Coherence

To enable the phase-contrast phenomena described in the previous sections, the incident X-ray beam has to fulfil certain criteria, also known as coherence. Optical coherence can be loosely defined as the ability of a radiation beam to generate phase-related effects, such as interference or diffraction. Thus, for a wavefield to be coherent, it has to be highly correlated in space and time. For a simplified treatment, we will consider spatial (transverse) coherence and temporal (longitudinal) coherence separately. It has to be noted that this is an approximation, since both effects are random and intertwined [Russo, 2017].

Constructive interference occurs if two waves meet with a phase shift of $n \cdot 2\pi$, with n being an integer. This happens for example, if two waves of the same wavelength λ have an optical path difference of $n \cdot \lambda$. A point source represents an X-ray source with perfect transverse coherence. For a point source, every ray traces back to the same point and two neighbouring waves follow a similar optical path. Thus, merely refraction effects induced by a sample cause path differences and thereby an interference pattern. A source with a certain spatial extent (X-ray focal spot radius r_x) causes a 'blurring' of the interference pattern. Two waves hitting the sample at the same point may have followed largely varying optical paths and may, thus, feature largely varying incident angles leading to varying exit angles from the sample. This effect is also referred to as penumbra blurring. An interference pattern caused by waves exiting the sample with a mutual distance of A may still be observed, if the penumbra blurring is smaller than the distance between two interference maxima. The following expression of the

transverse coherence length L_t is based on this relation:

$$L_\mathrm{t} = \frac{d \cdot \lambda}{2r_\mathrm{x}} \geqslant A, \tag{3.32}$$

with d the mean path length from source to the exit point of the sample, r_x the radius of the X-ray focal spot, and A the size of the sample structure.

A further cause for blurring of the interference pattern is a non-zero wavelength bandwidth $\Delta\lambda$. As the refraction angle α induced by a sample directly depends on the wavelength λ of the beam, different wavelengths necessarily lead to different optical paths. The interference pattern is still visible if the wavelength λ is at least as small or smaller than the longitudinal coherence length L_l:

$$L_\mathrm{l} = \frac{\lambda^2}{\Delta\lambda} \geqslant \lambda, \tag{3.33}$$

with $\Delta\lambda$ the wavelength bandwidth of the X-ray beam [Russo, 2017]. At this point it should be noted that the precise expression in Eq. 3.32 and Eq. 3.33 may slightly vary with respect to the formalism used for derivation [Als-Nielsen, 2011].

4 X-ray Nanotomography

After describing the relevant processes for X-ray imaging to obtain a 2D projection image of an object (Chapter 3), this chapter gives an introduction into X-ray nanotomography imaging. For this purpose, the first part conveys the basic principles of computed tomography. Building upon this knowledge, this chapter subsequently introduces the relevant concepts and techniques in modern X-ray nanotomography. Thereby, the NanoCT system is set in context with other high-resolution X-ray tomography approaches.

4.1 Basic Concepts of Computed Tomography

The development of computed tomography (CT) revolutionised the field of X-ray imaging. It allows for reconstructing the three-dimensional structure of an object, whereas conventional radiography only reproduces a 2D projection image of a 3D object, which results in the loss of valuable spatial information. A CT reconstruction is based on an array of radiographic projection images taken over a wide range of projection angles.

This chapter explains the fundamental principles underlying computed tomography, followed by a brief introduction to tomographic reconstruction using filtered back projection. For the sake of simplicity, the case of a monochromatic, parallel X-ray beam with a uniform intensity of I_0 is considered. Furthermore, only processes in the (x, z)-plane, perpendicular to the tomographic rotation axis, are investigated.

4.1.1 Radon Transform

The parallel X-ray beam illuminates a sample with a 2D distribution of the linear attenuation coefficient of $\mu(x, z)$. Subsequently, a line of detector pixels records an intensity profile $I(x)$ which is given by Lambert-Beer's law (Eq. 3.13):

$$I(x) = I_0 \cdot e^{-\int \mu(x,z)\ \mathrm{d}z}, \tag{4.1}$$

with I_0 the intensity of the incident X-ray beam. Let's consider the case, where the X-ray beam projects the sample under a certain angle θ onto the detector. This scenario is illustrated in Fig. 4.1.

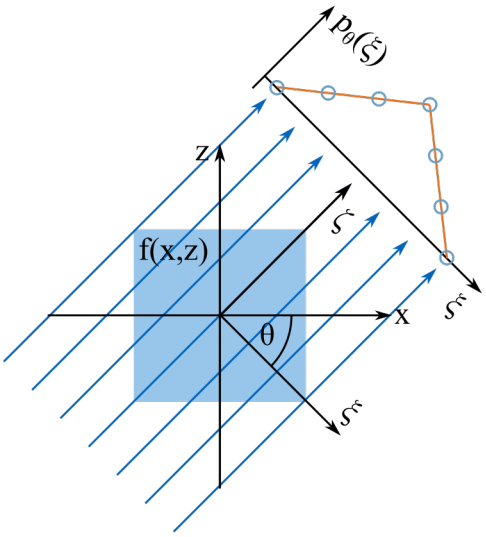

Figure 4.1: **Parallel Beam Projection.** A parallel, monochromatic beam with a uniform intensity distribution I_0 projects an object function $f(x, z)$ under the angle θ to generate a line profile $p_\theta(\xi)$.

Therefore, we introduce the rotated coordinate system (ξ, ζ), which depends on the projection angle θ:

$$\xi = x \cdot \cos(\theta) + z \cdot \sin(\theta), \quad \text{and} \quad \zeta = -x \cdot \sin(\theta) + z \cdot \cos(\theta).$$

Changing from the fixed coordinate system (x, z) to the angle-dependent coordinate system (ξ, ζ) and reformulating of Eq. 4.1 provides the following expression:

$$\log_e \left(\frac{I_0}{I(\xi)} \right) = \int \mu(\xi, \zeta) \, \mathrm{d}\zeta. \tag{4.2}$$

This equation clearly indicates that the logarithmic ratio of the incoming intensity and the intensity profile at a certain coordinate ξ, perpendicular to the X-ray beam, reproduces the line integral of the attenuation distribution in beam direction ζ. Thus, the logarithmic intensity ratio in Eq. 4.2 also depends on the projection angle θ. This defines the projection function $p_\theta(\xi)$:

$$p_\theta(\xi) = \int \mu(\xi, \zeta) \, \mathrm{d}\zeta, \tag{4.3}$$

The full set of line profiles $p_\theta(\xi)$ for all projection angles θ and all coordinates ξ is known as the Radon transform. Transforming Eq. 4.3 into the original coordinate system (x, z), we obtain:

$$p_\theta(\xi) = \int \int f(x, z) \cdot \delta(x \cdot \cos(\theta) + z \cdot \sin(\theta) - \xi) \, \mathrm{d}x \, \mathrm{d}y, \tag{4.4}$$

with the function $f(x, z)$, which describes the distribution of attenuation coefficients in the fixed coordinate system (x, z), and with δ the Dirac-delta function, which discriminates all function values except for those at a constant coordinate of ξ [Als-Nielsen, 2011; Buzug, 2008].

4.1.2 Fourier Slice Theorem

The Fourier slice theorem forms the basis for solving the inverse problem of retrieving the function $f(x, z)$ from the Radon transform $p_\theta(\xi)$. Its main statement is that the 1D Fourier transform (FT) $P_\theta(q)$ of the Radon transform $p_\theta(\xi)$ corresponds to a line in the 2D FT $F(u, v)$ of the object function $f(x, z)$ at an angle θ:

$$F(u, v)|_{u=q\cos(\theta), v=q\sin(\theta)} = P_\theta(q), \tag{4.5}$$

with (u, v) the Cartesian coordinates in Fourier space, (q, θ) the polar coordinates in Fourier space and with:

$$F(u, v) = \mathfrak{F}_{2D}\left[\, f(x, z) \,\right], \quad \text{and} \quad P_\theta(q) = \mathfrak{F}_{1D}\left[\, p_\theta(\xi) \,\right].$$

This principle is further illustrated in Fig. 4.2.

Fig. 4.2a shows the radon transform for a projection angle $\theta = 45°$ of a square-shaped object function which results in a triangular projection profile $p_{\theta=45°}(\xi)$. The 1D FT of this triangular shaped function results in a sinc^2-function for $P_{\theta=45°}(q)$ (Fig. 4.2b). By filling the Fourier space with further lines $P_\theta(q)$ for an angular interval of $\theta \in [0; 180]°$, it is possible to determine the object function in Fourier space $F(u, v)$ (Fig. 4.2b, c). In a CT acquisition, the finite number of detector pixels and angular rotation steps, leads to a discrete sampling of $F(u, v)$ in polar coordinates with a decreasing sampling density towards larger spatial frequencies (Fig. 4.2b). Therefore, an interpolation is performed between the sampling points to calculate the object function $F(u, v)$ (Fig. 4.2c). This, however, leads to an increasing error of the reconstruction data with increasing spatial frequencies, which causes artefacts in the resulting object function $f(x, z)$ [Russo, 2017; Als-Nielsen, 2011; Buzug, 2008].

4.1.3 Filtered Back-Projection

The interpolation in Fourier space to obtain $F(u, v)$ and the associated high-frequency undersampling errors are the biggest handicap of direct reconstruction based on the Fourier slice theorem. Conventionally the inverse 2D FT of $F(u, v)$ is defined as such:

$$f(x, z) = \int_{-\infty}^{\infty}\int_{-\infty}^{\infty} F(u, v) \cdot e^{2\pi i(ux+vz)}\, \mathrm{d}u\, \mathrm{d}v. \tag{4.6}$$

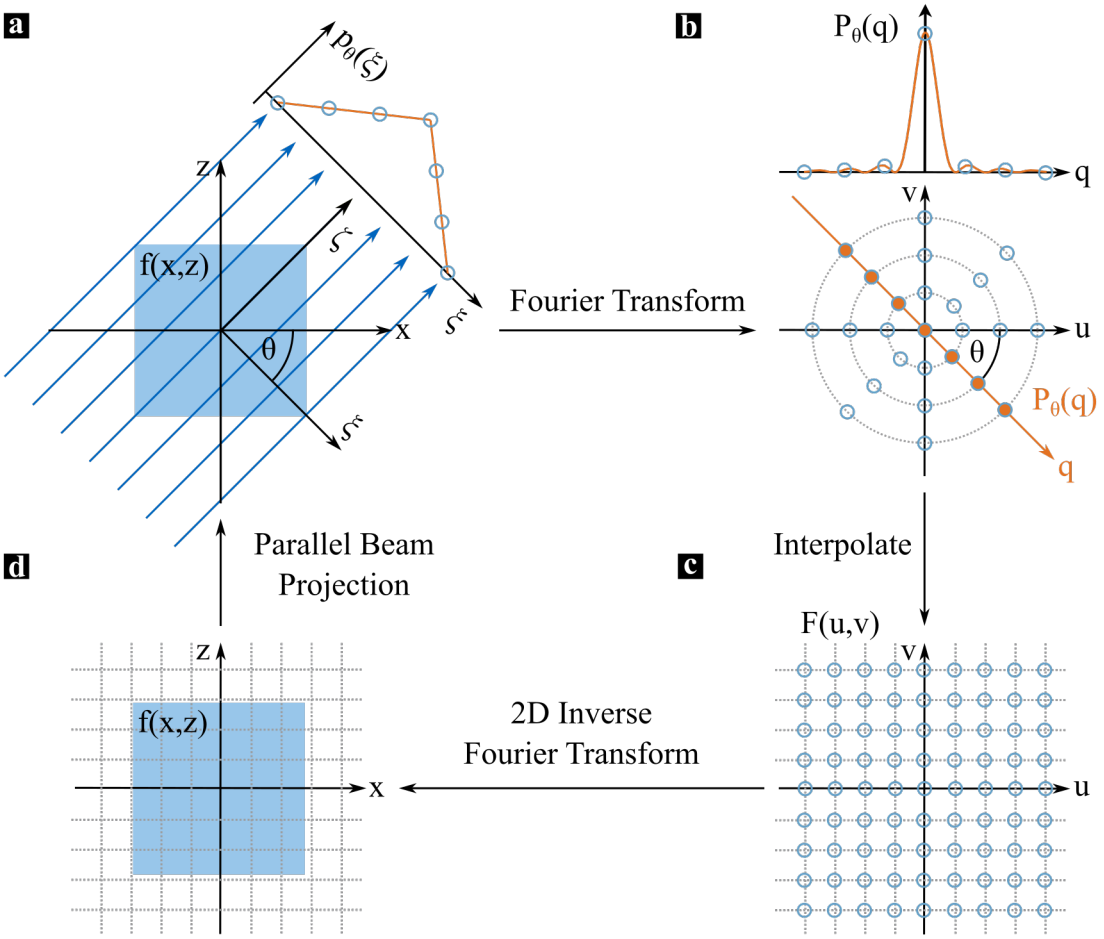

Figure 4.2: **Fourier Slice Theorem.** (a) Profile function $p_\theta(\xi)$ through a parallel projection of an object function $f(x, z)$ under an angle θ. (b) 1D FT of the profile in (a) leads to a slice under the same angle θ through the object function $F(u, v)$ in Fourier space. (c) By filling the Fourier space with many slices $P_\theta(q)$ for a variety of angles θ and interpolation, the object function $F(u, v)$ in Fourier space can be retrieved. (d) The 2D inverse FT provides the original object function $f(x, z)$.

The interpolation step can be bypassed by converting this equation into polar coordinates with:

$$u = q \cdot \cos(\theta), \quad \text{and} \quad v = q \cdot \sin(\theta).$$

Thus, we obtain the following expression:

$$\begin{aligned} f(x,z) &= \int_0^{2\pi}\int_0^{\infty} F(q,\theta) \cdot e^{2\pi i q(x\cdot\cos(\theta)+z\cdot\sin(\theta))}\ q\ \mathrm{d}q\ \mathrm{d}\theta \\ &= \int_0^{\pi}\int_{-\infty}^{\infty} P_\theta(q) \cdot e^{2\pi i q\xi}\ |q|\ \mathrm{d}q\ \mathrm{d}\theta. \end{aligned} \tag{4.7}$$

The last step was possible due to the Fourier slice theorem and due to the property:

$$F(q, \theta + 180°) = F(-q, \theta).$$

Equation 4.7 describes the principle of filtered back-projection (FBP), as the factor $|q|$ acts as a high-pass or linear ramp filter. This filter is also referred to as the Ram-Lak filter. To reduce high-frequency noise, other filters can be applied, such as the Hamming or the Shepp-Logan filter [Buzug, 2008; Kak, 1988].

4.2 Concepts of X-ray Nanotomography

Towards resolutions in the submicron range, X-ray microscopy systems face a number of challenges. One major challenge is beam stability and mechanical stability between the setup components. This is especially true for imaging techniques, which require long exposure times or for imaging techniques, where slight instabilities of components result in the sample being out-of-focus. Another relevant aspect is the precision of the rotation stage used for tomography. While most rotation stages are sufficient for imaging at the µm-scale, this is often not true for higher resolutions. To correct for these misalignments, fiducial markers or software-based methods, such as cross-correlation based algorithms, are employed. For more details on that subject, the reader is referred to Section 5.3. A limiting factor all X-ray nanotomography methods struggle with, is sample size. In general, an increase in spatial resolution results in a decrease of the acceptable sample size. One reason for this behaviour is that reconstruction algorithms conventionally require the full extent of the sample within the field of view (FOV) of the detector. Another reason can be the decrease of the depth of field for higher resolutions in optics-based X-ray microscopy systems [Withers, 2007; Ferstl, 2020a; Chao, 2005].

Despite these challenges, a large variety of configurations of X-ray microscopes has been developed. While this means a rich diversity in components, acquisition techniques and image processing, there is only a handful of strategies underlying most of these techniques. Here, a detailed description of these strategies is provided and their capabilities and limitations with respect to high-resolution imaging are discussed. Thereby, both synchrotron- and laboratory-based systems are considered.

Regarding X-ray microscopy systems, there are two major categories: Optics-based systems and geometry-based systems. Optics-based systems, as their name suggests, use X-ray or visible light optics to reach the desired magnifications. In contrast to that, geometry-based systems forego the use of any optics and merely use geometric effects for magnification [Withers, 2007]. For the sake of conciseness, among optics-based systems only X-ray optics are further treated in the following text.

Before this chapter turns to the respective strategies, two figures of merit are to be introduced, which are particularly relevant in the context of microscopy: the spatial resolution δ_x and the depth of field (DOF). The spatial resolution of an optics-based imaging system is largely defined by the resolution of the individual optical elements. The resolution δ_x for a perfect lens with a diameter d and a focal length of f is given by the Rayleigh criterion:

$$\delta_x = 1.22 \cdot \frac{\lambda f}{d} = 0.61 \cdot \frac{\lambda}{\mathrm{NA}}, \tag{4.8}$$

with λ the wavelength of the incident radiation and NA, the numerical aperture of the lens. The numerical aperture is defined by the opening angle of the lens α and the

refractive index n of the medium in front of the lens:

$$\mathrm{NA} = n \cdot \sin \alpha. \tag{4.9}$$

The expression in Eq. 4.8 indicates that the resolution of a lens can be optimised by minimising the focal length or maximising the NA of the lens [Als-Nielsen, 2011; Demtröder, 2009]. In contrast to that, in geometry-based imaging systems, the setup geometry dictates the resolution-defining aspect. While parallel-beam projection concepts mostly rely on small detector pixel sizes, cone-beam projection imaging is mostly limited by the focal spot size of the X-ray source [Withers, 2007].

The DOF, as the second central figure of merit, defines the distance between the two positions along the optical axis, where a sample is still in focus and, thus, enables a sharp image. While geometry-based systems practically have an infinite DOF, many optics-based systems struggle with setup alignment and limitations in sample size due to their limited DOF. In general, the NA of a lens and the DOF are inversely proportional. The larger the NA the smaller usually the DOF [Chao, 2005; Russo, 2017].

4.2.1 Optics-based Systems

The central purpose of an optics-based system is to generate a magnified image of the sample on the detector. In traditional optics designed for visible light, this is achieved by bending the light trajectory through changes in the refractive index at the interfaces of a lens. In contrast to visible-light-based systems, the focusing of X-rays is not as trivial. The refractive indices for soft X-rays are very close to unity with deviations in the order of 10^{-5}, which renders traditional (refractive) optics impractical.

To solve this problem a number of concepts has been developed. An overview of these concepts is given in Fig. 4.3: successive parabolic lenses (Fig. 4.3a), Kirkpatrick-Baez optics (Fig. 4.3b), Bragg multiplier systems (Fig. 4.3c), and Fresnel zone plates (Fig. 4.3d) [Lengeler, 1999; Kirkpatrick, 1948; Boettinger, 1979; Chao, 2005]. In the following, more in-depth information about these techniques is provided [Russo, 2017; Withers, 2007; Als-Nielsen, 2011].

Compound Refractive Imaging

As already mentioned, the refractive index has a rather different behaviour for X-rays than for visible light. While the refractive index for visible light is greater than one, the refractive index for photon energies in the X-ray regime is smaller than one. This implies, that the shape of a converging X-ray lens should correspond to the shape of a diverging optical lens. Thus, for X-ray focusing, parabolic lenses, which are conventionally made from aluminium or beryllium, are used (Fig. 4.3a).

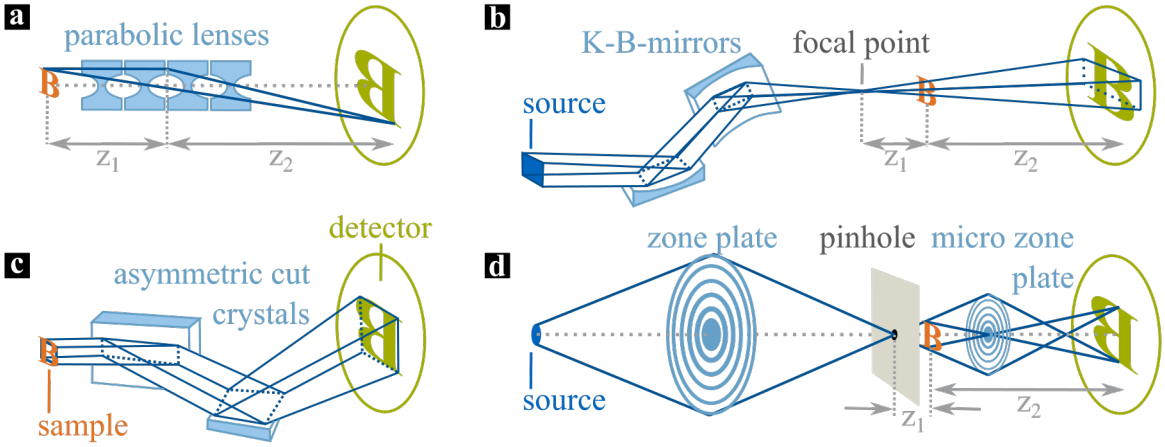

Figure 4.3: **Optics-based X-ray Microscopy Techniques.** (a) Compound refractive system. (b) Kirkpatrick-Baez optics setup. (c) Bragg multiplier system. (d) Fresnel zone plate setup. With characteristic distances z_1 (focal point to sample) and z_2 (sample/focal point to detector) . Figure based on [Withers, 2007].

Beyond that, the value of the refractive index for X-rays deviates only slightly from unity. This has dramatic consequences for X-ray lenses, as the focal length f of a single X-ray lens would be in the range of 100 m, which is rather inconvenient for most applications. Stacking of the parabolic lenses to form a compound lens (Fig. 4.3a), however, enables focal lengths compatible with the typical dimensions of a X-ray synchrotron beam line [Snigirev, 1996; Russo, 2017].

While the attenuation losses in compound lenses were a challenge in the beginning, developments have made it possible to reduce these losses for practical applications. Nevertheless, they still rely on the high-fluxes only synchrotrons can provide. Nowadays, compound lenses are typically used as an optical element in hard X-ray microscopy beam lines and enable FOVs of ≈ 1 mm.

In a configuration, such as depicted in Fig. 4.3a, the image is formed at a distance of $z_2 = z_1 \cdot f/(z_1 - f)$ with a magnification of z_2/z_1, with z_1 the sample lens distance. The spatial resolution δ_x can be calculated from the wavelength λ, and the numerical aperture of the compound lens NA:

$$\delta_x \approx 0.75 \cdot \frac{\lambda}{2 \cdot \mathrm{NA}}. \tag{4.10}$$

The DOF can be equally calculated from these values:

$$\mathrm{DOF} \approx 0.64 \cdot \frac{\lambda}{\mathrm{NA}^2}, \tag{4.11}$$

Equation 4.11 clearly shows that there is a trade-off between the DOF and the spatial resolution δ_x.

In practice, it has been shown that it is possible to reach resolutions down to $\delta_x \approx 230\,\text{nm}$ with a DOF of 2.5 mm in a setup of $z_1 \approx 1\,\text{m}$, $z_2 \approx 23\,\text{m}$ at X-ray energies of 24.9 keV [Schroer, 2002]. Estimations regarding this method's resolution have yielded a resolution limit of around 30 nm [Als-Nielsen, 2011; Withers, 2007; Russo, 2017; Lengeler, 1999].

Kirkpatrick-Baez Optics

Another optics system suitable for hard X-ray microscopy are Kirkpatrick-Baez (KB) mirrors. In this concept, two orthogonal reflecting surfaces with elliptical shapes, the KB mirrors, are in charge of focusing the X-ray beam, as depicted in Fig. 4.3b. Their most attractive feature is the ability of achromatic focusing. However, also KB optics suffer from rather long focus lengths and are prone to aberrations, such as distortions in the sample projection due to profile errors in the mirrors. Therefore, they are mostly used at synchrotrons as upstream prefocus devices [Withers, 2007; Russo, 2017].

KB optics systems produce images containing propagation-based phase signal and, thus, promote imaging techniques such as holotomography. In holotomography quantitative phase information is retrieved by acquiring data sets at multiple distances z_1, as illustrated in Fig. 4.3b [Withers, 2007; Clœtens, 1999].

With respect to resolutions, KB mirrors proved to achieve $\delta_x \approx 90\,\text{nm}$ at X-ray energies of 20.5 keV [Hignette, 2005].

Bragg Magnifier Systems

Bragg magnifier systems apply the principle of asymmetrical Bragg diffraction for magnification, as shown in Fig. 4.3c. The magnification is very sensitive to the incident X-ray energies. In case of 8° asymmetrically cut silicon(220)-crystals, an X-ray energy of 21.1 keV leads to a 20x magnification, whereas an X-ray energy of 22.75 keV leads to a 100× magnification. Therefore, Bragg magnifier systems depend on the tunable sharp energy of a synchrotron.

There are two major advantages inherent to Bragg magnifier systems: The method generates images with differential phase contrast and it is very efficient for hard X-rays. With Bragg magnifiers, resolutions were demonstrated of $\delta_x \approx 400\,\text{nm}$ at X-ray energies of 8.22 keV [Withers, 2007; Modregger, 2006; Modregger, 2007].

Fresnel Zone Plates

In contrast to refractive parabolic lenses (Fig. 4.3a), Fresnel zone plates (FZP) use diffraction to manipulate the trajectory of an X-ray beam. In a typical FZP setup, as depicted in Fig. 4.3d, a FZP or a glass capillary is used as a condenser. As a high-resolution objective, a micro FZP is used to generate a magnified full-field image of the sample. One of the greatest benefits of this configuration is the rather large focal point sample distance z_1, which allows for integrating stages to simulate certain sample environments [Withers, 2007; Youn, 2010; Russo, 2017].

FZP-based microscopy, has been first implemented using soft X-rays ($0.25 - 1.8\,\mathrm{keV}$). For this energy regime, it is relatively easy to produce high-quality, efficient micro FZPs [Russo, 2017].

Imaging with harder X-rays ($E_i \geqslant 8\,\mathrm{keV}$) requires FZPs with very high aspect ratios (the ratio of the plate thickness to the outermost zone width d_r). For instance, resolutions of $\delta_x < 50\,\mathrm{nm}$ were reached using gold FZPs with a thickness of 890 nm and a zone width of $d_r = 50\,\mathrm{nm}$ with 20% efficiency at X-ray energies of 8 keV [Withers, 2007].

The resolution of FZPs can be calculated with the modified Rayleigh criterion:

$$\delta_x \approx 1.22 \cdot \frac{d_r}{m}, \tag{4.12}$$

with δ_x the resolution, d_r the outer zone width of the FZP, and m the order of diffraction. Equation 4.12 suggests, that the resolution can be improved by using higher diffraction orders. It was found, however, that the efficiencies of FZPs decreases drastically for higher order diffraction. The third-order focus contains only about 1/9-th of the intensity exhibited in the first-order focus. For a typical first-order efficiency of 10% of a FZP for 8 keV-X-rays, this means a third-order efficiency of only $\approx 1\%$[Withers, 2007].

The DOF can be determined from the outer zone width d_r and the wavelength of the X-rays λ:

$$\mathrm{DOF} = \frac{2d_r^2}{\lambda}. \tag{4.13}$$

This equation clearly shows that the DOF increases for higher X-ray energies. Combining Eq. 4.12 and Eq. 4.13, it is evident that the DOF decreases towards finer resolutions to the power of two. The DOF defines the maximum sample size which can be imaged so that the entire sample is in-focus. Consequently, the resolution δ_x also limits the appropriate sample size. Typical relevant sample sizes around $1 - 10\,\mu\mathrm{m}$ suggest a resolution limit of FZP-based microscopy of $\delta_{x,max} \approx 10\,\mathrm{nm}$ [Russo, 2017; Chao, 2005].

FZP-based imaging systems are widely used at synchrotron facilities. At a synchrotron beam line, a resolution of $\delta_x \approx 12\,\mathrm{nm}$ was demonstrated at X-ray energies of 0.815 keV.

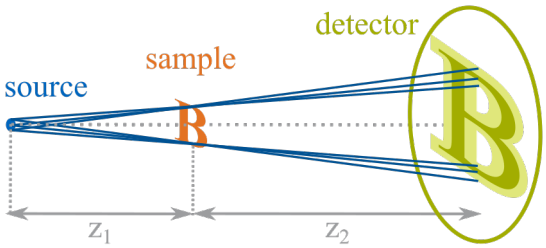

Figure 4.4: **Geometry-based X-ray Microscopy Concepts.** (a) Parallel projection system. (b) Cone beam system with penumbra effects in the detected image. Legend: z_1: the source-sample distance, z_2: the sample-detector distance. Figure based on [Withers, 2007].

While X-rays in this energy regime achieve adequate levels of contrast in biological samples, their penetration depth is very low, which limits the sample size beyond the available DOF [Chao, 2005].

In a laboratory environment, developments have led to commercially available systems with resolutions smaller than 50 nm. These systems conventionally use the characteristic lines of the polychromatic spectrum of an X-ray tube. This matches well with the demands of high-resolution FZPs regarding monochromaticity [Tkachuk, 2009].

An increase in resolution is usually associated with a loss in efficiency and, thereby, longer exposure times. It has been found that exposure times are inversely proportional the fourth power of the spatial resolution. For resolutions in the sub-50 nm-regime with a lab system, this results in very long exposure times in the range of minutes. Due to these long exposure times, blurring artefacts due to mechanical instabilities reduce the spatial resolution. To conclude, brightness limitations of current X-ray tubes hamper the feasibility of X-ray nanotomography with resolutions significantly below 30 nm beyond synchrotron facilities [Withers, 2007].

4.2.2 Geometry-based Systems

In contrast to the previously presented systems, geometry-based imaging, also known as projection imaging foregoes the use of any X-ray optics. Its biggest strength is, therefore, simplicity. Figure 4.4 depicts the two fundamental concepts of projection imaging: Parallel-beam projection (Fig. 4.4a) and cone-beam projection (Fig. 4.4b). The two following sections, describe these two imaging concepts and the underlying principles in detail [Withers, 2007].

Parallel-beam Projection

In a parallel projection imaging configuration (Fig. 4.4a), the source-sample distance z_1 is very large, and a quasi parallel beam projects an image of the same size as the object onto the detector [Withers, 2007].

These large source-sample distances z_1 represent the biggest advantage of parallel projection imaging. A large distance z_1 provides a large DOF and a lot of space to mount large samples or environmental stages. Large distances ($z_1 \approx 100\,\mathrm{m}$), however, are usually only feasible at synchrotron beam lines and makes this concept impractical for a laboratory environment [Weitkamp, 2010].

In this concept, the resolution limit is defined by the effective pixel size of the detection system. Up until now, charge-coupled device (CCD) detectors feature the smallest available pixel sizes. Parallel projection systems, thus, normally combine a scintillator layer converting X-ray photons into visible light with a CCD chip for image formation. This detector configuration enables to introduce visible light optics to produce a magnified image on the CCD chip. With such a system, effective detector pixel sizes of 180 nm are feasible [Weitkamp, 2010]. Considerations, taking into account the optical efficiency of the scintillator and diffraction of visible light, have yielded a spatial resolution limit of parallel projection imaging of $\delta_{x,max} \approx 300\,\mathrm{nm}$ [Koch, 1998; Withers, 2007].

Cone-beam Projection

Cone-beam projection systems are most straight forward in terms of imaging and utility. In such a system, the sample is kept in relatively short distances z_1 from the source and a cone beam projects a magnified image of the sample onto the detection device (Fig. 4.4b). Such systems are conventionally laboratory-based.

The greatest asset of such systems lies in an immense flexibility regarding sample sizes and resolutions. Due to the small X-ray focal spots used in cone-beam projection setups the resulting projection images inherently provide propagation-based phase effects, which can be used for contrast enhancement. The highest resolutions are achieved at minimum sample-source distances $z_1 \approx 1\,\mathrm{mm}$ [Mayo, 2002; Paganin, 2002].

Such small values of z_1, however, hamper the integration of environmental stages. But the biggest challenge such imaging systems face is stability, both mechanical stability of the setup components and beam stability. The X-ray flux decreases with the X-ray focal spot size. Thus, long exposure times are required for sufficient low noise levels. During such long exposures, instabilities can cause severe blurring of the resulting image [Withers, 2007; Ferstl, 2019].

Apart from instability blurring, the key aspect limiting the spatial resolution in cone-

beam projection systems is the size of the X-ray focal spot. The larger the spatial extent of the source spot the wider the area which is affected by penumbra blurring, as shown in Fig. 4.4b. Thus, the design of the X-ray tube is crucial to ensure minimum X-ray focal spots [Withers, 2007].

There are generally two types of X-ray sources used for such applications: Fine-focus X-ray tubes and scanning electron microscope (SEM) sources. Regarding fine-focus X-ray tubes, both reflection and transmission targets exist, whereby it is said that transmission targets reach smaller spot sizes. Fine-focus transmission tubes often use very thin X-ray targets to limit the size of the electron interaction volume. The NanoCT, presented in this work, integrates such a fine-focus X-ray tube into a cone-beam configuration with a single-photon-counting detector. Thereby, resolutions of $\delta_x \approx 100\,\mathrm{nm}$ were demonstrated in the reconstructed data at a mean X-ray energy of 20 keV [Withers, 2007; Müller, 2017]. More information on the configuration of the NanoCT can be gained in Chapter 5. For more in-depth information on fine-focus X-ray tubes, the reader is referred to Chapter 2.

A different approach for cone beam projection imaging is to use a SEM as an X-ray source. With the development of field-emission cathodes and improvements in detection systems, such methods can come close to the highest resolutions achieved at synchrotron facilities. Similar to fine-focus X-ray tubes, the spatial resolution and X-ray flux largely depends upon the target material and thickness. With such SEM sources, resolutions better than 60 nm were achieved at an X-ray energy of 8 keV [Withers, 2007; Mayo, 2002; Mayo, 2005].

Experimental Setup and Data Processing 5

In this chapter, the central methods used in this work are described: the NanoCT setup and its components, the relevant techniques to apply the setup for tomography acquisition, and the image processing routines employed to obtain the reconstructed volume data from the acquired projection images.

5.1 The NanoCT setup

The fundamental concept of our in-house-built nanoscopic X-ray computed tomography system (NanoCT) is based on cone-beam projection imaging, as described in Chapter 4 (Fig. 4.4). Thus, the NanoCT refrains from using any visible light or X-ray optics. This results in a very simple set-up design, and reduces the number of devices which require a precise alignment along the optical axis. Beyond that, it decreases the number of potential error sources. Therefore, the NanoCT's simplicity represents its most powerful asset.

The two central components which make up the NanoCT are the nanofocus X-ray source (NanoTube) and the single-photon-counting detector (Pilatus). The following sections convey these two components including their characteristics, as well as how these characteristics serve to complement one another. After that, this chapter investigates the NanoCT system as a whole and its application for X-ray nanotomography.

5.1.1 The NanoTube

The ultimate resolution limit of a cone-beam projection microscope is set by the X-ray focal spot size due to penumbra effects (Chapter 2). To minimise these penumbra effects and achieve optimum resolutions a nanofocus X-ray source prototype (Excillum AB, Sweden) was chosen as the centre piece of the NanoCT system. The corresponding product version of this X-ray source has been launched in the recent past. The results presented in this thesis, however, were generated using the prototype version. The prototype nanofocus X-ray source will be referred to as the NanoTube throughout this thesis.

Figure 5.1 displays the general structure of the Nanotube. It is devised as a transmission

tube with a sophisticated electro-optical column. Thus, the conceptual design of the NanoTube bears many similarities to electron microscopes [Goldstein, 2018].

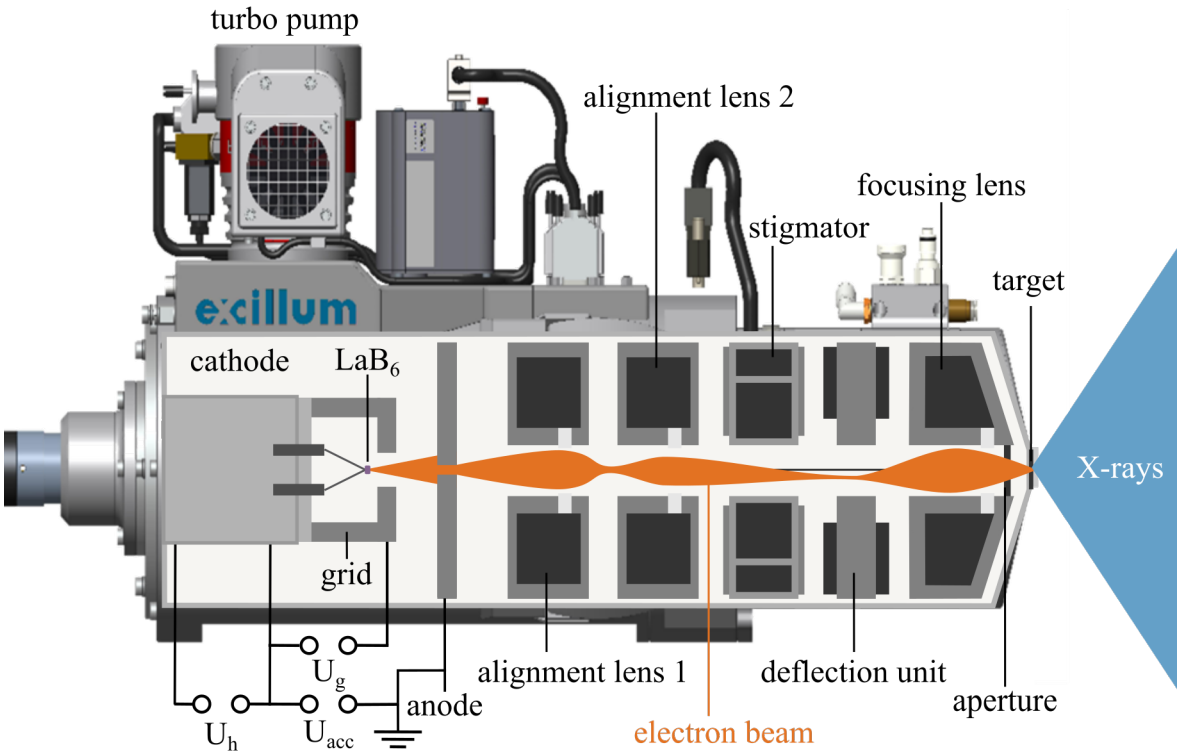

Figure 5.1: **Configuration of the NanoTube.** The tube housing with an approximate length of 65 cm ends in a wedge-shaped head holding the transmission target. The firing unit is operated with a heating voltage U_h, a grid voltage U_g and an acceleration voltage U_{acc}. The electro-optical column manipulating the electron beam shape and trajectory consists of six electron lenses. Figure based on [Ferstl, 2015].

Cathode and Acceleration Gap

Via thermionic emission, a LaB_6 single crystal emits electrons which are then accelerated towards a hole aperture by an acceleration voltage U_{acc}. Thereby, the cathode reaches emission currents of $I \approx 100\,\mu A$, which results in a maximum emitted power of 6 W (at $U_{acc} = 60\,kV$). The high-voltage generator providing the U_{acc}, allows for adjusting the U_{acc}-value from 10 kV to 60 kV and provides a precise voltage output with a minimum voltage wobble. This precision is invaluable to reduce chromatic aberration effects which contribute to an increase of the minimum achievable electron spot size (2.16).

Via an integrated calibration software, the optimum currents of the alignment lenses (Fig. 5.1 alignment lens 1, alignment lens 2) are calculated. To further improve the cathode alignment, it is advisable to also perform a mechanical alignment. By adjusting a number of set screws at the back of the NanoTube housing and, thus, manipulating the cathode position in space with reference to the hole aperture the optimum alignment lens currents are minimised. The cathode alignment is essential to optimise the current of electrons passing through the hole aperture in the anode and thus optimise the electron current impinging on the X-ray target.

As described in Chapter 2, additional bias voltages, here denoted as the grid voltage (Fig. 5.1, U_g), are often applied for electrostatic suppression to confine electron emission to a certain area on the emitter surface. Increasing the grid voltage leads to a larger divergence angle of the emitted electron beam from the cathode ϑ_c and a smaller cathode source spot radius r_c. Due to the hole aperture, the effective divergence angle ϑ_a of the electrons used for X-ray generation is rather constant, as illustrated in Fig. 5.2. Thus, according to Eq. 2.3, a larger U_g value provides a smaller effective emittance. This allows for focusing to smaller electron spots on the X-ray target, due to the conservation principle of the emittance in an optical system (Eq. 2.4). This is, however, achieved at the expense of the electron current which can be used for X-ray generation and, thereby, at the expense of X-ray flux. This principle is illustrated in Fig. 5.2b, c. Based on these effects, adjusting the grid voltage U_g provides a variety of different modes to operate the NanoTube in. These range from a high-resolution-mode with low-X-ray-flux (U_g large) to a low-resolution-mode with high-X-ray-flux (U_g small). If the NanoTube is operated in the high-resolution mode electron currents of merely $\approx 0.5\,\mu A$ are recorded on the X-ray target. This accounts for only 0.5 % of the original emission current at the cathode.

Electro-Optical Column

After passing through the hole aperture in the anode the electrons enter a complex array of electro-optical elements. The electro-optical column is similar to the electron optics in an electron microscope, and provides control over the shape and size of the electron spot on the X-ray target. It consists of two alignment coils, a stigmator lens, a deflection unit and a focusing coil (Fig. 5.1). The geometry of each of these electron lenses is determined by the respective purpose, as previously shown in Fig. 2.4.

The alignment coils provide a pre-alignment of the electron beam onto the X-ray target. The stigmator consists of two quadrupole lenses forming an octopole lens, which manipulates the beam shape and, thus, corrects for astigmatism effects. The deflection unit defines a specific position on the X-ray target, which the electron beam impinges on. This guarantees a reproducible and highly stable spatial spot position. The focus-

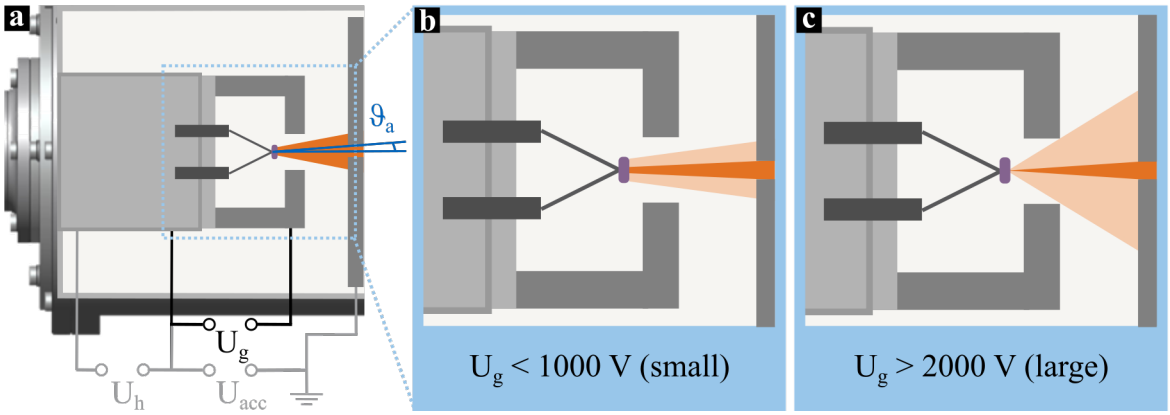

Figure 5.2: **Effects of Grid Voltage Alterations.** (a) Enlarged section of the firing unit shown in Fig. 5.1 with the aperture divergence angle ϑ_a marked in blue. (b) Enlarged ROI from (a) with a small grid voltage U_g leading to a small divergence angle of the emitted electrons and a rather large proportion of the electrons pass through the hole aperture (coloured in bright orange) compared to the electrons which hit the anode (light orange). (c) The same enlarged ROI as shown in (b) at a large grid voltage leading to a large emission divergence angle and only a small percentage of the emitted electrons pass through the hole aperture (bright orange).

ing coil is the final optical element before the electron hit the X-ray target. It focuses the electron beam and defines the size of the electron spot onto the X-ray target.

X-ray Target

To limit the extent of the electron-matter interaction volume (Fig. 2.5), a thin layer of tungsten (500 nm) on a diamond substrate (100 µm) is mounted as the X-ray transmission target. Confining the electron interaction volume results in the electron and the X-ray spot being closely correlated in terms of size and shape. This enables the NanoTube operator to indirectly control the X-ray spot by adjusting the electron spot. The thin transmission target, however, has the disadvantage that the generated X-ray flux is severely reduced. Operating the NanoTube in high-resolution mode provides only very low electron currents on the X-ray target. Combined with the thin transmission target only very low X-ray fluxes can be generated.

As shown in Fig. 5.1, the transmission target is installed at the wedge-shaped front of the NanoTube to allow for minimum source-sample distances (< 1 mm). These small source-sample distances are essential to achieve large magnifications in a cone-beam projection imaging microscope, such as the NanoCT (Chapter 4).

The resulting emission spectrum is displayed in Fig. 5.5. The emission spectrum will be studied more closely in Chapter 6.

Focusing Routine

The thin transmission target provides the operator with an indirect control mechanism over the X-ray spot via manipulating the electron spot on the X-ray target. To exploit this control mechanism, a focusing routine consisting of two modules was devised to optimise and characterise the electron spot in terms of size and shape.

The functioning of such a focusing routine requires some sort of feedback mechanism, in this case information on the electron spot size and shape. For this purpose, the NanoTube developers have drawn inspiration from electron microscopy imaging. In electron microscopy, the image resolution is defined by the shape and size of the electron spot illuminating the sample. This principle can be translated to the NanoTube: Imaging the X-ray target with the electron beam enables to derive the electron spot size and shape on the X-ray target. The deflection unit, depicted in Fig. 5.1, is used to successively alter the position of the electron spot onto the X-ray target. Thereby, the X-ray target surface is scanned with the electron beam. By recording the generated target current for each spot position, an image of the X-ray target surface is formed similar to SEM imaging.

The sharpness of the structures in such an image is given by a convolution of the sharpness of the structure itself and the point-spread-function (PSF) of the electron beam. Hence, to obtain an image, which allows for directly determining the electron PSF, a structure containing steep edges was etched into the tungsten layer of the X-ray target exposing the diamond substrate underneath. The resulting pattern consists of multiple square-shaped regions (tungsten and diamond squares), which form a chequerboard-pattern extending over the entire target surface.

Based on these target scans, the focusing routine determines the optimum values of the three relevant optics parameters:

(stigmator current 1, stigmator current 2, focus current)$= (I_{stigm,1}, I_{stigm,2}, I_{foc})$.

As previously mentioned the stigmator unit is a combination of two quadrupole lenses $(I_{stigm,1}, I_{stigm,2})$ in order to correct for axial astigmatism. By adjusting the focus current, the strength of the focusing lens is altered to minimise the electron spot size on the X-ray target. For more insights into the subject of axial astigmatism the reader is referred to [Ferstl, 2015]. The automated focusing routine used throughout this work combines two modules: a dynamic coarse focusing of the three optics coil currents and a static fine focusing which includes the electron spot size calibration [Rudnaya, 2010]. Both routines were derived from electron microscopy, due to the similarity of the problem. An overview over the two modules is given in Fig. 5.3.

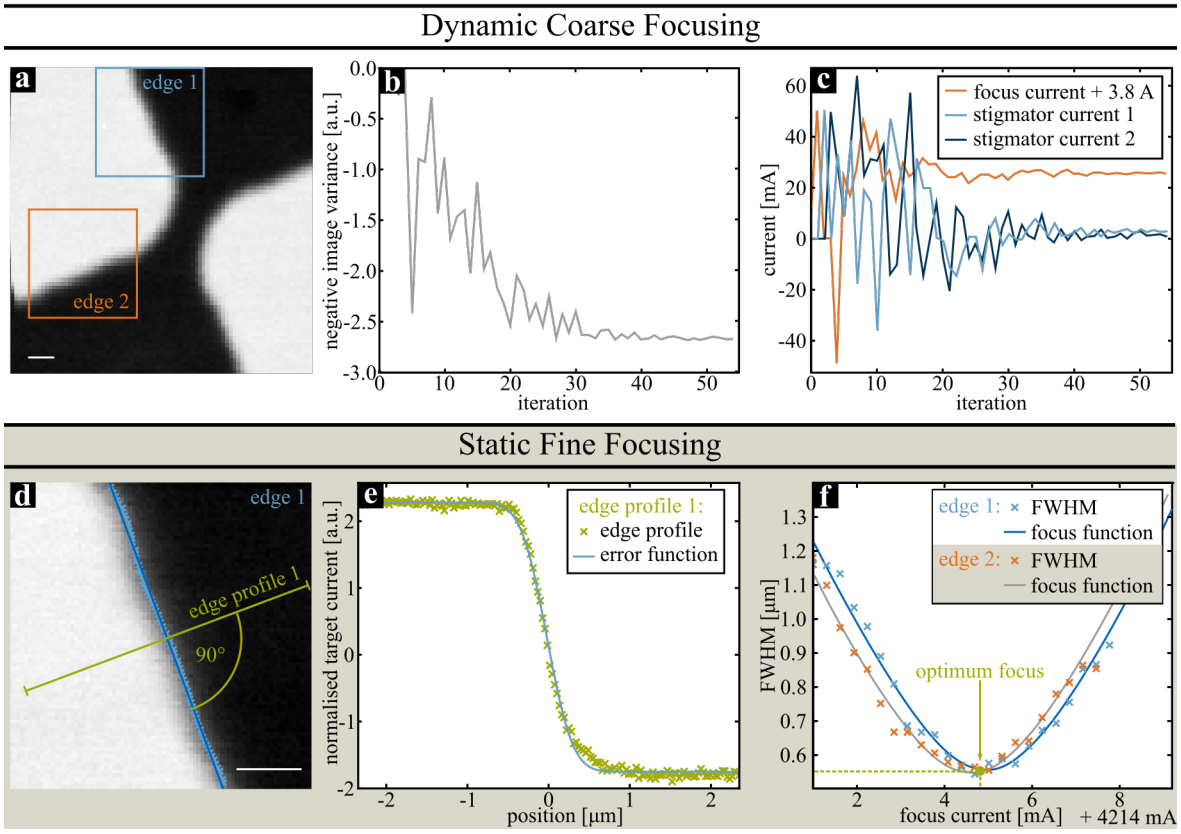

Figure 5.3: **NanoTube Focusing.** (a)-(c) Dynamic coarse focusing (three parameter optimisation). (d)-(f) Static fine focusing and electron spot calibration. (a) Typical target scan image used as input for the dynamic focusing module, with two ROIs (blue: edge 1, orange: edge 2). (b) The negative image variance as the sharpness measure during the dynamic optimisation. (c) The relevant current parameters optimised in the dynamic focusing routine over the iterations. (d) Typical target scan image of the "edge 1"-ROI from (a) indicating the scan axis (green, edge profile 1) to acquire the edge profile perpendicular to the detected edge. (e) Edge profile recorded along the line shown in (d) with an error function fit to calculate the FWHM of the electron spot. (f) The FWHM values for two perpendicular edges (edge 1, edge 2) over different focus current values and focus function fits. The optimum focus is marked in green. Scalebars: 1 µm.

Dynamic Coarse Focusing: In Fig. 5.3a-c, the dynamic coarse focusing module is illustrated. A ROI is selected which contains edge features in multiple spatial directions in the imaging plane, to retrieve isotropic sharpness information (Fig. 5.3a). The

dark regions in Fig. 5.3a mark low target currents and thus diamond regions and the bright regions denote high target currents, or tungsten regions.
The dynamic focus module then records a target scan of the ROI for an initial guess of coil currents: $(I_{stigm,1}, I_{stigm,2}, I_{foc})$ and calculates the negative image variance $(-1 \cdot \mathrm{Var(img)})$ for the resulting target scan. As a result we obtain a point in a 4-dimensional space: $(I_{stigm,1}, I_{stigm,2}, I_{foc}, -1 \cdot \mathrm{Var(img)})$. The image variance is a measure for the isotropic image sharpness and is, thus, a function of the three coil currents. The greatest image sharpness is achieved, if the image variance reaches its maximum.

To find the global minimum of the negative image variance and with that the optimum coil currents, a Nelder-Mead simplex optimisation algorithm explores the 4-dimensional parameter space [Rudnaya, 2012; Nelder, 1964]. Thereby, the optimisation scheme successively acquires target scans of the same ROI while varying the coil currents and analysing the associated negative image variance. Figure 5.3b, c depicts this optimisation process during one run of the dynamic focusing routine.

As multiple-parameter optimisations are generally more challenging in terms of robustness and precision compared to one-parameter optimisations, this dynamic focusing routine is used as a coarse pre-focusing and astigmatism correction. To determine the precise optimum focus current a second static focusing routine varying only the focus current is applied.

Static Fine Focusing: Figures 5.3d-f illustrate the static fine focusing routine. In a static approach, a number of measurements are performed over a varying parameter and subsequently analysed. The static fine focusing routine, thus, acquires a number of edge profiles, as shown in Fig. 5.3e, over a range of focus currents. During the analysis, an error function is fitted to each of these edge profiles to derive the full-width-at-half-maximum (FWHM), which denotes the electron spot diameter along the edge profile. To eliminate errors in the FWHM-calculation, an edge detection algorithm determines the edge angle and defines a scanning trajectory for the edge profile scan perpendicular to the edge (Fig. 5.3d). As a result, a set of FWHM values is obtained over a range of focus currents. To these FWHM values a focus function fit is applied to determine the optimum focus current along with the associated electron spot size, the FWHM. This process is carried out for two mutually orthogonal edges which leads to two focus function curves, as shown in Fig. 5.3f. Thereby, the beam roundness can be assessed and the stigmator settings can be further refined, if necessary. The closer the minima of the two focus function curves are to each other, the weaker the remaining astigmatism. It should be noted here, that differences in the focus function minima below 0.3 mA have negligible effects on the electron spot FWHM. The optimum focus current for the system is then calculated as the mean value of the two focus function minima. For more information on the fine focusing routine the reader is referred to [Ferstl, 2015].

The combination of these two focusing modules allows for defining the optimum set of coil currents ($I_{stigm,1}, I_{stigm,2}, I_{foc}$) for a specific state of the NanoTube, depending on the alignment currents, the grid voltage, the acceleration voltage and the stage in the cathode ageing process. Thereby, electron spot diameters down to 170 nm could be achieved with a fresh cathode, a high grid voltage and a low acceleration voltage. This focusing routine, which was exclusively used throughout this work, was developed by Simone Ferstl during her master's thesis and her project at Excillum AB (Sweden).

5.1.2 The Pilatus Detector

Apart from the various advantages of the NanoTube, imaging applications struggle with the low emitted X-ray flux. Therefore, a single-photon counting detector, a Pilatus 300K-W (Dectris, Switzerland), was installed as the NanoTube's counterpart.

Figure 5.4 displays a rendering of the Pilatus detector and illustrates the underlying principle of the hybrid-pixel detection technology. This detector features a wide detection area of 251.4 mm × 33.5 mm (Fig. 5.4a). The detection area is composed of three horizontally installed modules of 487 pixel × 195 pixel, which results in a total pixel count of 1475 pixel × 195 pixel. Thereby, the total horizontal pixel count of 1475 defines the horizontal FOV (field of view) available for imaging at a given effective pixel size. Each detector pixel has a square shape with an edge length of 172 µm. The modules are separated by detector gaps with a width of 7 pixel. In these detector gaps no data is acquired. Moreover, there are 17 randomly distributed unresponsive pixels, which are also known as dead pixels.

Hybrid Pixel Structure

The structure of one hybrid pixel is formed by a sensor and a readout circuit. These two parts are connected via an indium bump bond to form one independent unit (Fig. 5.4c).

The sensor pixel is formed by a 1 mm-thick layer of silicon in a p-in-n diode configuration. A high-voltage bias is applied, which removes any intrinsic charge carriers from the sensor layer. An incident X-ray photon generates a certain number of electron-hole pairs dependent on the absorbed amount of the photon's energy. The electron-hole pairs then migrate in the electric field of the high-voltage bias towards the electrodes of the sensor pixel. There, they generate a charge pulse which is further processed in the readout electronics.

In the readout pixel, or the application specific integrated circuit (ASIC), each charge pulse, ideally representing one photon absorption event, is processed individually. After amplifying the charge pulse, a pulse shaper is used to improve the signal-to-noise ratio (SNR) of the charge pulse (Fig. 5.4c). The discriminator discards any pulses below an

externally adjustable threshold. If the charge pulse exceeds the threshold it is digitally recorded by a 20-bit counter [Russo, 2017]. As the incoming charge pulse depends on the energy of the absorbed X-ray photon, the threshold acts as a discrimination tool with respect to the photon energy. The threshold of the Pilatus detector is continuously adjustable in the range of $[2.7; 18]$ keV.

This concept enables a fast signal readout and the Pilatus provides a high dynamic range of 20 bit. However, the pixel size is quite large compared to CCD-based X-ray cameras, as it is limited by the minimum size of the ASIC [Russo, 2017].

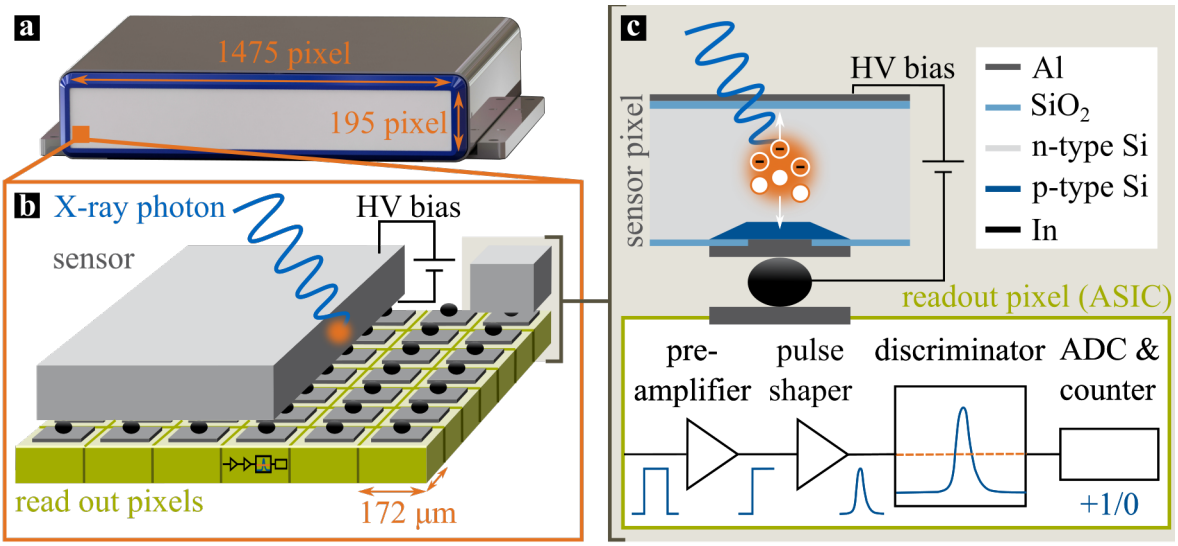

Figure 5.4: **The Single-Photon-Counting Pilatus Detector.** (a) Rendering of the Pilatus 300K-W detector with an active detection area of 251.4 mm × 33.5 mm and 1475 pixel × 195 pixel. (b) Structure of the hybrid-pixel array with a semiconducting sensor layer connected over bump bonds to the read out pixels. (c) Enlarged schematic of one single hybrid pixel from (b) with the absorption of an X-ray photon in the sensor layer, which generates a charge pulse which is then processed in the ASIC. If a charge pulse representing a photon absorption event exceeds the externally set threshold (dashed orange line) in the discriminator it is recorded by the counter. Panel (a) adapted from [Müller, 2019] and panel (b), (c) based on [Ehn, 2017].

Characteristics of the Pilatus Detector

Noise Characteristic: The signal discrimination represents a crucial feature of the Pilatus detector, since it eliminates readout and dark-current noise, a well-known prob-

lem of integrating detectors. Dark current is called the intrinsic effect of thermal fluctuations in the sensor layer causing additional electron-hole pairs. In integrating detectors, dark current contributes to the recorded signal proportional to the exposure time. The absence of readout and dark-current noise enables the Pilatus detector to record image data with an improved SNR, which is particularly useful for imaging with the low X-ray flux provided by the NanoTube.

Charge-Sharing: An absorbed photon causes a Gaussian-like charge-distribution across the electrode surface. Thus, the centre pixel shares a part of its charge with adjacent readout pixels (charge-sharing). For very low detection thresholds, it may occur that these charges in the adjacent pixels contribute to the recorded signal. Thereby, charge-sharing increases the size of the detector's point spread function (PSF). For higher detection thresholds, these contributions can be removed from the signal, charge-sharing effects can be suppressed and the detector PSF is decreased. This way, the detection threshold takes a direct influence on the detector PSF. An adequate threshold setting allows for a detector PSF of the size of one pixel. Increasing the threshold, however, not only means to discard unwanted signal but also to reduce the image SNR. Adjusting the detector threshold is, thus, a trade-off between PSF size and SNR.

Direct Conversion: Another major asset of the Pilatus detector is the use of direct conversion, which means the X-ray photons are directly converted into a charge pulse without the need for scintillation crystals. Scintillation crystals are used in other detectors to convert the incident X-ray photons into visible light. Depending on the thickness of the crystal layer, this can lead to a significant signal spread and thus increase of the detector PSF.

Sensor Material and Quantum Efficiency: The Pilatus detector uses silicon as a sensor material. Silicon has the major advantage that it can be easily fabricated with little defects, thus reducing the effects of charge trapping. Charge trapping can hinder electrons and holes from migrating towards the electrodes. This particularly hampers signal detection from low energy X-ray photons [Russo, 2017].

An important figure of merit regarding X-ray cameras is the detection quantum efficiency (QE). It describes the detected proportion of incident photons. For a direct conversion detector, the energy-dependent QE of the sensor layer can be described by applying the Lambert-Beer law (Eq. 3.13):

$$\mathrm{QE}(E) = 1 - e^{-\mu_\mathrm{s}(E)\cdot d_\mathrm{s}}, \tag{5.1}$$

with $\mu_\mathrm{s}(E)$ the energy-dependent linear absorption coefficient of the sensor material and d_s the thickness of the sensor layer [Ehn, 2017]. At this point, it should be noted

that the final effective detection QE depends beyond the sensor QE on the chosen detector threshold. Employing this formula for the 1 mm-thick silicon layer of the Pilatus detector results in a theoretic QE curve.

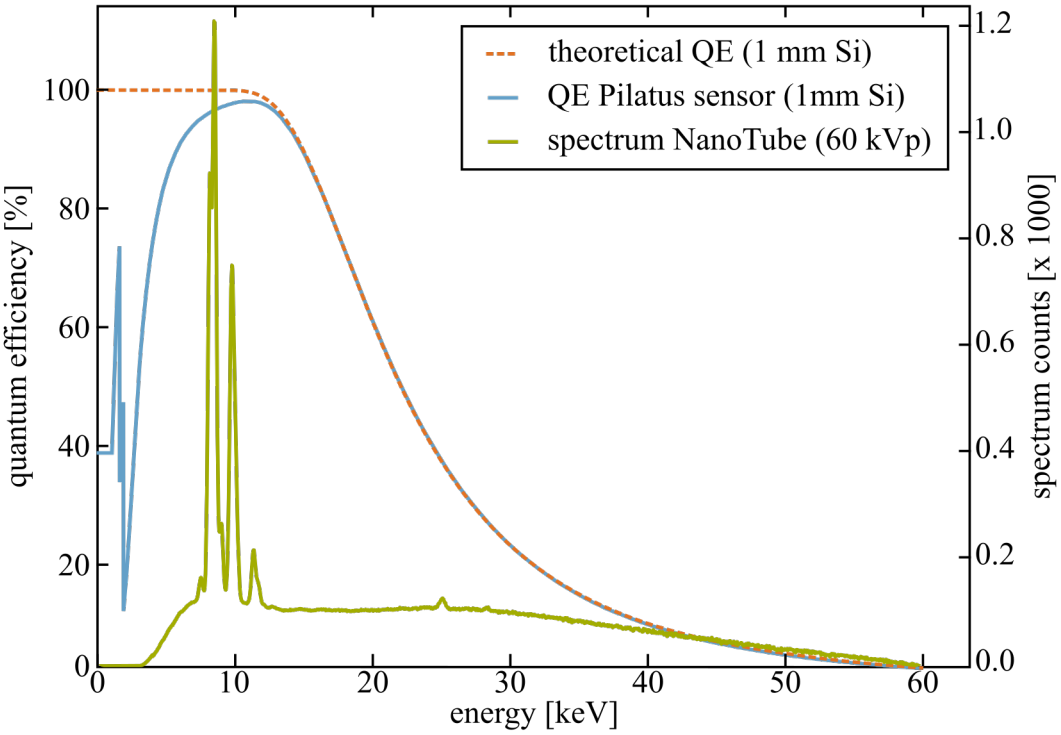

Figure 5.5: **Quantum Efficiency (QE) of the Pilatus Detector and Emission Spectrum of the NanoTube.** The theoretical QE of a 1 mm-thick silicon-layer, the measured QE of the Pilatus sensor and the emitted source spectrum of the NanoTube with an acceleration voltage of $U_{acc} = 60\,kV$ plotted over the X-ray energy. QE data of the Pilatus sensor courtesy of [Müller, 2019].

Figure 5.5 displays the theoretic QE curve plotted over the X-ray energies together with the actual QE of the Pilatus and the emission spectrum of the NanoTube. It can be clearly seen that the theoretic prediction matches the actual QE values very well. For energies above 15 keV the QE decreases rapidly dampening any signal originating from higher-energy X-ray photons. Whereas this would mean a significant signal loss when coupled with higher-energy X-ray tubes, it suits the spectrum of the NanoTube rather well. The NanoTube spectrum is dominated by the characteristic L-lines of tungsten, which lie well below 15 keV. For X-ray energies below 13 keV the theoretic QE clearly deviates from the actual value. These deviations can be traced back to absorption effects of other thin layers installed around the sensor layer, as sketched in Fig. 5.4c).

Other materials, such as cadmium telluride (CdTe) have a superior sensor QE for higher energy X-rays. CdTe, however, is also much more affected by charge trapping effects, which renders it unattractive for applications using softer X-rays sources, such as the NanoTube.

More detailed information on the Pilatus detector can be found in [Bech, 2008; Kraft, 2009] and a thorough investigation of the performance combining the NanoTube with the Pilatus detector can be found in [Müller, 2019] and in Chapter 6 of this thesis.

5.1.3 Configuration of the NanoCT

As previously mentioned, the magnification of the NanoCT is purely defined by the setup geometry. Thus, the magnification M can be directly calculated from the distance of the source to the tomography rotation axis d_{sa} and the source-detector distance d_{sd}:

$$M = \frac{d_{\mathrm{sd}}}{d_{\mathrm{sa}}}. \tag{5.2}$$

This magnification results in an effective voxel size v_{eff} in the reconstructed data:

$$v_{\mathrm{eff}} = \frac{p_{\mathrm{det}}}{M}, \tag{5.3}$$

whereby p_{det} denotes the detector pixel size. Throughout this thesis, voxel and pixel sizes are given on multiple occasions. These values denote the effective isotropic edge length of a square pixel or a cubic voxel, unless otherwise indicated.

Figure 5.6 illustrates the structure of the NanoCT and introduces the setup specific coordinate system. Thereby the z-axis is defined along the optical axis, the x-axis lies in the horizontal plane perpendicular to the optical axis and the y-axis defines the vertical direction. The origin of the coordinate system is set to the estimated position of the X-ray source spot.

The entire NanoCT is installed on top of an optical table (Newport RP Reliance) from Newport Corporation (USA). It features passive pneumatic vibration isolation legs, which ensure the stability of the setup.

The NanoTube and the Pilatus detector, as the main components, are both laid out for high-resolution imaging and complement each other to form a powerful combination. The NanoTube provides very small source PSFs and high stability of the source spot position over time. Furthermore, the Pilatus detector allows for a detector PSF of one pixel given adequate threshold settings. Beyond that, the detector enables high SNR images even with the low X-ray flux of the NanoTube and the QE of the silicon sensor is well suited for the NanoTube's energy spectrum.

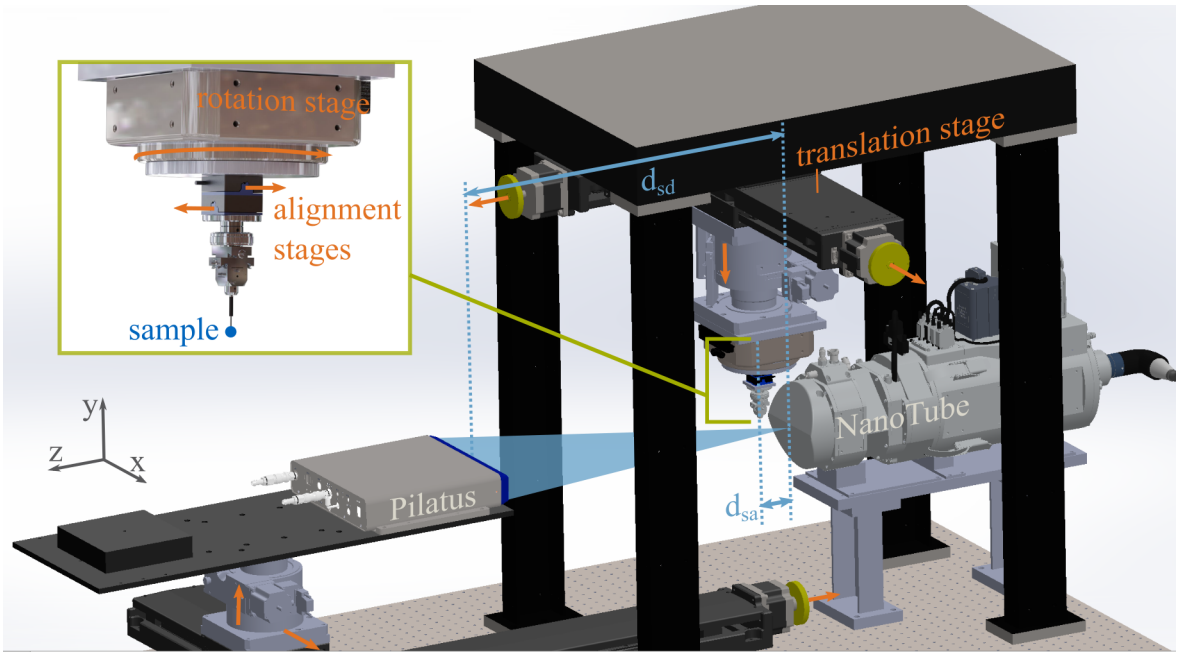

Figure 5.6: **Configuration of the NanoCT.** An enlarged image shows the rotation and alignment stages, as well as the pin holding the sample. The NanoTube, and the Pilatus detector are labelled in light grey and some of the relevant motorised stages (translation, rotation, alignment stage) are designated in orange. The orange arrows denote the available directions of motion with the motorised stages. The sample position is labelled in blue. The two light blue arrows d_{sd} and d_{sa} indicate the source-detector and the source-axis distances, which define the system's magnification. Rendering with courtesy of Johannes Brantl.

Apart from the detector and the X-ray source, the rotation stage is an essential part to enable tomography imaging. To reduce positioning errors and axis wobble to a minimum, an air-bearing rotation stage with a cogging-free direct motor (RT 150S) from LAB Motion Systems (Belgium) is installed in the NanoCT (Fig. 5.6).

Below the rotation stage, the sample is mounted (Fig. 5.6, enlarged image). In between, additional high-precision piezo stages (M-663.4) from PI (Germany) and a manual goniometer head (1005) from Huber Diffraktionstechnik (Germany) are installed to facilitate translation and angular alignment of the sample onto the centre of rotation. Such an alignment is crucial, since an offset of the sample from the rotation centre reduces the effective field of view (FOV) available for imaging and contributes to increasing d_{sa} values and, thus, a less efficient imaging process.

The original concept of the NanoCT was designed to allow imaging of samples in a

water bath. Therefore, the rotation stage and the attached components as well as the sample are mounted upside down using an overhead construction, as depicted in Fig. 5.6.

The NanoCT includes six motorised linear stages for translation movements with micrometer precision (Fig. 5.6, orange arrows). While the NanoTube's location is fixed, both the rotation stage and the detector can be moved in x-, y- and z-direction using the linear stages. Adjusting the position in x- and y-direction is essential to align the components onto the optical axis. Via translations in z-direction, the magnification can be modified continuously. Thereby, d_{sd} can be varied in the range of $[190; 1690]$ mm and typical values of d_{sa} lie in the range of $[0.5; 2]$ mm. This results in v_{eff}-values ranging from 50 nm to 2 µm and an associated FOV from (70 µm × 9 µm) to (3 mm × 0.4 mm).

5.2 Tomography Acquisition with the NanoCT

Tomography acquisition with the NanoCT requires high precision in every aspect. The design of the NanoCT and its components were selected to facilitate this high precision. Nevertheless, generating high-quality NanoCT data still remains a non-trivial task. In this section, the key measures and processes which tomography acquisition with the NanoCT entails are described in detail.

The specific setup geometry is an essential input for the reconstruction routine. This renders a precise geometry calibration of every component in the NanoCT vital. In the following, the calibration routine, which was used in this work, is explained and assessed. Beyond that, a further promising approach for geometry calibration is introduced which may contribute to advancing the NanoCT system in the future.

While the geometry of the system remains constant over a certain period of time, there are some routines which need to be repeated for every new tomography scan. Thus, the following section further presents these routines alongside a number of valuable insights. For more information on tomography acquisition with the NanoCT, a list of relevant tomography parameters is explained and typical values are presented in the appendix A.1.

5.2.1 Geometry Calibration of the NanoCT

The NanoCT's geometry is characterised by a wide cone beam. In such a configuration slight changes in the components' positions have an enormous impact on the resulting projection images during a tomography. The setup geometry is fed to the reconstruction algorithm to facilitate consistent CT reconstruction. Thus, a precise calibration of the setup components' positions with respect to the optical axis is crucial to obtain high-quality NanoCT volume data.

In the following, the optical axis shall be defined as the normal to the detector surface passing through the X-ray source spot. The point where the optical axis hits the detector surface shall be referred to as the projection principle point (ppp). A component's position along the optical axis shall be referred to as the longitudinal position. The longitudinal position of the detector can be also referred to as the source-detector distance (d_{sd}) and the longitudinal position of the tomography axis as the source-axis distance (d_{sa}). Moreover, the transverse position of a component denotes the position on a plane orthogonal to the optical axis. The transverse position, thus, consists of a horizontal and a vertical component.

For constant electron optics values in the NanoTube, the position of the X-ray source spot is fixed. Furthermore, we assume the detector surface to be stable and orthogonal

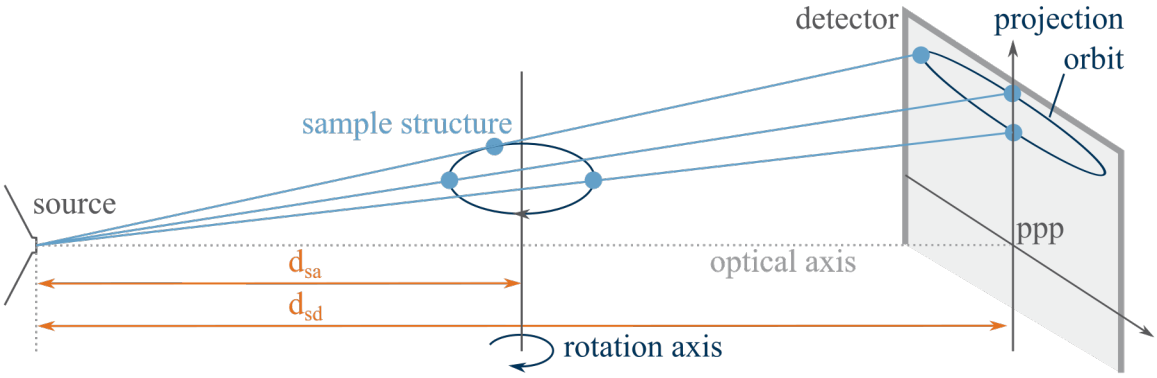

Figure 5.7: **Projection Orbit of a Point-Like Sample Structure in a Cone-Beam Geometry.** The sample structure describes a circular trajectory rotating around the tomography axis. This trajectory is projected onto the detector resulting in an elliptic shape. The source-axis distance is denoted as d_{sa} and the source-detector distance as d_{sd}.

to the beam direction and to the linear stage adjusting the longitudinal detector position. This results in a well-defined, fixed optical axis and a constant transverse position of the ppp on the detector. Based on these assumptions, merely the longitudinal and transverse position of the detector and the tomography axis remain to be calibrated. Thereby, the tomography axis position is used as a synonym for the location of the centre of rotation during a tomography scan.

It is possible to determine these geometry parameters simultaneously using a phantom containing a number of point-like fiducial markers. In a tomography, a point-like structure describes a circular trajectory which is projected by a cone-beam onto the detector at a certain angle, resulting in a so-called circular projection orbit. This principle is illustrated in Fig. 5.7. By analysing the projection orbits of multiple randomly distributed, point-like objects, it is possible to derive the entire set of geometry parameters, including tilt angles of the detector and the tomography axis. This approach has successfully been implemented for cone-beam microCT systems by von Smekal *et al.* [Von Smekal, 2004] and Dittmann *et al.* [Dittmann, 2018]. Applying this approach to the NanoCT, however, requires to fabricate a phantom with adequate precision suitable for the typical FOV and v_{eff}-values of the NanoCT. Thus, the objects in the phantom used for tracking the projection orbit must be very small, and have clear boundaries. First attempts have been made to fabricate such a phantom without yielding satisfactory results. Therefore, this approach has not been used throughout this work, but certainly represents an interesting tool for advancing the NanoCT in the future.

In the following, the specific calibration routine, which was used in this work, is described. In contrast to the previously described simultaneous calibration principle, it

consists of an array of calibration steps which are successively carried out following a specific order. Thereby, the longitudinal detector position must always be calibrated first, since all other calibration steps are based on its result. The transverse detector position calibration and the longitudinal tomography axis calibration can be also performed in the reverse order. They do not depend on each other. In contrast to that, the transverse tomography axis position calibration requires the results from the other calibration routines, and, thus, has to be carried out as the final step. All these calibrations are a non-trivial task. While there is still room for improvement, the current calibration routines yield highly satisfactory results through an iterative application of the specific steps.

Longitudinal Detector Position

The longitudinal detector position may be also referred to as the source-detector distance (d_{sd}). In the NanoCT data presented in this thesis, it ranges from values between 200 mm and 900 mm. To calibrate this value an expandable folding rule with a scale down to 1 mm was used. This leads to an approximate systematic calibration error of 0.5 mm. Considering alignment errors when using the folding rule, we assume a statistical error of 1 mm. Thus, we obtain a longitudinal detector position of $d_{\mathrm{sd}} \pm 1.5\,\mathrm{mm}$.

Transverse Detector Position

To determine the transverse detector position, the longitudinal detector position has to be calibrated. The transverse detector position is defined as the distance of the detector centre ($(x_{\mathrm{c}}, y_{\mathrm{c}}) = (1475/2\,\mathrm{pixel}, 195/2\,\mathrm{pixel}) = (126.85\,\mathrm{mm}, 16.77\,\mathrm{mm})$) from the ppp ($x_{\mathrm{ppp}}$, y_{ppp}). For the sake of simplicity, only the procedure to determine the horizontal component of the transverse detector position is considered in the following.

In Fig. 5.8, the underlying principle for calculating the horizontal component of the transverse detector position is schematically explained. At least two images (image_1, image_2) of the same sample structure are acquired with different longitudinal detector positions (source-detector distances: $d_{\mathrm{sd},1}, d_{\mathrm{sd},2}$). Due to the cone-beam geometry of the NanoCT, the sample structure is projected to a different horizontal pixel position on the detector (x_1, x_2) in the two images. The sample structure itself grows for increasing source-detector distances. Therefore, it is wise to select a sufficiently fine and well-defined sample structure to avoid uncertainties, when measuring x_1 and x_2.

According to the intercept theorem, there is a relation between the horizontal structure coordinates (x_1, x_2), the source-detector distances ($d_{\mathrm{sd},1}, d_{\mathrm{sd},2}$) and the ppp coordinate

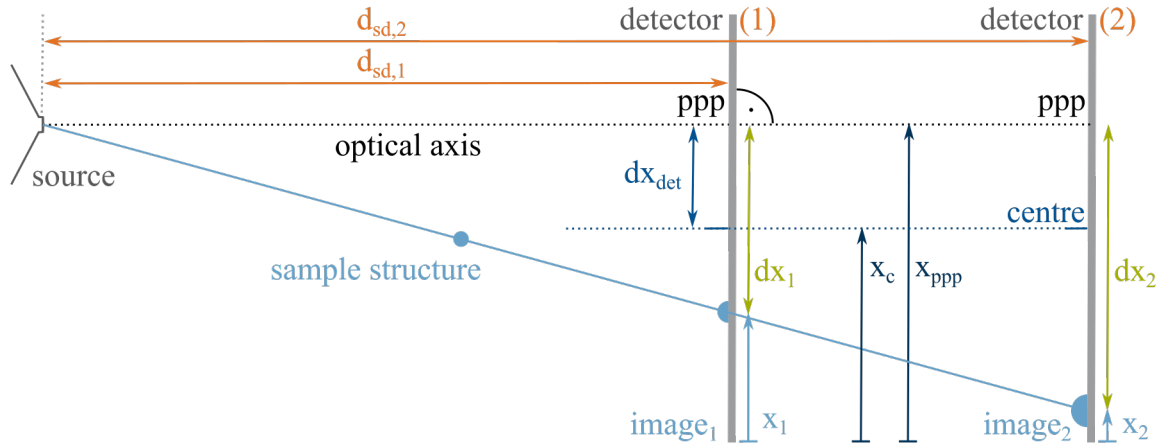

Figure 5.8: **Strategy for Calculating the Horizontal Component of the Transverse Detector Position.** Two images ($\text{image}_1, \text{image}_2$) at different longitudinal detector positions ($d_{\text{sd},1}, d_{\text{sd},2}$) exhibit two different positions of a sample structure (x_1, x_2). The horizontal coordinate of the detector centre is described by x_c and the horizontal position of the ppp is given by x_ppp. The variables dx_1 and dx_2 denote the horizontal distances of the sample structure from the ppp in the images which allow for calculating dx_det the horizontal component of the transverse detector position.

(x_ppp):

$$\frac{d_{\text{sd},1}}{d_{\text{sd},2}} = \frac{dx_1}{dx_2} = \frac{x_\text{ppp} - x_1}{x_\text{ppp} - x_2}. \tag{5.4}$$

Rearranging Eq. 5.4 provides an expression for x_ppp. Based on this expression, we can calculate the horizontal component of the transverse detector position dx_det:

$$dx_\text{det} = x_\text{ppp} - x_\text{c} = \frac{x_1 \cdot d_{\text{sd},2} - x_2 \cdot d_{\text{sd},1}}{d_{\text{sd},2} - d_{\text{sd},1}} - 126.85\,\text{mm}. \tag{5.5}$$

The described principle can be transferred to determine the vertical component of the transverse detector position. Hence, Eq. 5.5 provides a solution for calculating the transverse detector position from a minimum of two images acquired at well-defined source-detector distances. To minimise the statistic error, though, it is advisable to acquire a higher number of images at varying detector distances and to track many different sample structures within the images. The calibration procedure is based on the assumption of the motorised, longitudinal detector-stage generating a motion perfectly parallel to the optical axis. Otherwise, the position of the ppp in the detector FOV does not remain constant for different source-detector distances. Therefore, it is crucial to ensure the detector surface is perpendicular to the motorised, longitudinal

detector-stage. Deviations on that matter, materialise through errors in the calibration of the transverse detector position. Furthermore, calibration errors can originate from uncertainties in the longitudinal detector position.

Longitudinal Tomography Axis Position

The longitudinal positions of the tomography axis and of the detector determine the magnification in the reconstructed NanoCT data (Eq. 5.2). The longitudinal axis position or source-axis distance (d_{sa}), is conventionally in the range of 1 mm during a NanoCT acquisition. In contrast to that, the longitudinal detector positions (d_{sd}) are typically larger than 200 mm. As a result, small errors in the d_{sa}-calibration have much more severe consequences than deviations in the d_{sd}-value. Therefore, precisely determining the longitudinal axis position is crucial to correctly define the magnification and to calibrate the sample stages of the NanoCT. For the longitudinal axis position calibration, the longitudinal detector position must be calibrated beforehand.

Figure 5.9 conveys one approach for the calibration process. Here, at least four images are recorded at a constant d_{sa}-, and d_{sd}-value. In Fig. 5.9 the sample has an offset from the rotation axis. After acquiring image_1, the sample is rotated by 180° to generate image_2. Subsequently, the rotation axis and, thereby, the sample is moved by dx perpendicular to the optical axis and image_3 is recorded. Finally, the sample is rotated back by −180° which is followed by the acquisition of image_4.

The positions of the sample structure in the images (x_1, x_2, x_3, x_4) describe the magnification from the translation distance dx to the image of this distance on the detector (dx_1, dx_2). Thereby, the two translation distances dx_1, and dx_2 represent two different sample planes caused by the sample offset from the rotation axis. The magnification in the longitudinal axis position can be, thus, derived from the mean value of these two imaged distance values (dx_1, dx_2) and the true translation distance dx:

$$M = \frac{\frac{1}{2}\left(dx_1 + dx_2\right)}{dx}, \tag{5.6}$$

with $dx_1 = x_1 - x_4$ and $dx_2 = x_2 - x_3$ (Fig. 5.9). From this magnification value and the known longitudinal detector position d_{sd}, we can derive the longitudinal axis position d_{sa}:

$$d_{\mathrm{sa}} = \frac{1}{M} \cdot d_{\mathrm{sd}} = \frac{2 \cdot dx}{dx_1 + dx_2} \cdot d_{\mathrm{sd}} \tag{5.7}$$

Similar to the transverse detector position calibration, a repeated application of the described routine for different sample structures and for varying combinations of d_{sa}- and d_{sd}-values allows for minimising statistical errors.

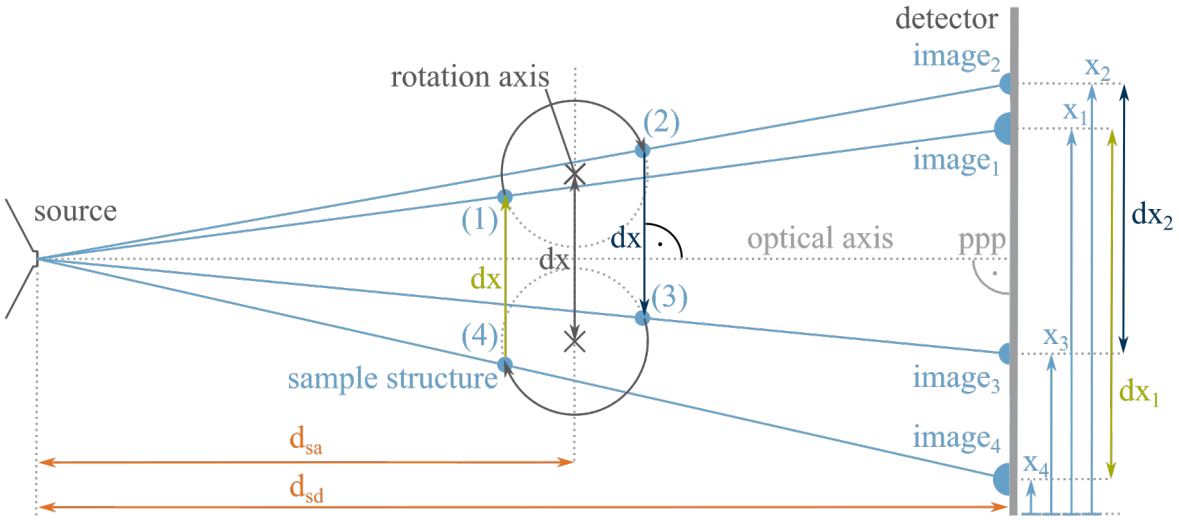

Figure 5.9: **Strategy for Calibrating the Longitudinal Axis Position.** Four images at different positions (but at a constant longitudinal axis position and detector position - d_{sa}, d_{sd}) are taken: (1)-(2) rotation by 180°, (2)-(3) translation by dx, (3)-(4) rotation by −180°. The translation distance dx is magnified to result in the distances dx_1, and dx_2, which can be calculated from the four images. In this scheme, the detector is shown centred around the optical axis.

This calibration method, however, has one major disadvantage. It assumes that the translation dx happens perfectly perpendicular to the optical axis. Angular deviations cause significant deviations in the measured dx_1-, and dx_2-values and finally lead to an erroneous calibration result. A further source for errors are any deviations in the calibrated longitudinal detector position d_{sd}.

To eliminate angular deviations as an error source, alternate approaches rely on other magnification measures than the translation distance dx. A different approach to determine the magnification is to acquire images of a rotationally symmetric sample of a known diameter. This approach involves the analysis of two images at a constant longitudinal axis position d_{sa} but taken at different rotation angles: one image at a rotation angle, where the sample diameter appears smallest, thus representing the largest source-sample distance $d_{sam,max} = d_{sa} + dx_{sam}$ (Fig. 5.11), and one image, where the sample diameter appears largest, thus representing the smallest source-sample distance $d_{sam,min} = d_{sa} - dx_{sam}$. The sample offset from the rotation axis is, here, considered in the form of dx_{sam}. By determining the source-sample distances $d_{sam,max}$, $d_{sam,min}$, the sample offset can be eliminated providing the longitudinal axis position. The precision of this approach, however, largely depends on the fabrication precision of the

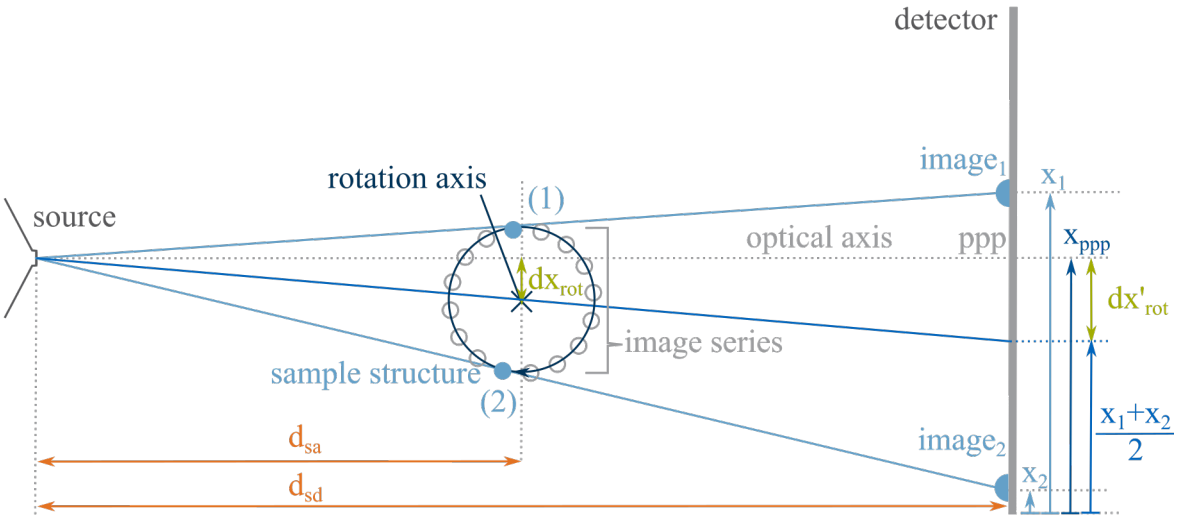

Figure 5.10: **Strategy for Determining the Transverse Axis Position.** From the image series image_1 and image_2 featuring the largest deflection of the imaged sample structure from the rotation centre are selected. Based on the two images the magnified transverse axis position dx'_{rot} and the true transverse axis position dx_{rot} are calculated. The detector is shown in an aligned configuration with the ppp in the centre and, thus, $x_{\text{ppp}} = 126.85\,\text{mm}$.

rotationally symmetric sample.

Transverse Tomography Axis Position

Apart from the necessity of the transverse axis position as input for CT reconstruction, an insufficient alignment of the rotation axis onto the optical axis causes the space available in the FOV to not be efficiently used. This ultimately results in an inefficiency of the entire NanoCT system, regarding sample sizes, effective voxel sizes, exposure times, and many other parameters. Thus, determining the transverse axis position for aligning the rotation axis onto the optical axis is highly relevant to optimise the performance of the NanoCT. For the success of the transverse axis position calibration, the longitudinal and transverse detector position as well as the longitudinal axis position must be known.

The principle of the calibration technique is visualised in Fig. 5.10. It is based on two images (image_1, image_2) containing a well-defined sample-structure (Fig. 5.10). To obtain these two images, a series of images, with at least 36 elements, are acquired for different rotation angles over a range of 360°. From this series, the two images

are selected where the deflection of the imaged sample structure from the centre of rotation appears greatest. Note that the specific rotation angles of these two images do not necessarily have to enclose an angle of 180° (Fig. 5.10).

From the two selected images (image_1, image_2), the magnified transverse axis position dx'_{rot} can be determined. It is given by the distance of the centre of rotation based in the images from the ppp:

$$dx'_{\text{rot}} = x_{\text{ppp}} - \frac{x_1 + x_2}{2} \tag{5.8}$$

By including the magnification, we obtain the true transverse axis position dx_{rot}:

$$dx_{\text{rot}} = \frac{1}{M}\, dx'_{\text{rot}} = \frac{1}{M}\left(x_{\text{ppp}} - \frac{x_1 + x_2}{2}\right). \tag{5.9}$$

Similar to the previous calibration methods, a repetitive execution of this process for various source-axis and source-detector distances decreases the statistical error and increases the precision of the calibration. Finally, the rotation axis can be aligned via shifting the rotation axis by the resulting dx'_{rot}-value.

5.2.2 Steps Towards Tomography Acquisition

The setup geometry is considered as rather constant over time. The geometry calibration, thus, has to be repeated only after a long period of time or if an incidence raises suspicion about changes in the geometry, such as a cathode exchange.

In contrast to that, there are some routines which have to be performed prior to each new tomography. Every new application and sample has specific demands and needs and requires a reassessment of the tomography parameters. In the following the most important steps of these routines are presented.

Sample Mounting

The sample is mounted on a 3D printed pin using superglue. The mounting should be performed as early as possible, so that the glue is completely polymerised to provide optimum stability. This is particularly important to avoid motion blurring due to mechanical instabilities during tomography acquisition.

During the mounting process, it is crucial to ensure a centred position of the sample on top of the pin. This will later enable to minimise the source-axis distance d_{sa} and according to Eq. 5.2 to maximise the magnification.

Another relevant aspect is to avoid covering unnecessarily large areas of the sample with superglue, in particular when handling CPD samples. Due to the strong capillary forces in CPD samples, the glue is sucked into the porous tissue like water into a sponge.

This not only poses a risk for corrupting the sample structure, but also diminishes propagation-based phase effects which contribute to the overall soft-tissue contrast.

Sample Alignment to the Rotation Axis

After mounting the sample onto the pin, it is fixed to the lower part of the goniometer head, which is attached to the sample alignment stages, as illustrated in Fig. 5.6. In the next step the sample is aligned to the rotation axis, using the sample alignment stages, to enable an efficient use of the available FOV and to achieve smaller source-axis distances.

Rough Alignment: For a convenient rough alignment, a camera is installed perpendicular to the optical axis in the NanoCT. Its FOV is adjusted to cover the X-ray target of the NanoTube and some of the space in front of it. The camera optics and the distance from the X-ray target are chosen to obtain a focus plane which passes through the X-ray target.

In a first step, the sample is moved into the FOV of the sample camera by decreasing the source-axis distance. Subsequently, the sample alignment stages are used to move the sample into the focus plane of the sample camera. This provides a rough centring of the sample in front of the X-ray target.

In the second step, the sample position is adjusted, so that the sample is in the FOV of the detector. For this purpose, the NanoTube is switched to operation mode, the detector is prepared for image acquisition and a small source-detector distance of $\approx$ 200 mm for a larger imaging FOV is chosen. The operator, then, alternates between acquiring a projection image and correcting the sample position based on the respective image. Thereby, the sample can be successively centred in the detector FOV using the alignment stages.

Fine Alignment: The principle of the fine alignment is shown in Fig. 5.11. This alignment is based on an iterative process. In every loop of this process, an image series over an angular interval of 360° with at least 36 images is taken. Similar to the calibration of the transverse axis position, the two images exhibiting the largest sample deflection from the centre of rotation are most relevant. Thereby, the centre of rotation should lie in the centre of the image in the calibrated NanoCT. For one of these two images the sample offset from the centre of rotation in the image dx'_{sam} is calculated. This provides an estimation of the true sample offset dx_{sam}:

$$dx_{\mathrm{sam}} = \frac{1}{M}\, dx'_{\mathrm{sam}} - x_{\mathrm{rest}}, \tag{5.10}$$

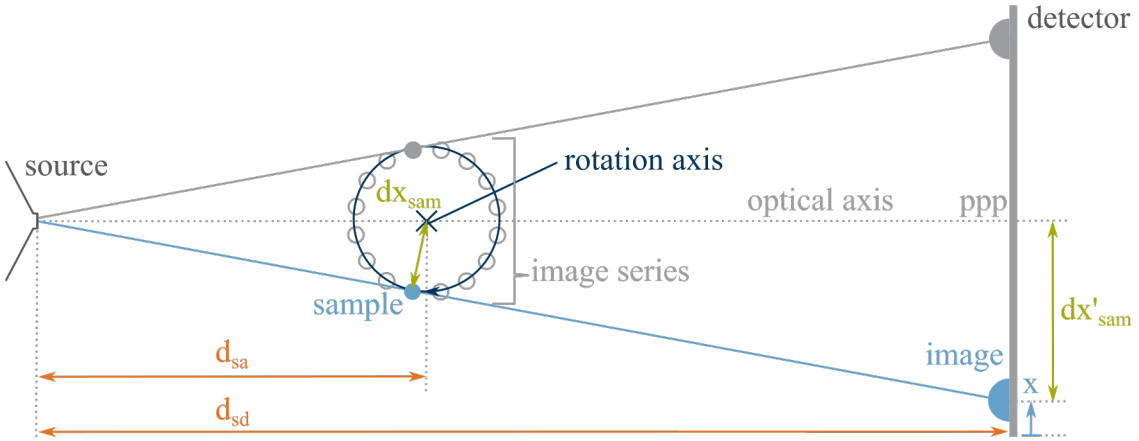

Figure 5.11: **Fine Alignment of the Sample to the Rotation Axis.** In an image series over 360°, there are two images showing a maximum sample deflection from the centre of rotation dx'_{sam}, which corresponds to the ppp and the centre of the image in the calibrated setup. Either of these two images can be used to estimate the sample offset from the rotation axis dx_{sam}.

whereby x_{rest} is a correction term which describes the overestimation by $\frac{1}{M}\, dx'_{\text{sam}}$. The sample position is, then, adjusted by $\frac{1}{M} dx'_{\text{sam}}$, which causes an over-correction of the sample offset by x_{rest}. These steps represent one loop of the fine alignment.

By repeating this loop for different d_{sa}- and d_{sd}-values, the overestimation decreases towards zero. Thereby, it can be observed that the x_{rest}-value increases for smaller d_{sa}-values and decreases the smaller sample offsets get. Furthermore, larger magnifications enable a higher precision when determining the dx'_{sam}-value. Consequently, large magnifications at rather large d_{sa}-values ($d_{\text{sa}} \approx 3 - 5\,\text{mm}$) lead to a more precise estimation of the sample offset. However, large magnifications are always associated with small FOVs using a cone-beam geometry.

To conclude, it is advisable to start the iterative process with small magnifications ($d_{\text{sa}} \approx 3 - 5\,\text{mm}$, $d_{\text{sd}} \approx 200\,\text{mm}$), which provide a large FOV to capture the initially large sample offset, and, then, to slowly converge towards the desired final magnification by increasing the d_{sd}-value.

For the tomography, a small d_{sa}-value ($d_{\text{sa}} < 1\,\text{mm}$) is beneficial as it allows to minimise exposure times. It is, thus, wise to re-examine the sample alignment by taking one final image series using the d_{sa}- and d_{sd}-values intended for the tomography scan.

NanoTube Focusing

The NanoCT was built to strive for the highest possible resolutions. The optimum resolution, however, is not always reached for the minimum achievable size. On the contrary, the resolution in the reconstructed data can benefit from using a larger electron spot. For larger electron spots, a smaller grid voltage U_g can be used which ultimately results in a higher emission X-ray flux. For higher X-ray fluxes, shorter exposure times suffice to obtain adequate SNRs. This in turn reduces the impact of motion blurring due to mechanical instabilities or source spot drifts, and finally may lead to a higher resolution in the reconstructed NanoCT data. Thus, it is advisable to use the maximum suitable electron spot size for the respective effective voxel size of the tomography ($\mathrm{FWHM}_{\mathrm{electron}} < 0.5\ v_{\mathrm{eff}}$). Varying the grid voltage U_g and subsequent refocusing with the rough and the static fine focusing routine allow to adjust the electron spot size (Fig. 5.3). The electron spot size can also be modified by merely changing the focus current I_{foc}. If the selected focus current, however, is not located in the minimum of the focus function curve (Fig. 5.3f), slight focus current fluctuations may cause severe changes in the electron spot size. To increase the stability of the electron spot size, the optimum focus current value should be used for tomography acquisitions and the electron spot size should rather be adjusted by varying the grid voltage.

After determining the adequate grid voltage, the static fine focusing routine should be run several times over ≈ 30 min until fluctuations of the optimum focus current are smaller than 0.3 mA. Furthermore, the astigmatism correction should be evaluated by assessing the beam roundness. This can be done by comparing the optimum focus currents for the two perpendicular edges, as displayed in Fig. 5.3f). Thereby, optimum stability of the electron spot size during the tomography acquisition can be ensured.

In general, the NanoTube should be in operation mode for at least 1 h prior to starting a tomography. This ensures that the source is in thermal equilibrium and the optimum stability of the source spot size and position is guaranteed. Otherwise, the setup geometry and the resulting data can be severely corrupted.

Extension of the Vertical FOV via Stitching

Figure 5.4a clearly illustrates the limited vertical FOV of the Pilatus detector. This can be also observed in the NanoCT slices of the single volumes in Fig. 5.12a. Often applications, however, require the investigation of VOIs which exceed the vertical extent of the FOV, such as the zebrafish sample presented in Fig. 5.12. The FOV can be easily extended along the vertical axis by acquiring multiple successive tomographies for different vertical positions of the sample (Fig. 5.12a). The resulting volumes can be then combined to a larger volume using a stitching algorithm (Fig. 5.12b).

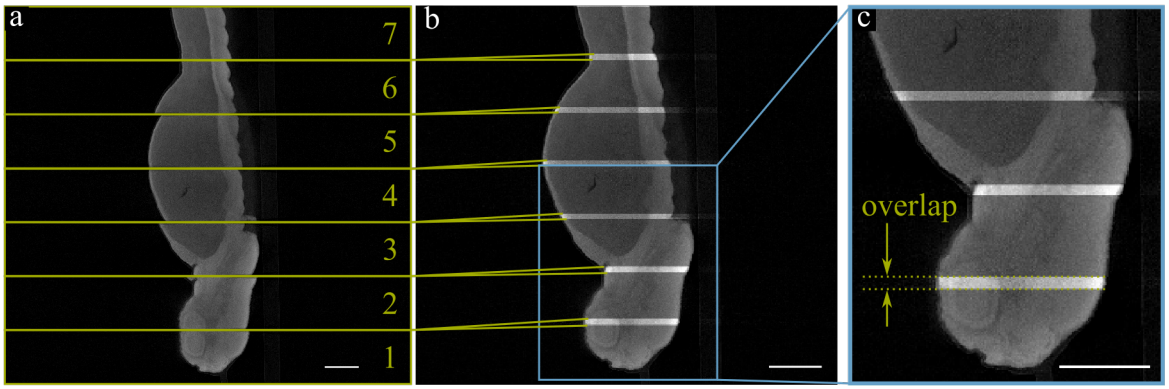

Figure 5.12: **Combining Multiple NanoCT Volumes of a Zebrafish Embryo via Stitching.** (a) NanoCT slices from seven single volumes for different vertical positions of the zebrafish sample. (b) NanoCT slice of the combined volume with the overlap regions highlighted. The volume was cropped for better visualisation. (c) Enlarged section of image (b) with the overlap indicated in green. Scalebars: 100 µm.

For this stitching algorithm to work, a vertical overlap of at least 50 pixels should be considered (Fig. 5.12c). On the one hand, this overlap provides the stitching algorithm with the necessary data to align the single volumes. On the other hand, the overlap compensates for under-sampling artefacts towards the bottom and the top of each NanoCT volume caused by the cone-beam projection geometry.

5.3 Image Processing

The image processing framework of the NanoCT is designed to retrieve high-resolution reconstruction volumes from the acquired tomography data sets composed of raw projection images. The majority of it is implemented in Python. Applying this framework, the specific parameter values were adapted with regard to image quality and visibility of structures of interest to fulfil the specific demands of each scientific question. It should be noted, here, that the resulting NanoCT volumes provide merely qualitative, not quantitative, information about the attenuation and phase-shift behaviour of the investigated sample.

In the following, the image processing routine, which was used throughout this work, is presented. Thereby, three particularly relevant steps will be explained more in-depth: the projection alignment, the phase retrieval and the deblurring technique.

As mentioned in the previous section of this chapter on tomography acquisition (Section 5.2), some of the applications presented in this work required a larger vertical FOV. For these applications, a stitching algorithm was used afterwards to combine the NanoCT volumes. This stitching algorithm calculates the 3D shift between the sub-volumes via cross-correlation to add them to the combined volume. Beyond that, segmentations, co-registrations and renderings of the 3D data were generated using the commercial software Avizo Fire 8.1 or Amira 6.4 (Thermo Fisher Scientific). Other data processing used in this work are presented in the corresponding method sections of the respective chapters.

Fig. 5.13 provides an overview of the standard NanoCT image processing work-flow. On the raw projection images an array of pre-processing corrections is applied, from flat-field over dead-pixel to intensity corrections (Fig. 5.13a). After that, the data is going through three successive feed-back loops based on the quality of the filtered-back projection data. Thereby, in Fig. 5.13b, c the reconstruction geometry is adjusted to correct for a global offset (centre shift correction: Fig. 5.13b) and to compensate for the orthogonal shift of each projection image individually (Fig. 5.13c). Afterwards, a propagation-based phase retrieval and deblurring is applied for contrast and resolution enhancement (Fig. 5.13d). The phase-retrieved and deblurred projections can be again used as input for a more stable and precise projection alignment. After optimising the reconstruction geometry, the phase-retrieval and the deblurring parameters, a final high-resolution NanoCT volume is obtained.

5.3.1 Pre-Processing of the Projection Data

Fig. 5.13a illustrates the successive pre-processing steps prior to an initial CT reconstruction. The pre-processing has a key role. It corrects for any artefacts which may

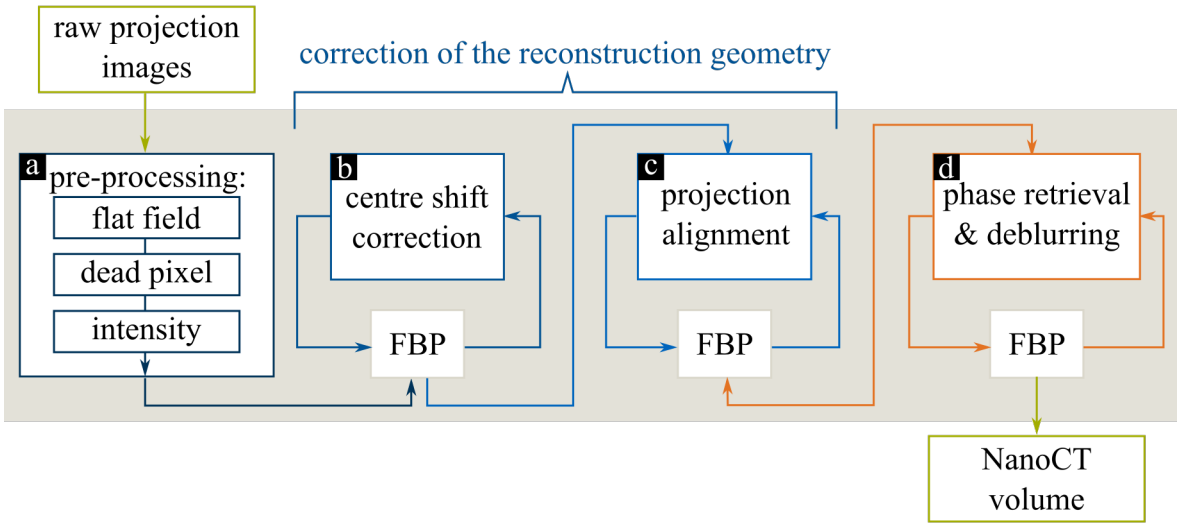

Figure 5.13: **NanoCT Image Processing Work-Flow.** Raw projection images serve as input to the image processing routine. (a) Pre-processing prior to the first filtered back-projection (FBP). (b) Correction of the centre shift based on the FBP for feedback. (c) Iterative correction of the individual alignment of each projection with the FBP for feedback. (d) Phase retrieval and deblurring of the processed projection images. For output, the final NanoCT volume is generated.

hamper the quality of the reconstructed data. The success of the projection alignment (Fig. 5.13c), in particular, depends on the pre-processing.

As a first step, a flat-field correction is performed. At the beginning of the tomography acquisition number of images with the sample removed from the FOV is recorded. These images are called flat-field images. To address the pixel positions without information (detector gaps, dead pixel) a horizontal, random typewriter shift is implemented for the acquisition of both projection and flat-field images. Taking into account the specific typewriter shifts, the flat-field images allow to retrieve and correct for the intensity distribution of the X-ray beam over the detector FOV and the individual detector pixel response. For more information on the acquisition routine and the typewriter, the reader is referred to the Appendix A.1.

In a subsequent step, the dead pixels including the detector module gaps are eliminated. To determine the position of these dead pixels an algorithm is applied which is based on the idea that pixel values of dead pixels show a minimum variance over the angular range of the sinogram. After locating the dead pixels, the horizontal positions of the projections are adjusted according to the typewriter shifts, to obtain a consistent sinogram for reconstruction. The dead pixel values are, then, interpolated by values

from the neighbouring projections.

As the X-ray flux may fluctuate during tomography acquisition, a further intensity correction over the number of projections is performed. Thereby, the mean pixel values in two region, at the left and at the right edge of the FOV, are tracked along the projection series. Thus, intensity ramps within each projection image, as well as intensity fluctuations between projection images can be corrected. This intensity correction, however, only works if the sample does not cover the entire FOV. If the sample exceeds the FOV, a median over each projection image as a whole can be used to detect any intensity fluctuations.

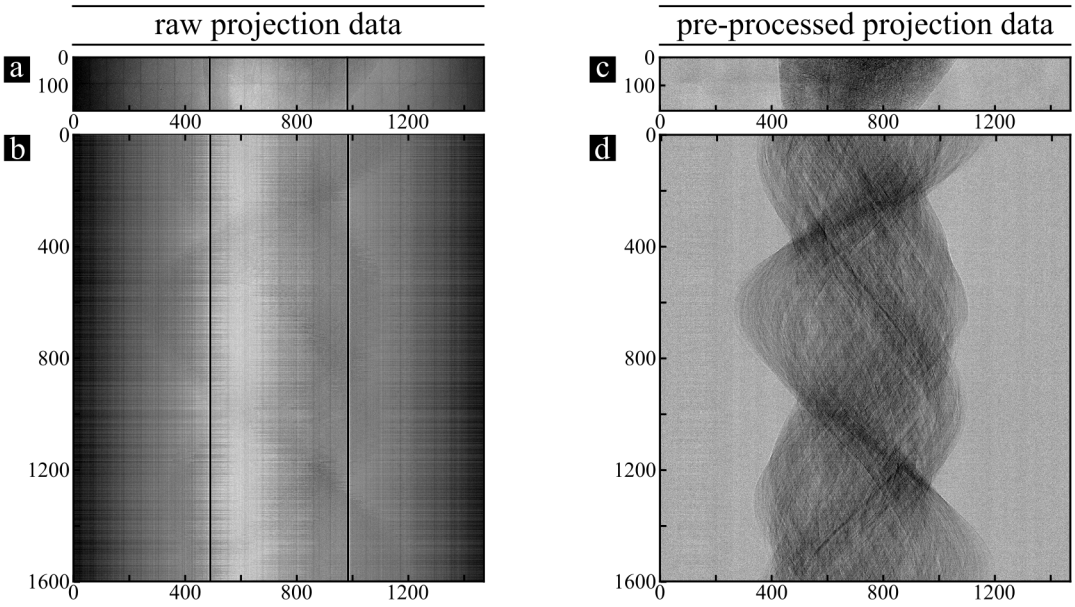

Figure 5.14: **NanoCT Projection Data before and after Pre-Processing.** (a) Raw projection image of a renal corpuscle in a human kidney tissue specimen. (b) Sinogram slice of the raw projection data of the same renal tissue specimen. (c) Projection image of the tissue specimen after the pre-processing steps shown in Fig. 5.13a. (d) Sinogram slice after pre-processing of the same tissue specimen. $v_{\text{eff}} \approx 450\,\text{nm}$.

The resulting projection data after performing these pre-processing steps is presented beside the raw image data in Fig. 5.14. In the raw data (Fig. 5.14a, b) the intensity distribution of the X-ray beam, and the detector gaps can be clearly seen. Furthermore, the sinogram in Fig. 5.14b illustrates the typewriter shifts. These typewriter shifts, as well as the intensity distribution and the detector gaps are corrected for in Fig. 5.14c, d.

5.3.2 Reconstruction and Correction of the Reconstruction Geometry

After the pre-processing, the natural logarithm is applied to the projection data. For a pure attenuation signal this step represents a conversion from an intensity ratio to a line integral over the attenuation coefficients. The NanoCT projection data, however, contains both attenuation and phase information. The logarithmic projection data is then reconstructed, performing a filtered back-projection featuring a cone-beam projector. Thereby, a variety of different filters is available. For instance, to account for the different path lengths of the X-rays through the sample in a cone-beam geometry, a Feldkamp filter can be used. As a result, a reconstructed volume such as the one displayed in Fig. 5.15 is generated.

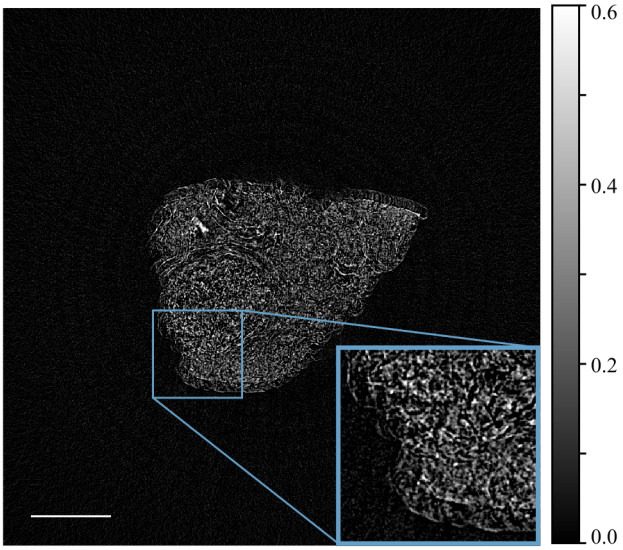

Figure 5.15: **NanoCT Slice of the Initial FBP.** Reconstructed slice from the pre-processed projection data from Fig. 5.14c, d of the renal corpuscle specimen. An enlarged view of the blue ROI is displayed for illustration of the reconstruction misalignment. $v_{\text{eff}} \approx 450\,\text{nm}$. Scalebar: 100 µm.

The reconstructed volume in Fig. 5.15 is, however, far from reproducing the true tissue structure of the sample. In X-ray nanotomography, typically, such flawed reconstruction results originate from a superposition of two effects: a global geometry misalignment, which is constant over the acquisition time of the tomography, and additional fluctuations in the system geometry over time, due to mechanical instabilities and source spot drifts.

To address these two effects, two correction steps are performed: To correct for any global offset during the tomography a centre shift correction is applied. To compensate

for any geometry fluctuations during the acquisition, an additional projection-wise alignment is performed.

Centre Shift Correction

The initial FBP reconstruction, as displayed in Fig. 5.16a, indicates a significant global offset of either the centre of rotation or the detector from the optical axis during the tomography. The definition of the system geometry in the image processing routine determines whether the detector or the rotation axis offset is adjusted during the centre shift correction.

Taking the typewriter shifts into account, the sinogram slice in Fig. 5.14b shows an offset of the centre of the beam from the centre of the detector FOV. This indicates a detector offset.

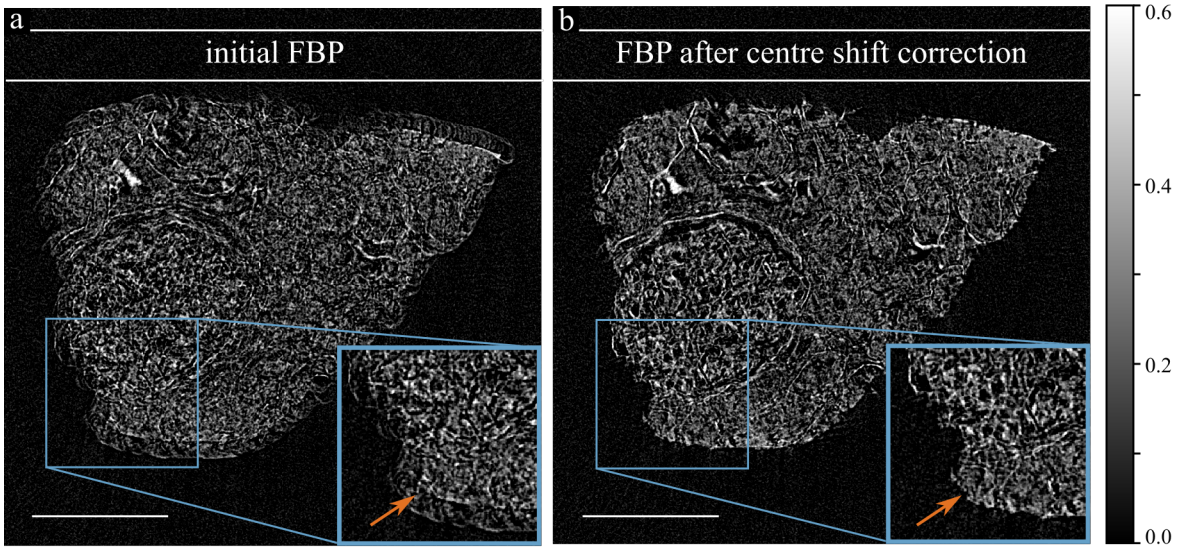

Figure 5.16: **Cropped NanoCT Slice without and with Centre Shift Correction.** (a) Cropped FBP slice of the renal corpuscle specimen from Fig. 5.15 without centre shift correction. (b) Cropped FBP slice of the same projection data but after correcting for a global centre shift. Detail images of the blue ROIs are displayed in both FBP slices. The orange arrow points to the sample edge where misalignment artefacts are most dominant. $v_{\text{eff}} \approx 450\,\text{nm}$. Scalebars: 100 µm.

To calculate an initial guess for this offset, anti-posed projection images are registered [Patel, 2009]. Based on this initial guess, a more refined centre shift correction is performed. Thereby, there are two techniques based on two different approaches available

in the NanoCT image processing framework: a static and a dynamic approach. In a static approach, the offset is varied over a range of different values around the initial guess. The resulting reconstructed slices are visually compared and the optimum offset value is manually selected. In the dynamic approach, a gradient-free line-search algorithm varies the offset value starting from the initial guess. It uses a sparsity metric to evaluate the quality of the alignment [Hehn, 2019].

Figure 5.16b displays a FBP slice reconstructed with a sparsity-based iterative approach to correct for the detector offset. A detector offset value of 2.3 mm was calculated.

Projection Alignment

For larger effective voxel sizes, the centre shift correction often suffices to generate precisely aligned reconstruction data. For v_{eff}-values, that rather push the resolution limit of the NanoCT ($v_{\text{eff}} \lessapprox 300\,\text{nm}$), fluctuations of the system geometry over time may severely degrade the quality of the resulting reconstruction volume. Thus, two techniques were devised which allow for correcting the system geometry for each individual projection. A cross-correlation based projection alignment, which was implemented by S. Allner, and a sparsity-metric based projection alignment, which was developed by L. Hehn.

Thereby, both the original pre-processed projection data as well as the phase-retrieved and deblurred projection images can be used as input for the two projection alignment routines (Fig. 5.13).

Cross-Correlation Based Projection Alignment: The first of the two techniques is based on iterative estimations of the projection shifts via cross-correlation. Thereby, an initial FBP volume is generated. By forward projecting this volume, a set of artificial projection images is obtained. A cross-correlation algorithm is used to calculate the positional offsets between the original projection images and the forward projected data. These offsets are used as input for a revised FBP reconstruction, which is again used for forward projection. These steps form a loop, in which the projection alignment is iteratively refined. The thought behind this alignment procedure is, that the geometry of a reconstructed tomography has an intrinsically consistent relation to the system geometry in the projection data. Therefore, this technique is also referred to as tomoconsistency [Parkinson, 2012; Mayo, 2007; Guizar-Sicairos, 2015; Gürsoy, 2017].

While most cross-correlation based techniques are based on a parallel beam assumption, the algorithm used in the NanoCT framework was adapted to the cone-beam geometry of the system. Furthermore, the algorithm allows for optimising the horizontal and the vertical projection shifts simultaneously. To improve the stability and outcome of

the optimisation, the algorithm provides a number of options. A differentiation of the projection data can be applied for more pronounced edge features and outer regions, which may hamper the projection alignment, can be excluded from the alignment procedure.

Sparsity-Metric Based Projection Alignment: The second approach is similar to the previously described dynamic centre shift correction method. Again, the sparsity of the reconstructed data is optimised. In the projection alignment, however, this process is carried out to calculate the transverse detector offset from the optical axis for each projection individually. Therefore, this technique is rather computationally expensive. It has the enormous advantage, though, that its concept allows for correcting any parameter in the system geometry, including tilting angles of the rotation axis and the source-detector distance, and is not limited to solely optimising the detector offset [Ferstl, 2019].

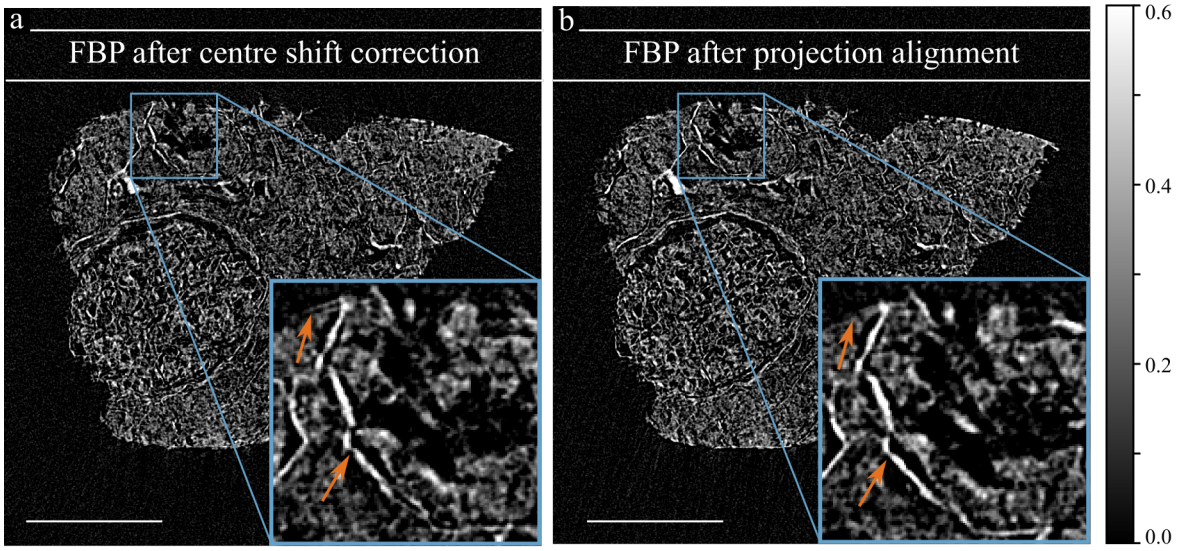

Figure 5.17: **Cropped NanoCT Slice without and with Projection Alignment.** (a) Cropped FBP slice from Fig. 5.16b with only centre shift correction. (b) Cropped FBP slice of the same data but with a sparsity-based projection alignment. Detail images (blue ROIs) are displayed in both FBP slices. The orange arrows point to differences caused by the projection alignment. $v_{\text{eff}} \approx 450\,\text{nm}$. Scalebars: 100 µm.

Figure 5.17 and Fig. 5.18 show two cases of NanoCT data which were reconstructed with and without projection alignment. With respect to the projection alignment only the results of the sparsity-based technique are presented, here. For merely optimising

the detector offsets, as is the case for the data included in this work, both methods yield the same results.

Figure 5.17 show data acquired with an effective voxel size of ≈ 450 nm. Here only a slight improvement can be observed in the reconstructed slices, indicated by the orange arrows. Figure 5.18a shows a slight double edge artefact (orange arrow) originating from a misalignment of the projection images.

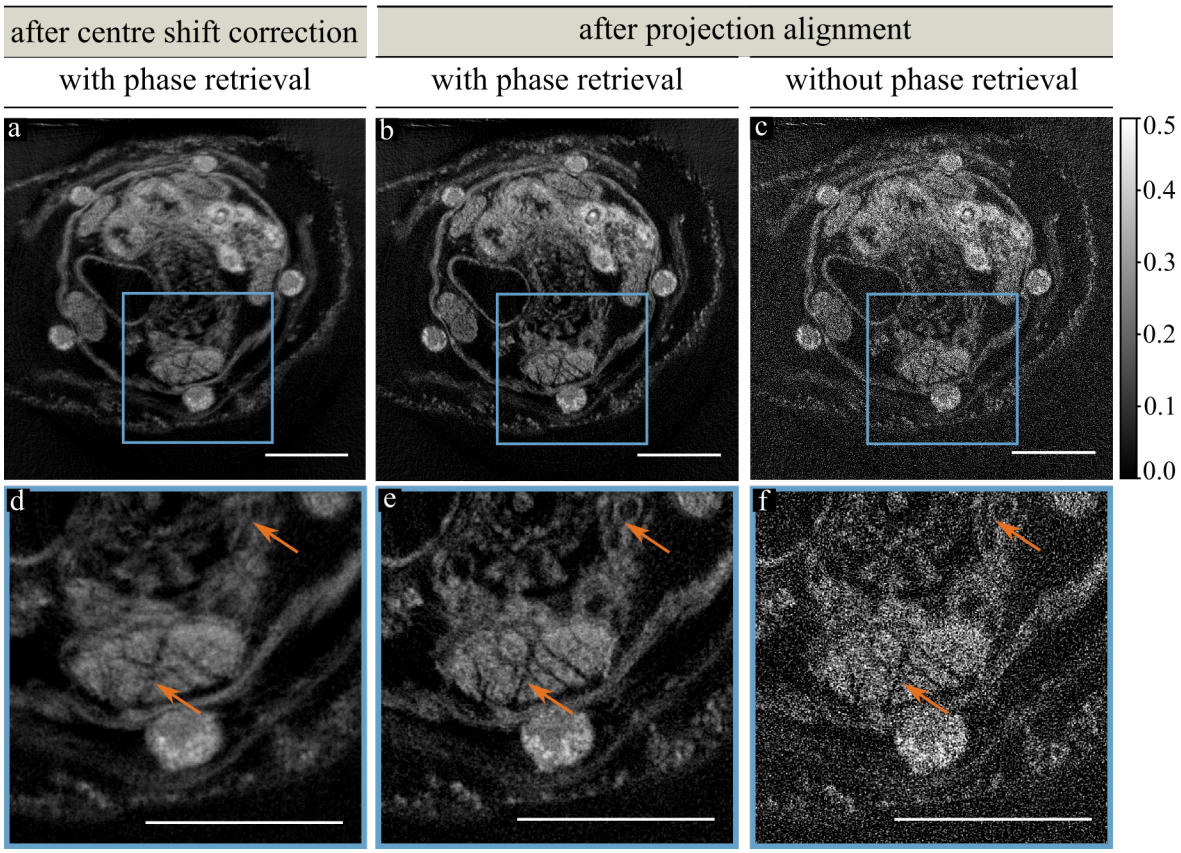

Figure 5.18: **NanoCT Slice without and with Projection Alignment.** (a) FBP slice of phase-retrieved projection data of a tiny sea cucumber with only centre shift correction. (b) FBP slice of the same phase-retrieved data with a sparsity-based projection alignment. (c) The same NanoCT slice as in (b) without phase retrieval. (d)-(f) Detail images (blue ROIs). The orange arrows point to differences due to the projection alignment. v_{eff} ≈ 290 nm. Scalebars: 100 µm. Figure adapted from [Ferstl, 2019].

In contrast to that, Fig. 5.18 shows an immense improvement in the data quality for the NanoCT data with a v_{eff} ≈ 290 nm through projection alignment. To facilitate

comparative analyses, Paganin's phase retrieval was employed to the data shown in Fig. 5.18a,b,d,e to enhance the CNR and, thus, improve visibility of the relevant structures. For reference, a NanoCT slice without phase retrieval was added (Fig. 5.18c,f). The features indicated by the orange arrows are significantly easier to distinguish. Thereby, the projection-alignment data (Fig. 5.18b, e) enable a precise segmentation of the relevant structures, such as the ring canal, which is not feasible in the data without projection alignment (Fig. 5.18a, d). A more extensive investigation of this data set is provided in Chapter 8.

5.3.3 Phase Retrieval and Image Deblurring

The small X-ray focal spot provided by the NanoTube induces propagation-based phase effects in the form of Fresnel fringes at material interfaces. Applying numerical phase retrieval techniques allows for eliminating these fringes. Beyond that, via phase retrieval the Fresnel fringes can be even used to benefit the data quality for enhancing the image CNR and for image deblurring.

In the following, the phase retrieval and image deblurring techniques which are most relevant to this work are presented. The described methods enable to generate quantitative results for monochromatic X-rays and a single-material sample. However, since the NanoTube generates a polychromatic X-ray spectrum and the NanoCT is mostly used to investigate samples comprised of multiple materials, only qualitative information is provided. Thus, the respective processing parameters are optimised based on the visual image quality.

Propagation-Based Phase Retrieval

The NanoCT data, as all data acquired with propagation-based phase-contrast techniques, carry a combination of absorption and phase information. There is a variety of numerical phase retrieval techniques, which are based on different assumptions and approximations. Despite the differences in their theoretic background, they all follow the same principle and are basically centred around a filtering step in the frequency domain $H(u, v)$ with (u, v) the spatial frequency. The working principle of obtaining the phase-retrieved projection image $D_\Phi(x, y)$ from the intensity distribution $I(x, y)$ can be expressed by one formalism:

$$D_\Phi(x, y) = f\underbrace{\left(\mathfrak{F}^{-1}\left\{H(u, v) \cdot \mathfrak{F}\left[g(I)\right]\right\}\right)}_{g_\mathrm{F}}. \tag{5.11}$$

Thereby, the filter $H(u, v)$ is applied to the Fourier transform of a function $g(I)$. The inverse Fourier transform of this term yields the filtered intensity function g_F. Applying

the function $f(g_\mathrm{F})$ results in the final phase-retrieved projection image $D_\Phi(x, y)$. The filter $H(u, v)$, as well as the two functions g and f, vary for each propagation-based phase retrieval approach [Burvall, 2011].

The most widely used among these techniques are Paganin's and Bronnikov's phase retrieval [Paganin, 2002; Bronnikov, 2002]. Both of these techniques can be derived from the transport of intensity equation (Eq. 3.31). While Bronnikov's phase retrieval merely considers pure phase objects, Paganin's phase retrieval uses the approximation of a single-material sample, also known as the homogeneity assumption. Regarding most samples investigated with the NanoCT, the single-material rather than the weak-absorption approximation applies. Thus, for the sake of consistency, we decided to adhere to Paganin's phase retrieval for processing the presented NanoCT data.

In Paganin's phase retrieval, the function $g(I)$ is merely a normalisation step:

$$g\left[I(x, y)\right] = \frac{I(x, y)}{I_0}, \tag{5.12}$$

with I_0 the intensity of the incident beam. The filter $H(u, v)$ is defined as such:

$$H(u, v) = \left[4\pi^2 d \cdot \frac{\delta}{\mu}|\vec{w}|^2 + 1\right]^{-1}, \tag{5.13}$$

with d the effective propagation distance, the vector $\vec{w} = (u, v)^T$, δ the phase coefficient, and μ the linear attenuation coefficient of the material. The function applied to the filtered intensity function $f(g_\mathrm{F})$ is given by the following expression:

$$f(g_\mathrm{F}) = -\frac{1}{\mu}\ln\left(g_\mathrm{F}\right), \tag{5.14}$$

with μ the linear attenuation coefficient of the material [Burvall, 2011]. Furthermore, it should be clarified, that $D_\Phi(x, y)$ does not actually denote a phase distribution in the projection image, but rather represents the projected thickness of the homogeneous sample [Paganin, 2002].

Figure 5.19 illustrates the effect of Paganin's phase retrieval on a typical NanoCT data set. The original data set in Fig. 5.19a exhibits the typical edge enhancement effects at the interfaces of sample and air (as illustrated in Fig. 3.3b) and a distinct noise background. Paganin's phase retrieval corrects for these edge enhancement effects and reduces the noise level considerably (Fig. 5.19b) while mostly preserving the edge sharpness.

As the coefficients μ and δ are only well-defined for a single material for monochromatic X-rays of a certain energy, the phase retrieval does not yield quantitative results of $\Phi(x, y)$ for the polychromatic spectrum of the NanoTube. Consequently, the values μ

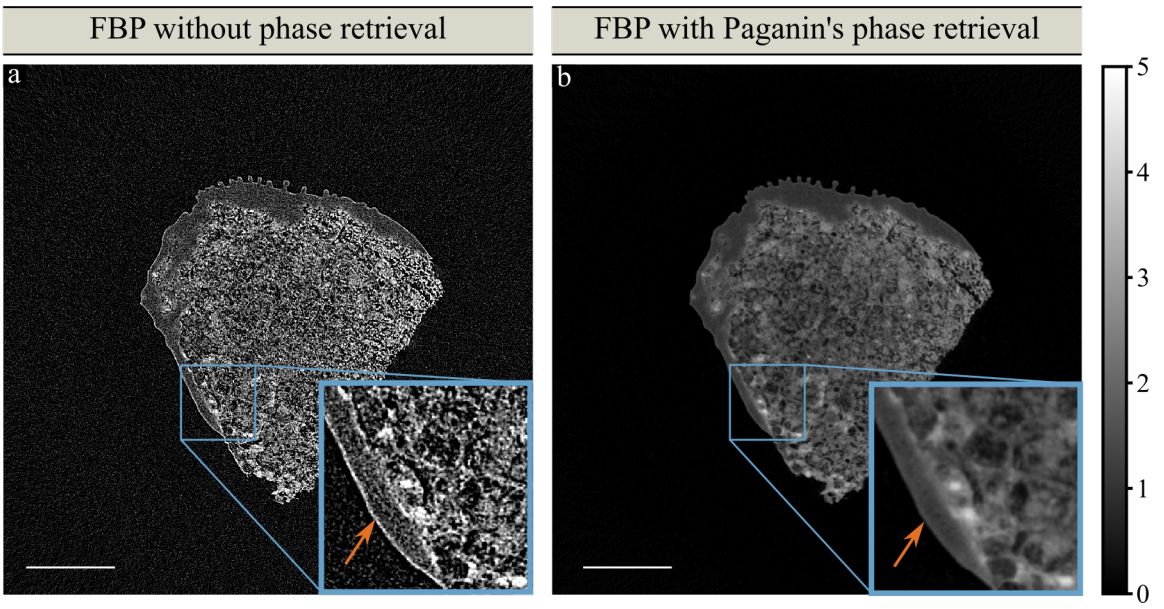

Figure 5.19: **NanoCT Data with and without Paganin's Phase Retrieval.** (a) NanoCT FBP slice of a murine liver specimen stained with a bismuth-oxo-cluster and mounted with superglue (arrow) [Busse, 2018a]. (b) The same NanoCT slice but with Paganin's phase retrieval. For better comparability, both data sets were normalised to air = 0 and superglue = 1, and the same grey value range was chosen. Detail images are included for better visualisation of the features with orange arrows pointing towards the superglue to air interface. $v_{\text{eff}} \approx 405\,\text{nm}$. Scalebars: 100 µm.

and δ are adjusted to optimise the image quality of the resulting reconstructed volumes. Generally, stronger phase retrieval was applied for larger propagation distances and stronger edge enhancement. A too strong phase retrieval causes blurring in the resulting data. A more in-depth investigation on this subject is presented in Chapter 7.

Image Deblurring by Means of Defocus

A common figure of merit for characterising the resolution of an imaging system is the point-spread function (PSF). It describes the signal spread of a point-like sample in a projection image produced by the imaging system. The measured blurry image of a non-point-like sample $D(x, y)$ is given by the convolution of the PSF of the imaging system $\mathrm{PSF}_{\mathrm{system}}$ and the ideal sharp image of the sample $O(x, y)$ [Richardson, 1972]:

$$D(x, y) = O(x, y) \star \mathrm{PSF}_{\mathrm{system}}. \tag{5.15}$$

To enhance the image resolution and ideally retrieve the sharp sample image $O(x, y)$, Richardson and Lucy first developed a numerical PSF-deconvolution technique [Richardson, 1972; Lucy, 1974]. This technique is, thus, also referred to as the Richardson-Lucy deconvolution (RL-deconvolution).

As the deconvolution problem is mathematically ill-posed, it can only be carried out in an iterative, computationally expensive and, thus, time-consuming process. Furthermore, this process is associated with an immense noise amplification from the original to the deconvolved projection data [Gureyev, 2004].

To overcome these weaknesses, we implemented the rapid deblurring approach based on partial deconvolution proposed by Gureyev et al. [Gureyev, 2004]. In principle, this approach uses the diffraction fringes in propagation-based phase imaging to correct for the blurring caused by the finite size of the system PSF.

Based on the transport of intensity equation (Eq. 3.31) and Eq. 5.15, a term for estimating the ideal deblurred image $O(x, y)$ is derived:

$$O(x, y) \approx (1 - \xi) \cdot D_{\Phi}(x, y) + \xi \cdot D_{\mathrm{z}}(x, y), \tag{5.16}$$

whereby $D_{\mathrm{z}}(x, y)$ represents a slightly de-focused image which was acquired in a propagation distance z behind the object. Furthermore, $D_{\Phi}(x, y)$ represents the phase-retrieved de-focused image. Considering a PSF with a perfectly symmetric Gaussian shape, the variable ξ is defined by the following expression:

$$\xi = \frac{\sigma^2 k \beta}{z \delta}, \tag{5.17}$$

with δ the phase coefficient, and β the attenuation coefficient of the complex refractive index of the sample material. Furthermore, k represents the absolute value of the wave vector, z the propagation distance of the wave behind the sample and σ the standard deviation of the Gaussian PSF [Gureyev, 2004].

Equation 5.16 shows, that the time-consuming RL deconvolution process can be replaced by merely adding the properly weighted phase-retrieved image $D_{\Phi}(x, y)$ to the

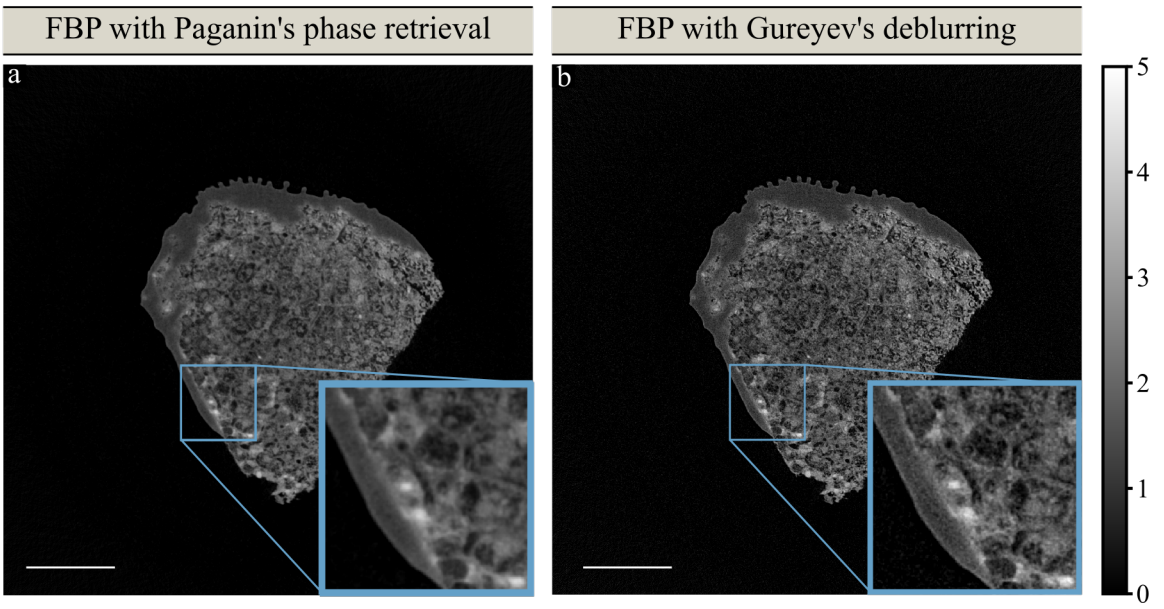

Figure 5.20: **NanoCT Data with Paganin's Phase Retrieval and with Gureyev's Deblurring.** (a) The same NanoCT slice as shown in Fig. 5.19b. (b) The same NanoCT slice as in (a) but with additional Gureyev's deblurring. For better comparability, both data sets were normalised to air = 0 and superglue = 1, and the same grey value range was chosen. Detail images are included for better visualisation of the features. $v_{\text{eff}} \approx 405\,\text{nm}$. Scalebars: 100 µm.

de-focus image $D_z(x, y)$. In Fig. 5.20 the effect of Gureyev's deblurring compared to only Paganin's phase retrieval is illustrated for a NanoCT data set. Paganin's phase retrieval rather acts as a low-pass filter in the frequency domain. This has the advantage of reducing high-frequency noise, but also of slightly decreasing the edge sharpness. With Gureyev's deblurring these edge features are restored. Since the NanoCT uses a polychromatic spectrum to image non-homogeneous samples, the parameter ξ is not well-defined. Thus, this parameter is adjusted with respect to optimum image quality in the reconstructed data.

The equivalence of RL deconvolution with subsequent Paganin's phase retrieval, as performed by Müller et al. [Müller, 2017], and Paganin's phase retrieval combined with Gureyev's deblurring was further verified. For this purpose, the NanoCT data set presented in Fig. 5.20 was both processed with the former processing protocol and the new technique featuring Gureyev's deblurring. The data sets were normalised and a difference volume was calculated. NanoCT slices of the resulting normalised volumes and the difference volume are displayed in Fig. 5.21a-c. Of each data set, a histogram

of the grey value distribution was calculated, as shown in Fig. 5.21d-f. Both data sets (Fig. 5.21a, b) appear very similar, which is reflected in the histograms. The difference image (Fig. 5.21c) is mostly dominated by noise and and the grey values lie an order of magnitude below the two data sets. The histogram of the difference volume (Fig. 5.21f) depicts a Gaussian-like grey value distribution centred around zero. This further supports the impression of a negligible difference between the results of the two different deblurring methods.

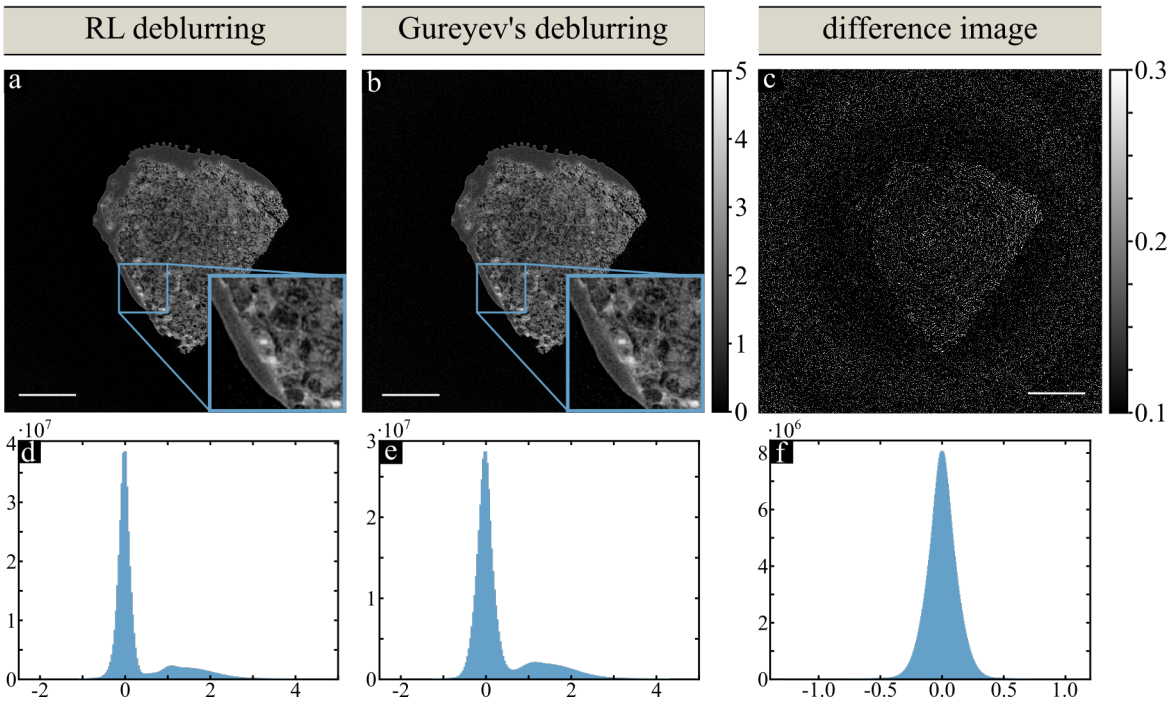

Figure 5.21: **Comparison of Deblurring Methods.** (a) Virtual slice through the NanoCT data set shown in Fig. 5.20a but with Richardson-Lucy deconvolution (RL deblurring) applied prior to Paganin's phase retrieval. (b) The same NanoCT slice as shown in Fig. 5.20b with Gureyev's deblurring applied after Paganin's phase retrieval. For better comparability, both data sets in (a) and (b) were normalised to air = 0 and superglue = 1, and the same grey value range was chosen. (c) The CT slice of the difference volume between (a) and (b). (d)-(f) corresponding grey value distribution to (a)-(c). $v_{\text{eff}} \approx 405\,\text{nm}$. Scalebars: 100 µm.

In conclusion, Gureyev's deblurring is enormously faster than RL deconvolution by replacing an iterative process by a sum operation. Thereby, it allows for a dynamic adjustment of the relevant parameters and, thus, saves data storage space and contributes to a more effective NanoCT image processing.

5.4 Scientific Contributions

The NanoCT was conceived and set up by Mark Müller in collaboration with Excillum AB, Martin Dierolf and Simone Ferstl and the support of Franz Pfeiffer. The focusing routine for the NanoTube was designed and implemented by Simone Ferstl. The geometry calibration techniques were developed by Mark Müller with the support of Florian Schaff. Throughout the research projects in this work, Simone Ferstl was in charge of the supervision and maintenance of the NanoCT setup.
The original script for the NanoCT data image processing was implemented by Sebastian Allner. This script was further adapted and refined by Lorenz Hehn and Simone Ferstl. Lorenz Hehn particularly contributed regarding advanced projection alignment and phase retrieval. Simone Ferstl implemented Gureyev's algorithm for image deblurring.

Optimisation of Acquisition Parameters in the NanoCT 6

6.1 Introduction

When assessing the quality of a reconstructed X-ray CT data set, there are two central criteria: the contrast-to-noise ratio (CNR) and the resolution, which can be characterised by the point-spread function (PSF). In the NanoCT, the following parameters most strongly influence these quality criteria: the acceleration voltage of the NanoTube, the threshold of the single-photon-counting Pilatus detector, the employed image processing and reconstruction routines, the strength of propagation-based phase effects and the employed sample processing including X-ray staining.

The CNR for a certain material r to a reference material, such as air, can be determined from the following expression:

$$\mathrm{CNR_r} = \frac{m_\mathrm{r} - m_\mathrm{ref}}{\sqrt{\sigma_\mathrm{r}^2 + \sigma_\mathrm{ref}^2}}, \tag{6.1}$$

with $m_\mathrm{r}/m_\mathrm{ref}$ the mean grey value in material r/ref and $\sigma_\mathrm{r}/\sigma_\mathrm{ref}$ the standard deviation or noise value in material r/ref [Russo, 2017].
The intensity reduction by a material r with air as reference material generates the attenuation contrast in a projection image, which is given in Eq. 6.1 as $(m_\mathrm{r} - m_\mathrm{ref})$. This intensity reduction directly depends on the attenuation coefficient of the material, as described in Chapter 3 (Eq. 3.12). The attenuation coefficient can be adjusted via suitable X-ray stains or by reducing the mean X-ray energy of the beam (Eq. 3.16).
In the NanoCT, the mean X-ray energy impinging on the sample is defined by the acceleration voltage of the NanoTube, whereas the mean detected X-ray energy can be further adjusted with the detection threshold of the Pilatus. Slight variations in the mean recorded X-ray energy may further be achieved by different propagation distances through air.

Alongside the contrast, the noise value plays an equally important role in defining the CNR (Eq. 6.1). Without altering the exposure time per projection image and without increasing the number of projection images per NanoCT scan, a reduction of the noise level can be obtained through a handful of approaches: The source-detector distance can be decreased, the detection efficiency of the Pilatus can be maximised, and the X-ray flux can be increased.

According to Eq. 2.11 and Eq. 2.12 (Chapter 2), the generated X-ray flux is closely intertwined with the acceleration voltage, just as the detection efficiency of the Pilatus detector is connected to the detection threshold (Section 5.1). Beyond that, the CNR can be significantly enhanced by exploiting propagation-based phase effects in the projection images [Paganin, 2002; Gureyev, 2017].

The resolution of an image is the second central quality criterion, especially in the context of the NanoCT. The resolution in a reconstructed NanoCT data set comprises the resolution of each projection image, the image processing routine applied to each projection image, as well as the CT reconstruction algorithm.
The resolution of a projection image can be characterised by its PSF. Assuming a linear and shift-invariant imaging system, the PSF of the system can be calculated from the convolution of the components' PSF values [Russo, 2017]:

$$\mathrm{PSF}_{\mathrm{system}} = \mathrm{PSF}_1 \star \mathrm{PSF}_2 \star ... \ \mathrm{PSF}_{\mathrm{n}}, \tag{6.2}$$

with $\mathrm{PSF}_{\mathrm{system}}$ the PSF of a system consisting of n components with $\mathrm{PSF}_{\mathrm{i}}$ denoting the PSF of the i-th component. The NanoCT merely consists of the NanoTube and the detector which contribute to the total PSF. Thus, the PSF of a NanoCT projection image is described by the convolution of the NanoTube PSF and the detector PSF. The NanoTube PSF is defined by the size of the electron spot on the X-ray target and by the size of the electron matter interaction volume inside the target. These two variables again depend, among other parameters, on the acceleration voltage (Chapter 2: Eq. 2.16, Eq.2.15, Eq. 2.9). The detector PSF can be manipulated by changing the detector threshold (Chapter 5).

In practice, however, mechanical and source spot instabilities during an exposure further contribute to an increase in a projection image's PSF [Withers, 2007]. The longer the exposure time, the greater the impact of instability blurring on the resolution in the resulting projection image. The minimum necessary exposure time is defined by the noise level in the resulting image. As previously mentioned, the noise level is connected to the acceleration voltage of the NanoTube and the Pilatus detector threshold. In contrast to that, instabilities occurring not during but between projection acquisitions can be largely corrected by projection alignment algorithms prior to reconstruction.

This chapter will investigate the influence of the acceleration voltage ($\mathrm{U_{acc}}$) on the NanoCT data quality. For more information on the detector threshold, its effects on the detector PSF and the detection efficiency, the reader is referred to [Müller, 2019]. The image processing and reconstruction routines of the NanoCT framework will also not be further discussed here, since these aspects were already explained and assessed throughout Section 5.3. Effects linked to propagation-based phase contrast will be treated in Chapter 7. While X-ray staining plays a central role throughout this work, discussing the optimisation of specific staining protocols is beyond the scope of this thesis.

6.2 Optimisation of the Acceleration Voltage

The acceleration voltage U_{acc} is a central parameter in the NanoCT. It does not only affect the energy spectrum and the X-ray flux emitted by the NanoTube, but also the minimum achievable X-ray source spot size, and with that the source PSF. The energy spectrum and the X-ray flux in turn significantly influence the CNR.

Thus, the behaviour of the following variables will be studied with respect to different U_{acc}-values: the electron spot size and the electron current on the X-ray target, the energy spectrum of the X-ray beam at the sample and at the detector, the CNR in a phantom composed of different materials and the associated X-ray flux at the detector.

6.2.1 Theoretical Estimations

For a thorough assessment of the experimental results, we start with some theoretical considerations to estimate the expected behaviour of the measured variables. For the sake of concision, only the resulting relationships between the respective variables and the U_{acc} value are presented here. The calculations leading up to these formalisms are described in detail in the corresponding methods section (Section 6.5).

The X-ray source spot is defined by the electron spot size on the X-ray target and the spot size expansion inside the X-ray target, which is given by the shape and size of the electron interaction volume (Fig. 2.5).
The minimum achievable electron spot size on the X-ray target is limited by the brightness, as well as chromatic and spherical aberrations (Eq. 2.13). These effects are all proportional to the reciprocal of the U_{acc}-value and the aberration effects even grow with the reciprocal of the quadratic U_{acc}-value. Combining these effects, we obtain the following expression for the brightness- and aberration-limited electron spot radius r_e:

$$r_e \propto \frac{1}{\sqrt{U_{acc}}}. \tag{6.3}$$

This expression indicates larger electron spots for smaller U_{acc} values.
Regarding the spot size expansion from the electron to the X-ray spot, the electron interaction volume inside the X-ray target needs to be studied. According to Eq. 2.9, the electron interaction volume in a thick X-ray target grows with increasing acceleration voltages:

$$R_{K-O} \propto {U_{acc}}^{1.67}, \tag{6.4}$$

with R_{K-O} the Kanaya Okayama range (Eq. 2.9). The limited thickness of the NanoTube's X-ray target (500 nm tungsten) and the specific pear-like shape of a typical electron interaction volume (Fig. 2.5), however, require Monte Carlo simulations to

allow for any substantiated assumptions about the spot size expansion for different U_{acc}-values [Goldstein, 2018].

A further highly-relevant variable is the X-ray flux. Integrating over the theoretical bremsstrahlung spectrum $I_x(E)$ (Eq. 2.10) yields the following relation between the X-ray flux, U_{acc}, and the electron current on the X-ray target I_e:

$$I_x \propto I_e \cdot U_{acc} \ln(U_{acc}). \tag{6.5}$$

Equation 6.5 suggests an increasing X-ray flux I_x for an increasing U_{acc} given a constant value of I_e. For the sake of simplicity, characteristic X-ray emission was not included in these theoretical estimations.

Alongside the X-ray flux, the mean X-ray energy is defined by the emitted energy spectrum. An integral over the product of the bremsstrahlung spectrum $I_x(E)$ and the energy E (Eq. 2.10), results in the following relation between the mean X-ray energy and the U_{acc}:

$$E_{mean} \propto \frac{U_{acc}}{\ln(U_{acc})}. \tag{6.6}$$

This formalism predicts higher mean X-ray energies E_{mean} for higher U_{acc}-values.

In Chapter 3, the physical processes regarding X-ray imaging were explained. According to these explanations, we expect to obtain stronger contrasts for lower X-ray energies (Eq. 3.17) and higher noise levels for lower X-ray flux.
Combining the previous considerations about the X-ray flux and the mean X-ray energy (Eq. 6.5, Eq. 6.6) and given a constant exposure time, we expect higher contrast values, but also higher noise levels for lower U_{acc}-values. A thorough calculation resulted in the following expression:

$$\mathrm{CNR} \propto \frac{(\ln(U_{acc}))^{7/2}}{U_{acc}^{5/2}}. \tag{6.7}$$

A closer look at the shape of this function of U_{acc} in Eq. 6.7 reveals a significant decrease of the CNR towards larger values of U_{acc}.

These theoretical estimations provide a direct connection between the relevant variables and the U_{acc} value. In the following, they will serve as reference to assess the experimental data.

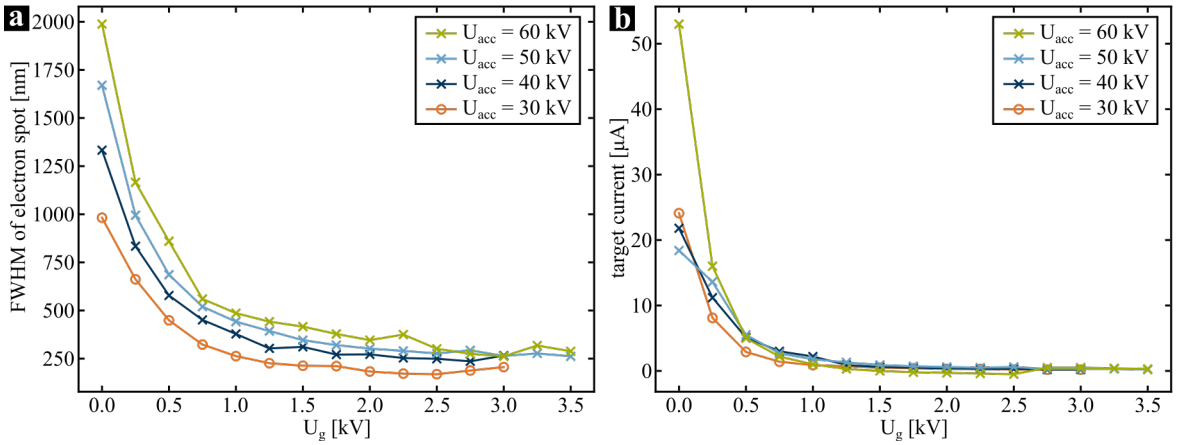

Figure 6.1: **The Electron Spot Size and the Target Current Plotted over the Cathode Grid Voltage for Different Acceleration Voltages.** (a) The FWHM of the electron spot plotted over U_g for different U_{acc} values. (b) The target current for different U_{acc} values plotted over U_g.

6.2.2 Electron Spot Size for Different Acceleration Voltages

As previously mentioned, the electron spot size on the X-ray target is directly connected to the X-ray spot size of the NanoTube. Here, the optimum achievable electron spot size is studied more closely with respect to different U_{acc} values. Thereby, the optimum achievable electron spot size denotes the electron spot size which was obtained after applying the automated focusing routines for a given U_{acc} value and grid voltage U_g (Section 5.1).
As explained in Fig. 5.2, the U_g value controls the divergence angle of the electron beam from the emitter surface of the cathode. This way, the U_g value influences the cathode emittance ϵ_c and the minimum achievable electron spot size on the X-ray target (Section 2.1). Larger U_g values facilitate smaller electron spots but at the expense of the target current.
The target current denotes the electron current onto the X-ray target I_e for a given set of focusing parameters and voltage values of U_g and U_{acc}.

Figure 6.1 presents the electron spot size (FWHM) and the target current plotted over the grid voltage U_g for different U_{acc} values. As expected, both the electron spot size and the target current decrease for larger U_g values. Furthermore, Fig. 6.1a indicates a tendency towards smaller electron spots for the same U_g and smaller U_{acc} values. Such a tendency is not clearly observed in the target current plot (Fig. 6.1b).

The target current has a direct influence on the emitted X-ray flux (Eq. 6.5). Therefore, it is highly interesting to gain information on the behaviour of the electron spot size at

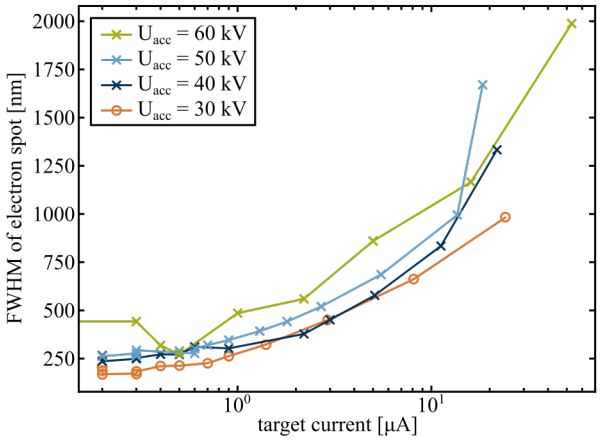

Figure 6.2: **The Electron Spot Size Plotted over the Target Current for Different Acceleration Voltages.** The FWHM of the electron spot plotted over the target current for different U_{acc} in a semi-logarithmic plot.

a constant target current for different U_{acc}. Since this information cannot be directly retrieved from comparing the two panels in Fig. 6.1, further plots were generated.

Figure 6.2 presents a combination of the two panels in Fig. 6.1. It displays the electron spot size over the associated target current for the different U_{acc} values. Figure 6.2 clearly exhibits a rather constant electron spot size for a constant target current with a slight tendency towards smaller electron spots for smaller U_{acc}. It should be noted here, however, that the target current tends to fluctuate in the range of $\approx 0.05\,\mu A$. Hence, the data points at the small target currents are afflicted with uncertainties along the target current axis.

6.2.3 Spectrum for Different Acceleration Voltages

Interactions of X-rays with a sample material, as well as the detection process strongly depend on the X-ray energy (Eq. 3.17). Hence, the X-ray spectrum, as it arrives at the sample and as it is detected by the Pilatus detector, as well as the associated effective mean energy, are highly relevant to understand the image formation process in the NanoCT.

Instead of studying the spectrum at the sample, we investigate the X-ray source spectrum as it is emitted by the NanoTube. It can be assumed that the spectrum at the sample is very similar to the NanoTube source spectrum, due to the typically very small source-sample distances ($< 1\,mm$) in the NanoCT.

Figure 6.3 shows the X-ray emission spectrum of the NanoTube for $U_{acc} = 60\,kV$. The NanoTube spectrum is composed of a continuous bremsstrahlung signal with few

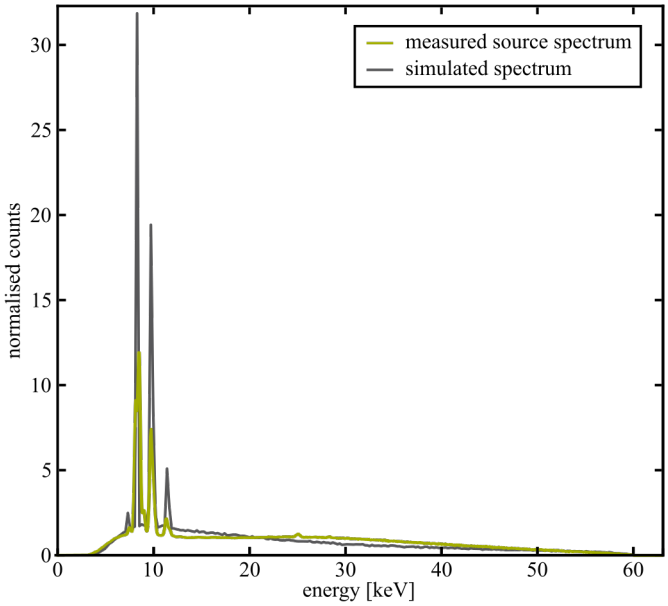

Figure 6.3: **NanoTube Source Spectrum and Simulation.** Measured and simulated X-ray source spectrum of the NanoTube for $U_{acc} = 60\,kV$.

sharp characteristic emission lines. In this case, the L-emission lines of tungsten can be observed ($E(L_\alpha) \approx 8.3\,keV$, $E(L_\beta) \approx 9.8\,keV$ and $E(L_\gamma) \approx 11.3\,keV$). An additional small emission peak is exhibited around 25 keV, which is equivalent to a characteristic emission energy of tin $E(K_\alpha) \approx 25\,keV$. X-rays exciting soldering tin in the electronic circuit behind the silicon sensor of the spectrometer may serve as a possible explanation for this peak. Furthermore, the minimum energy in the spectrum is determined by self-absorption inside the X-ray target and lies around 4 keV, whereas the maximum energy is defined by the U_{acc} value (Fig. 6.3).
In one aspect, however, the NanoTube spectrum differs from many other X-ray tube spectra, such as the one presented in Fig. 2.6b: The characteristic emission lines in the NanoTube spectrum are very dominant compared to the bremsstrahlung signal.

Beside the measured NanoTube spectrum, a simulated spectrum is shown in Fig. 6.3. The simulation models the conditions in the NanoTube and, hence, assumes an electron beam with an energy of 60 keV hitting a transmission X-ray target of 500 nm tungsten on a 100 µm-thick diamond substrate. The resulting simulation data conforms to the experimental spectrum, except for some slight deviations in the shape of the bremsstrahlung signal and even more dominant characteristic emission lines (Fig. 6.3).

Figure 6.4 displays a number of measured NanoTube source spectra for different U_{acc}. The spectral data were acquired at a constant power of 0.1 W (Fig. 6.4a). To facilitate

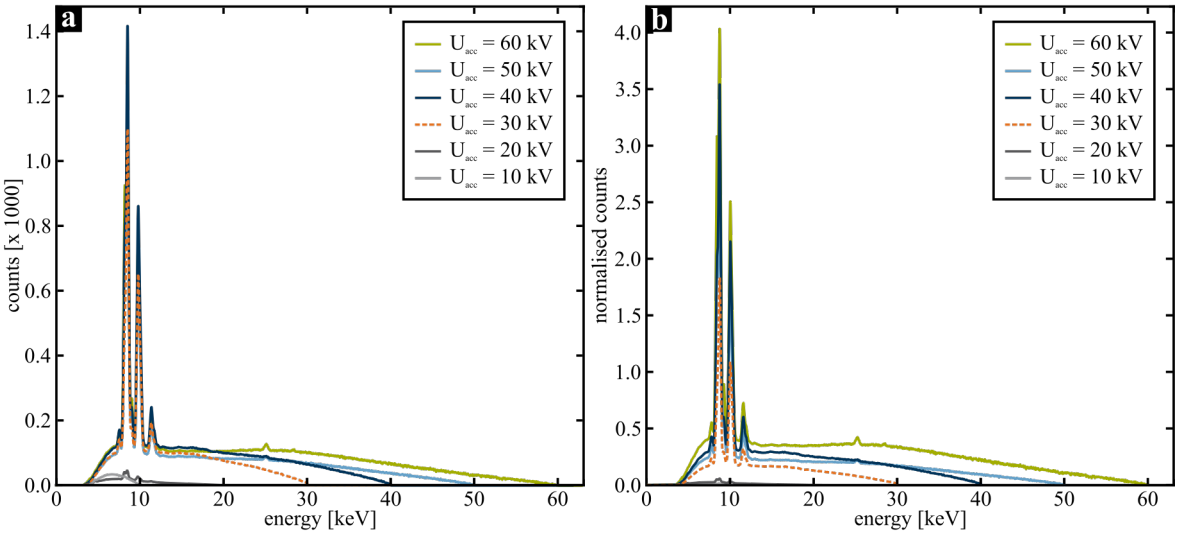

Figure 6.4: **NanoTube Source Spectrum for Different Acceleration Voltages.** (a) Measured X-ray source spectrum of the NanoTube for different U_{acc} values for a constant power of 0.1 W. (b) The same X-ray source spectrum data as in (a) but normalised with the target current.

a comparison including the X-ray generation efficiency, Fig. 6.4b presents the same spectral data after normalisation with the corresponding target current (Table 6.3). In Fig. 6.4a, the spectra for $U_{acc} \in [30; 60]$kV have rather similar shapes and counts up to an energy of ≈ 20 keV until they gradually decrease towards their respective maximum energy. Opposed to that, the spectra for $U_{acc} \in \{10; 20\}$kV exhibit much lower counts and only weak to no characteristic emission lines. This observation is even more pronounced in the normalised data in Fig. 6.4b, where the two spectra for $U_{acc} \in \{10; 20\}$kV are hardly visible. Therefore, these two spectra will not be included in further studies. Beyond that, Fig. 6.4b clearly shows a general reduction in the X-ray generation efficiency towards lower U_{acc} values.

Beside the source spectrum, the energy spectrum detected by the Pilatus detector is studied or in other words the photon signal that actually contributes to a NanoCT projection image. In the NanoCT, the magnification is adjusted by altering the source-detector distance. Thus, to simulate the detected energy spectrum, not only the absorption behaviour of the silicon sensor of the Pilatus, but also the air absorption for different source-detector distances was taken into account.

Figure 6.5 provides the detected energy spectra for different source-detector distances, which are typically used for NanoCT scans, and a single U_{acc} of 60 kV. For a better comparison of the energy distribution, the quadratic intensity reduction for increasing source-detector distances were not considered in Fig. 6.5. Compared to the source

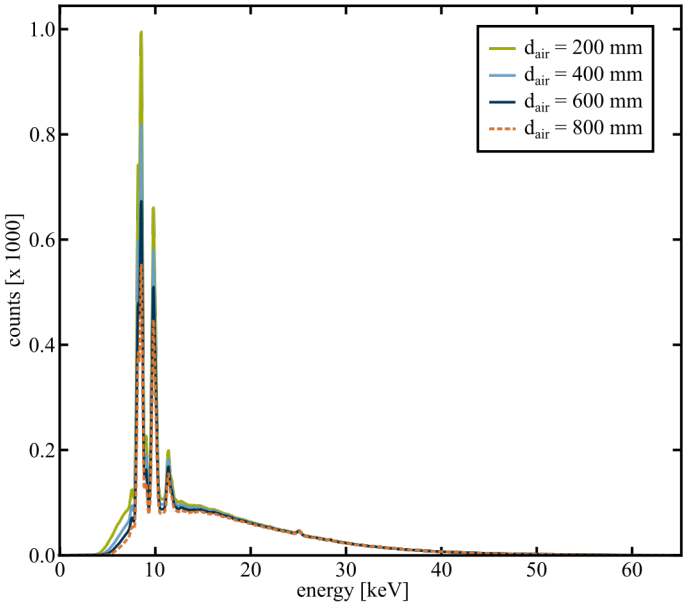

Figure 6.5: **Detected Spectrum for Typical Air Absorption Distances.** The calculated spectrum considers the Si-sensor of the Pilatus and a constant acceleration voltage of $U_{acc} = 60\,kV$ was selected. It has to be noted here that the flux decrease for larger propagation distances was only determined from the air absorption. The quadratic intensity reduction for larger source-detector distances were not included in the calculation.

spectrum in Fig. 6.3, photon energies above 20 keV are strongly suppressed so that the curve almost reaches zero at 40 keV. Moreover, air absorption particularly reduces the photon counts of energies below 15 keV.

After examining the detected X-ray spectrum for different distances and a single U_{acc} value, the detected spectra for different U_{acc} values are investigated. Thereby, air absorption effects were considered for two different source-detector distances, which are commonly used in NanoCT scans. The resulting spectra are plotted in Fig. 6.6. As in Fig. 6.5, a significant suppression of larger photon energies compared to the emitted source spectra is visible. As a result, only slight differences between spectra with different U_{acc} values remain. A comparison between Fig. 6.6a and b yields a distinctively decreased height of the characteristic emission lines for the larger source-detector distance by a factor of two, despite quadratic intensity reduction effects not being considered by the plot.

To facilitate further comparative analyses between the different spectra, the mean effective energy is calculated for each of the spectra shown in Fig. 6.3, Fig. 6.4, Fig. 6.5 and Fig. 6.6. The resulting values are listed in Table 6.1. The mean energy of the

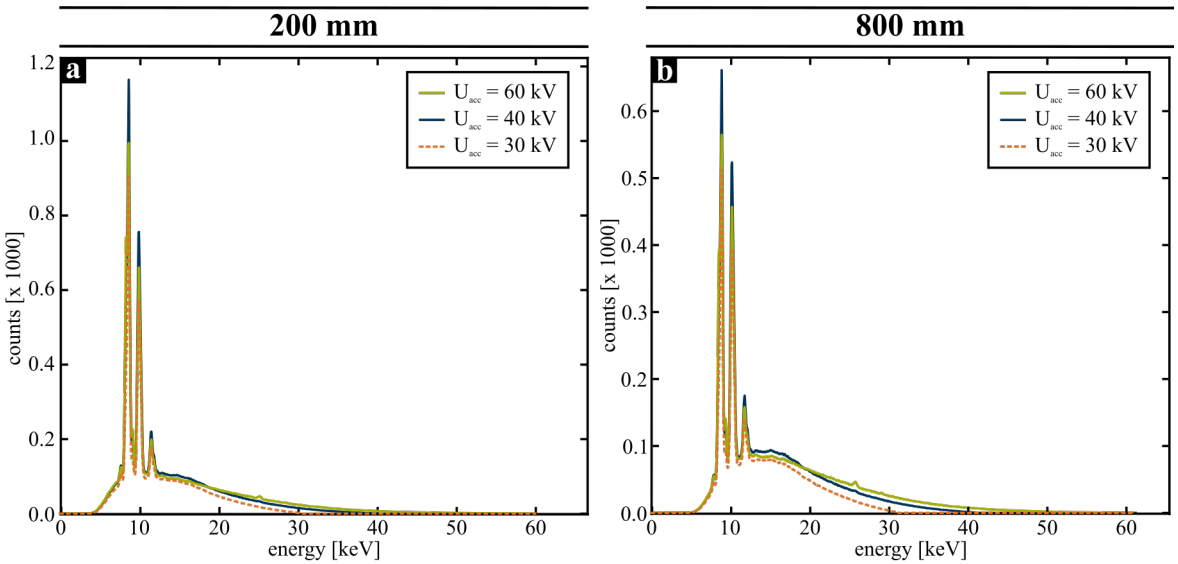

Figure 6.6: **Detected Spectrum for Different Acceleration Voltages and Two Different Typical Air Absorption Distances.** (a) d_{air} = 200 mm. (b) d_{air} = 800 mm. The spectra were acquired at a constant power of 0.1 W and only air absorption was taken into account for larger propagation distances.

source spectrum increases with growing U_{acc} values. The mean energy of the detected spectrum is generally smaller than the mean energy of the source spectrum with the same U_{acc} value, except for the detected spectrum at U_{acc}= 30 kV and d_{air} = 800 mm. Furthermore, the mean energy of the detected spectrum is higher for larger air absorption distances and the same U_{acc}. However, the most striking aspect which is revealed in Table 6.1 is that the mean energies off the detected spectra differ much less for different U_{acc} than the mean energies of the source spectra.

	U_{acc} [kV]	10	20	30		40		50	60			
Source Spectrum:	E_{mean} [keV]	6.9	9.3	13.3		16.0		18.9	22.1			
	d_{air} [mm]	–	–	200	800	200	800	–	200	400	600	800
Detected Spectrum:	E_{mean} [keV]	–	–	12.4	13.6	13.3	14.7	–	14.7	15.4	16.0	16.6

Table 6.1: **Mean Energies of the Energy Spectra for Different Acceleration Voltages and Distances.** The mean energies are listed for the source spectra in Fig. 6.3 and Fig. 6.4 and for the detected spectra in Fig. 6.5 and Fig. 6.6. Legend: E_{mean}: mean energy, d_{air}: air absorption distance.

6.2.4 CNR for Different Acceleration Voltages

To analyse the CNR, a phantom was devised consisting of three thin rods assembled with superglue. PMMA was chosen to imitate the absorption behaviour of soft tissue and PVC and teflon were selected to imitate materials with higher X-ray absorption, such as bone or X-ray stained tissues.[1]
Of this phantom, four NanoCT data sets were acquired using four different U_{acc} values: $U_{acc} \in \{30, 40, 50, 60\}$kV. The spectral measurements clearly showed that the U_{acc} values of 10 kV and 20 kV are not relevant for imaging in the NanoCT, due to their very low generated X-ray flux. As a consequence, these U_{acc} values are not included in this study.
For better comparability of the data sets, the NanoTube settings were adapted to generate similar target currents for each of the different U_{acc} values. In Table 6.2, the specific target current values are listed along with the resulting average photon count per detector pixel, and the electron spot size.
Table 6.2 shows rather similar values for the detected photon count per pixel and no patterns or tendencies for the different U_{acc} values can be observed here. Opposed to that, the electron spot shows a clear tendency towards smaller sizes for decreasing U_{acc} values.

U_{acc}	[kV]	30	40	50	60
Target Current	[µA]	3.44	3.36	3.31	3.47
Electron Spot r_e	[nm]	180	230	250	280
Photon Count	[per pixel]	6.3e3	7.3e3	6.9e3	7.7e3

Table 6.2: **NanoTube Parameters in the CNR Study for Different Acceleration Voltages.** The electron spot radius r_e is given by $0.5 \cdot$ FWHM. The detected photon count denotes the average photon count per detector pixel.

The resulting NanoCT data sets were normalised to redefine the mean value of air as zero and the mean value inside the PMMA rod as one. Furthermore, VOIs were defined for determining the mean values m_r and the standard deviation values σ_r for each material r to calculate the CNR (Eq. 6.1).

Virtual slices through the resulting normalised NanoCT volumes and the VOIs are displayed in Fig. 6.7a-d for the different U_{acc} values. In the NanoCT slices, the circular cross-section through the cylindrical rods of the three phantom materials can be observed, with PVC appearing the brightest (dark blue VOI), followed by teflon (green VOI) and finally PMMA (light blue VOI). It is rather striking that in the NanoCT

[1] The attenuation coefficients, as well as the phase coefficients of these materials are presented for typical X-ray energies of the NanoTube in Fig. A.1.

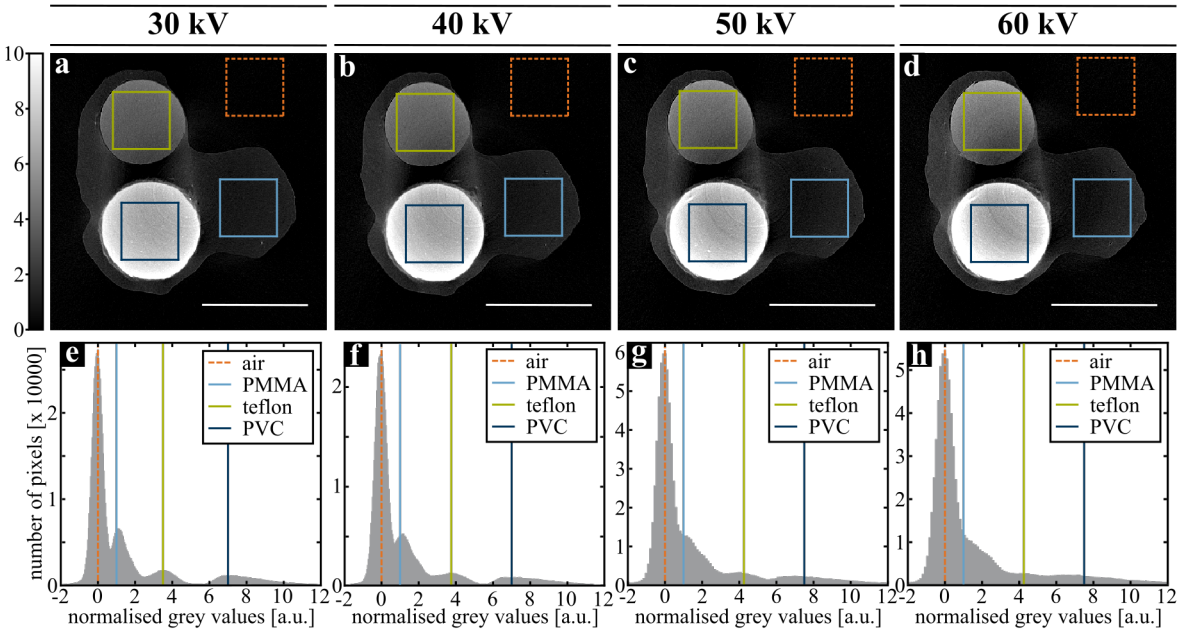

Figure 6.7: **Normalised NanoCT Slices of the CNR Phantom and Corresponding Histograms for Different Acceleration Voltages.** (a) - (d) Virtual slices through the normalised NanoCT volumes and the material VOIs for different U_{acc} values (from left to right: $U_{acc} \in \{30, 40, 50, 60\}$kV). The slices show the CNR phantom of PVC (dark blue VOI), teflon (green VOI) and PMMA (light blue VOI). The air VOI is depicted in orange. (e) - (f) Corresponding histograms with the mean values of the material VOIs marked in the respective VOI colour. Scalebars: 500 µm.

slices the PMMA rod can not be distinguished from the superglue surrounding the rods.[2] Moreover, in all NanoCT slices distinct cupping artefacts are visible. Cupping describes the grey value decrease towards the centre of a sample in a reconstructed X-ray CT data set. These artefacts are present in the PVC rod and between PVC and teflon. Furthermore, the artefacts appear weaker towards lower U_{acc} values (Fig. 6.7 from d to a).

Fig. 6.7e-h displays the corresponding histograms along with the mean values for each material VOI. Due to the normalisation, these histograms show a high peak around zero representing air and a neighbouring peak around one representing PMMA. The mean grey values of the remaining materials are slightly shifted towards smaller values and the shapes of the corresponding peaks appear more defined for smaller U_{acc} values.

[2] PMMA and superglue have very similar attenuation and phase shift properties, as it can be seen in Fig. A.2. Hence, the PMMA VOI slightly extending into areas with superglue should not result in any significant errors of the CNR.

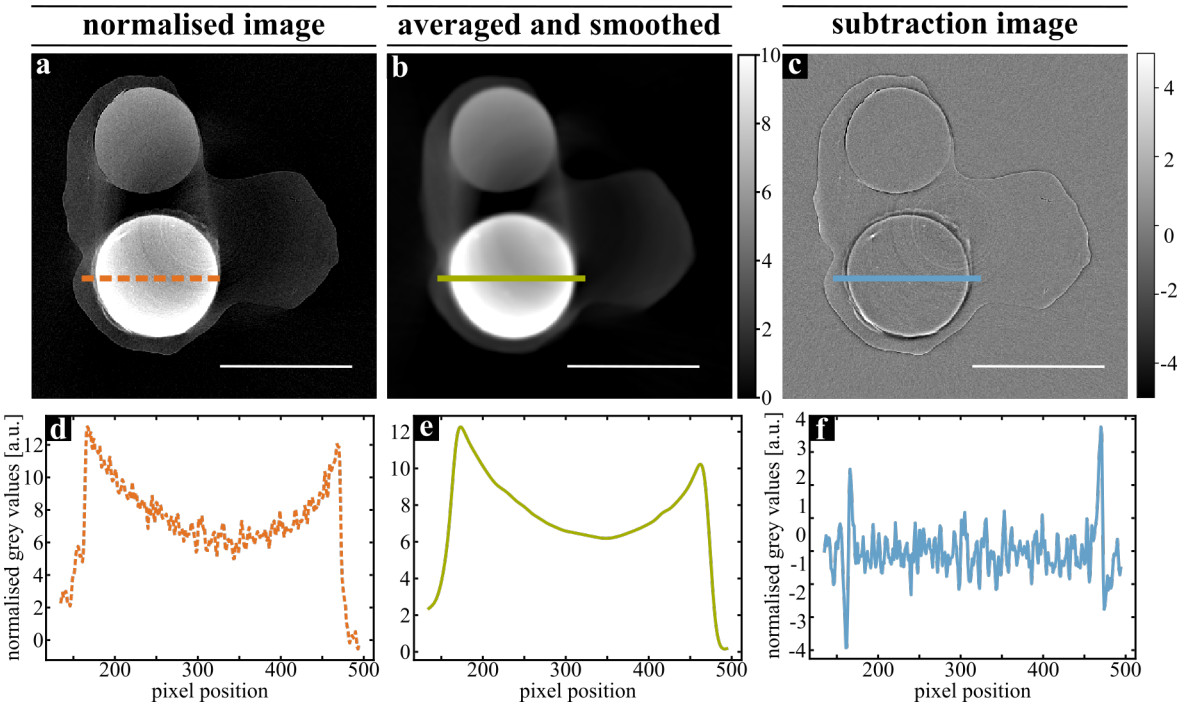

Figure 6.8: **The NanoCT Image Information Split into Contrast and Noise Signal.** (a) Normalised NanoCT slice of the CNR phantom at U_{acc} = 60 kV. (b) Averaged and smoothed image from the NanoCT data (a) representing the contrast signal. (c) Slice through the subtraction volume of the averaged and smoothed image (b) from the original NanoCT volume (a) representing the noise signal. Panel (a) and (b) share the same grey value scale, whereas the subtraction volume is depicted with a different grey value scale. (d) - (e) Corresponding line plots to (a) - (c) through the PVC rod. Scalebars: 500 µm.

Due to the cupping artefacts in the NanoCT data, both the mean grey values and the noise values were not trivial to determine for the CNR (Eq. 6.1). The mean grey values for the calculation of the CNR were retrieved from the material VOIs of the NanoCT data shown in Fig. 6.7a-d and the resulting mean values are included in the histograms in Fig. 6.7e-h.
To calculate the noise values despite the cupping artefacts, a subtraction volume was calculated of an averaged and smoothed image (Fig. 6.8b) from the original NanoCT data (Fig. 6.8a). The NanoCT slices and the line plots through PVC in Figure 6.8 illustrate that the averaged and smoothed image only contains the contrast and the cupping, while the subtraction image only contains noise. From the resulting subtraction volume, the noise value can be conveniently calculated for each of the material

VOIs. Furthermore, the subtraction image in Fig. 6.8c, exhibits features resembling edge enhancement effects. It is most likely though that these edge enhancement effects are not related to propagation-based phase imaging but are mostly generated by the subtraction of the smoothed image from the original volume.

Inserting the mean and the noise values into Eq. 6.1 yielded the CNR values, which are plotted in Fig. 6.9. Among the phantom materials, PVC features the highest CNR and PMMA the lowest. Furthermore, the CNR values of all materials show a slight decrease for increasing U_{acc}, whereby this decrease appears to be strongest in PVC and weakest in PMMA.

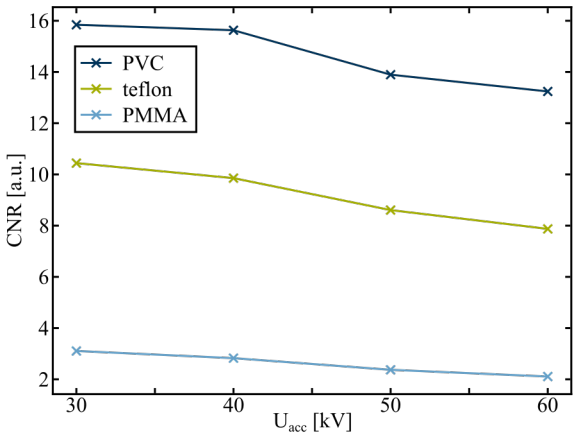

Figure 6.9: **CNR Values with Reference to Air for the Phantom Materials for Different Acceleration Voltages.** The CNR values from Eq. 6.1 of the materials PVC, teflon and PMMA with air as reference.

For the interpretation of the CNR values, a good grasp on the behaviour of the cupping artefacts in these data sets is crucial. For this purpose, line plots were generated through the averaged smoothed images of the NanoCT data (Fig. 6.10).
First, a comparison between the different materials for one U_{acc} was conducted (Fig. 6.10a, b). For this, $U_{acc} = 60\,kV$ was used, as this data set shows the strongest artefacts. Then, PVC, which is most affected by cupping, is studied for different U_{acc} values (Fig. 6.10c). As the normalised NanoCT slices in Fig. 6.7 already indicated, the line plots in Fig. 6.10b illustrate that PVC suffers most from cupping, while PMMA is only slightly affected. Figure 6.10c confirms that the cupping artefacts decrease towards smaller U_{acc} values.

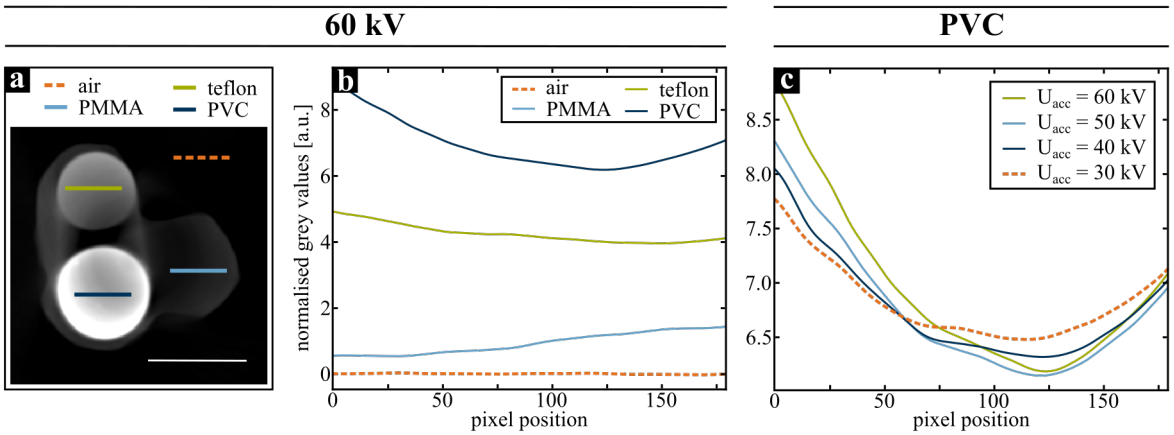

Figure 6.10: **Line Plots Through Averaged and Smoothed NanoCT Images to Visualise Cupping.** (a) Averaged and smoothed NanoCT image depicting the CNR phantom at $U_{acc} = 60\,kV$ with coloured lines indicating the pixel coordinates of the line plots through the materials. (b) Line plots through the lines shown in (a). (c) Line plots through PVC for the different U_{acc} values. Scalebar: 500 µm.

6.3 Discussion

In the following, the findings from the previous sections are interpreted according to the theoretical background provided in Chapter 2 and Chapter 3. In particular, the theoretical estimations from Section 6.2.1 serve as a reference. In some cases, the different studies have an overlap. In these cases, the results of the overlapping studies are combined for a holistic understanding.

6.3.1 Electron Spot Size for Different Acceleration Voltages

As illustrated in Fig. 5.2, there is a clear trade-off between small electron spot sizes and the target current. This was clearly seen in Fig. 6.2, where the electron spot size rapidly increased with the target current.
According to our theoretical estimations in Eq. 6.3, we expected larger electron spot sizes for smaller U_{acc} values . The experimental data, however, showed a different behaviour: In Fig. 6.2 the electron spot size was rather unaffected by changes in the U_{acc} value with even a slight tendency towards smaller electron spots for smaller acceleration voltages.
A reason for this contradiction could be a shortcoming of the theoretical estimations. Regarding chromatic aberrations, we assumed a constant voltage uncertainty in the high-voltage generator which was not influenced by changes in the absolute U_{acc} value. If chromatic aberrations were the dominant contribution to the electron spot size, and if the voltage ripple ΔU_{acc} from the high-voltage generator increased with U_{acc}, the theoretical estimations would predict smaller electron spots for smaller U_{acc} and would thus be conform with the empirical observations in this chapter. It is, however, not trivial to establish a direct relation between the voltage ripple and the U_{acc} value, since the voltage ripple typically is a complicated function of various technical factors [Russo, 2017].

6.3.2 Spectrum for Different Acceleration Voltages

Apart from the electron spot size, the energy spectrum is one of the central aspects to characterise the imaging properties of the NanoCT. The most striking feature of the NanoTube's emission spectrum was the dominance of the characteristic emission lines compared to the bremsstrahlung signal.
This effect indicates a very thin X-ray target, which spatially confines the electron-matter interaction volume. Figure 2.5 depicts the interaction volume with the different zones assigned to the respective prevailing physical interaction. This figure shows the zone of bremsstrahlung generation surrounding the zone of characteristic X-ray

generation. If the tungsten layer is thin compared to the interaction volume, the bremsstrahlung zone is strongly reduced, which may result in the specific shape of the NanoTube's spectrum. Furthermore, the simulation which considers the relevant parameters for X-ray generation in the NanoTube including the thickness of the X-ray target predicted a very similar emission spectrum.

Comparing the emission spectra in Fig. 6.4b which had been normalised to the target current, the X-ray generation efficiency decreases for decreasing U_{acc} values. This behaviour agrees with the predictions from Eq. 6.5. In the two spectra with $U_{acc} \in \{10, 20\}$kV, the X-ray flux was decreased even more severely. Consequently, U_{acc} values below 30 kV can be regarded as irrelevant for imaging with the NanoCT.

In Fig. 6.5, the detected spectrum for different air absorption distances was studied. Compared to the emission spectrum, energies > 20 keV were suppressed due to the quantum efficiency of the silicon sensor of the Pilatus detector (Fig. 5.5). Furthermore, air absorption decreased the photon counts towards smaller X-ray energies.

This reduction is evident when comparing the height of the spectral curves for the two air absorption distances $d_{air} = 200$ mm and $d_{air} = 800$ mm in Fig. 6.5. For the larger source-detector distance, the air absorption reduced the spectrum's height to approximately half the height than for the smaller distance $d_{air} = 200$ mm. This effect also occurred for lower U_{acc} values, as could be observed in Fig. 6.6a and b. Beyond air absorption, quadratic intensity reduction plays a major role in reducing X-ray flux for larger source-detector distances. Taking into account both air absorption and quadratic intensity reduction, only about 1/32-th of the X-ray flux for $d_{air} = 200$ mm reaches the detector at $d_{air} = 800$ mm.
The detected spectra for different U_{acc} values showed very similar energy distributions as a result of high energy suppression by the Pilatus detector.

In the introduction of this section, Eq. 6.6 was presented, which estimated an increase in the mean X-ray energy of the emitted spectrum towards larger U_{acc} values. This was perfectly reflected in the calculated mean energies in Table 6.1. Moreover, as already indicated in Fig. 6.6, the variations between the mean energies was much smaller in the detected spectra than in the emission spectra.

To conclude, only values of $U_{acc} \geqslant 30$ kV provided sufficient X-ray flux for efficient imaging. Furthermore, the results showed that the sample experiences rather different energy spectra for different U_{acc}. This was in contrast to the detected spectra, where the variation in the U_{acc} hardly had any effect on the energy distribution. This was, however, not the case for the X-ray generation efficiency, which decreased towards smaller U_{acc}. Nevertheless, a smaller U_{acc} value was here also rewarded with smaller electron spots (Table 6.3).

6.3.3 CNR for Different Acceleration Voltages

The spectral measurements clearly showed that only acceleration voltages of $U_{acc} \geqslant 30\,kV$ are relevant for further investigations. Hence, the CNR study was performed for $U_{acc} \in \{30, 40, 50, 60\}kV$.

Table 6.2 allowed for further deductions about the behaviour of the photon flux and the electron spot for similar target currents with different U_{acc} values. Regarding the photon flux, we expected a reduction towards smaller U_{acc} values, according to Eq. 2.11, Eq. 2.12 and according to the acquired spectra. These expectations could not be confirmed with the data presented in Table 6.2, which entailed rather similar X-ray photon counts over the range of U_{acc} at similar target currents. Comparing the photon flux values from the spectral measurements with the values from the CNR study, it should be considered that the spectra were acquired at a minimum emission current. At such low emission current values ($\leqslant 10\,\mu A$), fluctuations of the target current may have a non-negligible effect on the normalised results presented in Fig. 6.4b. Moreover, other physical effects may occur for larger emission currents ($100\,\mu A$) which may have lead to the behaviour presented in Table 6.2. Furthermore, the theoretical estimations assumed a thick X-ray target, opposed to the thin tungsten X-ray target in the NanoTube. This assumption excluded any cases where a constrained interaction volume due to the thickness of the X-ray target causes a reduction in the X-ray generation efficiency. According to the Kanaya Okayama range (Eq. 2.9), the electron interaction volume at a U_{acc} value of $30\,kV$ is already larger than the $500\,nm$-thick tungsten layer of the NanoTube's X-ray target (tungsten: $A = 184\,g/mol$, $Z = 74$, $\rho = 19.25\,g/cm^3$, $R_{K-O} = 1.7\,\mu m$). For $U_{acc} = 60\,kV$, the electron-interaction volume has a radius of $\approx 5.3\,\mu m$. Hence, in the NanoTube, the electron interaction volume is always constrained by the thickness of the tungsten layer, which may result in this deviating behaviour from the theoretically predicted X-ray generation efficiency. Consequently, it might be actually true for the NanoTube that higher U_{acc} values do not necessarily entail higher X-ray flux.

Beyond that, Table 6.2 further showed a decrease in the electron spot size for similar target currents towards smaller U_{acc}-values. To gain a better understanding of the electron spot size values, the data was set in context to the values obtained in the electron spot size study (Fig. 6.2). In the resulting semi-logarithmic plot in Fig. 6.11, it can be clearly seen that the target currents are indeed very similar throughout the CNR study. The measured electron spot sizes from the CNR study are even smaller than the values from the electron spot size study. This can be explained by the two different data sets having been measured with different cathodes at different stages in their cathode life span. The offset of the LaB_6 crystal to the cathode surface generally varies between cathodes and has a considerable influence on the emission divergence angle and with that the minimum achievable electron spot. Furthermore, an earlier

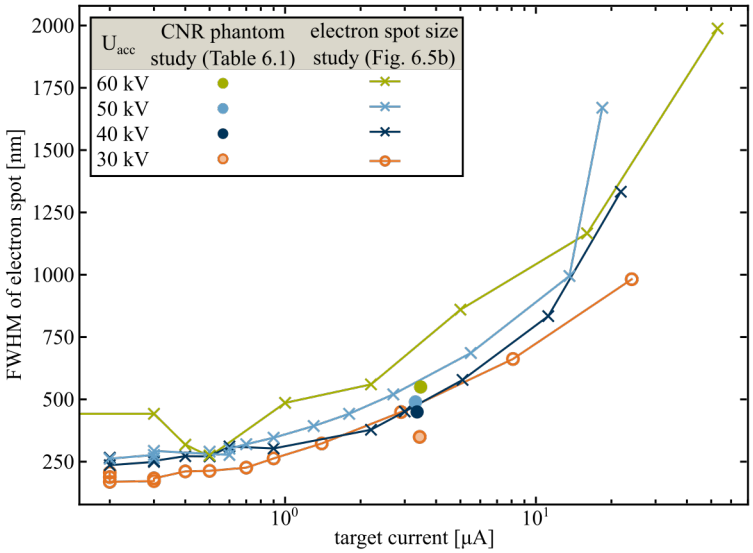

Figure 6.11: **Electron Spot Size Values from the CNR Study and the Electron Spot Size Study for Different Acceleration Voltages.** The FWHM of the electron spot in a semi-logarithmic plot over the target current for different acceleration voltages. Electron spot sizes from two different measurements using different cathodes are displayed (Fig. 6.2, Table 6.2).

stage in a cathode's life span allows for smaller electron spots. All in all, both data sets underline the slight tendency of the NanoTube to provide smaller electron spots for smaller U_{acc}-values at similar target currents.

In the normalised NanoCT slices in Fig. 6.7a-d an initial impression was gained regarding the CNR. Thereby, particularly the cupping artefacts were striking, whereby a decrease of the artefacts was observed towards lower U_{acc} values. With less cupping, the distribution of grey values in a single material is expected to be more narrow. This was perfectly illustrated by the histograms in Fig. 6.7e-h, where the grey value peaks appear more defined and narrow for smaller U_{acc} values. Furthermore, the grey value distribution of PMMA is sharpest in the histograms, which agrees with PMMA being least affected by cupping in the corresponding NanoCT slices.

To minimise the influence of cupping artefacts on the calculated CNR values, the noise signal was split from the contrast signal, and thereby from the cupping artefacts (Fig. 6.8). However, it was not possible to find an elegant solution for separating the contrast signal and the cupping artefacts. It is, thus, very likely that the resulting CNR values are affected by the cupping artefacts up to a certain extent.
The CNR plots in Fig. 6.9 presented increasing values for decreasing U_{acc} values for all three materials with reference to air. The increase of the absolute CNR value

was strongest for PVC and teflon, while the relative gain in CNR was strongest for PMMA.
PVC and teflon were affected most by cupping artefacts with a decreasing severity towards smaller U_{acc} values. This was clearly observed in the line plots through PVC in Fig. 6.10c. This may have caused higher mean values and, thereby, stronger contrast in PVC and teflon for smaller U_{acc}. Opposed to that, PMMA was hardly exhibiting any cupping (Fig. 6.10b). Nevertheless, the CNR curve of PMMA featured a strong relative increase towards smaller U_{acc}. This behaviour is in perfect accordance with theory (Eq. 6.7), which predicted an incline of the CNR curve for decreasing U_{acc}.

To summarise, the U_{acc} appears to have a considerable influence on both cupping artefacts, and the CNR, especially regarding relative changes of the CNR values. The relative gain in the CNR was particularly large in PMMA. This is rather fortunate for most NanoCT applications which focus on soft-tissue specimens, since the absorption behaviour of soft tissue is rather similar to PMMA in the relevant energy range (Fig. A.1).

6.4 Conclusion and Outlook

The central parameter studied throughout this chapter was the acceleration voltage U_{acc}. Several studies were performed to assess the influence of the U_{acc} on the NanoCT data quality. As quality criteria, two figures of merit were selected: the resolution given by the PSF and the CNR.
As previously mentioned, the NanoTube PSF is defined by the electron spot size and the size of the electron matter interaction volume. The empirical findings clearly demonstrated that smaller electron spots are reached for smaller U_{acc} values while obtaining the same target current.
Moreover, theory predicted a growing electron matter interaction volume with an increasing U_{acc} value. Thus, we expect smaller X-ray focal spots with decreasing U_{acc} values even at a constant electron spot size. To confirm this theory, though, a quantitative assessment of the X-ray focal spot dependent on the U_{acc}, the electron spot size and the target current is required. At any rate, we expect a significant improvement of the NanoTube PSF for smaller U_{acc}, according to the current state of knowledge.

Both the NanoTube PSF and the PSF of the Pilatus detector contribute to the final PSF in the projection image. The detector PSF was investigated in previous work by Mark Müller [Müller, 2019]. These investigations were based on the noise power spectrum of flat field images for different detector thresholds. According to the results, a higher detector threshold enables an improvement on the detector PSF through suppression of charge sharing. A larger detector threshold, however, is generally associated with signal loss. The detector threshold which represents an optimum compromise between signal detection and detector PSF was suggested to be in the range of $(6-8)$keV.
For further exploring the implications of these results, additional quantitative measurements are necessary of the resulting image PSF for different detector thresholds. Thereby, a resolution pattern may prove as a valuable tool for quantifying the image PSF.

The CNR, as the second quality criterion in this chapter, is formed by the contrast and the noise level. The contrast, on the one hand, is influenced by the sample material and the energy spectrum of the X-rays. The noise level, on the other hand, is strongly connected to the X-ray flux.
The spectral measurements showed that while the sample experiences still rather different energy spectra for different U_{acc}, the detected energy distributions are very similar. Moreover, the spectral measurements clearly demonstrated the immense influence of the source-detector distance on the detected X-ray flux as a result of air absorption and a quadratic intensity reduction. In contrast to that, the findings were inconclusive regarding a decrease in X-ray flux at smaller U_{acc} values down to 30 kV and require further experimental research. Due to the thin X-ray target of the NanoTube, it would

be hardly surprising if a smaller U_{acc} value did not result in significantly lower X-ray flux. U_{acc} values below 30 kV, however, hardly generated any measurable X-ray flux. The CNR study of a phantom showed that adjusting the U_{acc} between 30 kV and 60 kV results in considerable relative changes of the CNR. Furthermore, smaller U_{acc} values had a significant positive influence on reducing cupping artefacts.

To conclude, smaller U_{acc} values down to 30 kV enable a significant improvement on the NanoTube PSF and help to reduce cupping artefacts in strongly absorbing materials. Beyond specific sample materials, staining techniques, or minimum source-detector distances, adjustments of the U_{acc} towards 30 kV are well suited for optimising the CNR, especially with respect to soft-tissue samples. Furthermore, a detector threshold in the range of $(6 - 8)$keV shows great promise to further improve the image PSF.

This gained knowledge can be implemented to optimise the quality of NanoCT data in the future. The verification of these results on an actual NanoCT sample, such as stained human renal tissue (Chapter 9), however, is still pending and to be addressed by future measurements.

6.5 Materials and Methods

6.5.1 Theoretical Estimations

The theoretical estimations presented in the introduction of this section, are based on information given in the theory chapters: Chapter 2 and Chapter 3.

The Electron Spot and the Acceleration Voltage

First we want to estimate the relation between the brightness-aberration-limited electron spot on the X-ray target and the U_{acc} value. Eq. 2.15, Eq. 2.16, and Eq. 2.17 contain the relevant contributions to the electron spot radius on the X-ray target in dependence of the U_{acc} value. Concerning chromatic aberrations, we assume a constant voltage ripple from the high-voltage generator which is independent from U_{acc}. Thus, we obtain for the brightness-limited electron spot r_β, for the chromatic aberrations r_{Ch}, and for the spherical aberrations r_s:

$$r_\beta \propto \frac{1}{\sqrt{U_{acc}}}, \quad r_{Ch} \propto \frac{1}{U_{acc}^2}, \quad r_S \propto \frac{1}{U_{acc}^2} \tag{6.8}$$

From these expressions and Eq. 2.13, we can calculate the total aberration-limited electron spot on the X-ray target and its behaviour for different U_{acc}:

$$r_e = \sqrt{r_\beta^2 + r_{Ch}^2 + r_S^2} \propto \frac{\sqrt{U_{acc}^3 + 2}}{U_{acc}^2} \approx \frac{1}{\sqrt{U_{acc}}}. \tag{6.9}$$

The size of the electron matter interaction volume R_{K-O} was simply derived from the Kanaya Okayama range (Eq. 2.9) by replacing the energy of the incoming electron by $E_0 = e \cdot U_{acc}$:

$$R_{K-O} \propto E_0^{1.67} = e \cdot U_{acc}^{1.67}. \tag{6.10}$$

X-ray Flux and the Acceleration Voltage

The total emitted X-ray flux comprises of bremsstrahlung and characteristic X-rays. For the sake of simplicity, we neglect the characteristic X-ray flux in this case and consider the bremsstrahlung flux as the total emitted X-ray flux: $I_x \approx I_{brems}$. From

the expression $I_{\text{brems}}(E)$ in Eq. 2.10, we calculate the total X-ray flux:

$$\begin{aligned} I_{\text{x}} &= \int_{E_{\text{min}}}^{E_{\text{max}}} I_{\text{x}}(E)\ \mathrm{d}E \\ &\approx \int_{E_{\text{min}}}^{E_{\text{max}}} I_{\text{e}} Z \cdot \frac{E_{\text{max}} - E}{E}\ \mathrm{d}E = \\ &= I_{\text{e}} Z E_{\text{max}} \left[\ln\left(\frac{E_{\text{max}}}{E_{\text{min}}}\right) - 1 + \frac{E_{\text{min}}}{E_{\text{max}}} \right] \end{aligned} \tag{6.11}$$

with $E_{\text{max}} = e \cdot U_{\text{acc}}$, E_{min} a small energy value close to 0, Z the atomic number of the X-ray target material, and I_{e} the electron current onto the X-ray target. Thus, we obtain the following simplified relation of the X-ray flux and $\mathrm{U_{acc}}$:

$$I_{\text{x}} \propto I_{\text{e}} \cdot U_{\text{acc}} \ln(U_{\text{acc}}). \tag{6.12}$$

The Mean X-ray Energy and the Acceleration Voltage

The mean energy of the emitted X-rays can be calculated via integration over the energy spectrum. Here, we insert the energy-dependent X-ray flux from Eq. 6.11:

$$\begin{aligned} E_{\text{mean}} &= \frac{\int_{E_{\text{min}}}^{E_{\text{max}}} I_{\text{x}}(E) \cdot E\ \mathrm{d}E}{\int_{E_{\text{min}}}^{E_{\text{max}}} I_{\text{x}}(E)\ \mathrm{d}E} \\ &\approx \frac{I_{\text{e}} Z \cdot \int_{E_{\text{min}}}^{E_{\text{max}}} E_{\text{max}} - E\ \mathrm{d}E}{I_{\text{e}} Z E_{\text{max}} \left[\ln(\frac{E_{\text{max}}}{E_{\text{min}}}) - 1 + \frac{E_{\text{min}}}{E_{\text{max}}} \right]} = \\ &= \frac{\frac{1}{2}\left(E_{\text{max}} - E_{\text{min}}\right)^2}{E_{\text{max}} \left[\ln(\frac{E_{\text{max}}}{E_{\text{min}}}) - 1 + \frac{E_{\text{min}}}{E_{\text{max}}} \right]}. \end{aligned} \tag{6.13}$$

Considering small values for E_{min}, a simplified relation between E_{mean} and U_{acc} can be obtained:

$$E_{\text{mean}} \propto \frac{U_{\text{acc}}}{\ln(U_{\text{acc}})}. \tag{6.14}$$

Hence, the mean energy of the emitted X-ray spectrum grows with increasing $\mathrm{U_{acc}}$ values.

The CNR and the Acceleration Voltage

To estimate the behaviour of the CNR, we have to investigate the numerator and the denominator in Eq. 6.1: or the mean grey value m and the image noise value σ.

The mean grey value m_r in a material r can be considered as directly proportional to the linear attenuation coefficient μ_r. According to Eq. 3.17 and Eq. 6.14, we obtain the following expression for the attenuation coefficient μ_r:

$$m_\mathrm{r} \propto \mu_\mathrm{r} \propto \frac{Z_\mathrm{r}^4}{E_\mathrm{mean}^3} \propto \frac{Z_\mathrm{r}^4 (\ln(U_\mathrm{acc}))^3}{U_\mathrm{acc}^3}, \tag{6.15}$$

with Z_r the atomic number of material r.

For the contrast between material r and a reference material, providing the numerator for the CNR in Eq. 6.1, we thus obtain the following relation to U_acc:

$$(m_\mathrm{r} - m_\mathrm{ref}) \propto \frac{(Z_\mathrm{r} - Z_\mathrm{ref})^4 (\ln(U_\mathrm{acc}))^3}{U_\mathrm{acc}^3} \propto \frac{(\ln(U_\mathrm{acc}))^3}{U_\mathrm{acc}^3}. \tag{6.16}$$

To gain information on the image noise, the signal processing by the X-ray detector has to be considered. The Pilatus detector applies a threshold to the measured signal and thereby foregoes dark-field current and read-out noise. Therefore, we can assume that the image noise in a NanoCT projection image merely originates from a statistical process with a Poisson distribution. The standard deviation σ in a Poisson distribution is directly proportional to the square root of the mean value x_mean of the distribution:

$$\sigma \propto \sqrt{x_\mathrm{mean}} = \sqrt{N_\mathrm{x}}. \tag{6.17}$$

In this context, the mean value x_mean represents the number of detected photons N_x, and the standard deviation can be defined as equivalent to the noise level in the projection image [Fahrmeir, 2016].

The X-ray current or X-ray flux is defined as particles per time unit ($I_\mathrm{x} = \mathrm{d}N_\mathrm{x}/\mathrm{d}t$). Thereby, a connection can be generated between the standard deviation noise value, the X-ray flux and with Eq. 6.12 the acceleration voltage $\mathrm{U_{acc}}$:

$$\sigma_\mathrm{r} \propto \sqrt{I_\mathrm{x}} \propto \sqrt{U_\mathrm{acc} \ln(U_\mathrm{acc})}. \tag{6.18}$$

Consequently, the denominator of the CNR (Eq. 6.1) should exhibit the following behaviour for different $\mathrm{U_{acc}}$:

$$\sqrt{\sigma_\mathrm{r}^2 + \sigma_\mathrm{ref}^2} \propto \sqrt{U_\mathrm{acc} \ln(U_\mathrm{acc})}. \tag{6.19}$$

Combining the numerator (Eq. 6.16) and the denominator (Eq. 6.19), gives us for the CNR, the following expression:

$$\mathrm{CNR} \propto \frac{(\ln(U_\mathrm{acc}))^3}{U_\mathrm{acc}^3 \cdot \sqrt{U_\mathrm{acc} \ln(U_\mathrm{acc})}} \propto \frac{(\ln(U_\mathrm{acc}))^{5/2}}{U_\mathrm{acc}^{7/2}}. \tag{6.20}$$

This expression indicates a decreasing CNR value for increasing $\mathrm{U_{acc}}$.

6.5.2 Electron Spot Size for Different Acceleration Voltages

Data Acquisition

For all electron spot measurements, the maximum emission current of 100 µA was chosen. The U_{acc} value was varied ($U_{acc} \in \{10, 20, 30, 40, 50, 60\}$kV). For each of these U_{acc} values, the cathode grid voltage U_g was altered in the range of $[0; 3500]$V.
After adjusting the U_{acc} value, the dynamic coarse focusing routine, which optimises the stigmator values and the focus current, was applied, as shown in Fig. 5.3a-c. For each of the used grid voltages, the static fine focusing routine was used to achieve the optimum electron spot size (Fig. 5.3d-f). For the resulting settings, the electron spot size in the form of the FWHM and the associated target current were recorded.
For every modification in the U_{acc} value, special care was taken to use the same edge structures on the X-ray target to calibrate the electron spot to achieve the best possible comparability between the resulting electron spot sizes.

Data Processing

The resulting electron spot FWHMs and target current values were plotted over the respective cathode grid voltage in Fig. 6.1. According to Section 2.1, there is a direct relation between the target current and the minimum achievable electron spot size. Therefore, both plots in Fig. 6.1 were combined to generate a plot of the electron spot over the target current (Fig. 6.2). As the majority of data points has been obtained for small target current values, below 10 µA, a semi-logarithmic plot was used to provide more clarity.

6.5.3 Energy Spectrum for Different Acceleration Voltages

Data Acquisition

For the acquisition of the spectral data, an X-ray spectrometer (X123 GammaRad, Amptek, USA) was used, which was equipped with a 0.5 mm-thick silicon sensor behind a 25.4 µm-thick beryllium window and was controlled with the software ADMCA. The spectrometer was mounted in a distance of 18 mm from the NanoTube and aligned to maximise the measured count rate. Subsequently, the spectrometer was calibrated using the known visible characteristic emission lines of tin ($E(K_\alpha) = 25.3$ keV) and tungsten ($E(L_\alpha) \approx 8.3$ keV, $E(L_\beta) \approx 9.8$ keV and $E(L_\gamma) \approx 11.3$ keV). As the resolution for the spectral measurements, 1024 energy bins were used at $U_{acc} = 60$ kV and 8000 channels at $U_{acc} = 10$ kV. An exposure time of 600 s was chosen per spectrum

acquisition.

The energy spectrum was recorded for a selection of U_{acc} values ($U_{acc} \in \{10, 20, 30, 40, 50, 60\}$kV). As the spectrometer is only capable of recording photons up to a certain count rate, the source power was set to the minimum value of 0.1 W. Table 6.3 lists the remaining relevant NanoTube parameters, including the target current values which were used for normalisation of the spectral data in Fig. 6.4b.

U_{acc}	[kV]	10	20	30	40	50	60
Emission Current	[µA]	10	5	3.4	2.5	2.1	1.48
Target Current	[µA]	0.22	0.08	0.06	0.04	0.04	0.03
r_e	[nm]	100	80	130	160	200	210

Table 6.3: **NanoTube Parameters with Respect to the Acceleration Voltage for the Spectrum Acquisition.** The power of the NanoTube was minimised to 0.1 W leading to increasing emission currents for smaller U_{acc}. The electron spot radius on the X-ray target is referred to as $r_e = 0.5 \cdot FWHM$.

Data Processing

First, the original emission source spectra of the NanoTube (Fig. 6.3, Fig. 6.4) were retrieved from the measured spectra using Lambert-Beer's law (Eq. 3.13):

$$I_x(E) = I_{meas}(E) \cdot \frac{e^{+\mu_{air}(E)d_{air}} \cdot e^{+\mu_{Be}(E)d_{Be}}}{1 - e^{-\mu_{Si}(E)d_{Si}}}, \tag{6.21}$$

with $I_x(E)$ the source spectrum, $I_{meas}(E)$ the spectrum measured by the spectrometer, $\mu_{air/Be/Si}$ the linear absorption coefficient of air/beryllium/silicon, $d_{air} = 18\,mm$ the distance of the spectrometer from the NanoTube, $d_{Be} = 25.4\,\mu m$ the thickness of the beryllium window and $d_{Si} = 0.5\,mm$ the thickness of the silicon sensor of the spectrometer.

The simulated spectrum was generated with the Monte Carlo based open-source software pyPENELOPE [Salvat, 2006]. Thereby, an U_{acc} value of 60 kV, and the composition of the NanoTube's X-ray transmission target (500 nm tungsten on 100 µm diamond) were taken into account. For a better qualitative comparison of the measured spectrum and the simulation, both data sets were normalised to the number of counts at $E = 20\,keV$ resulting in the plot shown in Fig. 6.3.

For revealing the X-ray generation efficiency, as considered in the spectral data in Fig. 6.4b, the emission source spectra $I_x(E)$ (Fig. 6.4a) were normalised with the corresponding target current (Table 6.3).

The detected spectra of Fig. 6.5 and Fig. 6.6 were calculated from the source spectra similar to Eq. 6.21. Thereby, the absorption behaviour of the Pilatus detector's sensor (1 mm-thick silicon) and the absorption through air over a certain propagation distance d_{air} were considered:

$$I_{\mathrm{det}}(E) = I_{\mathrm{x}}(E) \cdot e^{-\mu_{\mathrm{air}}(E) d_{\mathrm{air}}} \left[1 - e^{-\mu_{\mathrm{Si}}(E) d_{\mathrm{Si}}}\right], \tag{6.22}$$

with $I_{\mathrm{det}}(E)$ the detected spectrum, $I_{\mathrm{x}}(E)$ the source spectrum, $\mu_{\mathrm{air/Si}}$ the linear absorption coefficient of air/silicon, and $d_{\mathrm{Si}} = 1\,\mathrm{mm}$ the thickness of the silicon sensor of the Pilatus detector.

The mean effective energy of each spectrum (Table 6.1) was calculated with the following equation:

$$E_{\mathrm{mean}} = \frac{\sum_{i=0}^{i=max} c_{\mathrm{i}} \cdot E_{\mathrm{i}}}{\sum_{i=0}^{i=max} c_{\mathrm{i}}}, \tag{6.23}$$

with c_{i} the counts for the energy E_{i} and $E_{\mathrm{max}} = e \cdot \mathrm{U_{acc}}$.

6.5.4 CNR for Different Acceleration Voltages

CNR Phantom

For the CNR phantom, homogeneous materials were chosen to facilitate a contrast and noise level measurement. In the NanoCT, mostly soft-tissue samples with X-ray stains are measured. Hence, for an adequate selection of materials, the energy dependent linear absorption coefficients were plotted for bone and soft tissue and compared with potential suitable phantom materials (Fig. A.1). Thereby, PMMA is well suited to simulate the absorption behaviour of soft tissue and PVC and teflon are adequate phantom materials for bone.
Furthermore, the phantom had to be small enough for the FOV of the NanoCT. Thus, three cylindrical rods of PVC, PMMA and teflon with a diameter $< 1\,\mathrm{mm}$, were fabricated and subsequently assembled with superglue to form the resulting CNR phantom.

Data Acquisition

Four NanoCT scans were acquired for different $\mathrm{U_{acc}}$ values ($\mathrm{U_{acc}} \in \{30, 40, 50, 60\}\mathrm{kV}$). Thereby, the maximum emission current of 100 µA was set and the grid voltage $\mathrm{U_g}$ was adjusted to reach similar target current values for every $\mathrm{U_{acc}}$ value. The focusing routines were applied for every $\mathrm{U_{acc}}$ value anew, the electron spot size was calibrated and the target current was recorded (Table 6.2). Special attention was paid to aim the electron beam to the same position on the X-ray target for each of the $\mathrm{U_{acc}}$ values, to avoid deviations from the calibrated setup geometry.

Each NanoCT scan was acquired with the minimum detector threshold of 2.7 keV by taking 1,599 evenly distributed projections over a rotation of 360° with an effective voxel size of $v_{\text{eff}} \approx 1.5\,\mu\text{m}$ and an exposure time of 2 s. This resulted in a total acquisition time of 2 h per NanoCT scan.

Image and Data Processing

The photon counts in Table 6.2 were calculated from the flat field images of each NanoCT scan, which were first corrected for dead pixels and detector gaps. The photon count per pixel was calculated from the mean total photon count over all corrected flat field images per NanoCT scan. This number was then divided by the total pixel number in one flat field (1475 × 195 pixel).

The image processing and reconstruction of the NanoCT data was performed according to the descriptions in Section 5.3. However, only a centre shift correction was performed. A projection alignment was not necessary due to the rather large effective voxel size. To avoid corruption of the contrast and noise values, no phase retrieval and no image deblurring were applied.

The CNR values were determined inside certain well-defined VOIs. Thereby four VOIs were defined in the four materials (PVC, PMMA, teflon, air) using a centre-of-intensity-based calculation to find the correct centre point in each material. To forego any errors due to undersampling at large distances from the optical axis as a result of the cone beam geometry, the VOIs are positioned close to the beam centre along the vertical (rotation) axis. The VOI edge lengths perpendicular to the rotation axis were set as 180 pixel and along the rotation axis as 100 pixel resulting in a volume of $180 \times 180 \times 100\,\text{pixel}^3$.

The resulting reconstructed NanoCT volumes were normalised so that the mean value of the air VOI is redefined as zero and the mean value of the PMMA VOI is redefined as one. Slices of the resulting normalised NanoCT data along with the histograms, as well as the horizontal cross-sections of the material VOIs are shown in Fig. 6.7.

The mean values for the CNR were determined over the mean inside the material VOIs of the normalised NanoCT volumes (Fig. 6.8a).
To obtain the noise values, an averaged and smoothed image was created from each of the normalised NanoCT data. The average was taken along the 100 central pixels of the vertical (rotation) axis and the smoothing was performed with a Gaussian filter. This averaged image is shown in Fig. 6.8b. The image was then subtracted from the original normalised volume to create a subtraction volume, which only contains noise (Fig. 6.8c). From each of the NanoCT subtraction volumes, the noise values for the CNR in form of the standard deviation was calculated inside the material VOIs. From the respective mean and noise values, the CNR was calculated with reference to air for

each U_{acc} value, according to Eq. 6.1 (Fig. 6.9).

6.5.5 Scientific Contributions

The theoretical estimations, the design of the CNR phantom, the spectral simulation, the data acquisition and processing, as well as the generation of the resulting figures was performed by Simone Ferstl.

7 Propagation-based Phase Contrast and X-ray Staining

7.1 Introduction

All NanoCT data sets presented throughout this work are subject to phase effects to some extent. Thus, it is highly relevant to get a better grasp on how these phase effects behave under certain imaging conditions and how they influence the resulting NanoCT data. This knowledge may facilitate a more targeted use of these phase effects to improve the quality of the NanoCT data.

From a different perspective, a good understanding of the phase effects is essential for assessing the functioning and benefits of a newly developed staining routine. Or more specifically speaking: It is crucial to distinguish, what part of an image's contrast originates from the stain and what part is owed to propagation-based phase effects.

First, some general estimations on the behaviour of propagation-based phase effects in the NanoCT are provided. These estimations are derived from theoretical considerations based on the information conveyed in Chapter 3. This further fosters a more substantiated analysis of the results that follow.

Subsequently, propagation-based phase effects in the NanoCT data are studied for different imaging parameters. Assuming a sample with a fixed distribution of attenuation and phase coefficients (μ, δ), the propagation-term of the transport of intensity equation (TIE) (Eq. 3.31) declares the propagation distance as the central relevant parameter in this respect. Hence, NanoCT data and the respective propagation-based phase effects are studied for two different typical propagation distances.

Finally, comparative analyses are performed between NanoCT data of unstained and stained tissue. For this purpose, the X-ray eosin stain has been chosen, since it has been implemented with great success in previous work with the NanoCT [Busse, 2018b; Ferstl, 2020a; Ferstl, 2020b]. A comparison between X-ray eosin stained tissue and unstained tissue has already been performed for microCT data of wet tissue specimens [Busse, 2018b; Müller, 2019]. For NanoCT data of critical-point dried (CPD) samples, such analyses are presented here for the first time.
In this study, NanoCT data sets of unstained and X-ray eosin stained CPD samples are analysed, which have been acquired at similar propagation distances and which have undergone the same image processing routine (Table 7.1).

7.2 Theoretical Considerations about Propagation-based Phase Effects in the NanoCT

To get a better grasp on propagation-based phase effects in the NanoCT, some theoretical considerations are carried out in the following. This part of this chapter merely presents the results from these considerations. More detailed calculations can be found in the methods section at the end of the chapter.

In general, for any phase-related effects to occur, the coherence conditions need to be fulfilled. In section 3.2.3, formalisms were introduced to calculate the longitudinal coherence length L_l and the transverse coherence length L_t (Eq. 3.33, Eq. 3.32). For the continuous source spectrum of the NanoTube at the typical acceleration voltage of $\mathrm{U_{acc}} = 60\,\mathrm{kV}$, we obtain a longitudinal coherence length of:

$$L_\mathrm{l} \approx 0.14\,\text{Å}. \tag{7.1}$$

The longitudinal coherence length of the NanoTube's emission spectrum is very short and smaller than the mean wavelength $\lambda \approx 0.56\,\text{Å}$ of the respective NanoTube source spectrum. Hence, only the higher-energy parts of the NanoTube spectrum are capable of fulfilling this coherence criterion.
For a smaller acceleration voltage of $\mathrm{U_{acc}} = 30\,\mathrm{kV}$, the longitudinal coherence length and the mean X-ray wavelength of the associated spectrum lie closer together:
$L_\mathrm{l} \approx 0.90\,\text{Å}$, $\lambda \approx 0.93\,\text{Å}$.
Consequently, a larger amount of the spectrum's X-ray photons fulfil the longitudinal coherence criterion for $\mathrm{U_{acc}} = 30\,\mathrm{kV}$, and phase effects should be more pronounced.

Regarding the transverse coherence length, the size of the X-ray source spot and the distance of the source from the sample exit point are crucial. Due to the close correlation between electron spot and X-ray source spot in the NanoTube, we expect an alteration in the edge enhancement for an alteration of the electron spot radius r_e.
The NanoTube features small X-ray spot radii down to $r_\mathrm{x} \approx 150\,\mathrm{nm}$. Consequently, a typical NanoCT data set acquired at $\mathrm{U_{acc}} = 60\,\mathrm{kV}$, and a distance of $d \approx 2\,\mathrm{mm}$ from the source to the sample exit point, is associated with a transverse coherence length of:

$$L_\mathrm{t} \approx 373\,\mathrm{nm}. \tag{7.2}$$

Hence, structures of $\leqslant 373\,\mathrm{nm}$ in size are capable of causing phase effects. This size lies in the range of typical v_eff values for high-resolution NanoCT scans. Therefore, we expect phase effects in the form of edge enhancement in the high-resolution regime of the NanoCT. The edge enhancement is expected to decrease towards larger v_eff values in the range of $1\,\mu\mathrm{m}$ and towards larger electron spots on the X-ray target of the NanoTube.

Having investigated the coherence conditions, in a next step the relevant imaging regime of the NanoCT is defined. A distinction is made between three different imaging regimes: contact region, Fresnel region, and Fraunhofer region. According to Eq. 3.23 in Chapter 3, imaging in the NanoCT is generally performed in the near-field, also called Fresnel region:

$$\text{Fresnel region}: R \approx \frac{a^2}{\lambda}, \tag{7.3}$$

with R the propagation distance, a the structure size and λ the wavelength of the incident X-rays. This estimation is based on the case of an acceleration voltage of U_{acc} = 60 kV, a typical propagation distance $R \approx 400$ mm and a structure size $a \approx 3.3$ µm, which was calculated from the radius of the first Fresnel zone [Clœtens, 1999]. For imaging in the Fresnel region, we expect phase effects in the form of edge enhancement, opposed to complex diffraction patterns as occurring in the Fraunhofer region, or no phase effects at all in the contact region.

For theoretically describing the behaviour of propagation-based phase effects in the near-field, the transport of intensity equation (TIE) is a convenient tool. According to the propagation-based phase term of the TIE in Eq. 3.31, propagation-based phase effects depend on the curvature of the phase directly behind the sample $\nabla^2_{\mathrm{T}}\Phi_{z_0}$, the X-ray energy in form of the wave vector k and the propagation distance Δz:

$$I_z(x,y) = ... + \underbrace{\frac{\Delta z}{k} I_{z_0}(x,y)\nabla^2_{\mathrm{T}}\Phi_{z_0}(x,y)}_{\text{III propagation-based phase}}. \tag{7.4}$$

For a given sample and, thereby, a given phase curvature behind the sample, we anticipate stronger edge enhancement for larger propagation distances, as well as for smaller X-ray energies.

Due to these dependencies of propagation-based phase effects, the formalism for Paganin's phase retrieval Eq. 5.13 includes the propagation distance d in addition to the energy-dependent material constants δ and μ:

$$D_\phi(x,y) = -\frac{1}{\mu}\ln\left(\mathfrak{F}^{-1}\left[\frac{\mathfrak{F}[I(x,y)\cdot I_0^{-1}]}{4\pi^2 d\cdot\frac{\delta}{\mu}|\vec{w}|^2+1}\right]\right). \tag{7.5}$$

Here $D_\Phi(x,y)$ denotes the phase-retrieved projection image, $I(x,y)$ the recorded image, and I_0 the incoming intensity.

As the homogeneity assumption (Section 5.3.3) is generally not fulfilled by NanoCT samples and due to the polychromatic spectrum of the NanoTube, the material parameters δ and μ are not well defined. This hampers a retrieval of quantitative phase information in the NanoCT data and the parameters are typically adjusted qualitatively to optimise the image quality.

Hence, an expression can be defined which combines the material constants δ and μ with the propagation distance d:

$$\xi = d \cdot \frac{\delta}{\mu}, \tag{7.6}$$

The introduced parameter ξ will be referred to as the filtering strength of Paganin's phase retrieval. This filtering strength ξ is inserted into Eq. 7.5 to obtain the following equation:

$$D_\phi(x,y) = -\frac{1}{\mu} \ln\left(\mathfrak{F}^{-1}\left[\frac{\mathfrak{F}[I(x,y)\cdot I_0^{-1}]}{4\pi^2\xi|\vec{w}|^2+1}\right]\right), \tag{7.7}$$

For better comparability in this chapter, the same filtering strength ξ was applied to NanoCT data with similar propagation distances d and stronger filtering was performed for larger propagation distances.

7.3 Propagation-based Phase Effects for Different Propagation Distances

The following section focuses on the propagation distance and its influence on the propagation-based phase effects in the NanoCT data. A first impression on this subject is gained by comparing two consecutive NanoCT data sets of the same sample acquired at two different source-detector distances d_{sd} ($d_{\mathrm{sd}} \in \{200\,\mathrm{mm}, 600\,\mathrm{mm}\}$), and at a constant source-axis distance of $d_{\mathrm{sa}} = 0.76\,\mathrm{mm}$, which results in two different propagation distances.

For an appropriate comparison, both NanoCT data sets were processed with mostly the same image processing protocol. Yet, stronger Paganin's phase retrieval (larger values of ξ, Eq. 7.6) was applied for the larger propagation distance, to comply with the theoretical considerations.

The resulting NanoCT data, without and with phase retrieval, are presented in Fig. 7.1. Thereby, NanoCT slices displaying corresponding tissue regions were chosen in Fig. 7.1a-d. The NanoCT slices were normalised to facilitate an easier comparison between the grey levels of the different images.

In the enlarged images without phase retrieval in Fig. 7.1e and f, it can be clearly seen that the edge enhancement is more pronounced for the larger propagation distance. The contrast appears stronger for the larger propagation distance in Fig. 7.1f compared to Fig. 7.1e, since the stronger edge enhancement creates a broader grey value distribution. This effect is further illustrated in the histograms in Fig. 7.1i, k. The influence of the stain on the grey values can still slightly be seen for the smaller d_{sd} value (Fig. 7.1i) as a second soft tissue peak which can be surmised beside the air peak. For the larger propagation distance in Fig. 7.1k, the phase effects fully dominate the histogram creating a single peak with a Gaussian-like shape centred around zero.

Compared to the NanoCT images without phase retrieval, the phase-retrieved NanoCT slices in Fig. 7.1c, d exhibit a much more pronounced overall soft-tissue contrast and a lower noise level. The histograms in Fig. 7.1l, m reflect this observation and show a much more narrow peak around zero representing air and a separate wider peak representing the stained soft tissue. The detail images in Fig. 7.1g, h appear rather similar, except for the increased edge sharpness for the larger d_{sd} value.

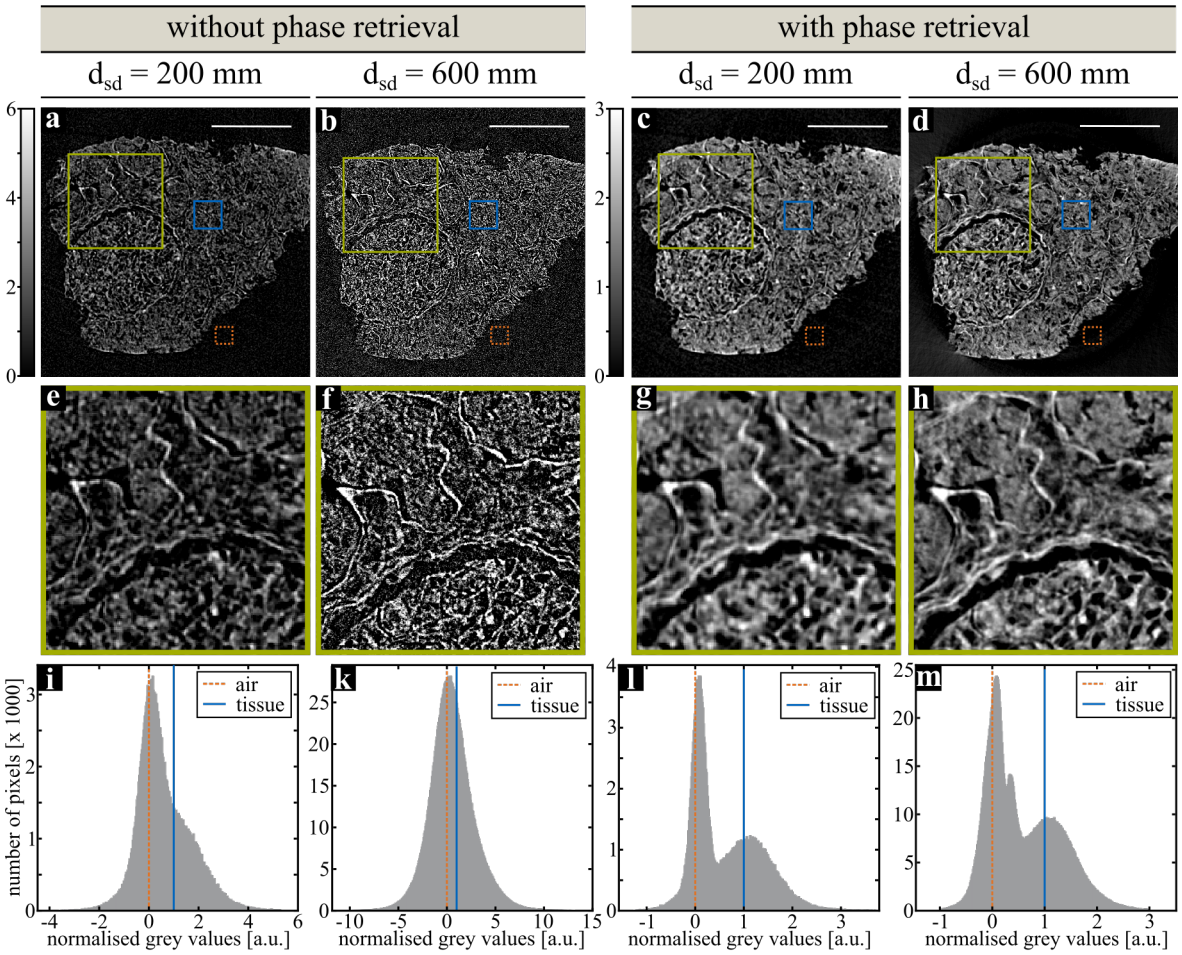

Figure 7.1: **Propagation-based Phase Effects in NanoCT Data of an X-ray Eosin Stained Human Kidney Tissue Specimen for Different Propagation Distances.** (a) - (d) Corresponding NanoCT slices for two source-detector distances d_{sd} (a,c: d_{sd} = 200 mm with $v_{eff} \approx 630$ nm and b,d: d_{sd} = 600 mm with $v_{eff} \approx 210$ nm) without (a,b) and with Paganin's phase retrieval (c,d). The source-axis distance d_{sa} was 0.76 mm. The NanoCT slices were normalised to the mean value of air (orange dashed ROI), which was set to zero, and the mean grey value of the tissue (blue ROI), which was set to one. (e) - (h) Enlarged images of the green ROIs in panels (a) - (d). (i) - (m) Grey value histograms from the normalised NanoCT slices in (a) - (d) with the mean value of air (orange dashed line) and the mean grey value of the tissue (blue line) marked. Note that the values for the number of pixels in the histograms are very different for the two d_{sd} values, since the presented images depict the same area with different v_{eff} values. Scalebars: 100 µm.

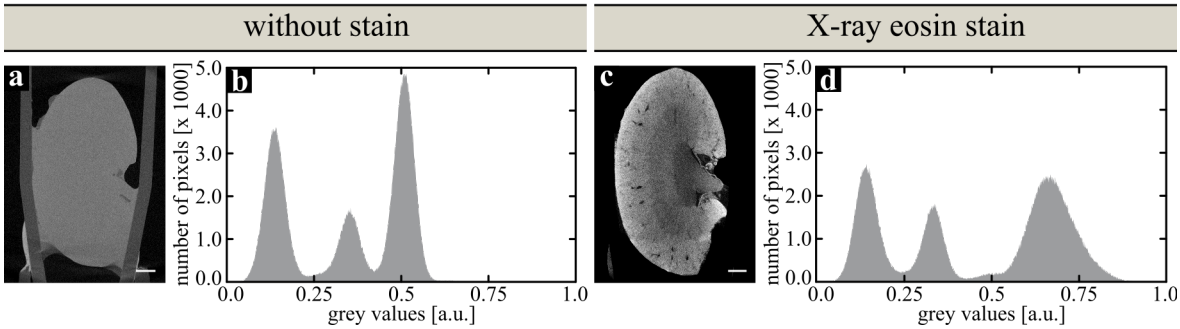

Figure 7.2: **MicroCT Slices of a Wet Mouse Kidney without and with X-ray Eosin Stain.** (a), (c) MicroCT slices of an entire mouse kidney before (a) and after (c) applying the X-ray eosin stain. The microCT data were recorded with the Xradia Versa 500 with identical acquisition parameters ($v_{\text{eff}} \approx 12\,\mu\text{m}$). (b), (d) Grey value distribution of the microCT data in (a), (c). Scalebars: 1 mm. Figure adapted from [Busse, 2018b].

7.4 Comparison of Unstained and X-ray Eosin Stained Tissue

Creating a better understanding of propagation-based phase effects, of X-ray staining and their impact on the NanoCT data is the main objective of this section. With this goal in mind, we attempt to compare the contrast contributions from phase with those from X-ray staining in the reconstructed NanoCT data.

As the X-ray stain in this study, X-ray eosin was selected. The X-ray eosin stain was first introduced to the scientific community in the scope of visualising murine renal tissue in 3D [Busse, 2018b]. In this work, a comparison between X-ray eosin stained tissue and unstained tissue was performed using microCT data of wet tissue specimens. The resulting microCT slices and the corresponding grey value histograms (Fig. 7.2) demonstrated a significant gain in soft-tissue contrast through the X-ray eosin stain [Busse, 2018b; Müller, 2019]. However, NanoCT data of unstained versus X-ray eosin stained CPD tissue have not been explored so far.

In the following, unstained and X-ray eosin stained CPD tissue specimens are examined, featuring the same types of tissues. The data sets were recorded with the NanoCT using similar propagation distances. The entire set of acquisition parameters for each of the NanoCT data sets can be found in the methods section of this chapter (Table 7.1). The reconstructed NanoCT data are both studied without phase retrieval and after applying Paganin's algorithm to the projection images. Thereby, the same image processing parameters were employed, to grant a maximum level of comparability.

7.4.1 Study of Murine Renal Tissue

The following results present NanoCT data of CPD samples from unstained and X-ray eosin stained murine renal tissue with and without Paganin's phase retrieval. First, NanoCT slices of murine renal tissue are investigated in Fig. 7.3 without phase retrieval. The NanoCT slices were normalised to an air ROI and a superglue ROI as reference.

The NanoCT slices in Fig. 7.3 and their corresponding detail images give a first impression of a rather similar appearance regardless of the differences in the sample preparation. In general, distinct edge enhancement can be observed. This is particularly well illustrated at the edges of the superglue in the detail images in Fig. 7.3d-f. The edge enhancement, however, prevents a clear visualisation of the samples' internal tissue structures. The data merely allows for distinguishing between the more homogeneous superglue regions and the strongly structured tissue regions.

This impression is further confirmed in the histograms in Fig. 7.3g-i. All three histograms show one single Gaussian-like peak. Based on these grey value distributions, it cannot be deduced that the samples are actually composed of multiple materials. Moreover, all peaks feature a similar spread, whereby the grey value distribution in Fig. 7.3h appears wider than the distributions in Fig. 7.3g, i.

Figure 7.4 shows the same data as Fig. 7.3 but after applying Paganin's algorithm. Compared to the data without phase retrieval in Fig. 7.3, the NanoCT slices in Fig. 7.4a-f exhibit less noise and the edge enhancement is dampened. Thereby, the contrast of soft-tissue and contact-glue appears stronger with respect to air. The internal tissue structures are now clearly visible in all NanoCT data of both unstained and stained tissue.

A more detailed view of the tissue architecture is provided in Fig. 7.4d-f. The NanoCT slices in Fig. 7.4d, f depict typical tissue morphologies of the renal cortex, such as glomeruli (Fig. 7.4 gl) and tubules, whereas Fig. 7.4e merely presents tubular tissue. The glomerulus in Fig. 7.4d, however, contains only little substructures, unlike the glomerulus in the centre of Fig. 7.4f. Similarly, the glomerulus in the upper right corner of Fig. 7.4f exhibits a similar lack of internal structure.

Studying the contrast of soft tissue compared to superglue in the NanoCT slices in Fig. 7.4a-c yields slight differences between the unstained and the X-ray eosin stained tissue. While the soft tissue of the unstained samples in Fig. 7.4a, b is darker than the superglue areas, the stained soft tissue in Fig. 7.4c appears just as bright and in some regions even brighter than superglue.

Beyond the NanoCT slices, the reduction of noise and edge enhancement due to Paganin's phase retrieval affects the corresponding grey value histograms in Fig. 7.4g-i. The grey values are distributed over a significantly narrower range than the grey values of the NanoCT data in Fig. 7.3.

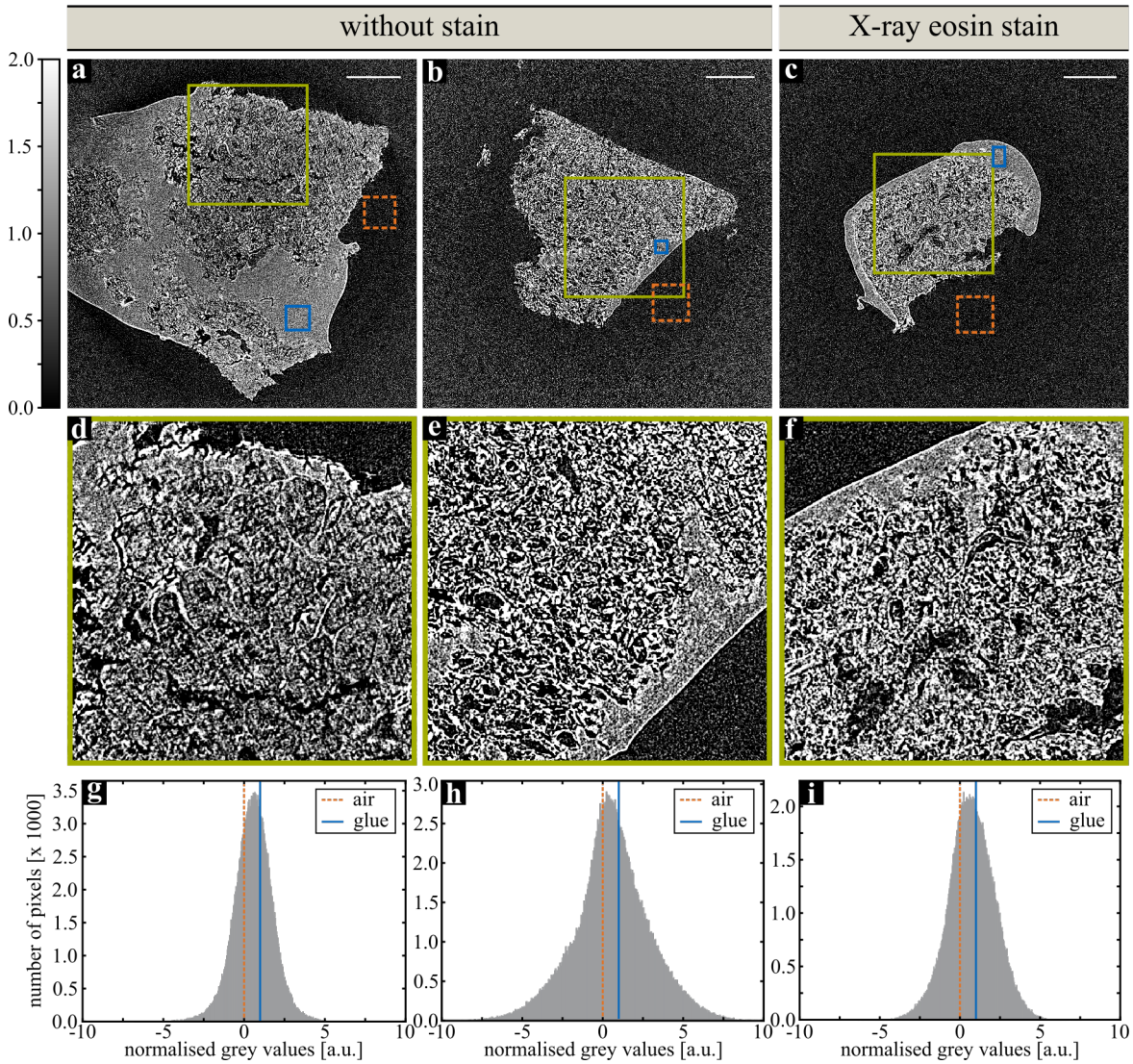

Figure 7.3: **NanoCT Slices of Murine Kidney Tissue without and with X-ray Eosin Stain without Phase Retrieval.** (a) - (c) NanoCT slices of unstained tissue (a,b) and X-ray eosin stained tissue (c) with a similar effective voxel size and a similar propagation distance (mean effective voxel size: $v_{\mathrm{eff,mean}} \approx 406\,\mathrm{nm}$, source-detector distance: $d_{\mathrm{sd}} \approx 400\,\mathrm{mm}$). The slices were normalised to the mean value of air (orange dashed ROI), which was set to zero, and the mean grey value of superglue (blue ROI), which was set to one. (d) - (f) Enlarged images of the green ROIs in panels (a) - (c). (g) - (i) Histograms of the respective grey value distribution of the enlarged images in (d) - (f). Scalebars: 100 µm.

Furthermore, the histograms of the phase-retrieved data comprise two peaks. One peak is centred around zero and, thus, corresponds to air. The second peak is located roughly at one, which corresponds to superglue and soft tissue.[1]

A closer look at the histograms in Fig. 7.4g and h reveals that most grey values in the right grey value peak lie below the grey level of the superglue ROI. This reflects the observation from the NanoCT slices in Fig. 7.4a and b, where soft tissue appears darker than superglue. In a similar manner, a non-negligible proportion of grey values surpass the grey value of superglue in the histogram (Fig. 7.4i) corresponding to the NanoCT slice in Fig. 7.4f, where some soft tissue regions appear brighter than superglue.

[1]The energy-dependent material constants δ and μ of superglue and soft tissue show a very similar behaviour in the energy range of the NanoTube. This is illustrated in Fig. A.2.

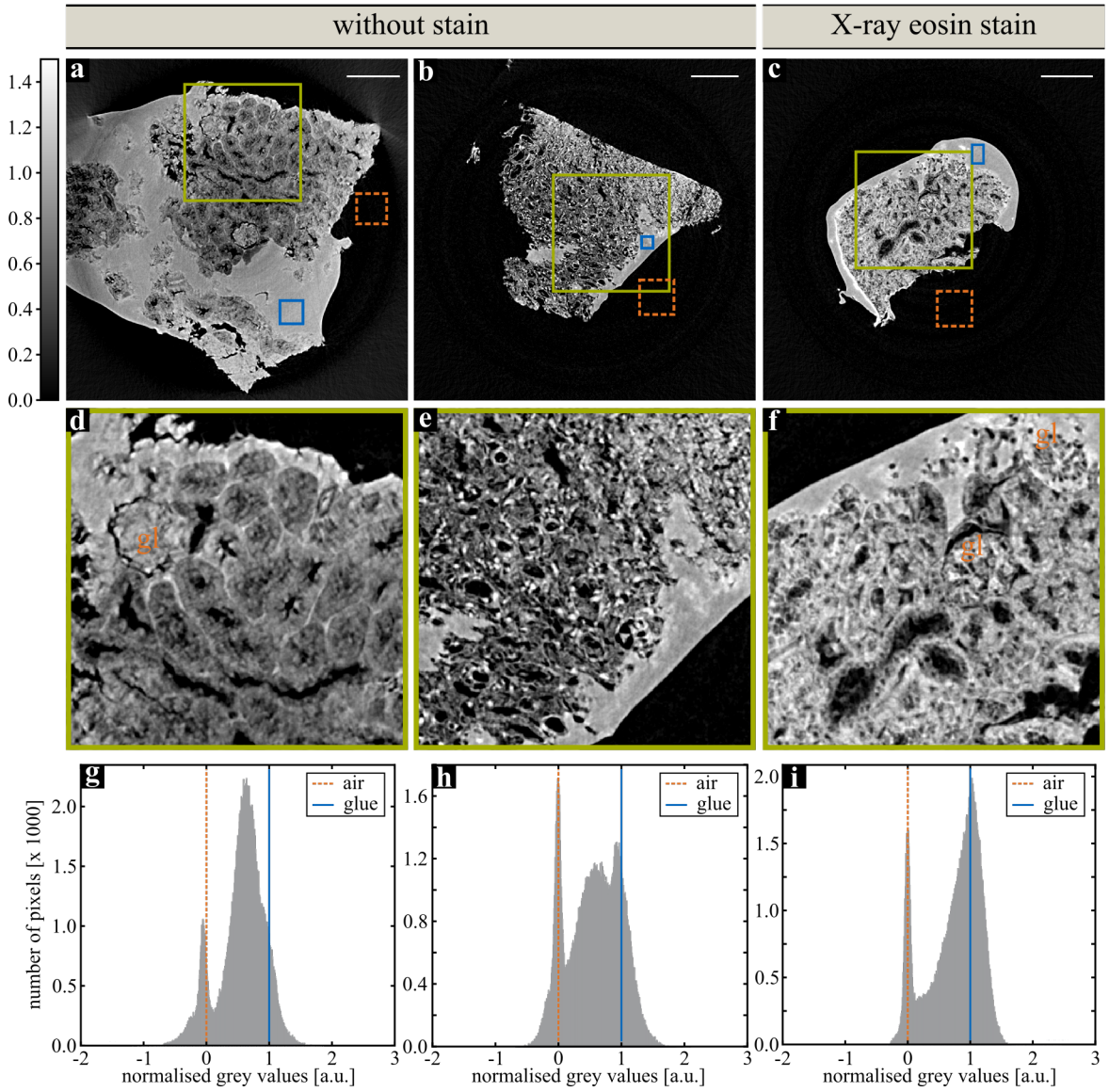

Figure 7.4: **NanoCT Slices of Murine Kidney Tissue without and with X-ray Eosin Stain with Paganin's Phase Retrieval.** (a) - (c) NanoCT slices of unstained tissue (a,b) and X-ray eosin stained tissue (c) with a similar effective voxel size and a similar propagation distance (mean effective voxel size: $v_{\text{eff,mean}} \approx 406\,\text{nm}$, source-detector distance: $d_{\text{sd}} \approx 400\,\text{mm}$). The slices were normalised to the mean grey value of air (orange dashed ROI), which was set to zero, and the mean grey value of superglue (blue ROI), which was set to one. (d) - (f) Enlarged images of the green ROIs in panels (a) - (c). (g) - (i) Histograms of the respective grey value distribution of the enlarged images in (d) - (f). Legend: gl: glomerulus. Scalebars: 100 µm.

7.4.2 Study of Human Skin Tissue

For a more comprehensive analysis of propagation-based phase effects versus X-ray staining for contrast enhancement, the previous assessment strategies used for the murine kidney samples are translated to another type of tissue: human skin.
Again, NanoCT data of unstained and X-ray eosin stained CPD samples are evaluated. The main focus of this evaluation lies on contrasts and grey level distributions. To learn more about the anatomy of human skin on a cellular level, the reader is invited to read Chapter 9.3.

For this study, NanoCT data were selected with similar propagation distances and an effective voxel size of $v_{\text{eff}} \approx 440\,\text{nm}$. The evaluation is performed twice for the same NanoCT data sets, but with different image processing applied: without phase retrieval (Fig. 7.5) and with Paganin's algorithm (Fig. 7.6). As for the previous NanoCT results in Fig. 7.3 and 7.4, a normalisation is performed on the NanoCT slices and the grey value of air is redefined as zero (orange dashed ROI). Here, however, only one of the two NanoCT data sets showed a region of superglue. Hence, the second normalisation ROI, for which the grey value was set to one, was defined inside the epidermis layer instead (Fig. 7.5, Fig. 7.6 blue ROI).

Figure 7.5 displays the resulting NanoCT data without phase retrieval. Both NanoCT slices in Fig. 7.5a, b exhibit a high level of noise and distinct edge enhancement. This hampers a clear differentiation between different tissues and merely allows for identifying the rough boarder between epidermis and dermis (Fig. 7.5 ed, der) or the interface between superglue and tissue in Fig. 7.5b.
Moreover, even stronger noise can be observed at the edges of the reconstructed slices due to undersampling (Fig. 7.5a, b).
The histograms of both NanoCT slices show one single symmetric peak with a Gaussian-like shape and a wide spread of grey values. This Gaussian-like grey value peak is wider for the NanoCT slice in Fig. 7.5b.

Applying Paganin's phase retrieval to the NanoCT projection images leads to the data presented in Fig. 7.6. The resulting NanoCT slices are characterised by a lower noise level and by the absence of any detectable edge enhancement. Thereby, the previously obscured tissue structures are now clearly discernible in the NanoCT slices of both the unstained and the stained tissue specimen. Nevertheless, the NanoCT slice depicting the stained tissue sample provides a larger variation of grey values throughout the different tissue layers in the skin.

Comparing the tissue morphologies in Fig. 7.6a and b, the epidermis appears rather similar, while the dermis looks very different in the two images (Fig. 7.6 ed, der). Moreover, the dermis region and the inner layer of the epidermis, conventionally referred to as stratum basale [Patton, 2014b], appear slightly brighter than the rest of

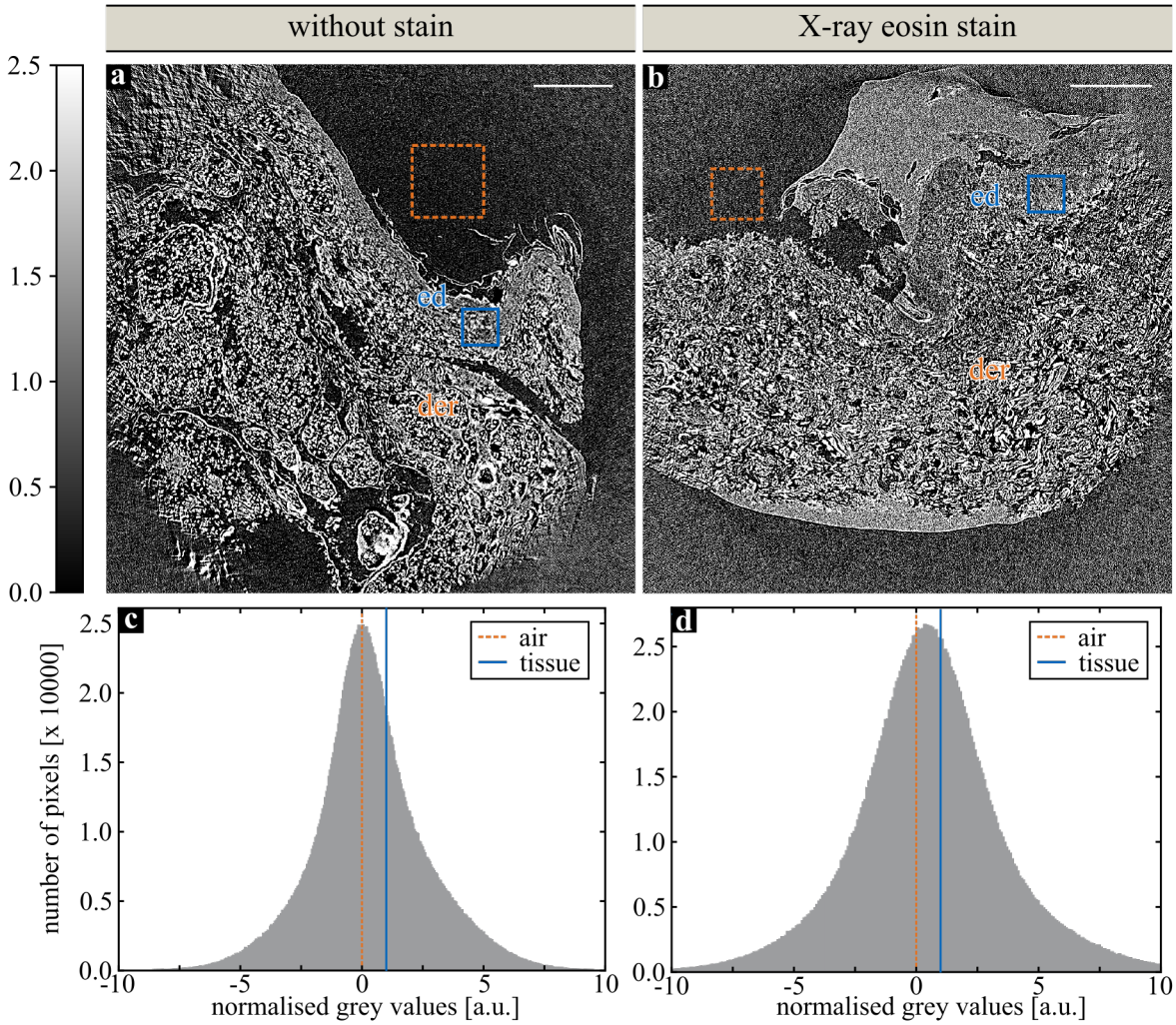

Figure 7.5: **NanoCT Slices of Human Skin Tissue without and with X-ray Eosin Stain without Phase Retrieval.** (a) - (b) NanoCT slices of unstained tissue (a) and X-ray eosin stained tissue (b) with a similar effective voxel size and a similar propagation distance (mean effective voxel size: $v_{\text{eff,mean}} \approx 440\,\text{nm}$, source-detector distance: $d_{\text{sd}} \approx 400\,\text{mm}$). The slices were normalised to air (orange dashed ROI), where the grey value was set to zero, and the mean grey value of a tissue layer in the epidermis (blue ROI), which was set to one. (c) - (d) Histograms of the respective grey value distribution of the images in (a,b). Legend: der: dermis, ed: epidermis. Scalebars: 100 µm.

the epidermis for the X-ray eosin stained tissue (Fig. 7.6b). In the NanoCT slice of the unstained tissue (Fig. 7.6a), the epidermis exhibits rather uniform grey values and the dermis region shows completely different substructures than the NanoCT slice of the stained skin specimen.

Regarding the grey value distribution in the histograms, the values in the phase-retrieved data in Fig. 7.6 are spread over a much smaller range than previously in the NanoCT data without phase retrieval. Both histograms (Fig. 7.6c, d) show two connected main peaks with a third small elevation situated in between.
The left peak is representative for air. In this regard, it is noticeable that the air peak in Fig. 7.6d appears not perfectly aligned with the normalisation, but is slightly shifted towards larger grey values.
The right peak of the histogram in Fig. 7.6c is centred around the grey value of the normalisation ROI in the epidermis. The darker grey values between zero and one most likely correspond to the darker dermis layer, shown in Fig. 7.6a.
The histogram in Fig. 7.6d shows an additional considerable amount of counts above the normalisation grey value inside the epidermis. These grey values correspond to the brighter regions in Fig. 7.6b, such as superglue, the inner layer of the epidermis and parts of the dermis.

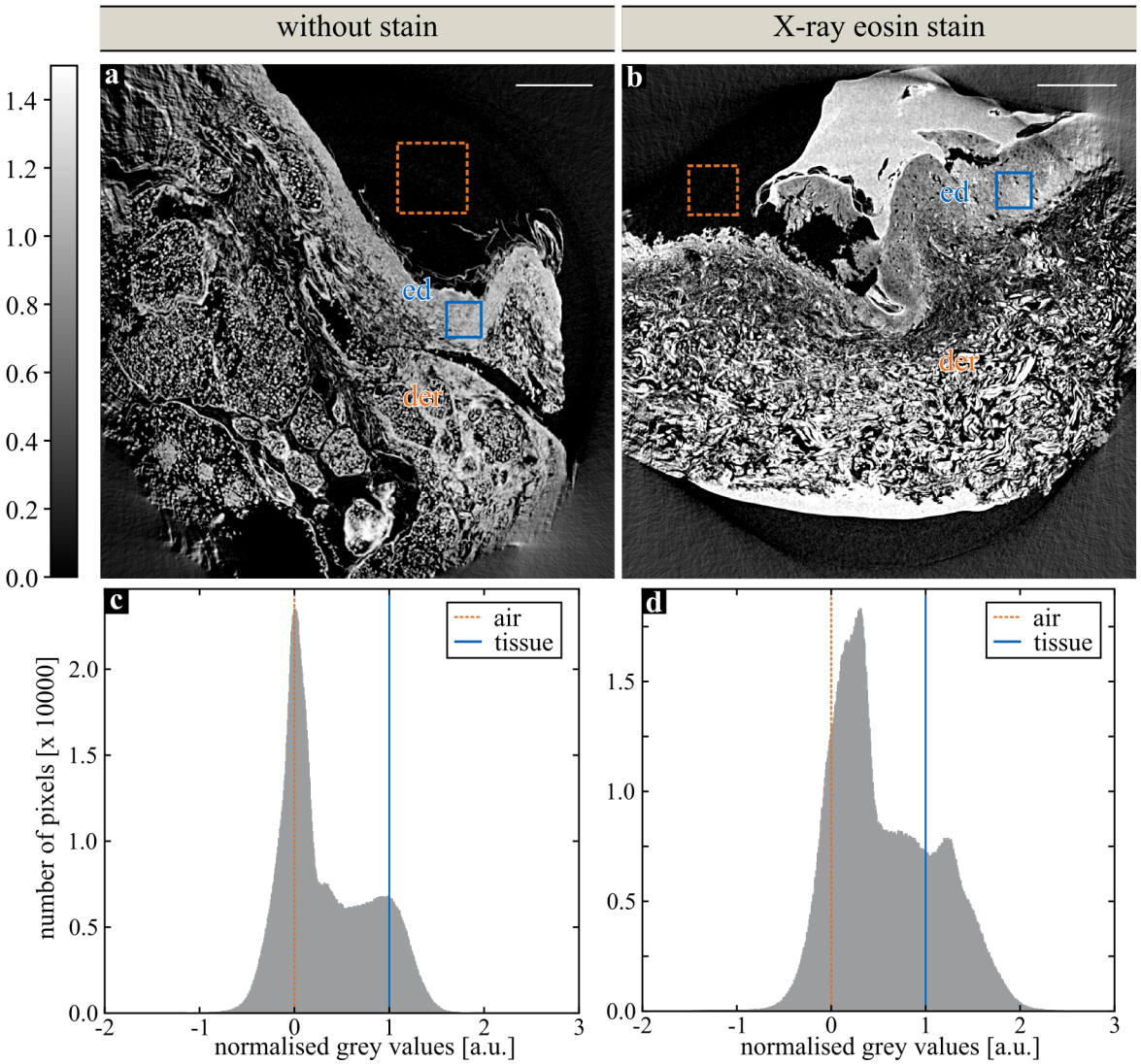

Figure 7.6: **NanoCT Slices of Human Skin Tissue without and with X-ray Eosin Stain with Paganin's Phase Retrieval.** (a) - (b) NanoCT slices of unstained tissue (a) and X-ray eosin stained tissue (b) with a similar effective voxel size and a similar propagation distance (mean effective voxel size: $v_{\mathrm{eff,mean}} \approx 440\,\mathrm{nm}$, source-detector distance: $d_{\mathrm{sd}} \approx 400\,\mathrm{mm}$). The slices were normalised to air (orange dashed ROI), where the grey value was set to zero, and the mean grey value of a tissue layer in the epidermis (blue ROI), which was set to one. (c) - (d) Histograms of the respective grey value distribution of the images in (a,b). Legend: der: dermis, ed: epidermis. Scalebars: 100 µm.

7.5 Discussion

This chapter inspected propagation-based phase effects in the NanoCT and the resulting contrast enhancement gained through phase retrieval and X-ray staining.

In the beginning of the chapter, some theoretical considerations regarding propagation-based phase effects in the NanoCT were performed. The resulting estimations predicted edge enhancement with increasing strength towards larger propagation distances, towards smaller electron spot sizes in the NanoTube and towards smaller effective voxel sizes in the NanoCT data.

In the subsequent experimental studies, there was a handful of aspects which were observed in all NanoCT data sets. The NanoCT slices without phase retrieval (Fig. 7.1a, b, e, f, Fig. 7.3, Fig. 7.5) exhibited propagation-based phase effects in the form of edge enhancement, particularly at interfaces from solids to air.
Next to noise, the edge enhancement was observed to promote a Gaussian-like grey value distribution in the NanoCT data. This influence of edge enhancement is capable of overpowering the attenuation contrast for larger propagation distances. This was demonstrated particularly well during the study of different propagation distances (Fig. 7.1). While the grey value distribution in Fig. 7.1i still displayed a slight second elevation from the attenuation signal of the stained soft tissue beside the main peak around zero, this attenuation signal was completely lost in the increased edge enhancement signal in the histogram for the large propagation distance (Fig. 7.1k). Here, the histogram merely comprised one Gaussian-shaped peak centred around zero. The same effect was experienced in the NanoCT data in Fig. 7.3 and Fig. 7.5 for both the unstained and the stained tissue specimens.
Moreover, the histograms of the NanoCT data displaying murine renal tissue in Fig. 7.3g-i are in agreement with the theoretical predictions regarding a relation between the NanoTube electron spot size and the strength of the propagation-based phase effects. The histogram in Fig. 7.3h showed the widest spread in the grey value distribution, indicating strong edge enhancement, while featuring the smallest electron spot (Table 7.1). This finding is further supported by the data in Fig. 7.5, where the wider histogram spread again coincided with a smaller electron spot.
Applying Paganin's phase retrieval to the NanoCT data had a dampening effect on the noise and the edge enhancement, which caused increased soft-tissue contrast in the resulting phase-retrieved data (Fig. 7.1c, d, g, h, Fig. 7.4, Fig. 7.6). Furthermore, the dampening of noise and edge enhancement via phase retrieval induced alterations in the corresponding histograms. The overall spread of the grey value distribution was reduced compared to the NanoCT data without phase retrieval and instead of one large peak around zero, the histogram showed two grey value peaks: one for air, and one for superglue/soft tissue. This further illustrates the contrast enhancement of soft tissues

compared to air through phase retrieval.

Regarding the first experimental study, NanoCT data with different propagation distances were inspected. The results clearly showed, that the propagation distance has an impact on the magnitude of the edge enhancement. As Fig. 7.1a, b illustrated, the edge enhancement increases for larger propagation distances. This further confirmed the theoretical prediction based on the TIE.
In the phase-retrieved NanoCT data (Fig. 7.1c, d, g, h), there was no remarkable gain in contrast through a larger propagation distance, but rather a higher level of detail due to the higher resolution. In this context, it should be noted, though, that the choice of the filtering strength ξ in Paganin's phase retrieval (Eq. 7.6) plays a central role in determining the final contrast and grey value distribution in the phase-retrieved NanoCT slices. Therefore, it is difficult to draw a fair comparison between the NanoCT slices in Fig. 7.1c, d, which require different filtering strengths ξ during phase retrieval.

Hence, for the subsequent analysis of NanoCT data featuring unstained tissue versus X-ray eosin stained tissue, similar propagation distances were selected and the same ξ-value was chosen during phase retrieval. For this study, murine renal tissue and human skin tissue were used. Despite the differences between these tissues regarding structure and composition, similar observations were made.
With respect to the overall soft-tissue contrast in the phase-retrieved NanoCT slices, there was a relatively small difference between the tissue specimens without staining and the tissue processed with the X-ray eosin stain (Fig. 7.4, Fig. 7.6). In the corresponding histograms, the grey value distributions were slightly more extended and the shape of the soft tissue peak was defined a little better for the stained tissue.
This does not match well with previous findings from microCT scans of wet murine renal tissue, where both microCT slices and the histograms showed an immense boost in soft-tissue contrast after application of the X-ray eosin stain (Fig. 7.2) [Busse, 2018b]. There are two potential reasons for these different observations. First of all, Paganin's phase retrieval increases the soft-tissue contrast in the NanoCT data regardless of the X-ray stain. This may contribute to a more similar appearance of the unstained and stained NanoCT data. The second explanation can be drawn from the dehydration series prior to CPD. In the dehydration series, the sample is exposed to an increasing concentration of ethanol, which might wash out large quantities of eosin from the previously X-ray eosin stained tissue specimens.

In the assessment of the contrast, the superglue regions in the NanoCT data sets were very valuable as a reference. Like PMMA, superglue has a similar complex refractive index as soft tissue and is, thus, well suited to mimic the attenuation and phase shift induced by soft tissue samples [Schoonjans, 2011].[2]

[2]Figure A.2 displays the attenuation and the phase coefficient (μ, δ) of superglue next to the values for PMMA and soft tissue over the typical energy range of the NanoTube spectrum.

In the phase-retrieved NanoCT slices in Fig. 7.4, only the stained tissue specimens contained areas which reached similar or brighter grey values than superglue, whereas unstained tissues were mostly darker than the neighbouring superglue region. The NanoCT data set of the unstained skin tissue specimen, however, did not include any superglue area. Thus, such an evaluation was not possible in this case. Moreover, even the stained phase-retrieved skin tissue specimen led to NanoCT images which only exhibited some regions with a grey value as high or higher than superglue (Fig. 7.6b, d).

In some of the NanoCT slices, a gradient towards darker grey values in the centre was visible (Fig. 7.3a, d, Fig. 7.4a, d, and Fig. 7.5a, b). This is a reconstruction artefact, which appears if a sample exceeds the FOV. Furthermore, regions outside of the detector FOV, such as the diagonals in the reconstructed NanoCT slices, were included in the histogram of Fig. 7.5 and 7.6. These two aspects directly influence the corresponding histograms. For instance, the histogram of stained skin in Fig. 7.6 exhibits a rather wide and slightly shifted air peak. This probably originates from deviating grey values and higher noise levels due to undersampling artefacts in the reconstructed slice outside the detector FOV.

Apart from the overall contrast, the accuracy of reproducing the tissue morphology in a sample is a central criterion for evaluating the NanoCT data. In this respect, it was remarkable how much of the tissue architecture was visualised in the NanoCT slices via mere propagation-based phase contrast without the involvement of any X-ray staining. Despite both unstained tissue and X-ray eosin stained tissue enabling the visualisation of relevant tissue structures, the NanoCT data of the stained tissue provide a larger amount of information. The specific binding behaviour of the X-ray eosin stain highlights different tissue structures in the NanoCT slices compared to unstained tissue. This generates a different appearance of the NanoCT slices even for the same tissue types.
In the murine renal tissue, the X-ray eosin stain highlighted the cytoplasm and, thereby, allowed for indirectly visualising the cell nuclei as black dots (Fig. 7.4f). This was not feasible for the unstained tissue specimens (Fig. 7.4d, e).
In the human skin tissue specimens (Fig. 7.6), the NanoCT slices of the stained tissue pieces, as opposed to the NanoCT slices of unstained tissue, showed sub-layers inside the epidermis and highlighted the network of loose connective tissue inside the dermis.

7.6 Conclusion and Outlook

The studies in this chapter revealed multiple aspects about the behaviour of propagation-based phase effects in the NanoCT and, thus, promote a better understanding of the physically relevant imaging mechanisms and the role of X-ray staining in the NanoCT data.
First, it was shown that an alteration of the propagation distance has a significant effect on the strength of the edge enhancement in the NanoCT data. Thereby, the gain in soft-tissue contrast in the phase-retrieved NanoCT data strongly depends on the filtering strength in Paganin's phase retrieval.
Comparative analyses of unstained and X-ray eosin stained tissue in the NanoCT yielded both expected and rather unexpected results. The results indicated a correlation between the electron spot size and the edge enhancement in the NanoCT data. Beyond that, it was rather striking how much information on the tissue morphology was already gained merely through propagation-based phase retrieval, without applying any X-ray staining at all. A normalisation of the NanoCT slices employing superglue as a reference material showed that the X-ray eosin stain has a significantly smaller impact on the overall soft-tissue contrast in NanoCT data of CPD specimens than in microCT data of wet tissue. Nevertheless, it was evident that the X-ray eosin stain adds another layer of information by specifically binding to certain tissue structures such as the cytoplasm or connective tissue. Thus, it allows for not only reproducing the tissue density as propagation-based phase retrieval does in soft tissues, but to access certain structural or functional entities throughout the tissue, such as the cell nuclei.

While the previous studies provided many new insights, there is still room for further improvements, which may serve as inspiration for future projects. First of all, the study only covers a small amount of data. In imaging with the NanoCT, a frequent observation is that following well-defined procedures with respect to sample preparation, acquisition, and image processing still frequently leads to rather different appearances in the resulting NanoCT volumes. It is common knowledge that there can always be artefacts from sample processing or from mechanical or thermal instabilities during the acquisition process which may impair the information in the resulting NanoCT data.

In some cases, a clear judgement on the image contrast was difficult despite the normalisation. There was a substantial time span between the sample preparation and acquisition of the stained and the unstained murine tissue specimens. For instance, this led to the use of superglue from two different manufacturers for the murine tissue specimens. It should be noted though that this hardly had any impact on the complex refractive index of the superglue and did not affect the NanoCT results.[3] However, there was no superglue at all in the NanoCT data set of unstained skin, which compli-

[3] More information can be found in the appendix in Fig. A.2.

cated a proper normalisation of the NanoCT slices. Beyond that, it should be taken into account that longer exposure times were used for acquiring the projection images of the unstained tissue pieces (Table 7.1).

For improved statistics, I propose further research on this subject with a larger amount of tissue samples, a greater variety of tissue types and diverse X-ray stains. It is highly recommended to select neighbouring pieces from the same tissue specimen for the study and to include superglue or a PMMA rod into the FOV of the NanoCT scan, to achieve optimum comparability.
Beyond analyses of microCT data of unstained and stained tissue, the development of novel staining routines in the future should always involve a comparison of phase-retrieved NanoCT data of unstained and stained CPD tissue from the same tissue specimen. Furthermore, the same acquisition and image processing parameters should be chosen and a normalisation should be performed on the NanoCT slices using a reference material, such as superglue or PMMA.
For understanding the effect of an X-ray stain on NanoCT data, a smart strategy is to focus on the attenuation signal. This requires a reduction of phase-related contributions in the image signal as far as possible. At synchrotron facilities, this is often done by destroying the beam coherence with a dynamically-changing diffuser. According to the definition of the coherence lengths, it is expected that this mostly affects the transverse coherence. In the NanoCT, propagation-based phase imaging is predominantly based on the transverse coherence of the system through the small X-ray source spots of the NanoTube, as it was shown in the beginning of this chapter. Empirical results, however, showed that such a diffuser has no measurable impact on the resulting NanoCT data (Fig. A.3, Fig. A.4).
A better technique of reducing propagation-based phase effects while preserving the image resolution may be resin embedding of the sample. Resin embedding widely removes tissue-air interfaces, which are associated with abrupt changes in the complex refractive index and conventionally generate the majority of propagation-based phase effects in the NanoCT data. This is further demonstrated in Chapter 8.

7.7 Materials and Methods

7.7.1 Theoretical Considerations

Coherence: The longitudinal coherence (Eq. 3.33) is defined by the wavelength bandwidth $\Delta\lambda$ of the source spectrum and the mean wavelength of the spectrum λ:

$$L_\mathrm{l} = \frac{\lambda^2}{\Delta\lambda} \geqslant \lambda. \tag{7.8}$$

At the acceleration voltage $\mathrm{U_{acc}} = 60\,\mathrm{kV}$, which has been used for all NanoCT scans so far, the NanoTube emits a continuous spectrum in an energy interval of $E \in [5\,\mathrm{keV}; 60\,\mathrm{keV}]$. This is equivalent to a wavelength bandwidth of $\Delta\lambda \approx 2.3\,\text{Å}$. The mean X-ray energy of such a source spectrum is $E_\mathrm{mean} \approx 22.1\,\mathrm{keV}$, which corresponds to a wavelength of $\lambda \approx 0.56\,\text{Å}$. Thus, we obtain a longitudinal coherence length of:

$$L_\mathrm{l} \approx 0.14\,\text{Å}. \tag{7.9}$$

For a smaller acceleration voltage of $\mathrm{U_{acc}} = 30\,\mathrm{kV}$, we obtain a a wavelength bandwidth of $\Delta\lambda \approx 2.06\,\text{Å}$, a mean X-ray energy of $E_\mathrm{mean} \approx 13.3\,\mathrm{keV}$ and, thus, a mean wavelength of $\lambda \approx 0.93\,\text{Å}$. Hence, the longitudinal coherence length for $\mathrm{U_{acc}} = 30\,\mathrm{kV}$ is:

$$L_\mathrm{l} \approx 0.90\,\text{Å}. \tag{7.10}$$

According to Eq. 3.32, the transverse coherence length can be determined from the X-ray source spot radius r_x, the distance of the source to the sample exit point d and the X-ray wavelength λ:

$$L_\mathrm{t} = \frac{d \cdot \lambda}{2 \cdot r_\mathrm{x}} \geqslant A \tag{7.11}$$

At an acceleration voltage of $\mathrm{U_{acc}} = 60\,\mathrm{kV}$, the NanoTube achieves typical source spots of $r_\mathrm{x} \approx 150\,\mathrm{nm}$ and a mean wavelength of $\lambda \approx 0.56\,\text{Å}$. Hence, for the typical distance of $d \approx 2\,\mathrm{mm}$, we obtain for the transverse coherence length:

$$L_\mathrm{t} \approx 373\,\mathrm{nm}. \tag{7.12}$$

The sample structure size A may be interpreted as the effective voxel size in a NanoCT data set.

Imaging Regime: To distinguish between the different imaging regimes (contact region, Fresnel region, Fraunhofer region), the following term (Eq. 3.23) is studied:

$$\frac{a^2}{\lambda}, \tag{7.13}$$

with a the structure size between which two wavelets interfere and λ the wavelength of the incident X-rays. This expression is then compared to the propagation distance R:

$$R = d_{\mathrm{sd}} - d_{\mathrm{sa}}, \tag{7.14}$$

with d_{sd} the source-detector distance with a typical value of 400 mm and d_{sa} the distance between the source and the tomography axis which typically lies in the range of 1 mm. Thus, we obtain for the propagation distance:

$$R = 399\,\mathrm{mm}. \tag{7.15}$$

At the standard acceleration voltage $\mathrm{U_{acc}}$= 60 kV of past NanoCT scans, we obtain a mean wavelength of $\lambda \approx 0.56$ Å. The structure size a in the NanoCT can be interpreted as the radius of the first Fresnel zone r_{F} [Cloetens, 1999]:

$$r_{\mathrm{F}}^2 = \lambda \cdot \frac{R \cdot d_{\mathrm{sd}}}{R + d_{\mathrm{sd}}}. \tag{7.16}$$

Inserting the values for R and d_{sd}, leads to the following result:

$$r_{\mathrm{F}} = \sqrt{0.056\,\mathrm{nm} \cdot \frac{(400\,\mathrm{mm} - 1\,\mathrm{mm}) \cdot 400\,\mathrm{mm}}{800\,\mathrm{mm} - 1\,\mathrm{mm}}} \approx 3.3\,\mu\mathrm{m}. \tag{7.17}$$

This provides us with the following expression for Eq. 7.13:

$$\frac{a^2}{\lambda} \approx \frac{(3.3\,\mu\mathrm{m})^2}{0.056\,\mathrm{nm}} = 195\,\mathrm{mm}. \tag{7.18}$$

Consequently, the propagation distance and the previous term in Eq. 7.18 are of the same order of magnitude:

$$R \approx \frac{a^2}{\lambda}. \tag{7.19}$$

This indicates the Fresnel region or near-field imaging regime.

7.7.2 Tissue Specimens

All studies in this chapter were approved by the local ethics committee. The human renal tissue specimen which is shown in Fig. 7.1 was provided by the Department of Pathology, Klinikum rechts der Isar, Technical University of Munich. The tissue specimen was retrieved from Patient C of the 3D histology study investigating human renal tissue, which is presented in Chapter 9.
The murine renal tissue specimens, which are displayed in Fig. 7.3 and Fig. 7.4, were obtained according to the descriptions in [Busse, 2018b]. Animal housing and organ

removal was provided by the Klinikum rechts der Isar, Technical University of Munich. All involved procedures were performed in accordance with European Union guidelines 2010/63, and the internal animal protection committee of the Center for Preclinical Research of Klinikum rechts der Isar, Munich, Germany (internal reference number 4-005-09). Moreover, the laboratories were examined according to the Organisation for Economic Co-operation and Development (OECD) principles of good laboratory practice.
The skin tissue specimens, which are presented in Fig. 7.5 and Fig. 7.6, were obtained from the Group of Prof. Christina Zielinski of the TranslaTUM and Institute for Virology, Technical University of Munich.

7.7.3 Sample Preparation

The obtained tissue specimens were formalin-fixed with 4% phosphate-buffered saline formalin solution. The samples presented in Fig. 7.1, Fig. 7.3c, f, Fig. 7.4c, f, Fig. 7.5b, d and Fig. 7.6b, d, were processed according to the X-ray eosin staining routine described in Chapter 9 and in [Busse, 2018b; Ferstl, 2020a; Ferstl, 2020b]. The rest of the tissue specimens, shown in this chapter, were merely formalin-fixed with 4% phosphate-buffered saline formalin solution without subsequent staining.
Afterwards, all tissue samples were stored in an ethanol vapour phase. From all tissue specimens, smaller pieces were cut with an edge length in the range of $0.5\,\mathrm{mm} - 1\,\mathrm{mm}$. The tissue pieces were then dehydrated in an ethanol series and critical-point dried (CPD), as explained in [Busse, 2018b; Ferstl, 2020a; Ferstl, 2020b]. The CPD tissue pieces were then mounted with superglue based on cyanoacrylate to a plastic pin. For the sample shown in Fig. 7.3c, f, i and Fig. 7.4c, f, i, the liquid superglue from Pattex (Henkel, Germany) with a density of $\rho_{\mathrm{pattex}} = 1.05\,\mathrm{g/cm^3}$ was used, for the other tissue samples a liquid superglue from Weicon (Germany) was used with a density of $\rho_{\mathrm{weicon}} = 1.07\,\mathrm{g/cm^3}$.

7.7.4 NanoCT Acquisition and Image Processing

For the acquisition of the NanoCT data presented in this chapter, 1,599 evenly distributed projections were recorded over a rotation angle of 360° at an acceleration voltage of 60 kV and a detector threshold of 2.7 keV. The rest of the acquisition parameters are presented in Table 7.1. More details on acquiring a tomography data set using the NanoCT can be found in Section 5.2 and in the Appendix A.1.

The acquired NanoCT projection images were processed and reconstructed according to the routine described in Section 5.3. For projection alignment, the sparsity-metric based algorithm was employed to the NanoCT data presented in Fig. 7.1a, c, e, g,

Figure		7.1		7.3, 7.4			7.5, 7.6	
Panels		a, c, e, g, i, l	b, d, f, h, k, m	a, d, g	b, e, h	c, f, i	a, c	b, d
v_{eff}	[nm]	630	210	390	430	400	450	430
d_{sa}	[mm]	0.76	0.76	0.91	1.01	0.94	1.05	1.01
d_{sd}	[mm]	200	600	400	400	400	400	400
r_{e}	[nm]	360	360	380	250	310	330	320
t_{exp}	[s]	1	8	6	6	3	4	3
$t_{\text{acq,tot}}$	[h]	2	5	4	4	3	3.5	3

Table 7.1: **NanoCT Acquisition Parameters for Investigating Propagation-Based Phase Contrast.** Legend: d_{sa}: distance of the source spot from the tomography axis, d_{sd}: distance of the detector from the source, t_{exp}: exposure time for one projection image, r_{e}: the electron spot radius ($0.5 \cdot$ FWHM) on the X-ray target prior to acquisition, $t_{\text{acq,tot}}$: total acquisition time for the NanoCT volume.

i, l. The remaining data sets in this chapter were aligned using the cross-correlation based approach. Paganin's phase retrieval was applied to the NanoCT data shown in Fig. 7.1c, d, g, h, l, m, Fig. 7.4 and in Fig. 7.6. For the NanoCT data of this chapter, no deblurring according to Guereyev's approach was applied. For Paganin's phase retrieval we introduce the filtering strength ξ with:

$$\xi = d \cdot \frac{\delta}{\mu}, \tag{7.20}$$

whereby d denotes the propagation distance, δ the phase coefficient, μ the attenuation coefficient of the material. This definition is inserted into Eq. 7.5. Thus we obtain the following expression:

$$D_{\phi}(x,y) = -\frac{1}{\mu} \ln\left(\mathfrak{F}^{-1}\left[\frac{\mathfrak{F}[I(x,y)\cdot I_0^{-1}]}{4\pi^2\xi|\vec{w}|^2+1}\right]\right), \tag{7.21}$$

To account for the different propagation distances of the NanoCT data in Fig. 7.1, for the data in Fig. 7.1c, g, l a lower filtering strength was chosen ($\xi = 1$), than for the data in Fig. 7.1d, h, m ($\xi = 20$). Nevertheless, concerning the selection of ξ, here, mostly the visual image quality was regarded. The other NanoCT data were acquired at similar effective propagation distances (Table 7.1) and the same filtering strength of $\xi = 10$ was used.

7.7.5 Post-Processing and Histograms

For Fig. 7.1, corresponding NanoCT slices were selected in both data sets. For this purpose, the image from the data set with the shorter propagation distance of d_{sd} = 200 mm was extracted from a specifically defined ROI. The selected images were then normalised to air as zero (orange ROI) and tissue as one (blue ROI). The histograms were calculated from the NanoCT images in Fig. 7.1a-d.

In Fig. 7.3 and Fig. 7.4, for normalisation a ROI in air (orange ROI) and a ROI in superglue (blue ROI) were established. The mean grey value of air was redefined as zero and the mean value of the superglue ROI was set to one. From these normalised images in Fig. 7.3a-c and Fig. 7.4a-c, enlarged images were extracted from ROIs (green) which include roughly similar proportions of tissue, superglue and air. From these resulting images (Fig. 7.3d-f and Fig. 7.4d-f), the histograms were determined.

For Fig. 7.5 and Fig. 7.6, the displayed NanoCT slices were normalised with air to zero (orange ROI) and tissue to one (blue ROI). The histograms in Fig. 7.5c, d and Fig. 7.6c, d show the grey value distribution of the resulting normalised NanoCT slices.

7.7.6 Scientific Contributions

The concept of this study was devised by Simone Ferstl. The human renal tissue sample, which is shown in Fig. 7.1, was stained and prepared by Toni Bürkner. The staining and sample preparation of the remaining tissue specimens was carried out by Madleen Busse. The microCT data in Fig. 7.2 was acquired by Madleen Busse. The sample shown in Fig. 7.3c, f and Fig. 7.4c, f was mounted and the respective NanoCT data was acquired by Mark Müller. The other tissue samples were mounted by Simone Ferstl and the associated NanoCT data sets were acquired by Simone Ferstl. The image processing, reconstruction and post processing of all NanoCT data sets included in this chapter as well as the creation of the resulting figures and the assignment of histological structures in the figures, was performed by Simone Ferstl.

NanoCT for Correlative Microscopy and Zoology 8

8.1 Introduction

Correlative microscopy allows for visualising the multiscale morphology of biological specimens, by combining several imaging techniques [Bradley, 2016; Caplan, 2011; Lavery, 2014]. Up until recently, generation of 3D data of an entire small biological specimen required most LM and EM techniques to resort to sectioning or other destructive techniques [Schneider, 2012; Gross, 2019]. This, however, affects the resulting data in the form of sectioning and alignment artefacts, such as distortions, and usually prevents isotropic resolutions in 3D [Handschuh, 2013; Giepmans, 2008].

As X-ray CT allows for non-destructively revealing internal 3D structures of a specimen, high-resolution X-ray CT has become increasingly popular in correlative studies [Bradley, 2016; Schneider, 2012; Smith, 2014; Walton, 2015; Bushong, 2014].

Adding a further imaging technique to a correlative microscopy approach is typically associated by the sample undergoing additional processing steps. This not only results in a more tedious and complex sample preparation, but also severely increases the risk for corrupting the sample microstructure. This aspect has motivated researchers to use only a minimum amount of sample processing [Handschuh, 2013; Sombke, 2015; Caplan, 2011].

In this context, Handschuh *et al.* [Handschuh, 2013] investigated a biological specimen which was solely prepared with the standard TEM sample processing protocol in a correlative approach which combined three imaging techniques: microCT, LM and TEM. Their work illustrates the numerous benefits of integrating high-resolution X-ray CT into correlative microscopy work-flows. The microCT device used in their study, however, is not capable of resolving many of the anatomical details in tiny biological animals with body sizes $\leqslant 1\,\mathrm{mm}$. It might be mentioned here that such animals make up the majority of organisms in biology [Gross, 2019].

In this chapter, a correlative study is presented combining the NanoCT with serial-sectioning light microscopy (ss-LM). The study is centred around a tiny meiofaunal sea cucumber, *Leptosynapta* cf. *minuta* (*L.* cf. *minuta*), which was solely prepared for TEM imaging. The TEM sample preparation protocol stipulates among other steps osmium tetroxide post-fixation and resin embedding [Ruthensteiner, 2008].

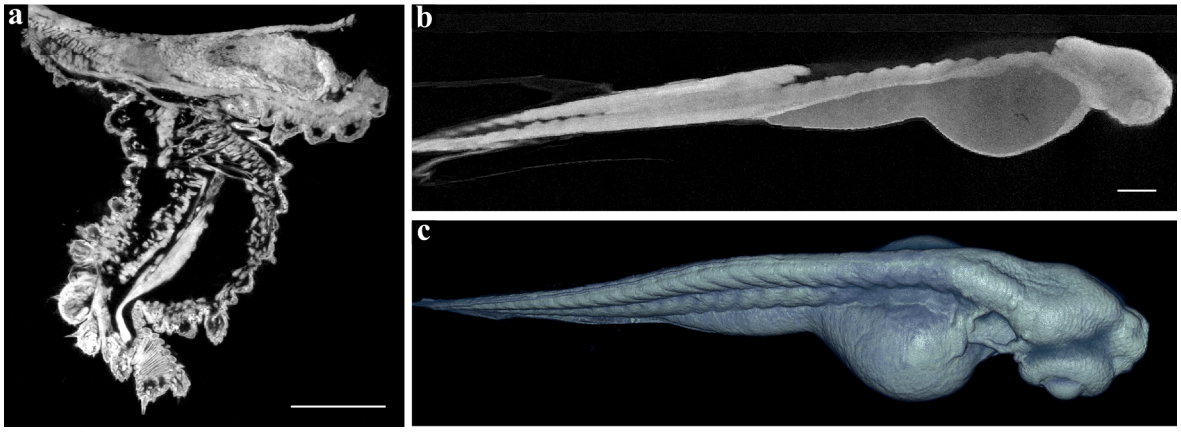

Figure 8.1: **NanoCT Data of Two Zoological Specimens Processed with Different Sample Preparation Techniques.** (a) NanoCT slice of a velvet worm limb prepared with CPD and osmium tetroxide for post-fixation and staining ($v_{\text{eff}} \approx 400\,\text{nm}$). (b) NanoCT slice of a zebrafish embryo 48 h post-fertilisation embedded into agarose and stained with phospho-tungstic acid (PTA) ($v_{\text{eff}} \approx 800\,\text{nm}$). (c) Volume rendering of the same NanoCT data set as in (b). Scalebars: 100 µm. Panel (a) adapted from [Müller, 2019].

In previous works, the NanoCT was successfully applied to study critical-point dried (CPD) and agarose-embedded biological specimens (Fig. 8.1) [Gross, 2019; Müller, 2017; Ferstl, 2018]. As shown in Fig. 8.1a osmium tetroxide, while generally used for post-fixation, qualifies as a proper X-ray stain in providing adequate contrast levels in the NanoCT data. There was, however, no pre-existing NanoCT data of any resin-embedded samples. While studying such samples is no challenge at the resolution range of microCT imaging, it poses a number of new problems for the NanoCT.

In the following, two NanoCT data sets of *L.* cf. *minuta* are presented: one data set was acquired to provide an overview over the entire sea cucumber specimen with an effective voxel size of $v_{\text{eff}} \approx 540\,\text{nm}$, and a high-resolution NanoCT volume ($v_{\text{eff}} \approx 290\,\text{nm}$) was generated for a more detailed investigation of a VOI. Afterwards, the specimen was sectioned to generate two 3D data sets using ss-LM (overview data: 10× objective lens, high-resolution data: 20× objective lens). Based on the NanoCT data, a segmentation is presented, which reveals the internal organ system of the sea cucumber in 3D. A comparative analysis of the NanoCT and ss-LM volumes is performed including a quantitative evaluation of the contrast-to-noise ratio (CNR) and a qualitative evaluation of the resolution. To verify the reproducibility of successfully applying the NanoCT to TEM-prepared samples, a further specimen, in this case a tiny marine snail *Rissoella* cf. *eliator* (*R.* cf. *eliator*), is investigated. In a critical assessment, the merits of integrating the NanoCT into correlative microscopy and its

strengths and weaknesses compared to other imaging techniques are discussed.
For the sake of conciseness, the zoological findings about *L.* cf. *minuta* and *R.* cf. *eliator* are only coarsely outlined. Thereby, only zoological details are included which contribute to a better understanding of the imaging results of this chapter. The publication [Ferstl, 2019] provides a more comprehensive presentation regarding the anatomy of *L.* cf. *minuta* including the findings shown in this chapter. Information on holothurians in general can be found in [Becher, 1906; Buddenbrock, 1912; Clark, 1907; Ehlers, 1997; Jans, 1989; Kerr, 2001; Massin, 2005; Miller, 2017; Stricker, 1985; Vandenspiegella, 1998].

8.2 3D Morphology of *L.* cf. *Minuta*

Up until recently, there was only little information available about *L.* cf. *minuta*, a tiny representative of a sea cucumber with a length of ≈ 1 mm, which is specialised to a meiofaunal lifestyle. Figure 8.2a shows a photograph of a living specimen. It appears rather transparent with denser areas of the calcareous ring, the gut and the epidermal cups (Fig. 8.2a). Apart from these features, only the outline of the animal with its characteristic tentacles can be distinguished.

With the NanoCT, we studied the specimen of *L.* cf. *minuta*, after the typical TEM sample preparation protocol, including post-fixation with osmium tetroxide and resin embedding. To study the internal morphology of *L.* cf. *minuta*, we acquired a NanoCT volume of the entire animal with an effective voxel size of $v_{\text{eff}} \approx 540\,\text{nm}$ without involving sectioning.

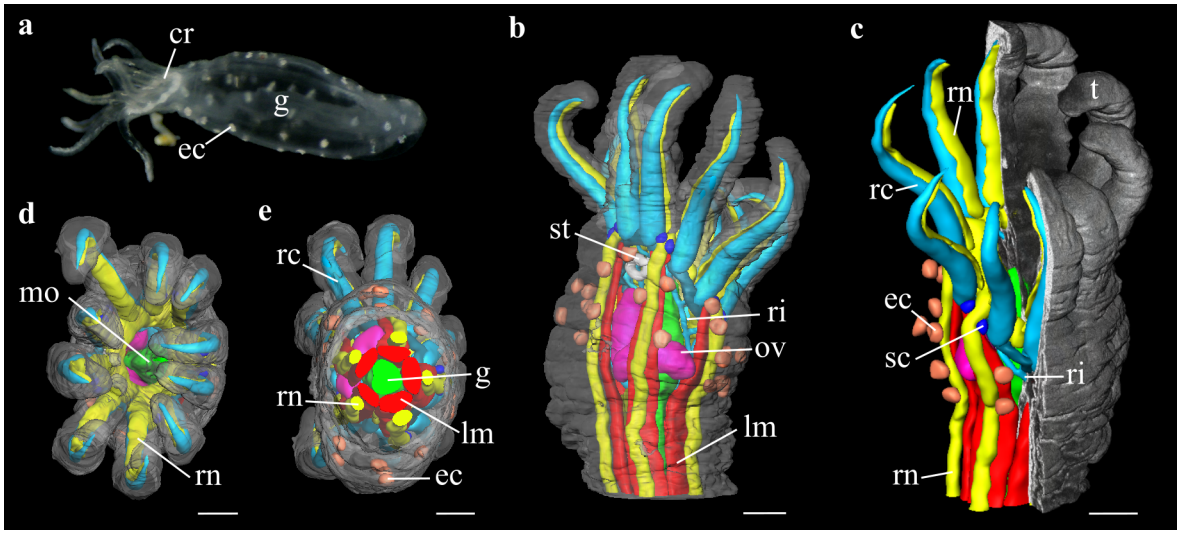

Figure 8.2: **Anatomy of *Leptosynapta* cf. *Minuta*.** (a) Photograph of a living animal. (b)-(e) Volume renderings of the overview NanoCT data from different vantage points revealing a segmentation of the inner organs ($v_{\text{eff}} \approx 540\,\text{nm}$). Legend: cr: calcareous ring, ec: epidermal cups, g: gut, lm: longitudinal muscle, mo: mouth opening, rc: radial canal in tentacle, ri: ring canal, rn: radial nerve, sc: statocyst, st: stone canal, t: tentacle, ov: ovary. Scalebars: 100 µm. Figure adapted from [Ferstl, 2019].

The resulting NanoCT volume provides isotropic resolutions and retains the true proportions of the specimen. While osmium tetroxide was originally devised as a post-fixative in the TEM preparation routine, it also qualifies as a suitable X-ray stain by providing an adequate overall contrast of the specific structures of *L.* cf. *minuta* in the

NanoCT data.
Thereby, the NanoCT volume allows for segmentation of the entire organ system of *L.* cf. *minuta* including delicate structures, such as the ring canal system. The resulting 3D renderings are presented in Fig. 8.2b-e.

Among the anatomical structures, the so-called statocysts were particularly interesting (Fig. 8.2c). A statocyst is composed of a sphere of nervous tissue surrounding a small, freely moving calcareous flake. This calcareous flake is also called a statolith. Thus, a statocyst acts as a mechanoreceptive balance organ [Becher, 1909].

8.3 Comparison of the NanoCT with SS-LM

To compare the NanoCT with ss-LM, two NanoCT data sets were acquired: an overview data set of the entire specimen with $v_{\text{eff}} \approx 540\,\text{nm}$ and a data set with almost twice the magnification with $v_{\text{eff}} \approx 290\,\text{nm}$ of a VOI.
Subsequently, a section series was produced from the same resin-block containing *L.* cf. *minuta* and the sections were stained with methylene blue-azure II to generate two corresponding ss-LM volumes: an overview ss-LM volume of the entire animal using a 10×objective lens and a high-resolution volume of a corresponding VOI as for the NanoCT data with a 20×objective lens. The grey values of the ss-LM data were inverted and adapted for better comparability with the NanoCT data. The resulting corresponding NanoCT and ss-LM volumes were co-registered, whereby the NanoCT volumes served as a reference to retrieve the correct proportions in the ss-LM volumes. In the following, comparative analyses are performed on the co-registered volumes from NanoCT and ss-LM for both magnification regimes.

8.3.1 NanoCT versus SS-LM - Overview Data

Figure 8.3 displays the resulting co-registered overview data from NanoCT and ss-LM imaging. At first sight, the 3D co-registration of the two volumes in Fig. 8.3a appears to be coherent. A second glance, however, reveals slight discrepancies in the co-registered virtual slices through the plane indicated in Fig. 8.3b. The position of the right statocyst in the slices in Fig. 8.3c and d does not match. The full extent of the mismatches is illustrated in an overlay of the two slices from Fig. 8.3c, and d, which is presented in Fig. 8.3e. In Fig. 8.3e, the deviations between the volumes appear to increase towards the upper part of the tentacles.

Despite these deviations, the structures displayed in the slices in Fig. 8.3c, d are sufficiently similar to allow for a comparative evaluation of the data quality in the two volumes. While both slices depict a high level of detail, the quality of the ss-LM data

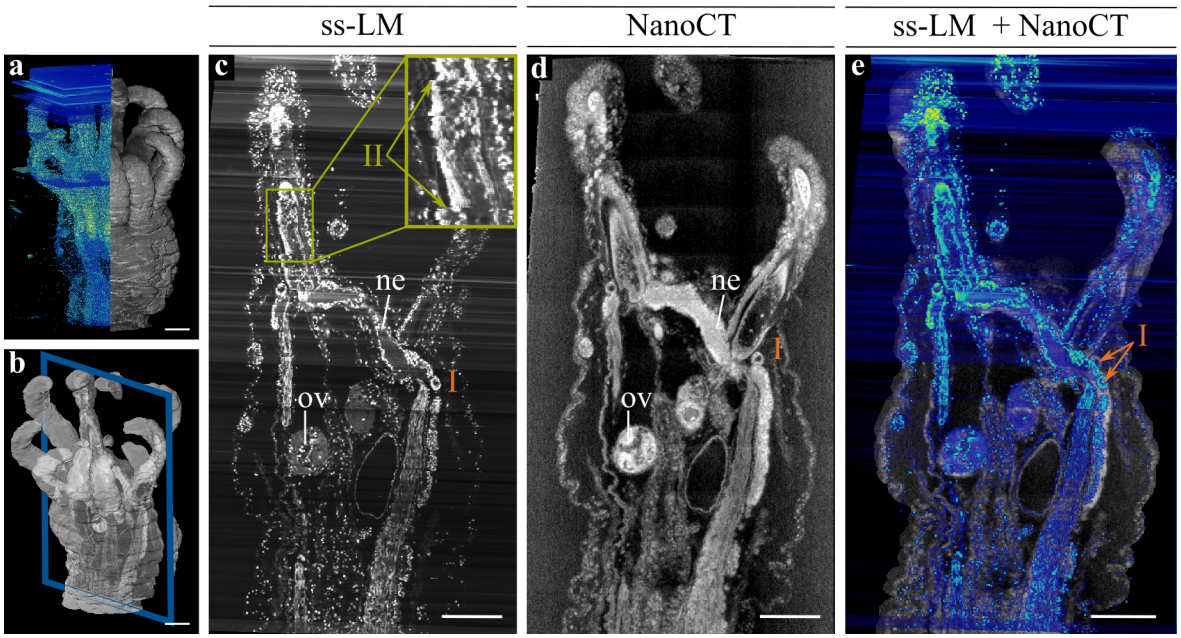

Figure 8.3: **Co-registered Overview Data from SS-LM (10×objective lens) and NanoCT ($v_{\text{eff}} \approx 540\,\text{nm}$).** For better comparability, the grey values of the ss-LM data are inverted. (a) Merged 3D rendering of the ss-LM volume (left, blue-green) and the NanoCT volume (right, grey). (b) Plane of interest, which is depicted in (c), (d) and (e). (c) Virtual section through the aligned ss-LM volume through the plane in (b). (d) Corresponding NanoCT slice through the same plane. (e) Overlay of the ss-LM image from (c) in blue-green and the NanoCT slice from (d) in grey. Legend: I: co-registration mismatch, II: alignment artefact, ne: nervous tissue, ov: ovary. Scalebars: 100 µm. Figure adapted from [Ferstl, 2019].

(Fig. 8.3c) is severely impaired by artefacts.
Brightness fluctuations during LM acquisition cause planar artefacts parallel to the sectioning plane in the ss-LM volume in Figure 8.3a, which are shown as lines in the corresponding virtual slice in Fig. 8.3c. Beyond that, alignment artefacts are visible in the ss-LM slice in Fig. 8.3c. These artefacts are typical to sectioning-based 3D imaging techniques.

Apart from artefacts in the ss-LM data, a difference in the grey value distribution between the NanoCT and the ss-LM slice in Fig. 8.3c, d can be observed. This is particularly striking in the ovaries. In the ss-LM image (Fig. 8.3c), there is a significant difference in the grey value between the ovaries and the nervous tissue. In the NanoCT slice (Fig. 8.3d), however, the ovaries appear just as bright as the nervous tissue. These effects are studied more closely for the high-resolution data in the following section.

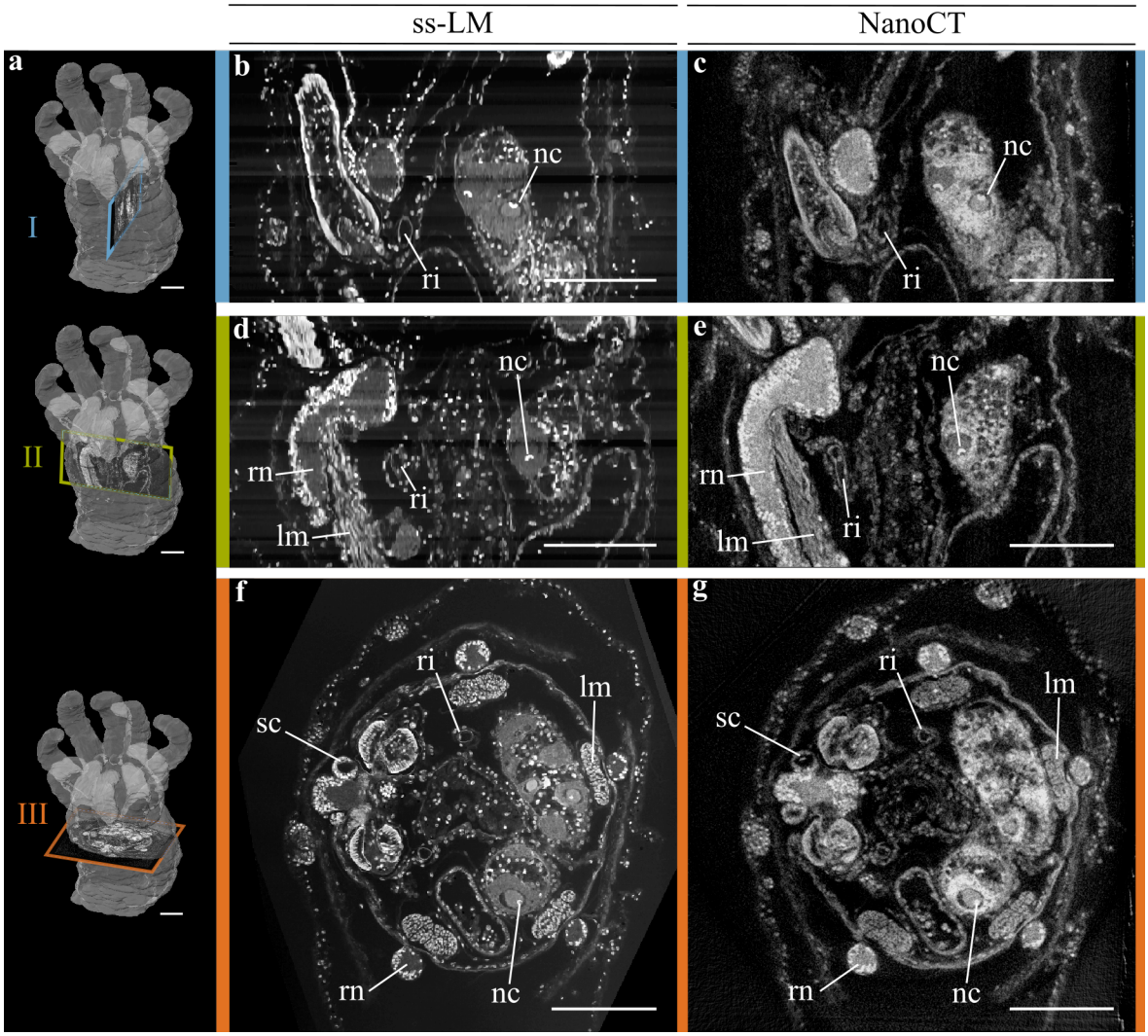

Figure 8.4: **Co-registered High-Resolution Data from SS-LM (20× objective lens) and NanoCT ($v_{\text{eff}} \approx 290\,\text{nm}$).** For better comparability, the grey values of the ss-LM data are inverted. (a) Planes of interest presented in (b)–(g). From top to bottom: I (b), (c), II (d), (e), III (f), (g). (b) Virtual ss-LM slice through plane I. (c) Corresponding NanoCT slice through plane I. (d) Virtual ss-LM slice through plane II. (e) Corresponding NanoCT slice through plane II. (f) Corresponding ss-LM slice through plane III. (g) Corresponding NanoCT slice through plane III. Legend: lm: longitudinal muscle, nc: nucleolus, ri: ring canal, rn: radial nerve, sc: statocyst. Scalebars: 100 µm. Figure adapted from [Ferstl, 2019].

8.3.2 NanoCT versus SS-LM - High-Resolution Data

For a more precise evaluation of the NanoCT with reference to ss-LM, a VOI was selected to generate volume data with an effective voxel size of $v_{\text{eff}} \approx 290\,\text{nm}$. The ss-LM data were acquired using a 20× objective lens. The high-resolution NanoCT and ss-LM data are displayed in Fig. 8.4.

Due to the co-registration, rather similar structures are displayed in the corresponding virtual NanoCT and ss-LM slices. A closer inspection, however, yields again slight discrepancies from a perfect co-registration. This is exemplified in the shape of the radial nerve in Fig. 8.4d compared to Fig. 8.4e.

Compared to the overview ss-LM data (Fig. 8.3c), the brightness and alignment artefacts in the high-resolution ss-LM slices in Fig. 8.4b, d are strongly reduced. In fact, alignment artefacts are hardly visible.

For better comparability and to reduce any unnecessary degradation of the image quality, re-sampling of the volume data was avoided as far as possible. Therefore, the virtual ss-LM slice in Fig. 8.4f was obtained from the original LM images of the section series. Furthermore, for the evaluation of the CNR and the resolution, the LM image from Fig. 8.4f and the corresponding NanoCT slice in Fig. 8.4g are used.

Quantitative Analysis of the CNR

Similar to the overview data, Fig. 8.4 indicates a differing grey value distribution in the NanoCT and in the ss-LM volume. This phenomenon is evaluated in a quantitative manner, by calculating the CNR for different tissues with respect to the resin background in the corresponding slices shown in Fig. 8.4f, g.
The CNR values and the associated mean and standard deviation values for each material are plotted in Fig. 8.5c-e. The mean value of resin was set to zero, so that the mean values of the materials in Fig. 8.5c directly indicate the contrast to resin. The standard deviation values provide a measure for the noise level in the images. The respective ROIs used for determining the CNR are shown in Fig. 8.5a, b.

Regarding the values in Fig. 8.5c-e, the NanoCT data generally provide higher contrast values compared to ss-LM, on the one hand. On the other hand, the NanoCT data are subject to significantly higher noise levels throughout all material ROIs (Fig. 8.5d). Therefore, the tissue type is pivotal when it comes to which imaging technique provides better CNR (Fig. 8.5e).

Regarding the nervous tissue and the cytoplasm of the oocytes, the NanoCT provides considerably higher contrast values which compensate for the high noise levels to result in an overall better CNR compared to ss-LM. In structures with similar contrasts for both imaging techniques, ss-LM provides superior CNRs. This is exemplified by the

CNR of the oocyte nucleus (Fig. 8.5e).

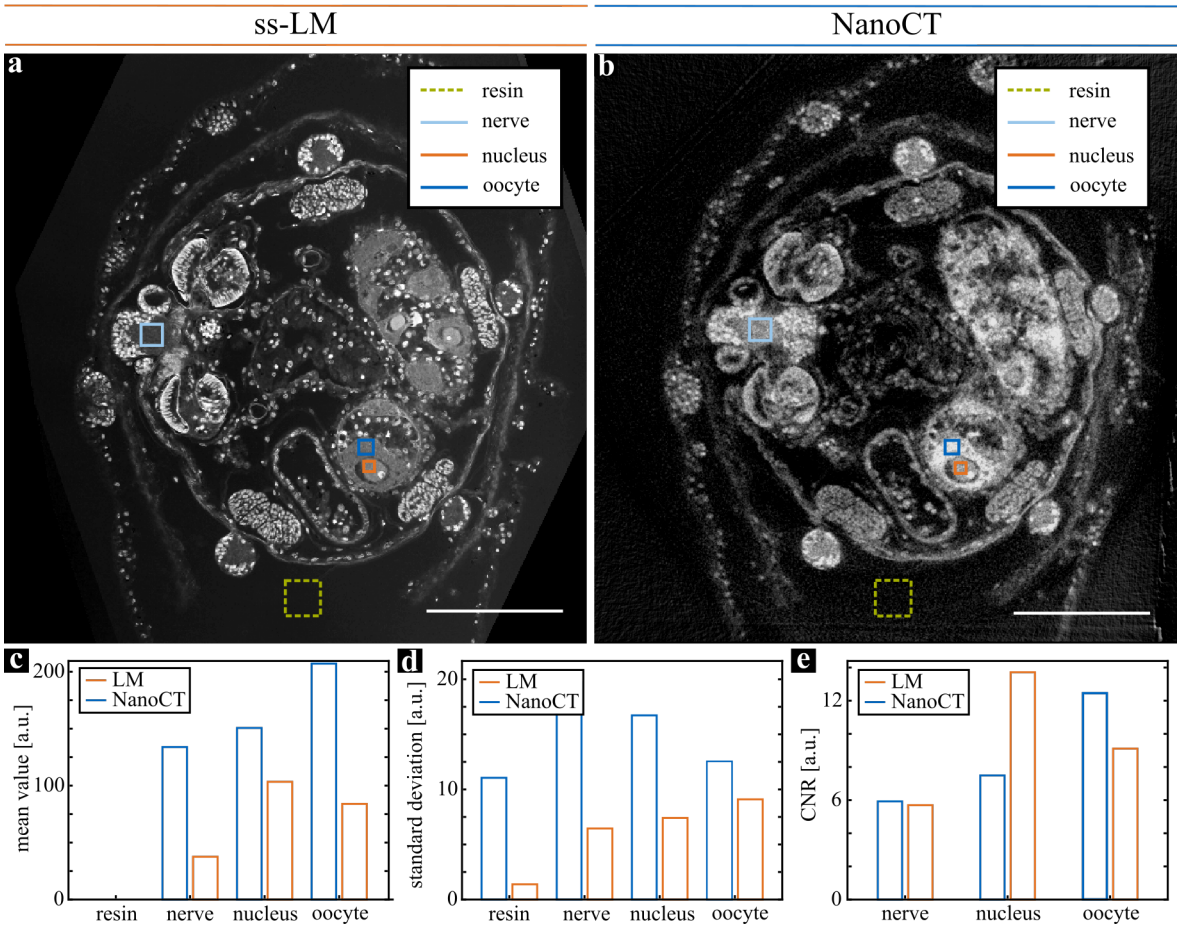

Figure 8.5: **The CNR of the NanoCT versus SS-LM.** (a), (b) Corresponding high-resolution slices from ss-LM and NanoCT with the ROIs used for CNR calculation (NanoCT: $v_{\text{eff}} \approx 290\,\text{nm}$, ss-LM: 20× objective lens). (c) Mean grey value of ss-LM and NanoCT data in the different ROIs. The mean value of resin was set to zero. (d) Noise value in form of the standard deviation of ss-LM and NanoCT data. (e) CNR values with reference to resin calculated from the values in (c) and (d). Scalebars: 100 µm. Figure adapted from [Ferstl, 2019].

Qualitative Analysis of the Spatial Resolution

Apart from the CNR, the spatial resolution in 3D is crucial to assess the two imaging techniques with respect to data quality.

A first view at the slices in Fig. 8.4 yields a high detail level in both volumes. The NanoCT data, just as the ss-LM images, resolve single muscle fibre bundles in the longitudinal muscles, the fine ring canals, the bright cell nuclei in the radial nerves, the precise shape of the nucleoli in the oocytes, and even the statolith inside the statocyst.

A closer look at the ss-LM volume reveals that the highest detail level is obtained in the sectioning plane (Fig. 8.4f), where the resolution is determined by the NA of the used objective lens and the light wavelength. According to the Rayleigh-criterion (Eq. 4.8), the resolution limit of the ss-LM image in the sectioning plane (Fig. 8.4f) is $\delta_x \approx 366\,\mathrm{nm}$ (Table 8.1). Perpendicular to the sectioning plane (Fig. 8.4b, d), the vertical edge length of an effective voxel is defined by the thickness of the sections ($\approx 1\,\mu\mathrm{m}$), setting a limit to the resolution.

In contrast, the NanoCT data provide isotropic resolutions. For the NanoCT data, it is, however, not as easy to estimate the resolution limit, as for the ss-LM data in the sectioning plane.

Here, we want to compare the resolution of the ss-LM volume at its optimum with the isotropic resolution of the NanoCT data. Thus, we consult an ss-LM image in the sectioning plane (Fig. 8.4f) and its corresponding virtual NanoCT slice (Fig. 8.4e). In Fig. 8.6a, b the two selected slices are marked with two perpendicular lines. Along these lines, the grey value distribution will be examined to enable a qualitative comparison of the image resolutions. For better comparability, special care was taken to ensure that the line profiles include the same sample structures.

Determining the resolution quantitatively would require an edge with a well-defined, known shape to allow for deriving the respective edge spread function. Sampling the edge spread function over an angular interval of 360° results in the point spread function (PSF). More information on the PSF and its role as a resolution measure can be found in the introduction of Chapter 6.

For the qualitative resolution assessment, the grey value distributions along the selected line profiles are plotted in Fig. 8.6c and d. In these graphs, the edge profiles of the LM data are distinctively steeper and contain more pronounced peaks. The peaks most likely stem from the bright cell nuclei. This finding complies with the impression obtained from the images in Fig. 8.6a, b, where the cell nuclei appear more clearly defined in the LM image.
Moreover, the higher contrast of nervous tissue in the NanoCT data is illustrated here further. Along the horizontal line (Fig. 8.6c), which goes through the nervous tissue, it can be clearly seen that the cell nuclei are significantly brighter than the nervous tissue in the LM line profile compared to the NanoCT line profile.

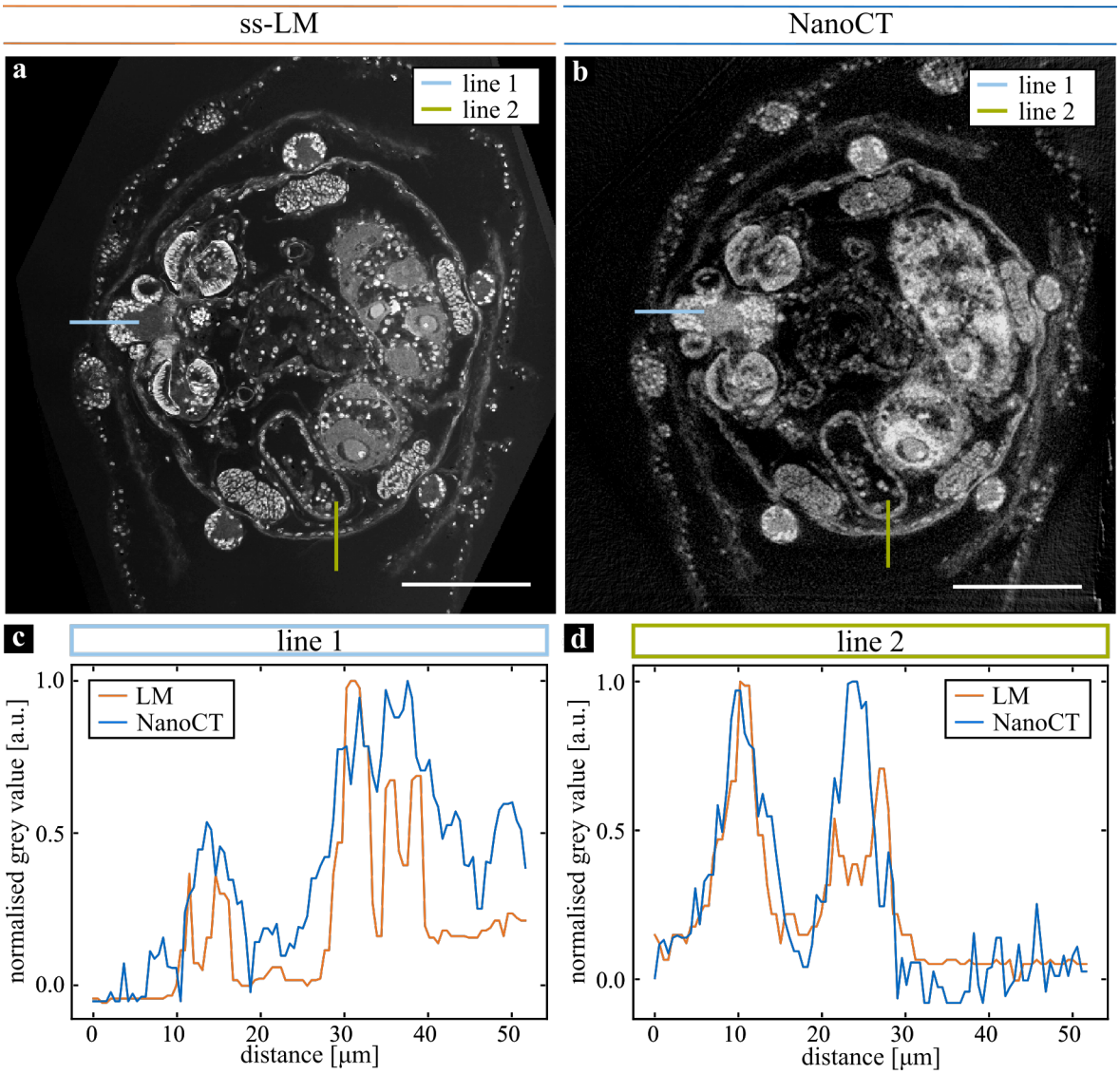

Figure 8.6: **Evaluation of the Spatial Resolution along Line Profiles of the NanoCT versus SS-LM.** (a), (b) Corresponding high-resolution slices from ss-LM and NanoCT with the spatial coordinates of the grey values used for the line profile plots indicated in light blue (line 1) and green (line 2) (NanoCT: $v_{\text{eff}} \approx 290\,\text{nm}$, ss-LM: 20× objective lens). (c) and (d) Grey value profile along line 1 and line 2 of the LM and the NanoCT image. Scalebars: 100 µm. Figure adapted from [Ferstl, 2019].

8.4 3D Morphology of *R.* cf. *Eliator*

Here, we examine the reproducibility of using the NanoCT to visualise the internal anatomy of a zoological specimen after undergoing TEM sample preparation. As a sample, we selected a tiny marine snail specimen, *Rissoella* cf. *eliator*, with dimensions of about 1 mm × 0.8 mm × 0.6 mm.

Figure 8.7 displays the resulting NanoCT data with an effective voxel size of $v_{\text{eff}} \approx$ 1.0 µm. To provide a preliminary impression of the NanoCT image quality with reference to LM and to convey a better understanding of the visualised structures, LM images of a different *Rissoella* specimen (*Rissoella globularis*), with a similar internal morphology, are included in Fig. 8.7c, f. To obtain the LM images, the sample was prepared following the same protocol as previously carried out for *L.* cf. *minuta*.

Similar to the NanoCT data in Fig. 8.3 - Fig. 8.6, the oocytes are particularly highlighted in Fig. 8.7b, d. The contrast in the rest of the specimen, however, is rather poor in the NanoCT slices (Fig. 8.7b, e) compared to the LM images (Fig. 8.7c, f). For instance, the intestine could not be identified with sufficient confidence in the NanoCT image (Fig. 8.7b), while it is clearly visible in the LM image (Fig. 8.7c). Opposed to that, the oocytes are least highlighted in the LM images in comparison with other tissue structures.

While the LM images display single cells, the NanoCT slices only coarsely allow for distinguishing between different tissues. This aspect is exemplified in the eye (Fig. 8.7b, f). The LM image allows for distinguishing the pigment cup inside the eye, whereas the NanoCT slice merely enables to detect the eye as a whole.

Nevertheless, it was possible to assign many of the characteristic features inside the animal, such as the pharynx with radula teeth (Fig. 8.7b, c, e, f), the operculum (Fig. 8.7e, f), a calcium cell (Fig. 8.7e, f), the nucleus inside an oocyte (Fig. 8.7c, d), and residues of the snail's shell from the decalcification process (Fig. 8.7a-c, e, f).

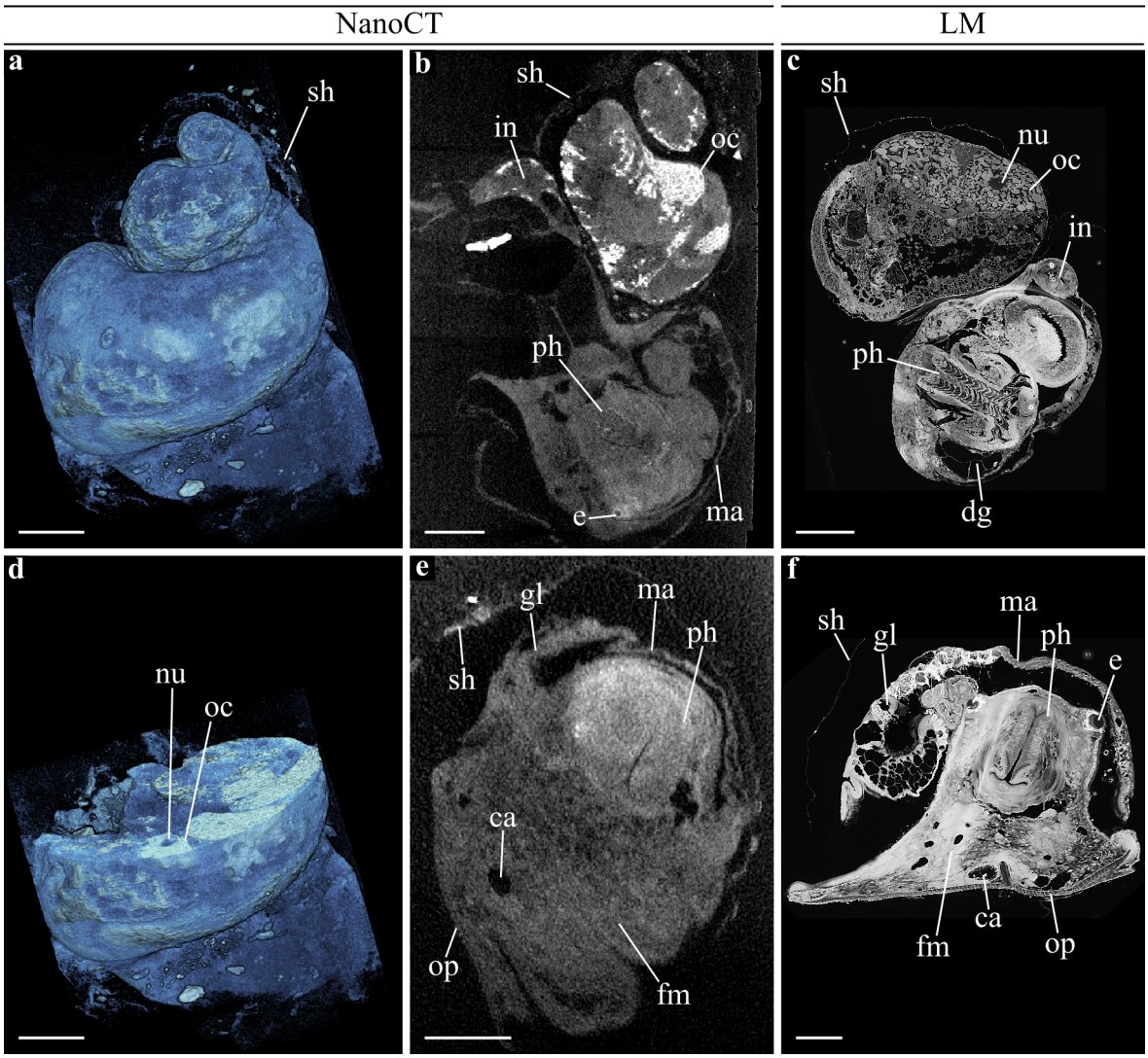

Figure 8.7: **Anatomy of *Rissoella* cf. *Eliator*.** (a) NanoCT volume rendering of *R.* cf. *eliator* ($v_{\text{eff}} \approx 1.0\,\mu\text{m}$). (b), (e) Orthogonal NanoCT slices through the volume shown in (a). (c), (f) LM images of another marine gastropod specimen (*Rissella globularis*) for comparison exhibiting similar morphologies. Legend: ca: calcium cell, dg: defensive gland, e: eye with lens, fm: foot musculature, gl: gland cells, in: intestine, ma: mantle roof, nu: nucleus of oocyte, oc: oocyte, op: operculum, ph: pharynx with radula teeth, sh: remains of the shell (after decalcification). Scalebars: 100 µm.

8.5 Discussion

In zoological research, correlative microscopy combining ss-LM and TEM is a standard approach to study the multiscale 3D morphology of a specimen [Handschuh, 2013]. In order evaluate the NanoCT in its usefulness for correlative microscopy and thereby to eradicate the benefits the NanoCT could contribute to this field, we performed a comparative study towards ss-LM. We applied both 3D imaging techniques to the same specimen of *L.* cf. *minuta*, a tiny sea cucumber with dimensions of 1 mm × 0.5 mm × 0.5 mm. After post-fixation with osmium tetroxide, the specimen was embedded into resin according to the standard TEM protocol.

With the NanoCT we managed to acquire data of the whole embedded specimen (Fig. 8.2, Fig. 8.3). Based on the NanoCT data, which precisely reproduced the internal microstructure, a 3D model of the entire organ system of *L.* cf. *minuta* could be generated (Fig. 8.2).

Beyond the removal of excess resin surrounding the sample, the NanoCT scans did not require any sectioning or other additional sample processing. Opposed to that, obtaining the ss-LM volumes, both involved sectioning and an additional staining step with methylene blue-azure II. These additional steps increase the risk of corrupting the sample structure. Sectioning in particular often leads to distortions or even ruptures [McInnes, 2005]. Such distortions might also be one of the reasons why a perfect co-registration of the NanoCT and the ss-LM volume in Fig. 8.3 was not possible.

Apart from distortions, typical artefacts of sectioning-based 3D imaging techniques concern the alignment of the image series and the brightness throughout the volume. Both alignment and brightness artefacts were clearly observed in the ss-LM volume in Fig. 8.3. Compared to that, such artefacts were less severe in the high-resolution ss-LM volume presented in Fig. 8.4, but nevertheless degraded the image quality considerably.

Furthermore, the NanoCT data provided isotropic effective voxel resolutions of 540 nm in the overview data (Fig. 8.3) and 290 nm in the high-resolution data (Fig. 8.4). This stands in contrast to the ss-LM data where the sectioning thickness of 1 µm defined the voxel edge length perpendicular to the sectioning plane in both volumes (Fig. 8.3, Fig. 8.4).

Another advantage of X-ray CT imaging is the preservation of the sample proportions. Consequently, NanoCT data qualify as a reference for retrieving the correct proportions in ss-LM volumes. This was particularly useful during this study to generate the ss-LM results in Fig. 8.3 and in Fig. 8.4. Moreover, this feature can be exploited for calculating sizes or volumes of certain anatomical structures inside a specimen.

Further important aspects for assessing the performance of a method, are time and usability. Comparing the acquisition times of both imaging techniques, the NanoCT

scans of *L.* cf. *minuta* demanded with ≈ 30 h considerably more time than the acquisition of the ss-LM image stacks with 1 h − 2.5 h (Table 8.1). In this context, it has to be taken into account, that the actual CT acquisition is automated, whereas the acquisition of the ss-LM data conventionally has to be carried out manually. The preparation time for a NanoCT acquisition by a trained operator lies currently in the range of 3 h. Weighing these aspects, both imaging modalities appear equally labour intensive. Considering the additional processing steps for ss-LM, such as sectioning, staining and section alignment, ss-LM appears to require more effort in total.
Regarding the usability, however, the NanoCT system being a research prototype still has a long way to go. Both the acquisition and the image processing of NanoCT data require expert knowledge and training to achieve adequate results (Chapter 5).

The greatest asset of ss-LM, or LM in general, lies in the immense variety of staining techniques. Such staining techniques not only serve as a plain enhancement of the general contrast in LM images, but also allow for selectively highlighting specific structures in a sample and thus grant access to a wealth of information.
Despite continuous research efforts on expanding the library of available X-ray stains, it will take a considerable amount of time until X-ray imaging can compete with LM in that aspect. In this context, it should be noted though that the majority of these staining techniques is tailored towards paraffin-embedded specimen slices. Although there are also a number of stains applicable to resin-embedded slices, the selection is much more limited.

Imaging of samples specifically prepared for TEM with the NanoCT simplifies a coupling of the two imaging techniques and paves the way for various multi-scale imaging applications. Despite this enormous benefit, NanoCT imaging of resin-embedded samples is also associated with a number of challenges.
Resin-embedding generally increases the sample size even if the sample is trimmed. In the NanoCT, this complicates not only the sample alignment, but also limits the minimum obtainable distance of the rotation axis from the source d_{sa}, as described in Section 5.2. With larger distances d_{sa}, larger source-detector distances d_{sd} are necessary to achieve the desired magnification or effective voxel size. This in turn leads to lower X-ray flux on the detector and, thus, to either higher noise levels in the resulting projection images or to higher exposure times per projection image.
For the X-ray spectrum of the NanoTube, the amount of X-rays absorbed in the resin is non-negligible. This again results in either higher noise levels or demands longer exposure times. Longer exposure times, however, are often accompanied by more severe instability artefacts from mechanical instabilities or thermal drifts.
Finally, the resin embedding causes less pronounced edge features and a lower sample to background contrast. Such features are crucial for the success of any projection alignment or centre shift correction algorithm, which are typically used to correct for instability artefacts (Section 5.3). Hence, resin-embedding not only may cause stronger

instability artefacts in the NanoCT data but also hampers the treatment of these artefacts. Therefore, an advanced projection alignment method based on a sparsity metric was devised (Fig. 5.17) to accomplish the high level of detail presented in the NanoCT data in Fig. 8.4 - Fig. 8.6. More details on this projection alignment approach can be found in Chapter 5.

In both the overview data in Fig. 8.3, as well as in the high-resolution data (Fig. 8.4), a difference in the grey value distribution between the NanoCT slices and the LM sections was clearly visible. There is a number of effects which contributed to this difference:
First of all, visible light and X-rays have a different absorption behaviour even for the same materials. Second, methylene blue-azure II was applied to the resin sections prior to LM imaging and provided the resulting LM images with the majority of the contrast. Finally, the retrieval of propagation-based phase effects strongly contributed to improving the general contrast in the NanoCT data (Section 5.3). While resin-embedding strongly reduced contributions from propagation-based phase effects, Paganin's phase retrieval still had a major impact on the CNR in the resulting NanoCT data. This impact was illustrated in a comparison between the original NanoCT slice and the phase-retrieved slice in Fig. 5.17b, c.
The contrast levels were more closely studied when quantifying the CNR in a corresponding NanoCT and LM image in Fig. 8.5. The results indicated that it depends mainly on the type of tissue whether the NanoCT or the LM data perform better. It is remarkable, though, that in some tissues the NanoCT achieved even higher CNR values despite the additional stain applied for the LM images. These findings, however, were obtained from only one specimen after applying one specific sample processing routine. The CNR values may differ for other samples and sample preparation protocols. For more representative results, a more comprehensive study involving a larger number of specimens is necessary.

The high-resolution data in Fig. 8.4 illustrated the NanoCT data offering a better image quality than the ss-LM data in all spatial planes other than the sectioning plane. In these spatial planes (Fig. 8.4b, d), the ss-LM data suffered from the previously mentioned alignment and brightness artefacts. In the sectioning plane, the ss-LM data revealed a higher depth of detail than the NanoCT data. This finding was further confirmed in corresponding line plots through the NanoCT and ss-LM data in Fig. 8.6. Nevertheless, the NanoCT images were able to reproduce fine structures such as the statolith in the statocyst (Fig. 8.4g) or the nucleoli in the oocytes (Fig. 8.4c, e, g) comparable to the ss-LM images.

The findings gained from *L.* cf. *minuta* were further verified for another zoological specimen, a marine snail *R.* cf. *eliator*, with similar dimensions of 1 mm × 0.8 mm × 0.6 mm. Except for the oocytes, which were highlighted as previously in the NanoCT

data of *L.* cf. *minuta* (Fig. 8.5), the NanoCT data of *R.* cf. *eliator* exhibited rather weak contrast compared to the LM images (Fig. 8.7). One reason for this lack of contrast may be the relatively large effective voxel size of 1 µm which is associated with a smaller effective propagation distance and, thus, weaker propagation-based phase effects to improve the soft-tissue contrast. It is, however, more likely that the dominant effect leading to this weak X-ray contrast was an insufficient concentration of osmium in the tissue. The diffusion of osmium into the tissue was certainly reduced by the periostracum of the marine snail.
While the NanoCT data of *L.* cf. *minuta* reached a similar detail level as ss-LM in the sectioning plane, the NanoCT images of *R.* cf. *eliator* appeared considerably inferior to LM with respect to resolution. This impression, however, is difficult to substantiate, since the contrast between tissues in the NanoCT data was too weak.

8.6 Conclusion and Outlook

In this chapter, we showed that it is possible to investigate TEM-prepared samples with the NanoCT and yield satisfying results which benefit zoological research. Beyond that, this project revealed the challenges and benefits of imaging resin-embedded samples with the NanoCT.
Despite the challenges, which mostly comprise handling various artefacts at lower contrast levels and a complicated acquisition process, adequate CNR levels and isotropic resolutions comparable to ss-LM in the sectioning plane were achieved in the NanoCT data. The NanoCT acquisition was non-destructive and did not demand additional sample processing steps. Thus, the NanoCT data was not degraded by sectioning and alignment artefacts, which are typical for sectioning-based techniques. The acquisition can be regarded as similarly or even slightly less laborious than ss-LM.

While the results for *L.* cf. *minuta* were very promising, the combination of osmium tetroxide post-fixation and resin-embedding does not always enable excellent contrasts for X-ray imaging. This was exemplified by the NanoCT results of the resin-embedded specimen *R.* cf. *eliator*, which did not reproduce the inner morphology with sufficient contrast for a comprehensive study of the animal's anatomy. In order to increase X-ray contrast, one possible approach is to draw on the array of staining techniques conventionally used for EM, such as uranylacetate or potassium ferricyanide [Titze, 2016].
Furthermore, resin-embedding of samples is not the solution to every scientific question. Studies regarding sample preparation protocols for X-ray microscopy indicate that CPD with PTA, osmium tetroxide or ruthenium red staining shows great potential to yield more information in future NanoCT scans [Sombke, 2015; Metscher, 2009; Jahn, 2018; Gabner, 2020].

Nevertheless, the possibilities and applications of the NanoCT for resin-embedded samples are numerous. Continuing down the path of the research project of this chapter, the next step may be a study involving correlative multi-scale imaging of NanoCT with TEM. In various future research applications, this combination has the potential for becoming a valid alternative to various CLEM approaches.
In other projects, the NanoCT could serve as a reference for retrieving the original sample proportions for various sectioning based microscopy techniques.
A further promising application is the combination of the NanoCT with FIB-SEM. FIB-SEM provides very high resolutions with isotropic voxels but requires an immense amount of time even for small sample volumes. In this respect, the NanoCT may offer a considerable benefit by providing an overview over the sample to predefine VOIs for further FIB-SEM investigations.
Finally, further intriguing applications can be developed by extending the library of available X-ray stains.

In conclusion, the findings of this chapter show, that the NanoCT has the potential of some day becoming a highly valuable tool to be integrated into various microscopy facilities.

8.7 Materials and Methods

8.7.1 Specimens and Sample Preparation

The sea cucumber specimen *L.* cf. *minuta* was obtained from bottom sand samples, which had been collected near the Observatoire Océanologique de Banyuls-sur-Mer (France) 2014. The marine snail specimen *R.* cf. *eliator* has been collected in the Northwest Pacific from red algae off the coast of the Miura peninsula south-west of Tokyo (Japan) in a depth of 1 m. The marine snail specimen for the LM images, *Rissoella globularis*, has been retrieved from green algae in the Mediterranean Sea near the Observatoire Océanologique de Banyuls-sur-Mer (France) in a depth of ≈ 6 m.
The preparation of all samples was executed as denoted in [Ferstl, 2019]. The most important steps were anaesthesia of the animals with seawater isotonic magnesium chloride, and fixation with glutaraldehyde. The shell of the marine snail samples was, then, decalcified. On all samples a post-fixation in osmium tetroxide was performed. Subsequently, the samples were dehydrated in an acetone series and embedded into epoxy resin. Finally, the resin blocks with the respective specimens were trimmed with a razor blade to reduce the sample size in the NanoCT scan.

8.7.2 NanoCT Acquisition and Image Processing

For the NanoCT data presented in the results of this chapter, 1,599 projections were acquired over an angular interval of 360° with a constant angular sampling, using an acceleration voltage of 60 kV and a detector threshold of 2.7 keV. Regarding the investigation of *L.* cf. *minuta*, Table 8.1 displays the remaining acquisition parameters. Thereby, an electron spot radius of $r_e \approx 330$ nm was reached on the X-ray target prior to acquisition. For extending the FOV in the vertical direction, a number of NanoCT scans were performed with varying vertical sample positions. Table 8.1, thus, includes the number of acquired sub-volumes (N_{vol}) and the total acquisition time for the resulting combined volume ($t_{acq,tot}$).
For the NanoCT data of *R.* cf. *eliator*, 7 NanoCT volumes were combined. Each of these volumes was acquired at an effective voxel edge length of $v_{eff} \approx 1.0$ µm and an exposure time per projection of 2 s during an acquisition time of 2 h. The total acquisition time of the combined volume was 14 h. Prior to acquisition, an electron spot radius of $r_e = 0.5 \cdot \text{FWHM} \approx 250$ nm was measured.
More information on tomography acquisitions with the NanoCT are provided in Section 5.2 or the Appendix A.1.

A detailed description of the image processing routine of the NanoCT, which was applied to the data in this chapter, is conveyed in Section 5.3. A static centre-

shift correction approach was performed on the NanoCT data displayed in Fig. 8.2, Fig. 8.3 and Fig. 8.7. The high-resolution NanoCT data of *L.* cf. *minuta* (Fig. 8.4 - Fig. 8.6) were processed using the sparsity-metric based dynamic approach for both correcting the global centre-shift as well as projection alignment. For deblurring and contrast-enhancement of the NanoCT data, Gureyev's approach was employed. The sub-volumes of the NanoCT data sets were combined with a stitching algorithm.

Technique		NanoCT		SS-LM	
Type		Overview	High-Resolution	Overview	High-Resolution
Figures		8.2, 8.3	8.4, 8.5, 8.6	8.3	8.4, 8.5, 8.6
v_{eff} (horizontal)	[nm]	540	290	230	110
v_{eff} (vertical)	[nm]	540	290	1000	1000
Objective		–	–	10×	20×
NA		–	–	0.4	0.75
δ_{x}	[nm]	–	–	686	366
t_{exp}	[s]	3	8	–	–
$t_{\text{acq,i}}$	[h]	2.5	5	2.4	1
N_{vol}		12	7	1	1
$\text{N}_{\text{sections}}$		–	–	1208	326
$t_{\text{acq,tot}}$	[h]	33	35	2.5	1

Table 8.1: **NanoCT and SS-LM Acquistion Parameters for Studying *Leptosynapta* cf. *Minuta*.** Legend: v_{eff} (horizontal): the effective voxel edge length in the horizontal sample plane (ss-LM: in the sectioning plane), v_{eff} (vertical): the effective voxel edge length in vertical direction (ss-LM perpendicular to the sectioning plane), Objective: objective lens magnification, NA: numerical aperture, δ_{x}: the resolution limit of the respective objective lens, t_{exp}: exposure time per projection image, $t_{\text{acq,i}}$: acquisition time for the i-th sub-volume, N_{vol}: number of sub-volumes for extending the vertical FOV, N_{sections}: the number of imaged sections for the ss-LM-data set, $t_{\text{acq,tot}}$: acquisition time for the total combined NanoCT volume or the ss-LM volume.

8.7.3 SS-LM Sample Preparation

The resin-embedded samples of *L.* cf. *minuta* (after NanoCT acquisition) and *Rissoella globularis* were examined and photographed with a light microscope. Prior to

LM acquisition, an ultramicrotome was used to generate sections of the resin-blocks containing the specimens (*L.* cf. *minuta*: section thickness of 1 µm, *Rissoella globularis*: section thickness of 1.5 µm). For staining methylene blue-azure II was used. More details on the sample preparation routine can be obtained in [Ferstl, 2019], and [Ruthensteiner, 2008].

8.7.4 SS-LM Acquisition and Image Processing

For the ss-LM volume of *L.* cf. *minuta*, the serial sections of the specimen were imaged with a microscope camera mounted on a compound microscope. For more in-depth information the reader is referred to [Ferstl, 2019]. The used acquisition parameters are listed in Table 8.1. The effective voxel edge length results from the used microscope camera and the used objective. The effective voxel edge length perpendicular to the sectioning plane is 1 µm equal to the section thickness. The resolution limit in the respective data sets was estimated from the Rayleigh-criterion (Eq. 4.8), assuming a dry lens objective and a mean visible light wavelength of 450 nm.
The image series was converted into grey scale with Photoshop CS6 (Adobe) to facilitate a comparison with the NanoCT data. Missing slices were filled in with using the previous or the following slice. To align the image stack and generate a consistent volume, a combination of automated modules in Amira (Thermo Fisher Scientific) and manual corrections was applied [Ferstl, 2019]. For better comparison with the NanoCT data, the grey values of the ss-LM data of *L.* cf. *minuta* were inverted and the grey value scale was uniformly adapted.

For the images of *Rissoella globularis* (Fig. 8.7c, f), LM images of several sections were acquired and converted into grey scale. The brightness and contrast were adjusted for a better comparison with the NanoCT slices in Fig. 8.7b, e.

8.7.5 Volume Co-Registration and Visualisation

The post-processing including the co-registration of the volumes featuring *L.* cf. *minuta*, the segmentation of *L.* cf. *minuta* and the visualisation of the volume renderings, was carried out in Amira 6.4 (Thermo Fisher Scientific).
To facilitate a co-registration of both volumes of *L.* cf. *minuta*, the ss-LM volume had to be stretched considerably in direction perpendicular to the sectioning plane to correct for the anisotropic scale of the image stack. For this process, the NanoCT volume was used as a reference. The alignment of both volumes was carried out with a manual rough-alignment followed by an automated alignment module in Amira. Due to distortion artefacts in the ss-LM volume, however, no perfect co-registration of the two volumes was possible.

8.7.6 Analysis of CNR and Resolution

The analysis of CNR and the line profiles (Fig. 8.5, Fig. 8.6), was carried using self-written python code. The basis for these analyses is formed by an LM image in the sectioning plane and the corresponding NanoCT slice (Fig. 8.5a, b, Fig. 8.6a, b).

For the CNR evaluation (Fig. 8.5), in both images 5 ROIs were selected, which contained sufficiently uniform grey values. Uniform contrast areas are important to minimise potential falsifications of the calculated noise levels due to underlying fine substructures. Furthermore, in the NanoCT slice and the LM image, corresponding regions including the same tissue type were selected as ROI. The mean value of the resin-background served as reference and was set to zero. The CNR calculation was performed according to Eq. 6.1.

For the qualitative resolution analysis (Fig. 8.6), perpendicular lines were selected in the corresponding images. Thereby, it was particularly important to include precisely the same structures into the selected line profiles. Due to slight deviations in the co-registration, however, a perfect match between line profiles was not attainable. For a better comparison, despite the given differences in the contrast properties, the line profiles were normalised to the maximum grey value with the resin background being set to zero for reference.

8.7.7 Scientific Contributions

The study design involving *L.* cf. *minuta* was devised by Bernhard Ruthensteiner, Thomas Schwaha and Simone Ferstl. The study design regarding the specimens of *Rissoella* was formed by Bastian Brenzinger and Simone Ferstl. The sea cucumber specimen was collected and prepared by Bernhard Ruthensteiner and the marine snail specimens by Bastian Brenzinger. The acquisition of the NanoCT data, and the image processing was performed by Simone Ferstl. The novel sparsity-metric based projection alignment was developed by Lorenz Hehn and subsequently applied to the NanoCT data by Simone Ferstl. The ss-LM volume was acquired and aligned by Thomas Schwaha. Thomas Schwaha further carried out the segmentation and assignment of anatomical features in the internal organ system of *L.* cf. *minuta*. The outer skin of *L.* cf. *minuta* was segmented by Simone Ferstl. The morphological structures in the *Rissoella* specimens were assigned by Bastian Brenzinger. The co-registration of the NanoCT and the ss-LM volume of *L.* cf. *minuta*, the generation of the presented images of both *L.* cf. *minuta* and *R.* cf. *eliator*, the CNR and the resolution analysis were carried out by Simone Ferstl.

NanoCT for 3D X-ray Histology 9

9.1 Introduction

In the conventional work-flow of histopathology, as illustrated in Fig. 9.1a, a tissue specimen is fixed, embedded into paraffin, sectioned by a microtome, stained and analysed with a LM. This methodology is setting the benchmark with respect to diagnostic 2D tissue analysis due to its robustness and its immense versatility. Its robustness is the result of over a century of development and research on suitable routines and classification criteria. Moreover, the two major aspects contributing to its versatility are the vast library of histological staining protocols and the adaptability of the LM magnification. Thereby, histology reliably enables multiscale investigations of the morphology of many different tissue types. Despite these advantages, though, this method is destructive and confined to two dimensions [DAgati, 2005; Suvarna, 2013].

In order to truly gain a precise understanding of a tissue architecture, 3D information is highly valuable. Beyond providing information about any virtual plane, 3D imaging allows for tracking crucial tissue structures throughout the imaged volume. These beneficial qualities have ever since inspired the field of 3D histology. However, to generate 3D data of a tissue specimen, most LM and EM-based techniques rely on destructive methods, which introduce artefacts degrading the data quality, and fail in providing isotropic resolutions in 3D [Knott, 2008; Denk, 2004; Braverman, 1986; Andreasen, 1992; Weninger, 1998; Merchan-Pérez, 2009; McInnes, 2005; Töpperwien, 2018b].

With 3D histology using X-rays (3D X-ray histology) beyond the soft-X-ray regime, larger soft-tissue specimens can be non-destructively visualised in 3D [Chao, 2005; Als-Nielsen, 2011]. On the downside, though, it is also more difficult to attain adequate contrast in these soft tissues. Therefore, 3D X-ray histology resorts to phase-contrast imaging or X-ray staining techniques [Töpperwien, 2018b; Metscher, 2009]. Since phase contrast is directly bound to the electron density of the respective tissue, it provides little control over which tissue structures are highlighted [Birnbacher, 2016; Töpperwien, 2018b]. Opposed to that, X-ray staining allows for specifically targeting certain tissue structures, such as cell nuclei or the cytoplasm [Müller, 2018; Busse, 2018b]. The drawback associated with X-ray staining is the additional sample processing it entails, which increases the risk of corrupting a sample's microstructure [Ferstl, 2019].

This chapter presents various 3D X-ray histology applications of investigating human tissue specimens using the NanoCT. To enhance soft-tissue contrasts, an approach was employed which has already been tested on murine kidney samples [Busse, 2018b]. It is based on both propagation-based phase contrast and a cytoplasm-specific eosin-based X-ray stain (X-ray eosin stain). Figure 9.1b illustrates the employed work-flow which ultimately resulted in NanoCT and microCT volume data of the respective tissue specimens. Based on this work-flow, an extensive multiscale study was performed on various structural regions of the kidney exhibiting different pathological alterations. In further studies, human tissue specimens from two additional organs were investigated: the skin and the lung.

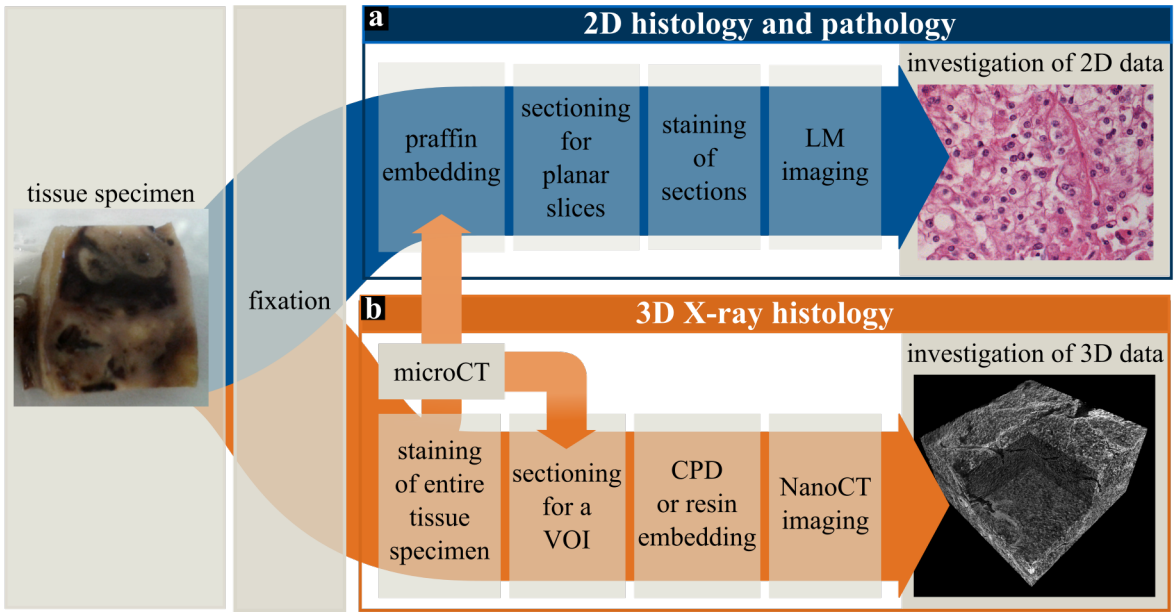

Figure 9.1: **Work-Flow of 2D Histology versus 3D X-ray Histology with the NanoCT.** Left: tissue specimen after fixation. (a) Sample processing of 2D histology resulting in a 2D LM image. The section has been stained with haematein and eosin. (b) Sample processing of 3D X-ray histology resulting in 3D NanoCT data of an X-ray eosin-stained tissue piece. Here, only CPD was used prior to NanoCT acquisition. The work-flow includes optional microCT imaging with a subsequent transfer of the stained sample to histology. Figure based on [Ferstl, 2020a].

The following sections of this chapter present the resulting NanoCT and microCT volumes, which reproduce the characteristic 3D tissue architecture of each organ and each pathology. The data was analysed and compared to representative histology images to evaluate the potential of the NanoCT for advanced diagnostic tissue analyses.

Finally, the compatibility of the X-ray eosin stain was verified regarding subsequent sample processing according to the standard, automated protocols of routine diagnostic histology.

When interpreting the X-ray and histology data, it should be considered that the X-ray eosin stain was applied to both the tissue specimen which were used for X-ray imaging and the ones which were analysed in histology. Hence, both the X-ray volume and the histology image display a map of the eosin distribution. This eosin distrubtion causes eosinophilic areas to appear bright in the X-ray CT data and pink in the histology images. Eosinophilic structures are typically characterised by a high protein content, such as the cytoplasm or erythrocytes.

The study of diseased human renal tissue resulted in two publications [Ferstl, 2020a; Ferstl, 2020b], while the findings on human skin and lung tissue still remain unpublished.

9.2 Targeted Multiscale Investigation of Diseased Human Renal Tissue

In the human body, the kidney has a number of vital functions. Apart from blood filtration, the kidney fulfils a central role in the control of the electrolyte and water household as well as the acid-base balance [DAgati, 2005]. Due to this key role, various local or systemic diseases are closely intertwined with morphological alterations of the kidney tissue. Hence, studying the kidney often yields crucial insights for the understanding of diseases [Gross, 2005; Tervaert, 2010].

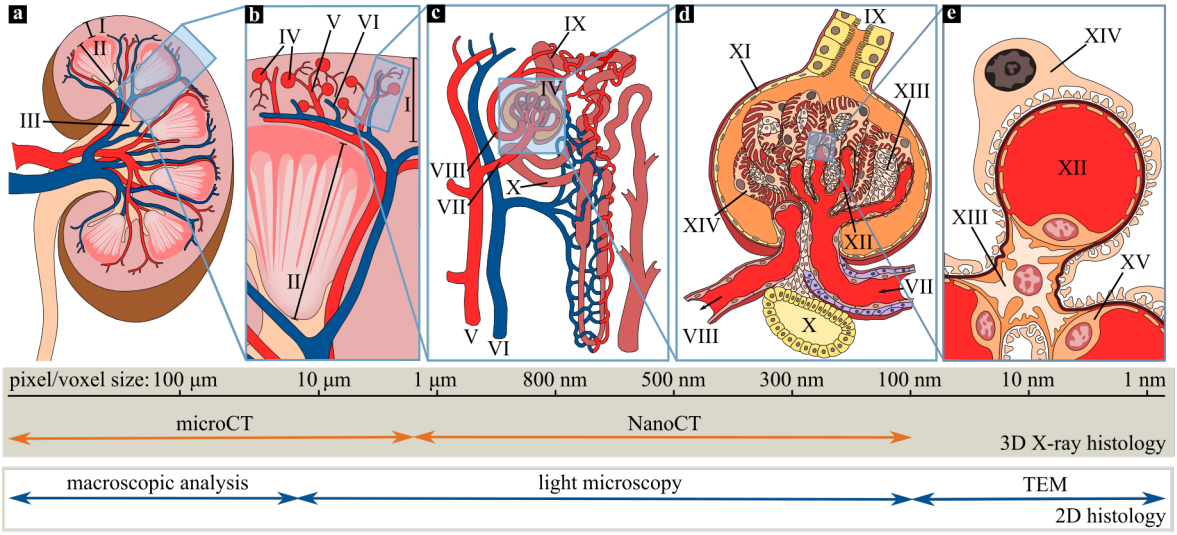

Figure 9.2: **Multiscale Kidney Anatomy.** Bottom: typical effective pixel/voxel sizes to image the above structures and the required imaging methods of 2D histology versus laboratory-based 3D X-ray histology. (a) Kidney. (b) Enlarged region with the nephron-arterial network. (c) Nephron. (d) Glomerulus. (e) Glomerular capillary. The relevant structures were assigned according to [DAgati, 2005]. Legend: I: cortex, II: medulla, III: pelvis, IV: glomerulus, V: interlobular artery, VI: interlobular vein, VII: afferent arteriole, VIII: efferent arteriole, IX: proximal tubule, X: distal tubule, XI: Bowman's capsule, XII: capillary, XIII: mesangial cell(s), XIV: podocyte, XV: endothelial cell. Figure adapted from [Ferstl, 2020b].

The complex tissue architecture of the kidney is composed of hierarchical structures, as illustrated in Fig. 9.2a-e. These structures span over a wide range of length scales, from the macroscopic scale (kidney cortex or pelvis, see Fig. 9.2a), down to microscopic dimensions (glomerulus, see Fig. 9.2d). One of the central structures on a microscopic

scale is the nephron. It represents the central functional unit of the kidney. It is formed by the glomerulus (Fig. 9.2 IV), the arterioles (Fig. 9.2 VII, VIII) and the tubules (Fig. 9.2 IX) [DAgati, 2005]. The incoming blood from the afferent arteriole is filtered through the capillary loops of the glomerulus (Fig. 9.2d). The initial filtrate is collected and further processed in the proximal and distal tubules. The efferent arteriole branches out in close proximity of the glomerulus and forms a vascular network around the distal tubules (Fig. 9.2c).
Due to the large variation of structure dimensions, renal tissue and potential pathological alterations can only be fully understood through multiscale imaging. For some cases, it is crucial to scan rather large tissue volumes with edge lengths in the cm-range. This is the case when it comes to screening a piece of cystic renal tissue [Ishikawa, 1993; Schwarz, 2007; Hajj, 2010]. In contrast to that, certain glomerulopathies require resolutions beyond the limits of LM. In these cases, pathologists conventionally consult TEM imaging (Fig. 9.2) [DAgati, 2011; Lai, 2015].

This configuration of diverse structures and challenges renders the kidney ideal for an initial assessment of the NanoCT with respect to tissue diagnostics. For the following study, tissue specimens from different kidney regions of five patients were chosen: polycystic kidney disease (patient A), alterations in tubular morphology (patient B), renal tissue with an acute shock (patient C), and renal cell carcinoma tissue specimens of two different grades (grade 2: patient D, grade 2-3: patient E).

To account for the multiscale tissue structures, microCT and NanoCT imaging were combined (Fig. 9.1b). Volume data with edge lengths from $\approx 6\,\mathrm{mm}$ down to $\approx 150\,\mu\mathrm{m}$ were acquired with effective voxel sizes ranging from $v_{\mathrm{eff}} \approx 15\,\mu\mathrm{m}$ to $v_{\mathrm{eff}} \approx 200\,\mathrm{nm}$. The associated histology LM images, which serve as ground truth, were produced from the X-ray eosin stained tissue specimens by applying a subsequent haematein counter-stain to highlight the cell nuclei. Thereby, regions containing similar tissue morphologies as in the microCT and NanoCT data were imaged with the LM. In the resulting images from both X-ray CT and histology, pathologists of our team assigned the relevant structures and performed a diagnostic interpretation. The following sections present the findings for each of the studied pathologies.

9.2.1 Cystic Kidney Disease

Cystic kidney disease is a typical example for morphological alterations over a large range of length scales. While some aberrations, for instance foam cell aggregates, require investigations with sub-cellular resolutions, some cysts are already visible on a macroscopic scale [DAgati, 2005].

To account for these various tissue structures, microCT data were acquired of a larger volume from a polycystic kidney tissue specimen. Inside this volume a VOI was defined, from which a smaller piece of tissue was resected for analyses with sub-cellular resolutions using the NanoCT. Figure 9.3 shows the resulting microCT data the NanoCT data of the VOI. A similar multiscale analysis is demonstrated in the histology images, where a region of interest (ROI) was reinvestigated with a high-magnification objective (Fig. 9.3e, k).

Beyond reflecting the tissue morphology exhibited in the histology image, including amorphous eosinophilic material and multilocular cysts (Fig. 9.3 I, III), the microCT data revealed a tiny nodular region in a cyst wall (Fig. 9.3 II).
Furthermore, the pathological analyses yielded a VOI indicating relevant sub-structures, which could not be resolved with the microCT (Fig. 9.3 IV). For deeper insights into the underlying tissue architecture, the respective VOI was investigated with the NanoCT. Pathological evaluations of the resulting NanoCT data (Fig. 9.3f-i) characterise the tissue inside the VOI as a foam cell aggregate. While the histology image accounts for the majority of the structures (Fig. 9.3k) shown in the NanoCT data (Fig. 9.3 V, VII), the cholesterol crystals were not discernible (Fig. 9.3 VI). Paraffin embedding dissolves cholesterol crystals inside of tissue.
Based on a precise analysis of the NanoCT data, it was possible to reassign the NanoCT volume to the orange-framed VOI inside the microCT volume, from which it was originally extracted. This proves the feasibility of correlative multiscale imaging through coupling the NanoCT with a microCT.

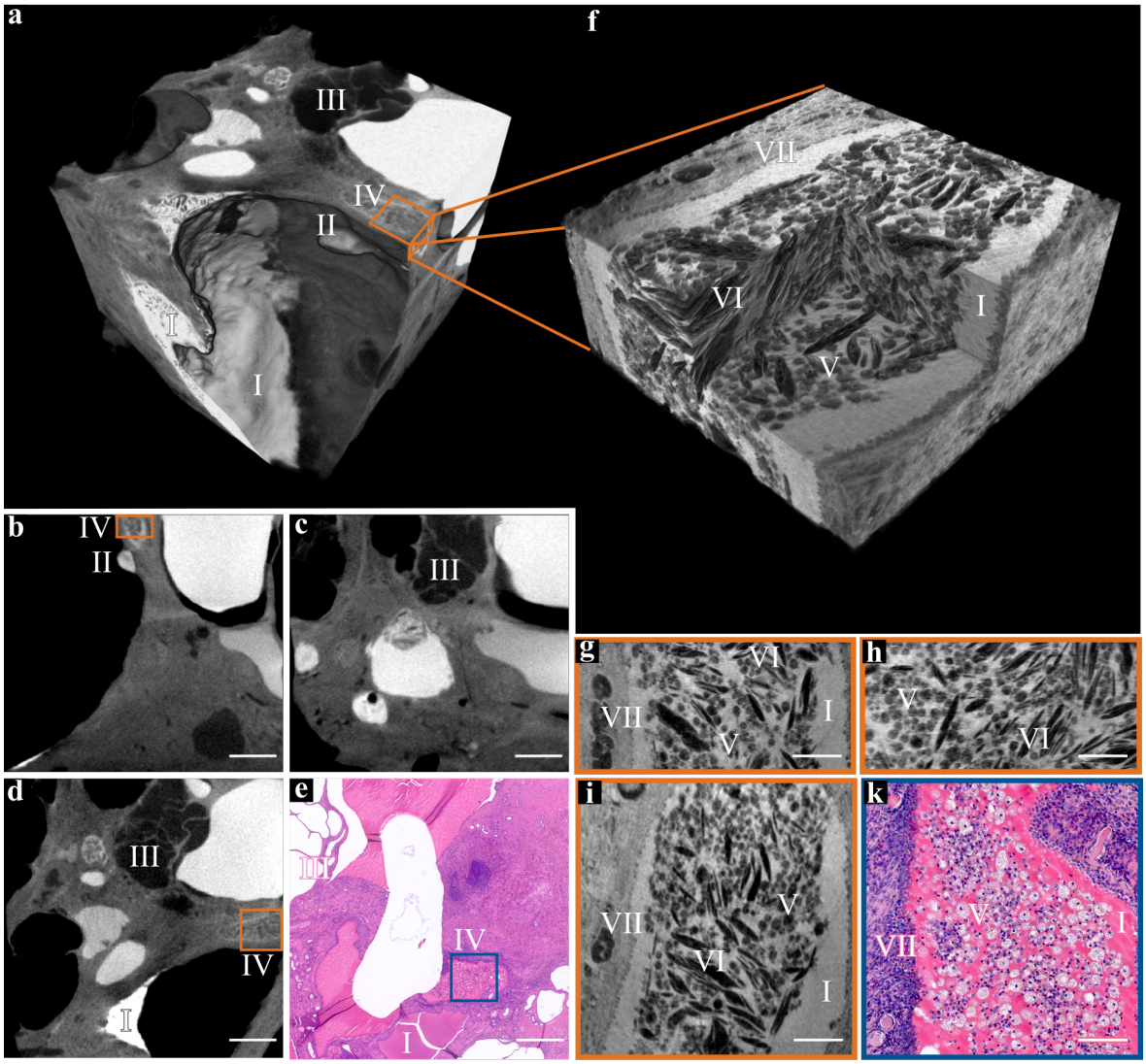

Figure 9.3: **MicroCT, NanoCT and Histology Images of a Polycystic Kidney (Patient A).** (a) Representative microCT volume of 5.8 mm × 5.8 mm × 5.5 mm with an orange VOI ($v_{\text{eff}} \approx 14.8\,\mu\text{m}$). (b) – (d) Orthogonal microCT slices through the volume in (a). (e) Representative histology image with haematein counter-staining and a blue ROI. (f) NanoCT volume of 500 µm × 500 µm × 270 µm of the orange VOI in (a) ($v_{\text{eff}} \approx 1.4\,\mu\text{m}$). (g) – (i) Orthogonal NanoCT slices through the volume in (f). (k) Enlarged histology image from the blue ROI in (e). Legend: I: amorphous eosinophilic material, II: nodular region in cyst wall, III: multilocular cyst, IV: foam cell aggregate ROI/VOI, V: foam cells, VI: cholesterol crystals, VII: lymphocytic demarcation. Scalebars: (a)-(e): 1 mm. (f)-(k): 100 µm. Figure adapted from [Ferstl, 2020b].

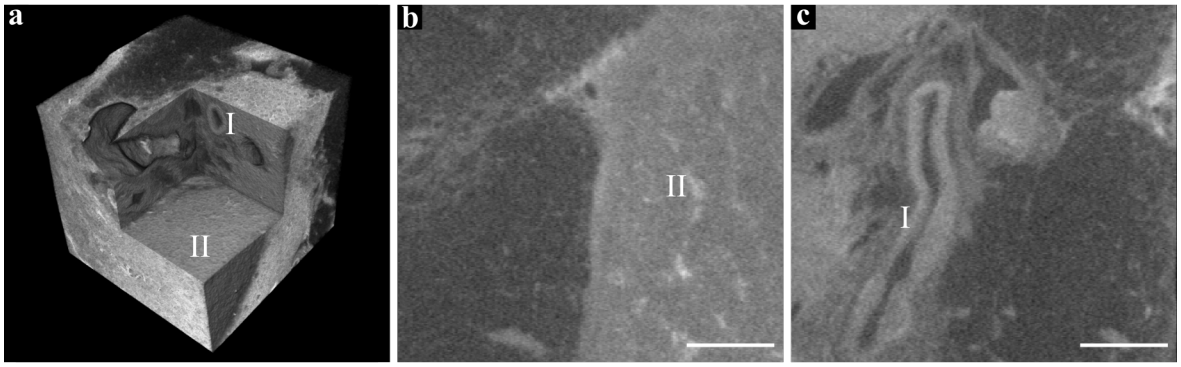

Figure 9.4: **MicroCT Data of a Kidney Tissue Specimen (Patient B).** (a) Representative microCT volume of 5.8 mm × 5.8 mm × 5.5 mm ($v_{\text{eff}} \approx 14.8\,\mu\text{m}$). (b), (c) Two orthogonal microCT slices through the volume shown in (a). Legend: I: blood vessel, II: irregularly stained tissue in the perivascular area, not further classifiable. Scalebars: 1 mm. Figure adapted from [Ferstl, 2020b].

9.2.2 Tubular Morphologies

The tubules represent a fundamental component of the nephron (Fig. 9.2 IX) and make up most of the volume in a normal renal cortex [DAgati, 2005]. Hence, disruptions in renal function and tubular degradations are directly connected. This connection is evident when studying the tissue structure of patient B suffering from an obstruction of the urinary tract.

Regarding the renal tubular network (Fig. 9.2c), only little information could be gained from the microCT data, as observed in Fig. 9.4. Hence, we selected several VOIs for further studies with the NanoCT. Among the resulting NanoCT volumes, two data sets were of particular interest. Both NanoCT and histology data in Fig. 9.5 visualise the typical morphology of altered tubular tissue in varying degrees of severity. These findings comply with the underlying disease. Two clear indicators for a degeneration of the tubular architecture are tubular dilation (Fig. 9.5 III) and bright erythrocytes in ectatic peritubular capillaries (Fig. 9.5 IV). The latter are significantly highlighted due to their high protein content.
Opposed to the histology slide in Fig. 9.5k, a stronger highlight of the tubular walls can be observed in the NanoCT slices in Fig. 9.5g-i. This can be interpreted as an effect from Paganin's propagation-based phase retrieval [Paganin, 2002]. For more details about propagation-based phase imaging with the NanoCT, the reader is referred to Chapter 7 and more information on propagation-based phase retrieval in general is provided in Chapter 5.

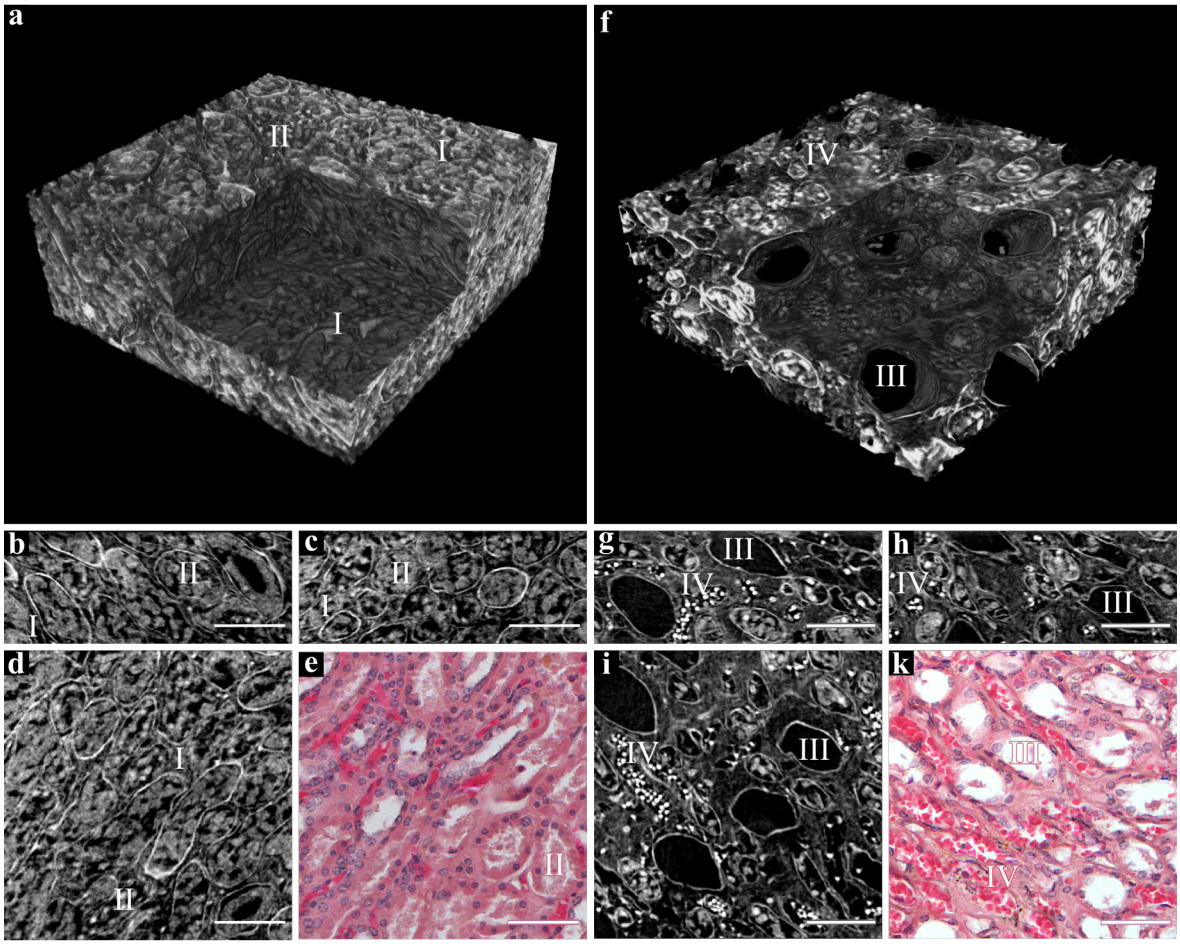

Figure 9.5: **NanoCT and Histology Images of Altered Renal Tubular Tissue (Patient B).** (a) – (e) Data of atmost slightly altered tubules. (f) – (k) Data of significantly degenerated tubules. (a), (f) Representative NanoCT volumes of 206 µm × 206 µm × 80 µm ($v_{\text{eff}} \approx 480\,\text{nm}$).(b) – (d), (g) – (i) Orthogonal NanoCT slices through the volume shown in (a) and (f). (e), (k) Representative histology images with haematein counter-staining, respectively. Legend: I: interstitial connective tissue, II: tubuli with intraluminal cell debris. III: tubular atrophy and tubular dilation, IV: erythrocytes in peritubular ectatic capillaries. Scalebars: 50 µm. Figure adapted from [Ferstl, 2020b].

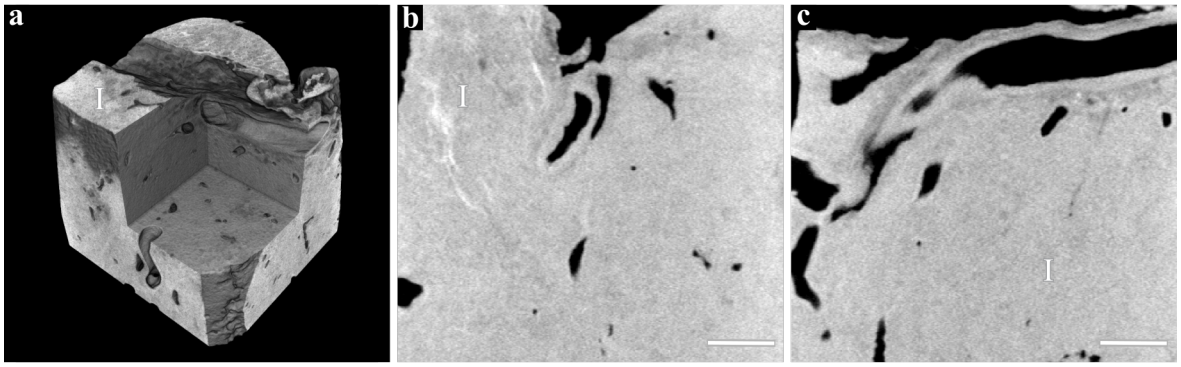

Figure 9.6: **MicroCT Data of a Kidney Tissue Specimen (Patient C).** (a) Representative microCT volume rendering of 5.8 mm × 5.8 mm × 5.5 mm (v_{eff} ≈ 14.8 µm). (b), (c) Two orthogonal microCT slices through the volume shown in (a). Legend: I: mottled stained tissue, not further classifiable. Scalebars: 1 mm. Figure adapted from [Ferstl, 2020b].

9.2.3 Renal Cortex Tissue with Acute Shock

While some diseases, such as diabetes mellitus, are specifically associated with renal degradation, a shock usually affects the entire organ system. Shock conventionally describes the state of insufficient blood supply in tissues caused by issues of the circulatory system. In its final stage it leads to tissue necrosis, multi-organ failure and eventually to death [Tervaert, 2010; DAgati, 2011; Campbell, 2017].

In patient C, these factors induced alterations in the renal tissue morphology. Due to the limited resolution of microCT, these alterations are not visible in the 3D data in Fig. 9.6. Consequently, further higher resolution data were acquired with the NanoCT. In this case, we selected tissue specimens from the kidney cortex to investigate the nephron network, and how the tissue structure of this integral filtering system has been affected by shock.

Nephron-Arterial Network

For an overview over the nephron-arterial network of patient C, a NanoCT volume was generated with an edge length of ≈ 500 µm and a coarse voxel resolution of v_{eff} ≈ 890 nm. The resulting NanoCT data and a haematein counter-stained histology image of a representative region are displayed in Fig. 9.7.

Comparable to the histology image in Fig. 9.7f, the NanoCT slices in Fig. 9.7c-e adequately reproduce the architecture of renal cortex tissue with multiple glomeruli, the associated vasculature, as well as the tubular network. Due to the smaller effective

propagation distance at the larger effective voxel size, propagation-based phase effects only have a minor impact on highlighting structures such as membranes in the NanoCT data in Fig. 9.7.
Nevertheless, the NanoCT data allowed for microsmorphological analyses, which revealed characteristic indicators for shock, such as a dilated vasculature (Fig. 9.7 IV). Moreover, a thickening was observed regarding vascular walls and of the Bowman's capsule surrounding the renal corpuscles (Fig. 9.7II, III).

Beyond the information available in 2D, the NanoCT volume enabled us to track the vasculature in 3D. Thereby, we gained a better view on the nephron-arterial network, which allowed us to assign the proper anatomical terms to the specific tissue structures in the volume, such as the interlobular artery (Fig. 9.7 I), the afferent arterioles (Fig. 9.7 IV) and the efferent arterioles (Fig. 9.7 V). The obtained knowledge was then used to benefit the 2D data by transferring the anatomical labels from the NanoCT volume to the 2D slices in Fig. 9.7c-e.
Furthermore, Fig. 9.7a, b illustrate how the NanoCT data allow for extracting the nephron-arterial network from the volume for a separate assessment, while at the same time providing the structure of the surrounding tissue.

Glomerulopathies

After studying the nephron-arterial network, we examined structural changes at the level of a single glomerulus. Within the nephron, the glomerulus represents the key filtering component (Fig. 9.2d). Pathological alterations of the glomeruli, also referred to as glomerulopathies, can cause a severe impairment of the kidney function which may ultimately lead to end-stage renal disease. This is the reason why glomerulopathies are considered of such great relevance by pathologists that certain cases of glomerulopathies even justify elaborate imaging techniques such as TEM [DAgati, 2011; Ng, 1983].

To enable a high-resolution assessment, NanoCT data of another tissue specimen from patient C was recorded with an effective voxel size of $v_{\text{eff}} \approx 210\,\text{nm}$. For this purpose, a tissue volume was chosen which was just large enough to contain one individual glomerulus. Blurring artefacts from mechanical instabilities and drifts were addressed with an advanced projection alignment technique for CT reconstruction [Hehn, 2019]. More in-depth information on this alignment algorithm is provided in Chapter 5.

Figure 9.8 reveals an entire glomerulus inside the resulting NanoCT volume, including parts of the arterioles and the proximal tubule.

The NanoCT slices reproduce the tissue structure of the glomerulus with a similar detail level as the histology image. The X-ray eosin stain provides sufficient soft-tissue contrast. The cell nuclei, which are not an attractive binding site for eosin, appear as slightly darker disks in the NanoCT slices. This is shown particularly well in Fig. 9.8d,

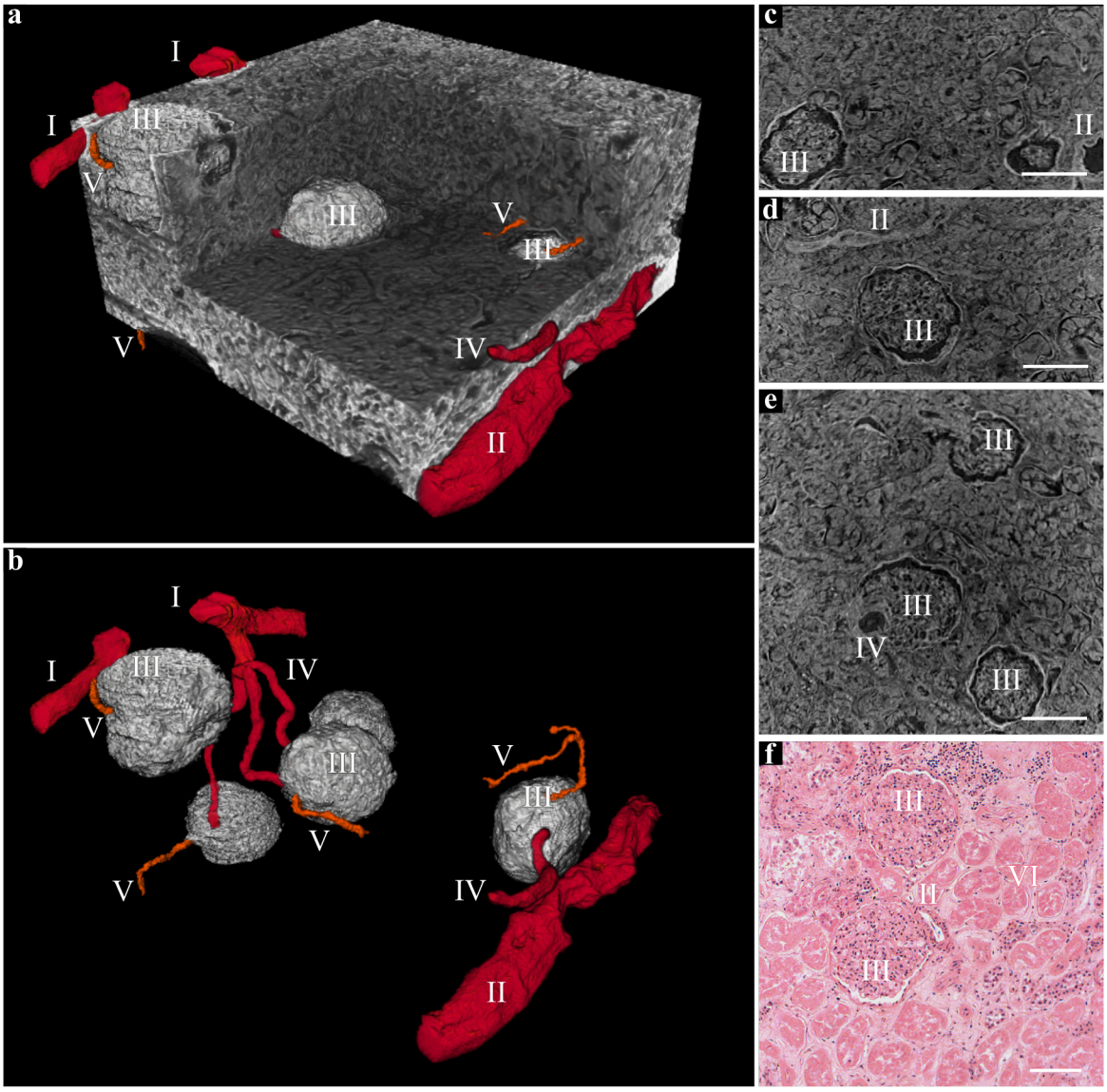

Figure 9.7: **NanoCT and Histology Images of a Renal Tissue Specimen from the Cortex Region with Shock (Patient C).** (a) Representative NanoCT volume rendering of 500 µm × 500 µm × 250 µm ($v_{\text{eff}} \approx 890$ nm). (b) 3D rendering of the glomeruli, the interlobular artery and the associated arterioles without the surrounding tissue within the volume shown in (a). (c) – (e) NanoCT slices derived from the orthogonal planes through the volume shown in (a). (f) Representative histological image with haematein counter-staining. Legend: I: Interlobular artery, II: blood vessel with thickened vascular wall, III: renal corpuscle with thickened Bowman's capsule, IV: dilated afferent arteriole, V: efferent arteriole, VI: tubular necrosis. Scalebars: 100 µm. Figure adapted from [Ferstl, 2020b].

inside the tubule tissue (light blue arrows). Opposed to that, erythrocytes, which contain a high amount of haemoglobin and no cell nucleus, are highly eosinophilic and are, thus, highlighted as bright disks in the NanoCT slices (Fig. 9.8e, orange arrows). In the histology image (Fig. 9.8f), the erythrocytes appear pink (orange arrow) due to the eosin and the cell nuclei blue (light blue arrow) due to the haematein counter-stain.

Beside the X-ray stain, the NanoCT data experiences a substantial boost in soft-tissue contrast through propagation-based phase effects as a result of the large effective propagation distance in this CT scan. This causes highlights particularly of the Bowman's capsule (Fig. 9.8 VI) and of the tubular membranes (Fig. 9.8 II). Since the structural assessment of the Bowman's capsule and the tubule membranes plays an important role, these highlights may ease pathological analyses.

Based on the NanoCT slices, pathologists were able to detect structures, such as the dilation of the capillaries (Fig. 9.8 IV), which can be assigned to shock. Moreover, diffuse and nodular glomerulosclerosis with mesangial thickening (Fig. 9.8 VI, VII) was visible. Thereby, a nodular mesangial thickening was only observable in one of the two orthogonal NanoCT slices (Fig. 9.8d).

In the 3D NanoCT data, we were able to segment the integral parts of the nehpron: the renal corpuscle (Fig. 9.8 I), the proximal tubule (Fig. 9.8 II) and the arterioles (Fig. 9.8 III). Furthermore, the immense detail level in the NanoCT data allowed for segmenting parts of the glomerular capillaries. In the resulting volume rendering in Fig. 9.8c, the irregular shape of the capillaries caused by shock is comprehensible in 3D.

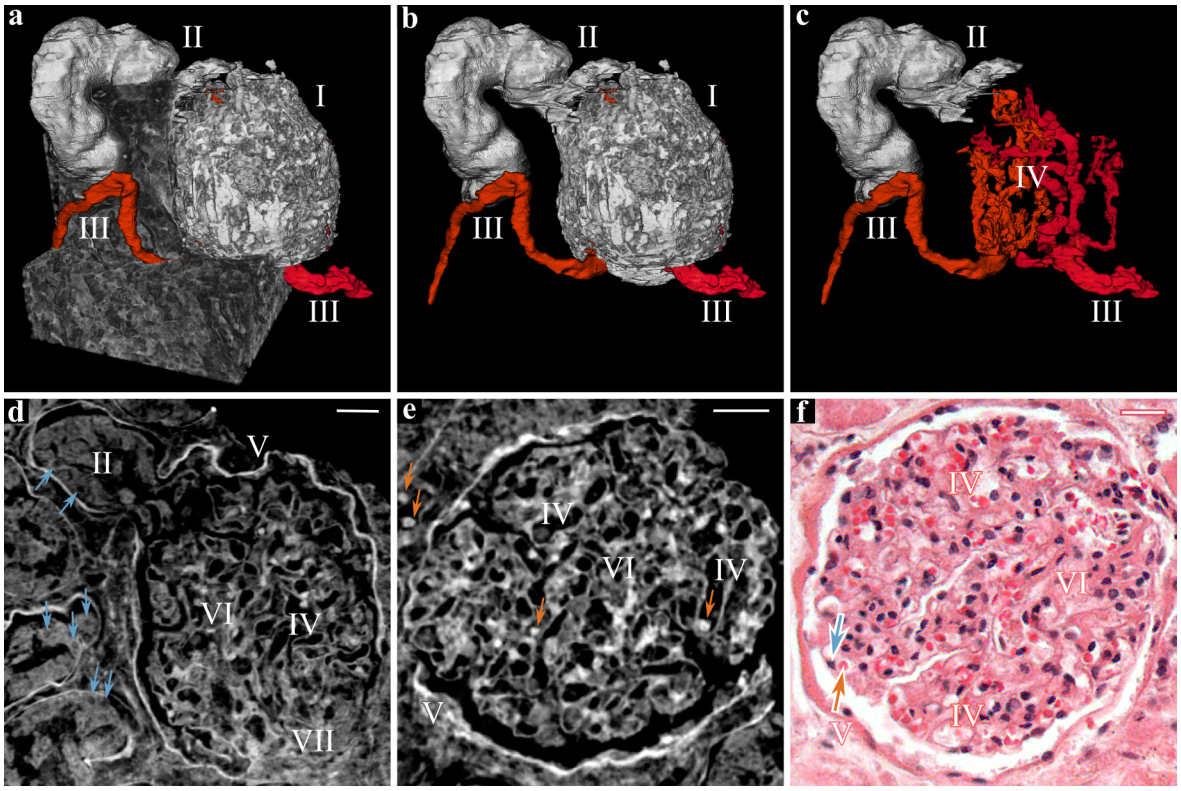

Figure 9.8: **NanoCT and Histology Images of a Single Partially Sclerotic Glomerulus (Patient C).** (a) NanoCT volume of 122 µm × 156 µm × 170 µm with a segmentation of the renal corpuscle, the arterioles and the proximal tubule ($v_{\text{eff}} \approx 210$ nm). (b) Segmentation from (a) without surrounding tissue. (c) Segmentation from (b) with partial segmentation of the capillaries. (d), (e) Orthogonal NanoCT slices through the volume in (a) with orange arrows indicating erythrocytes and light blue arrows pointing to cell nuclei. (f) Representative histology image with haematein counter-staining with an orange arrow at an erythrocyte and a light blue arrow at a cell nucleus. Legend: I: renal corpuscle, II: proximal tubule, III: afferent/efferent arteriole, IV: capillaries with irregular dilated shape, V: thickened Bowman's capsule, VI: slight diffuse mesangial thickening, VII: moderate nodular mesangial thickening, light blue arrow: cell nucleus, orange arrow: erythrocyte. Scalebars: 20 µm. Figure adapted from [Ferstl, 2020b].

9.2.4 Renal Cell Carcinoma

Renal cell carcinoma (RCC) has a mortality rate of 40 %. Due to a lack of early-warning signs, there is a high number of RCC patients with metastases. RCC develops in the renal cortex (Fig. 9.2 I) and often originates from cells in the proximal tubule of the nephron [Motzer, 1996; Muglia, 2015; Forman, 2014].

Pathologists analyse the cell structure, the tissue morphology and growth pattern inside the tumour for a histopathological classification. This classification allows for prognoses on the clinical behaviour of the tumour, such as growth rate and the formation of metastases. The tumour (pseudo)capsule and its relation to surrounding tissue are examined to determine the actual size of the tumour and to evaluate the severity of necrosis in the surrounding tissue. After an operative resection of a RCC tumour, the surrounding tissue is studied to verify a successful and complete removal of the tumour [Motzer, 1996].

Based on this knowledge, we used the NanoCT to investigate several tissue specimens throughout a RCC tumour explant (patient D), which are of high relevance to a histopathological assessment. From this tumour explant, we selected two tissue specimens from tissue surrounding the tumour, a specimen from the tumour (pseudo)capsule, and a tissue specimen from inside the tumour. Since RCC can have a rather heterogeneous tissue morphology, we analysed tumour tissue from an additional patient (patient E) for comparative purposes [Rini, 2009].

Surrounding Tissue

Figure 9.9 focuses on the tissue surrounding the tumour. It displays NanoCT data of two tissue pieces from the kidney cortex. Figure 9.9a-e shows an intact renal corpuscle embedded into tubular tissue. The 3D rendering in Fig. 9.9a illustrates the glomerular structure including the arteriole attachment site. In these data only few pathological alterations can be observed. The X-ray eosin stain highlights the erythrocytes and reveals an area with focal blood extravasation (Fig. 9.9 V). Moreover, a cystically dilated tubule with a protein cylinder is visible (Fig. 9.9 IV). The histology image (Fig. 9.9e) reproduces similar structures of a corresponding region.

Compared to Fig. 9.9a-d, the NanoCT data of a second tissue specimen (Fig. 9.9f-i) exhibits more severe deviations from an intact tissue morphology. Both the NanoCT data, as well as the corresponding histology image depict beyond multiple protein cylinders (Fig. 9.9 IV), inflammation and interstitial fibrosis (Fig. 9.9VI), and a degraded renal corpuscle (Fig. 9.9 VII).

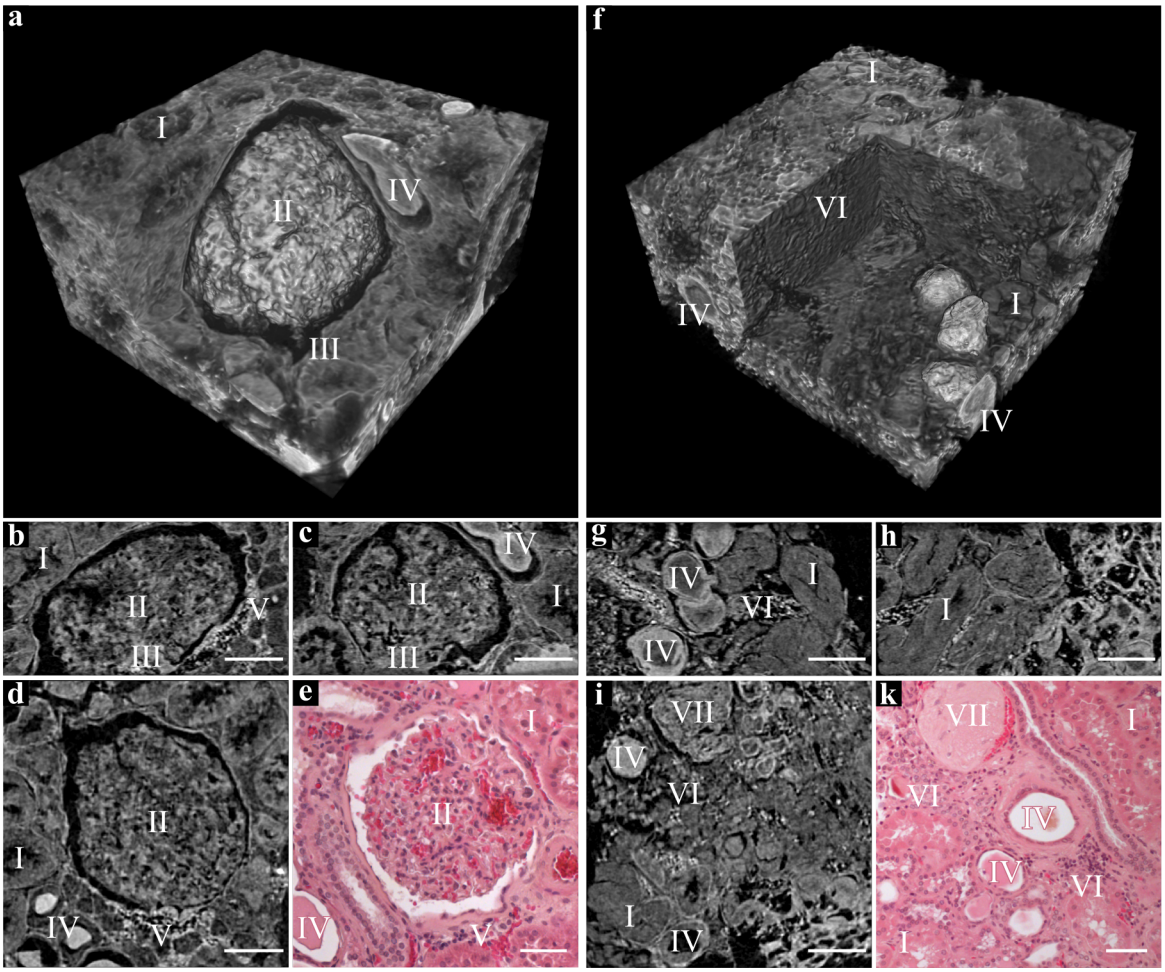

Figure 9.9: **NanoCT Data and Histology Image of Kidney Cortex Tissue Surrounding the Tumour (Patient D).** (a), (f) Representative NanoCT volume rendering of 250 µm × 250 µm × 135 µm ($v_{\text{eff}} \approx 730$ nm). (b) – (d), (g) - (h) Orthogonal NanoCT slices through the volume in (a) and (f), respectively. (e), (k) Representative histology image with haematein counterstaining. Legend: I: proximal tubule, II: renal corpuscle with Bowman's capsule, III: attachment site of efferent/afferent arteriole, IV: cystically dilated tubule with protein cylinder, V: focal area with blood extravasation, VI: inflammation/interstitial fibrosis, VII: degraded renal corpuscle. Scalebars: 50 µm. Figure adapted from [Ferstl, 2020a].

Tumour (Pseudo)Capsule

The junction zone between cancerous tissue and the non-neoplastic tissue neighbouring the tumour is also referred to as the tumour (pseudo)capsule. It plays a key role in the histopathological evaluation of an RCC explant [Motzer, 1996].

Analogous to the histopathology image, the pathological assessment of the NanoCT data yielded tissue structures such as blood vessels (Fig. 9.10 II), and haemorrhages (Fig. 9.10 IV).

The 3D information of the NanoCT data enabled the pathologists to reproduce the correct shape of the tumour (pseudo)capsule (Fig. 9.10a, white dotted line). Based upon this knowledge, they were able to modify and improve their results on the course of the tumour (pseudo)capsule in the corresponding 2D NanoCT slices (Fig. 9.10b-d, white dotted line). This is another example of how a knowledge transfer from 3D to 2D can lead to an over-all enhancement of information available in a data set.

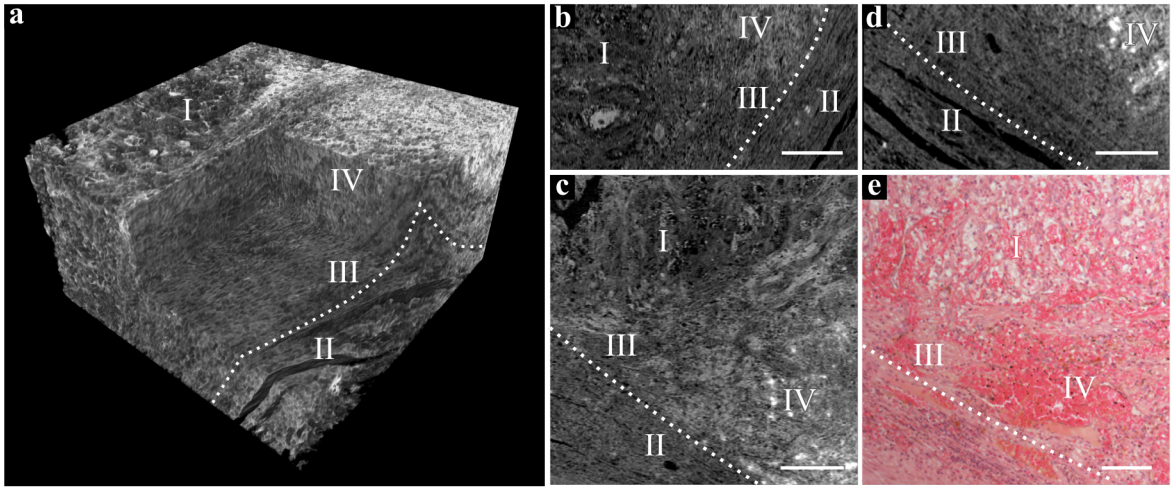

Figure 9.10: **NanoCT Data and Histology Image of the Tumour (Pseudo)Capsule (Patient D).** (a) Representative NanoCT volume of 500 µm × 500 µm × 270 µm ($v_{\text{eff}} \approx 1.25$ µm). (b) - (d) Orthogonal NanoCT slices through the volume in (a). (e) Representative histology image with haematein counter-staining. Legend: I: tumour, II: blood vessels, III: tumour (pseudo)capsule, IV: haemorrhage, white dotted line: tumour (pseudo)capsule. Scalebars: 100 µm. Figure adapted from [Ferstl, 2020a].

Comparison of RCC Tissue from Two Different Patients

After assessing surrounding tissue and the tumour (pseudo)capsule, we focus on the tissue morphology observable inside the carcinoma. Thereby, we compare tissue specimens from two different patients (patient D, patient E), which were both diagnosed with a clear-cell RCC of a similar grade.

The resulting NanoCT data in Fig. 9.11 illustrate the variation in growth patterns which can manifest despite identical tumour types. Particularly remarkable, is the growth pattern in Fig. 9.11f-i, which appears more nodular, compared to Fig. 9.11a-d, with distinct septa of connective tissue. The NanoCT data successfully reproduce both of these characteristic growth patterns precisely as depicted in the corresponding histology images (Fig. 9.11e, k).

Despite these distinct morphological differences, the NanoCT data of both tissue specimens visualise the tissue architecture which is typical for a clear-cell RCC. A clear-cell RCC is characterised by a low protein concentration in the cytoplasm which causes the cytoplasm to appear transparent or clear in an eosin-stained histology image [Rini, 2009]. This can be clearly seen in the histology images of Fig. 9.11. Analogous to the histology images, the NanoCT data presents cells with a dark cytoplasm, due to the lack of eosin in the stained tissue. Moreover, the NanoCT data display an arborising vasculature (Fig. 9.11 I) and nests of tumour cells (Fig. 9.11 II). In the NanoCT volume in Fig. 9.11a the spatial extent of a haemorrhage can be determined.

Despite these features, a precise histopathological classification includes the analysis of the cell nuclei. The distribution of the X-ray eosin provides the shape of the nuclei indirectly in case of cells with cytoplasm containing a normal protein level. In this case of a clear-cell RCC, however, no conclusions regarding the cell nuclei can be drawn from the NanoCT data, hindering a reliable histopathological classification.

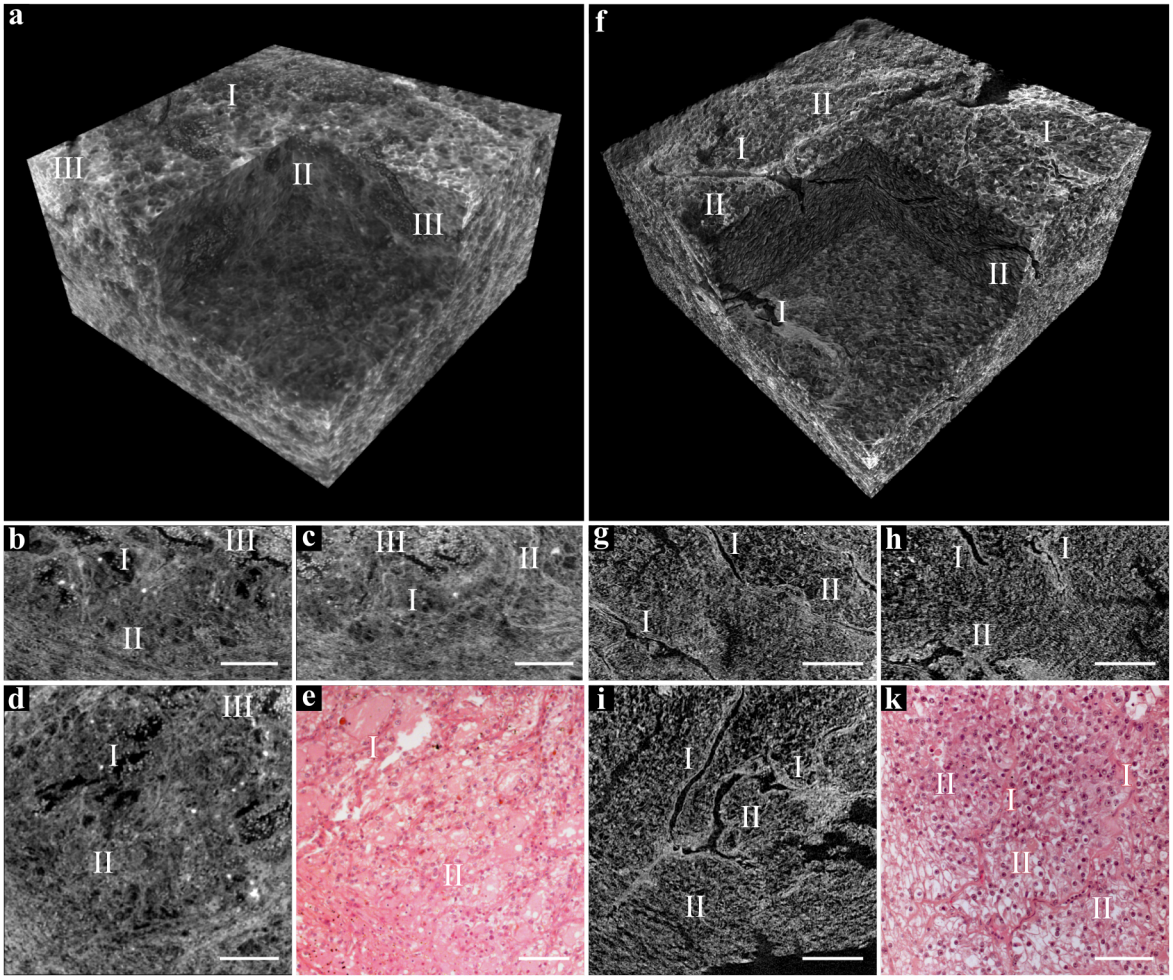

Figure 9.11: **NanoCT Data and Histology Images of RCC Tissue from Two Different Patients (Patient D, Patient E).** (a), (f) Representative NanoCT volume of 500 µm × 500 µm × 270 µm ($v_{\text{eff}} \approx 900$ nm). (b) - (d), (g) - (i) Orthogonal NanoCT slices through the volume in (a) and (f), respectively. (e), (k) Representative histology image with haematein counter-staining. Legend: I: arborising vasculature with connective tissue, II: compact nests of tumour cells, III: haemorrhage. Scalebars: 100 µm. Figure adapted from [Ferstl, 2020a].

9.3 Study of Further Tissue Types and Organs

As previously outlined, histopathology excels due to its versatility. The previous section, evaluated our method of combining the NanoCT with the X-ray eosin stain by imaging various tissue morphologies throughout the kidney over a large range of length scales. However, a crucial aspect of histology's versatility is the applicability to a variety of tissue types and organs [Suvarna, 2013]. Thus, for a more holistic evaluation of our technique with respect to histology, further human tissue specimens from different organs were studied.

Thereby, we chose tissue specimens from lung and skin. The tissue of these two organs largely differ from the kidney not only regarding the tissue structure, but also regarding the tissue composition and density (Fig. 9.12).

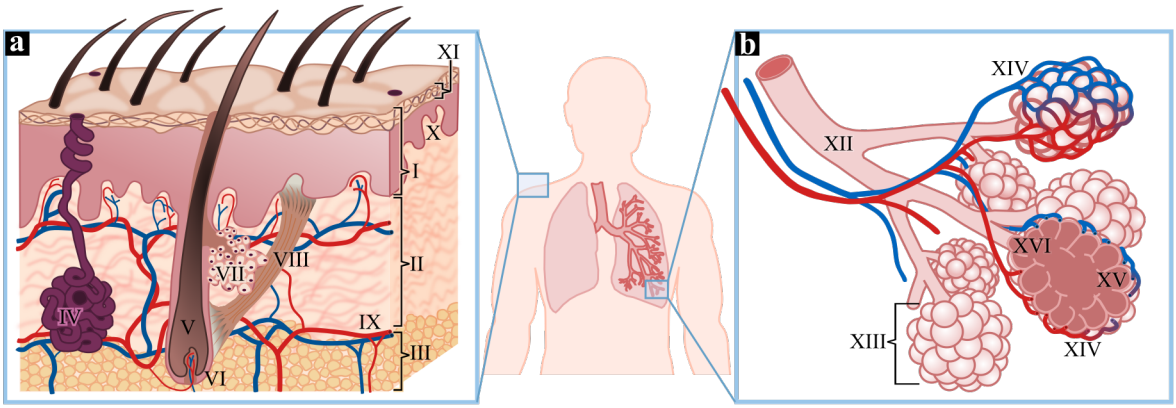

Figure 9.12: **Anatomy of Skin and Lung Tissue.** (a) Skin anatomy. For the sake of clarity, nervous structures are not included. (b) Lung anatomy. Legend: I: epidermis, II: dermis, III: adipose tissue, IV: sweat gland, V: hair, VI: hair follicle, VII: sebaceous gland, VIII: arrector pili muscle, IX: blood vessel, X: dermal papillae, XI: stratum corneum, XII: bronchiole, XIII: alveolar sac, XIV: capillaries, XV: alveolus, XVI: alveolar duct. The anatomically relevant structures were assigned according to [Patton, 2014a].

For instance, skin tissue contains a thick layer of adipose tissue opposed to the investigated inner tissue of the kidney (Fig. 9.12a). Adipose tissue contains a large amount of lipids. Lipids are apolar and are a rather unattractive binding site for the polar eosin in the X-ray eosin stain [Cerroni, 2016]. Thus, adipose tissue acts as a kind of barrier for the stain and represents a substantial challenge for a successful staining procedure of a 3D tissue block. Compared to the generally dense tissue of the kidney, lung tissue is dominated by cavities in the form of alveoli and bronchioles (Fig. 9.12b). Moreover, skin tissue is characterised by a layer structure, while the lung tissue structure is

formed by clusters of alveoli [Patton, 2014b; Tomashefski, 2008].

In the following, NanoCT data of healthy tissue specimens of human skin and lung are assessed. While these data are merely used, here, as verification of the applied technique, it can be also interpreted as a first step towards further studies of analysing pathological skin and lung tissue.

Histology images showing corresponding structures and tissue regions were obtained from literature sources [Cerroni, 2016; Tomashefski, 2008]. Since no further information on the magnification was provided in these sources, no scalebars are included in the histology images of the following figures. Furthermore, the literature did not offer any information on the applied staining techniques in the histology images. The appearance of the histology images, however, suggests that a haematein and eosin stain was used. The assignment of the crucial structures was performed to the best of my knowledge. The assessment has not been verified by a pathologist as in the previous sections of this chapter.

9.3.1 Human Skin Tissue

The resulting NanoCT data of human skin tissue specimens in Fig. 9.13 and Fig. 9.14 demonstrate the success of applying our method to this specific organ. The combination of propagation-based phase contrast and the X-ray eosin stain generated sufficient contrast for the NanoCT data to reproduce the relevant structures of skin tissue architecture. A more detailed analysis of these two contrast forming principles and their effects regarding human skin is conveyed in Chapter 7.

In Fig. 9.13a, b homogeneous bright areas are visible. They originate from excess superglue on the surface of the sample. Despite this sample preparation artefact, the NanoCT data visualise the outer layers of human skin: epidermis (Fig. 9.13 I, II) and dermis (Fig. 9.14 III). In accordance with the histology image in Fig. 9.13b, the NanoCT data shows the epidermis with the stratum corneum (Fig. 9.13 I) and an increasing number of cell nuclei (slightly darker spots in Fig. 9.13c-e II) towards the inner boarder of the epidermis. The dermis exhibits an intricately mottled morphology which is formed by a loose network of collagen fibres. Inside the dermis, blood vessels can be distinguished in Fig. 9.13b, c IV .

Beyond these structures, the tissue specimen in Fig. 9.14 presents a hair follicle (Fig. 9.14 I). Attached to the hair follicle is the sebaceous gland (Fig. 9.14 II) which provides the hair shaft with oil. Furthermore, vascular papillae with blood vessels are observable in Fig. 9.14c, e. The 3D information in the NanoCT data enabled the segmentation of a branching blood vessel in 3D, depicted in orange in Fig. 9.14b.

Sweat glands are the only structure not visible in the NanoCT data. Sweat glands are

hard to detect, due to their twisted channel structure and their resemblance to blood vessels.

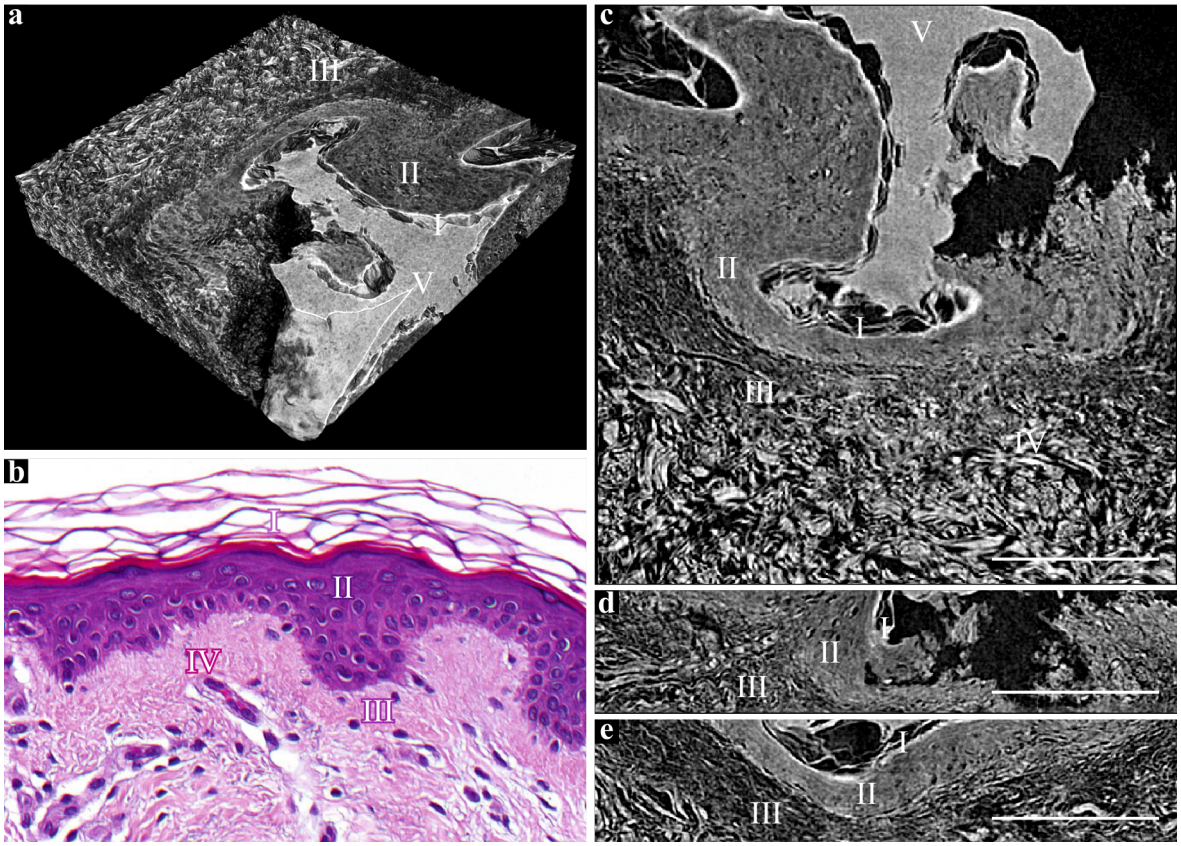

Figure 9.13: **NanoCT Data and Histology Image Illustrating the Characteristic Layer Structure of Human Skin.** (a) NanoCT volume of 350 µm × 350 µm × 70 µm ($v_{\text{eff}} \approx 430$ nm). (b) Histology image of a human skin specimen. Adapted by permission from Springer Nature: Springer "Histologische Strukturen der normalen Haut" by L. Held, G. Metzler, M. Schaller (Jan 1, 2016) [Cerroni, 2016]. (c)-(e) Orthogonal NanoCT slices through the volume shown in (a). Legend: I: stratum corneum, II: epidermis, III: dermis, IV: blood vessel, V: superglue. Scalebars: 100 µm.

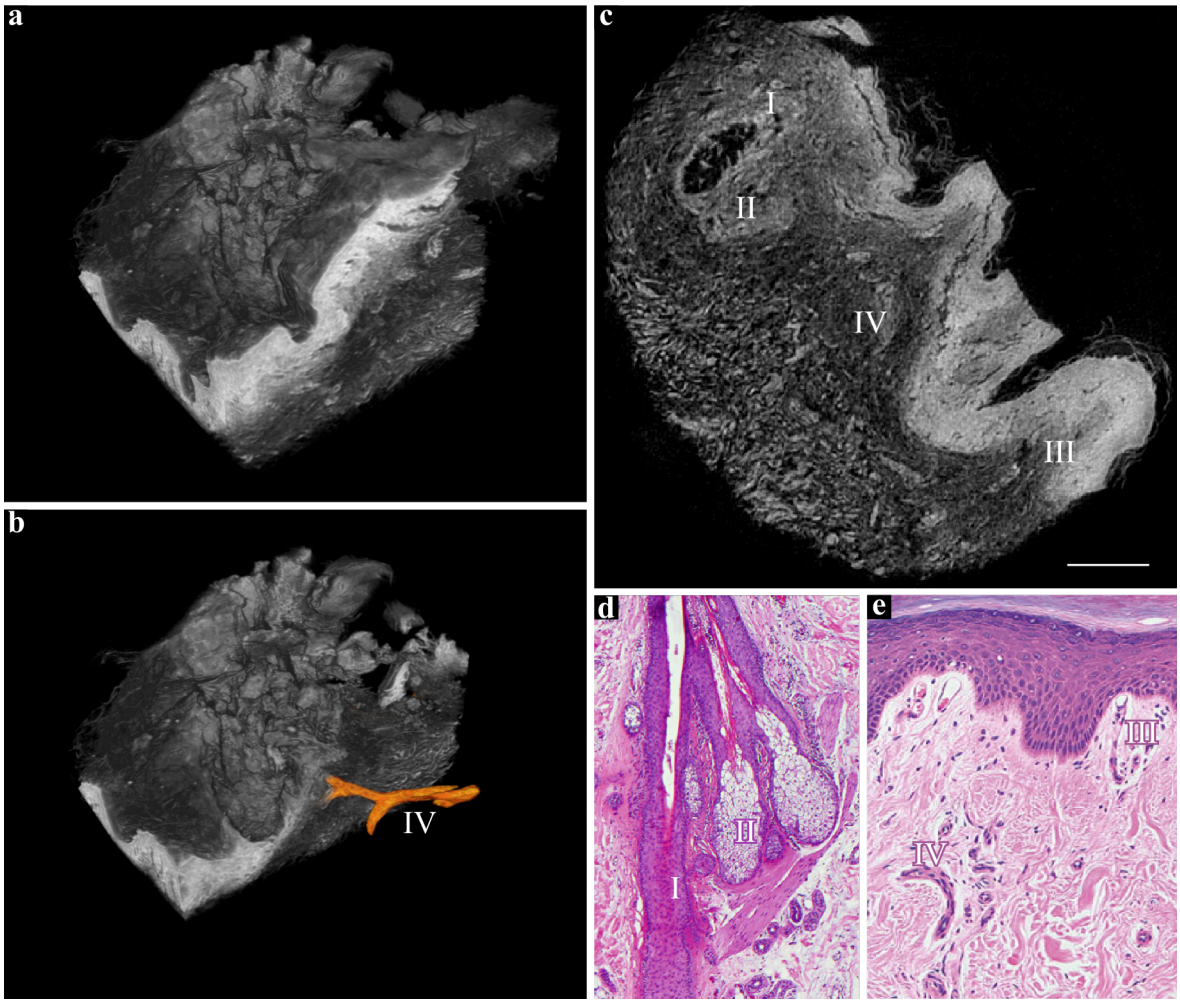

Figure 9.14: **NanoCT Data and Histology Images of Human Skin Tissue Showing a Hair Follicle and Vascular Papillae.** (a) NanoCT volume of 450 µm × 450 µm × 260 µm ($v_{\text{eff}} \approx 1.4$ µm) (b) The volume shown in (a) with a blood vessel segmented in 3D. (c) NanoCT slice through the volume shown in (a). (d), (e) Histology images of human skin specimens. Adapted by permission from Springer Nature: Springer "Histologische Strukturen der normalen Haut" by L. Held, G. Metzler, M. Schaller (Jan 1, 2016) [Cerroni, 2016]. Legend: I: hair follicle, II: sebaceous gland, III: vascular papillae, IV: blood vessel. Scalebars: 100 µm.

9.3.2 Human Lung Tissue

Biopsy specimens of the human lung are rather difficult to analyse since the lung tissue structure can be easily distorted due to the large proportion of cavities. Based on the structures visible in the histology image in Fig. 9.15d, bronchioles and alveolar structures could be assigned in the NanoCT images of Fig. 9.15 up to a tolerable degree of certainty. Furthermore, blood vessel containing a large amount of bright erythrocytes were clearly discernible (Fig. 9.15 I). Some morphologies in the NanoCT slices even indicate capillaries surrounding the alveoli. Further investigations are necessary to manifest these indications.

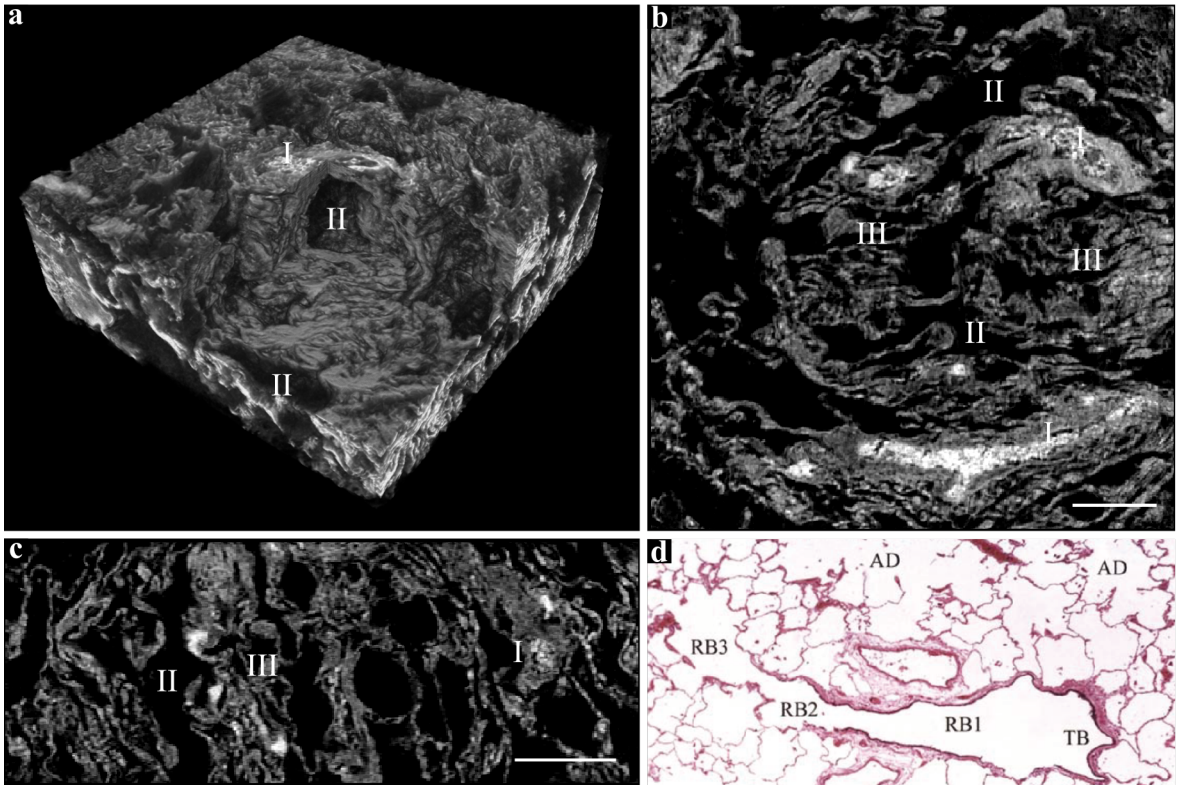

Figure 9.15: **NanoCT Data and Histology Image of Human Lung Tissue.** (a) NanoCT volume of 630 µm × 630 µm × 240 µm ($v_{\text{eff}} \approx 1.25$ µm). (b), (c) Orthogonal NanoCT slices through the volume shown in (a). (d) Histology image of a respiratory bronchiole and alveolar ducts. Adapted by permission from Springer Nature: Springer "Anatomy and Histology of the Lung" by Joseph F. Tomashefski, Carol F. Farver (Jan 1, 2008) [Tomashefski, 2008]. Legend: I: blood vessel, II: bronchiole, III: alveoli, TB: terminal bronchiole; RB1, 2, and 3: three orders of respiratory bronchiole; AD: representative alveolar ducts. Scalebars: 100 µm.

9.4 Compatibility with Histology

For our method to complement histopathology in the future, sample processing routines must be compatible. To verify the compatibility of the X-ray eosin stain with conventional histopathology, we selected four of the most common staining protocols in kidney histology to be performed on X-ray eosin stained tissue pieces from Patient E (Fig. 9.11f-k): haematein, Periodic acid-Schiff, Elastica van Giesson, and Gomorri. Performing these stains according to the standard automated routines resulted in the histology images displayed in Fig. 9.16e-h. For a ground truth, Fig. 9.16a-d present histology slides which were obtained by following the same work-flow, but without prior treatment with the X-ray eosin stain.

Comparative analyses of the histology images with and without prior X-ray eosin staining (Fig. 9.16) yielded an additional slight pink background in Fig. 9.16e-h from the X-ray eosin stain. Despite this background, the diagnostic value of the images for histopathological analyses was not significantly deteriorated.

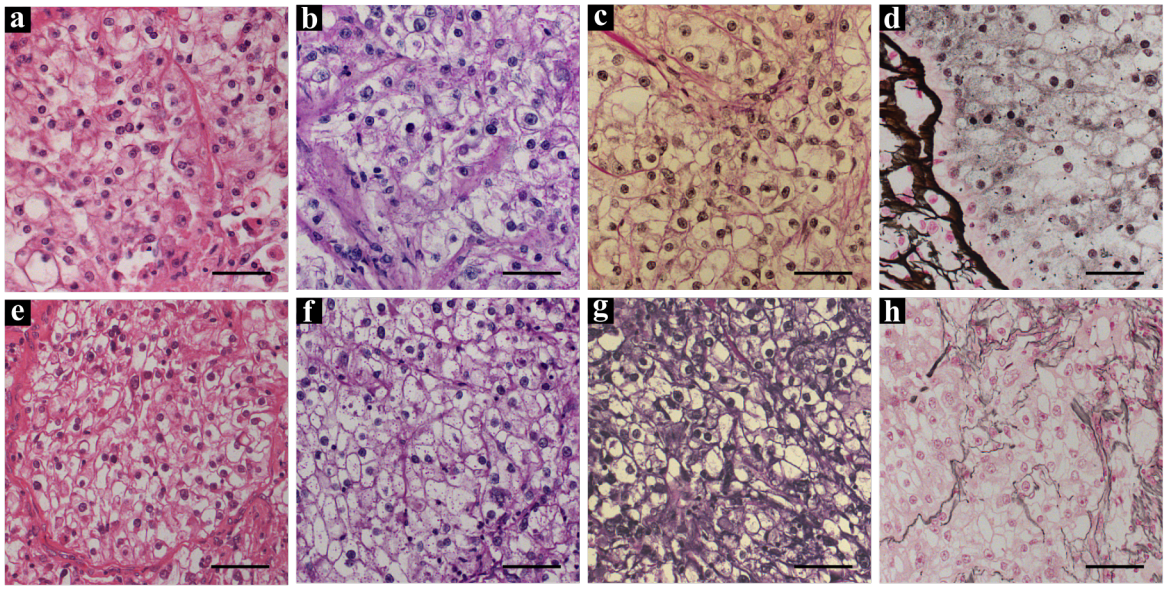

Figure 9.16: **Comparison of Histology Images of RCC Tissue (Patient E, see Section 9.2) with Different Stains.** (a)-(d) Histology images of tissue pieces without prior X-ray eosin staining. (e)-(h) Histology images of tissue pieces with prior X-ray eosin staining. The following stains were applied following the standard protocol: haematein and eosin (a), haematein (e), Periodic acid-Schiff (PAS) (b, f), Elastica van Gieson (c, g), Gomorri (d, h). Scalebars: 100 µm. Figure adapted from [Ferstl, 2020a].

9.5 Discussion

In previous work, a method was developed which combined microCT imaging and the NanoCT with the X-ray eosin stain for the purpose of 3D histology. The method was first tested on murine renal tissue [Busse, 2018b]. The prototypical studies presented in this chapter translated this method to the application on human tissue specimens [Ferstl, 2020a; Ferstl, 2020b]. The focus of these investigations was set on evaluating our method in its potential to complement and advance tissue analyses in the future.

One key element to translate this method to the examination of human tissue, was to understand the specific demands. Many tissue structures in humans are substantially larger than previously seen in the mouse kidney [Busse, 2018b]. Hence, some pathological questions in this chapter required the study of much larger tissue volumes than previously imaged for the investigation of mouse kidney tissue.
We varied the studied volumes from edge lengths of $\approx 6\,\mathrm{mm}$, as shown in Fig. 9.3a-c of the polycystic kidney, down to an edge length of $\approx 150\,\mu\mathrm{m}$ which corresponds to the size of a single human glomerulus (Fig. 9.8). We adjusted the effective voxel size accordingly from $v_{\mathrm{eff}} \approx 14.8\,\mu\mathrm{m}$ down to $v_{\mathrm{eff}} \approx 210\,\mathrm{nm}$. To cover this immense range of length scales, we combined microCT with the NanoCT. Thereby, we have shown the versatility of our method with respect to multiscale imaging similar to current histopathology techniques using LM.
Beyond that, we even demonstrated targeted correlative multiscale imaging by specifically selecting a VOI in the microCT data and analysing this tissue piece with the NanoCT. The resulting data sets allowed for co-registration of the microCT and the NanoCT volumes, as shown in Fig. 9.3.

Apart from multiscale imaging, the versatility of histopathology also includes the ability to analyse different organs and tissue types. By successfully applying our method to two other organs, the skin and the lung (Fig. 9.13 - Fig. 9.15), we have further shown that our method fulfils this aspect.

For the presented cases in Fig. 9.3 - Fig. 9.15, our method has reliably reproduced the characteristic tissue morphologies through sufficient contrast and spatial resolution.
Adequate contrast was provided through a combination of the X-ray eosin stain and propagation-based phase contrast. The X-ray eosin stain generates a 3D X-ray attenuation map in our X-ray CT data analogous to the pink eosin distribution known from conventional 2D histology. In addition to that, propagation-based phase contrast particularly highlights membranes, such as the tubular walls in Fig. 9.5 or the Bowman's capsule in Fig. 9.8. Nevertheless, it is non-trivial task to distinguish between the contrast contributions from X-ray staining and those from propagation-based phase contrast in the NanoCT data. Chapter 7 takes a closer look at this subject.
Furthermore, the NanoCT data exhibit a detail level mostly comparable to histol-

ogy (Fig. 9.8). The resolution limit of the used light microscope can be conveniently calculated using the Rayleigh criterion (Eq. 4.8) as $\delta_x \approx 550\,\text{nm}$. Opposed to that, a quantitative assessment of the resolution in the presented NanoCT data is not as easy. According to [Müller, 2017], the resolution limit of the NanoCT lies around $\delta_x \approx 100\,\text{nm}$. This value was, however, determined for a sample of a known geometry, a sphere, which was reconstructed using statistical iterative reconstruction. The resolution in NanoCT data of more complex samples reconstructed using FBP, as presented here, may strongly deviate from this value. Nevertheless, the NanoCT volume featuring a single glomerulus in Fig. 9.8 is able to clearly resolve the shape of single erythrocytes and cell nuclei comparable to the histology reference image.

Studying diseased human renal tissue, the NanoCT was able to visualise a variety of tissue architectures and enabled an assessment by pathologists. This variety ranged from foam cell aggregates (Fig. 9.3 IV), over tubular morphologies (Fig. 9.5, Fig. 9.7), alterations in the glomerular structure (Fig. 9.7, Fig. 9.8) to RCC tissue (Fig. 9.9 - Fig. 9.11). Some structures are even better reproduced in the NanoCT slices than in the histology image, such as cholesterol crystals (Fig. 9.3 VI). In contrast to that, highly relevant structures, which are merely indirectly accessible with our method are the cell nuclei. The cell nuclei, however, are crucial to identify inflammatory cells or to allow for a precise tumour grading.

Beyond these qualities that our method shares with conventional histopathology, it offers one substantial advantage: It generates full 3D volumes, where conventional histology only provides 2D images.
Not only does 3D X-ray histology enable the analysis of a large number of virtual tissue slices but also provides access to any spatial plane. This is a powerful tool for assessing tissue morphologies which vary for different vantage points. An example for this is given in the study of the single glomerulus (Fig. 9.8). A nodular mesangial thickening was only detected in one spatial plane of the NanoCT data (Fig. 9.8d).
Furthermore, some structures can only be truly understood in 3D and the thereby gained knowledge can be further used to enrich the information basis in 2D. Through segmentation of the glomerular-vascular network in Fig. 9.7, for instance, it was possible to identify the interlobular artery and the different arterioles and transfer these labels to the corresponding 2D NanoCT slices. Moreover, the NanoCT volume of RCC tissue in Fig. 9.10 helped the pathologists to get a better understanding of the actual shape of the tumour (pseudo)capsule which led to a corrected version of the shape in the corresponding 2D NanoCT slices (Fig. 9.10b-d).
The NanoCT volume of a single glomerulus enabled a highly-resolved 3D model of a nephron including the proximal tubule, the renal corpuscle and the arterioles. Beyond that, even parts of the capillaries were segmented in 3D illustrating the pathologically altered, irregular shape.

The segmentation of the capillaries, however, was accompanied by several challenges. In general, segmentation is a subjective process, which always depends on the interpretation of the operator up to a certain degree. In a glomerulus in particular, it is almost impossible to differentiate between a capillary lumen and other types of cavities, such as appearing between podocytes and capillary walls. Furthermore, the pathological altered state of the glomerulus in Fig. 9.8 as well as the sample processing may have caused ruptures in the capillary walls, thus, making the tracking of capillary lumina even more difficult. Therefore, the segmentation was performed by tracking the capillaries starting from the arterioles. Moreover, special care was taken when evaluating the segmentation and the validity of the segmented volume was verified by considering all three orthogonal spatial planes.

Finally, an essential part of our method's value for future tissue diagnostics lies in its compatibility with the current conventional histological routines. In this context, one immense benefit of our method is its non-destructive nature, since it enables subsequent coupling with other 2D histology methods such as TEM or LM.
Moreover, Fig. 9.16 proves the compatibility of the X-ray eosin stain with the standard sample processing routines of histology. For the NanoCT scans in this chapter, however, the sample processing involved CPD. This currently prevents any reintroduction of a sample into the standard histological routine of paraffin-embedding, sectioning and staining. The feasibility of measuring TEM-prepared samples with the NanoCT has been shown in the previous chapter (Chapter 8). This is particularly useful, since TEM is consulted for certain glomerulopathies. The high resolutions provided by TEM allow for evaluating the state of the glomerular basement membrane, and the podocytes, which largely contribute to the functioning of the glomerulus (Fig. 9.2).

9.6 Conclusion and Outlook

In conclusion, the findings of this chapter show that combining microCT imaging, and the NanoCT with the specific X-ray eosin stain, has the ability of accurately reproducing diverse tissue architectures in 3D. In principle, our method is non-destructive and, thus, enables subsequent imaging with other techniques. The versatility of our method has been demonstrated for a variety of pathologies affecting the human kidney, over a range of length scales, as well as for two additional organs, human skin and lung. Beyond enabling an assessment by a pathologist, it offers a wealth of information through generating 3D volumes with isotropic resolutions. It should be considered, though, that the actual medical benefits of 3D imaging on a cellular level still remain to be substantiated.

Beyond that, our method still struggles with a number of short-comings. These shortcomings may serve as inspiration for manifold future projects.

First of all, many but not all diagnostically relevant tissue structures or cellular components can be studied using the X-ray eosin stain. For instance, to detect inflammatory cells or define the tumour grade, the analysis of the cell nuclei is indispensable. A solution for this issue may be to couple multiple already existing X-ray stains and apply these on a single sample. The X-ray haematein stain, for instance, visualises the cell nuclei [Müller, 2018]. By successfully combining the X-ray eosin with the X-ray haematein stain, a more holistic histological evaluation might be facilitated, analogous to the haematein-eosin stain known from conventional histology.
Another approach to improve the histological evaluation with our method, is to expand the existing X-ray staining library by developing new specific X-ray stains [Busse, 2018a; Busse, 2020]. The vast library of staining techniques which are tailored towards a large range of applications is still the biggest advantage of conventional 2D histology over modern 3D X-ray histology.

The development of new stains and determining their specific staining behaviour is a challenging task. The NanoCT image data contains a mixture of signals consisting of attenuation and propagation-based phase contrast. Hence, it is hard to define what part of the contrast originates from the X-ray stain and what part stems from propagation-based phase contrast.
It is, thus, advisable to always first study unstained specimens of a new tissue and compare the unstained results with the data gained from stained tissue. Such experiments have been performed in the course of this dissertation on murine kidney tissue and human skin. The results are presented in Chapter 7.

Apart from staining, another important part of our methodology with room for improvement is the compatibility with conventional histopathology. While the compatibility of the X-ray eosin stain with conventional histology has been proven, the sample

processing used in this study prior to NanoCT imaging involves CPD and has so far prevented any subsequent analysis of the same sample with conventional histology. With further experiments on rehydration of CPD samples and subsequent paraffin embedding, the compatibility of our methodology and routine histology might be significantly improved.

As previously mentioned TEM is used in some cases for histology. It has already been shown for a zoological sample that TEM-prepared samples can be visualised with the NanoCT (Chapter 8). Hence, future promising research projects could entail correlative imaging with NanoCT and TEM for investigating human tissue specimens. Thereby, the NanoCT could be especially useful for defining VOIs for further TEM imaging. In the scope of such projects, glomerulopathies are particularly interesting as an application.

Translating a research prototype to a routine application, an integral aspect is time management. The X-ray eosin staining is still rather time expensive with an incubation time of 24 h. Moreover, the preparation and configuration of a NanoCT acquisition, as well as the subsequent image processing requires a lot of time and expert knowledge. Further research on reducing the incubation time of the X-ray eosin stain could be performed to reduce the time for the sample processing. To reduce the effort regarding the generation of NanoCT data, automated and reliable routines are required and a stable and user-friendly image processing framework is desirable.

A further slight short-coming of the presented method is that the resolution cannot be quantified with sufficient accuracy in the respective NanoCT data sets. Fiducial markers with defined structures in both NanoCT scans and histology images to determine the image PSF would allow for a better comparison of resolutions. However, fiducial markers take up space in the already limited FOV of the NanoCT and may cause limitations in the maximum achievable magnification. A better solution to this may be achieved by determining the relation between the X-ray spot and the electron spot size on the X-ray target of the NanoTube. Thereby, the electron spot calibration of the NanoTube would facilitate a resolution estimation in the projection images of each NanoCT data set.

Moreover, the presented NanoCT data of human skin and lung tissue is only the first step along the way of exploring the potential of our method for these organs. In a next step, it is crucial to obtain an expert assessment of the images by a trained pathologist. This may then lead to further studies of skin and lung tissue with pathological alterations, such as skin cancer and lung tumours.

Finally, to further explore the potential of this methodology in a medical context, a study may be conducted involving a statistically relevant number of patients with the focus on one specific pathology. For the impact of such a study, it is crucial to beforehand define a pathological question, which would significantly benefit from 3D

imaging. Thereby, the reliability of the method can be assessed and improvements regarding efficiency can be introduced and evaluated.

9.7 Materials and Methods

9.7.1 Study Design and Tissue Specimens

All studies in this chapter were approved by the local ethics committee.

For the study of diseased human renal tissue, presented in Section 9.2 and Section 9.4, the resection specimens were obtained from the Department of Pathology, Klinikum rechts der Isar, Technical University of Munich. Thereby, five patients with different pathologies were chosen: Patient A (64 years old, male) was diagnosed with polycystic kidney disease. In Patient B (68 years old, female) tubular degenerations were detected due to an obstructed urinary tract. The diagnostic report of Patient C (55 years old, male) states a post-operative shock. Patient D (49 years old, male) and patient E (78 years old, female) were both diagnosed with clear-cell RCC. Patient D was classified as pT1b R0 G2, and patient E as pT3b V2 pNx RX G2/3.

The skin specimens, which are presented in Section 9.3, were provided by the Group of Prof. Christina Zielinski of the TranslaTUM and Institute for Virology, Technical University of Munich. The lung tissue specimen from Section 9.3 was obtained from Gregor Zimmerman, Department of Pneumology, Klinikum rechts der Isar, Technical University of Munich.

9.7.2 X-ray Eosin Staining

The tissue specimens provided for the previous studies were formalin-fixed with 4% phosphate-buffered saline formalin solution. The subsequent sample processing routine was performed according to the steps described in [Busse, 2018b; Ferstl, 2020a; Ferstl, 2020b]. Briefly, these steps involve acidification, a washing step with phosphate buffered saline solution and staining with eosin Y over a time period of 24 h. Afterwards, the samples were stored in an ethanol vapour phase [Busse, 2018b; Ferstl, 2020a; Ferstl, 2020b].

9.7.3 MicroCT Acquisition and Image Processing

All microCT data included in this chapter (Fig. 9.3a-d, Fig. 9.4, Fig. 9.6) were measured with the same acquisition parameters at the Xradia Versa 500 (Zeiss): Over an angular interval of 360°, 1,601 projections were acquired using a peak voltage of 50 kV. An effective voxel size of $v_{\text{eff}} \approx 14.8\,\mu\text{m}$ was selected, at an exposure time of 2 s and the 0.39×-objective. No filter was used during CT acquisition. The total acquisition time per CT scan was ≈ 2 h.

The image processing of the microCT data was carried out using the NanoCT image processing framework (see Section 5.3) according to the descriptions in [Ferstl, 2020b]. The processing routine included a correction for ring and intensity fluctuation artefacts, FBP-reconstruction, centre-shift correction, as well as correlation-based projection alignment. The presented microCT volume renderings were created with Avizo Fire 8.1 (ThermoFisher Scientific).

9.7.4 NanoCT Sample Preparation

Based on the information gained in the microCT data, VOIs were selected for further investigation with the NanoCT. From these VOIs tissue pieces were cut to obtain an edge length in the range of $0.5 - 1\,\text{mm}$. These tissue specimens were then dehydrated in an ethanol series and critical-point dried (CPD), as explained in [Busse, 2018b; Ferstl, 2020a; Ferstl, 2020b].

9.7.5 NanoCT Acquisition and Image Processing

For all NanoCT data in this chapter, an acceleration voltage of 60 kV and a detector threshold of 2.7 keV were used. In each CT scan, 1,599 evenly distributed projections were acquired over a rotation angle of 360°. The remaining acquisition parameters are summarised in Table 9.1. To explore a larger volume in the vertical direction, multiple NanoCT sub-volumes were acquired for different vertical positions of the sample. The number of sub-volumes N_{vol} and the resulting total acquisition time of the combined volume $t_{acq,tot}$ are included in Table 9.1. For more in-depth information on tomography acquisition with the NanoCT, the reader is referred to Section 5.2 or the Appendix A.1.

The image processing of the NanoCT data sets was performed according to the routine described in Section 5.3. For the NanoCT data presented in Fig. 9.8, the sparsity-metric based projection alignment was used prior to reconstruction. All other NanoCT data in this chapter were corrected using the cross-correlation based projection alignment approach. For deblurring of the NanoCT data in Fig. 9.9 a Richardson-Lucy deconvolution was employed, while the rest of the NanoCT data was deblurred according to Gureyev's approach. NanoCT data consisting of multiple sub-volumes were combined with a stitching algorithm (Section 5.3).

9.7.6 Histology

The histology images displayed in Section 9.2 and Fig. 9.16e-h, were obtained from tissue fragments of the X-ray eosin stained tissue specimens. The tissue fragments were analysed in the Pathology Lab, according to standard protocols, as described in

Organ		Kidney								Skin		Lung
Figure		9.3	9.5	9.7	9.8	9.9	9.10	9.11a-d	9.11f-i	9.13	9.14	9.15
Patient		A	B	C	C	D	D	D	E	-	-	-
v_{eff}	[nm]	1400	480	890	210	730	1250	900	900	430	1400	1250
r_{e}	[nm]	340	320	320	360	260	350	240	230	320	320	350
t_{exp}	[s]	2	5	3	8	2	2	2	2	3	1	2
$t_{\text{acq,i}}$	[h]	2	4	2.5	5	2	2	2	2	2.5	1.5	2
N_{vol}		1	1	3	7	1	3	4	2	1	1	1
$t_{\text{acq,tot}}$	[h]	2	4	7.5	35	2	6	8	4	2.5	1.5	2

Table 9.1: **NanoCT Acquisition Parameters.** The listed parameters only concern the NanoCT data in the specified figure. If no panels within the figure are specified, the parameters are the same for all NanoCT data in this figure. Legend: r_{e}: the electron spot radius on the X-ray target ($0.5 \cdot$ FWHM) prior to acquisition, t_{exp}: exposure time for one projection image, $t_{\text{acq,i}}$: acquisition time of the i-th sub-volume, N_{vol}: number of sub-volumes for extending the vertical FOV, $t_{\text{acq,tot}}$: acquisition time for the total combined NanoCT volume.

[Ferstl, 2020a] and [Ferstl, 2020b]. The protocols include paraffin embedding, sectioning into thin slices (3 µm) with a microtome, deparaffinisation, rehydration, staining, dehydration, mounting and sealing with a cover slip.

The final histological slides were analysed using a light microscope (Zeiss, AxioImager II) with a dry objective lens, which was equipped with AxioVision software. The used objective magnification lenses are listed in Table 9.2, with the 10×-objective lens featuring a NA-value of 0.3 and the 20×-objective lens a NA-value of 0.5.

As mentioned in Section 4.2 Eq. 4.8, the resolution limit of a microscope can be calculated with the Rayleigh-criterion given the wavelength and the NA of the objective lens. Assuming a mean visible light wavelength of 450 nm and the 0.5 NA of the 20×-objective lens, we obtain 549 nm as the minimum resolvable feature size.

Figure	9.3e	9.3f	9.5e, k	9.7f	9.8f	9.9e, k	9.10e	9.11e, k	9.16
Objective	5×	20×	20×	10×	20×	20×	10×	10×	20×

Table 9.2: **Light Microscopy Parameters of the Histology Reference Images.** All used objective lenses were dry lenses.

The histology images presented in Section 9.3 were retrieved from two literature sources

[Cerroni, 2016; Tomashefski, 2008]. The used objectives of the histology images in Fig. 9.13b, Fig. 9.14d, e, and Fig. 9.15d are unknown and, hence, not included in Table 9.2.

9.7.7 Scientific Contributions

The concept of the human renal tissue study was devised by Franz Pfeiffer, Wilko Weichert, Madleen Busse, Melanie Kimm and Simone Ferstl. The X-ray eosin staining routine on the human kidney tissue specimens was carried out by Toni Bürkner and the X-ray eosin staining on the human skin and lung tissue specimens was done by Madleen Busse. The subsequent microCT acquisition and image processing was performed by Simone Ferstl. The NanoCT sample preparation was performed partially by Toni Bürkner and partially by Madleen Busse. The NanoCT acquisition and image processing was done by Simone Ferstl, except for the two data sets shown in Fig. 9.9, which were measured and reconstructed by Mark Müller. The segmentation and the generation of 3D renderings of the NanoCT data with Avizo Fire was performed by Simone Ferstl. The histological sample processing was performed by Irina Eskina and the histology images of the human renal study were acquired by Melanie Kimm. The histology images of the human skin and lung tissue specimens were obtained from [Cerroni, 2016; Tomashefski, 2008]. The histopathologically relevant structures in the human renal tissue study were assigned by Enken Drecoll and Katja Steiger and the resulting pathological annotations were reviewed by Wilko Weichert. The histological assignment of the human skin and lung tissue data was performed by Simone Ferstl. The final presented figures were generated by Simone Ferstl.

10 Summary

Several projects have been carried out throughout this work. In this summary, the NanoCT is set in context to other microscopy methods in Section 10.1. After that, a comprehensive overview is provided, focusing on the key message from each project (Section 10.2). Thereby, connections between the findings from different studies are established. Finally, the outlook section of this chapter (Section 10.3) offers inspirations for future work with the NanoCT. For a more detailed elaboration of the various topics, the reader is referred to the respective chapters (Chapter 6-9).

10.1 The NanoCT in the Field of Microscopy

In the introduction of this thesis (Chapter 1), various microscopy techniques were mentioned, from light over electron to X-ray microscopy. The following sections provide an overall comparison between these methods and the NanoCT, with the intention to create a better understanding of how the NanoCT fits into this vast field of research.

10.1.1 The NanoCT versus Light and Electron Microscopy

Compared to electron and light microscopy, the biggest advantage of X-ray microscopy beyond the soft X-ray regime (including the NanoCT) is the ability to non-destructively generate 3D information of relatively large samples with diameters above 100 µm. Electron and light microscopy are very limited regarding the sample thickness. Therefore, they often resort to destructive methods, such as sectioning, ablation, optical clearing or even corrosion casting to obtain 3D data of samples exceeding the penetration depth of the respective radiation [Bárcena, 2009; Keller, 2012; Keller, 2008; Albers, 2018]. With the help of modern single-electron-counting detectors, electron microscopy achieves, however, by far the highest spatial resolutions down to several Å [Li, 2013]. Beyond conventional diffraction-limited light microscopy, with an ultimate resolution limit of 230 nm[1], even super-resolution techniques struggle to resolve structures smaller than 50 nm [Kremer, 2015]. Nevertheless, light microscopy excels due to the enormous

[1] This was calculated from the Rayleigh criterion Eq. 4.8 assuming a minimum wavelength of visible light of 380 nm and a NA of 1.

variety of highly-specialised stains and fluorescent dyes which allow for highlighting specific morphologies and functional structures ranging from single actin filaments to cell nuclei [Suvarna, 2013; Giepmans, 2008]. Unlike electron microscopy, light microscopy enables the imaging of alive cells and thereby tracking structures over a certain period of time [Giepmans, 2008]. Exposure times per projection image of more than 1 s prevent the NanoCT from measuring alive specimens.

In the context of two projects in zoology and in 3D histology (Chapter 8, Chapter 9), a more specific evaluation of the NanoCT was performed versus two established imaging methods: ss-LM in zoological research and standard full-field LM in the field of histopathology. Thereby, direct insights into the functioning, advantages and weaknesses of each method were gained.
For zoological research, the biggest appeal of imaging with the NanoCT compared to the established method of ss-LM lies in isotropic 3D resolutions in the resulting volume data, and the preservation of the specimen's true proportions, without involving additional sample processing (Chapter 8). While ss-LM provided slightly higher spatial resolutions in the sectioning plane, the NanoCT data was free of alignment and brightness artefacts which are typical for sectioning-based 3D imaging techniques. These artefacts severely degraded the data quality in the ss-LM data in any spatial plane other than the sectioning plane.
The 3D histology study in Chapter 9 showed that 3D X-ray histology still has a long way to go to compete with the diversity and versatility of routine histopathology in terms of staining techniques. In return, the NanoCT offered the typical advantages associated with 3D X-ray imaging to reproduce inner morphologies in any spatial plane under any arbitrary angle and to facilitate the tracking of structures in 3D, such as tubules or blood vessels.

10.1.2 The NanoCT and X-ray Nanotomography

In the field of X-ray nanotomography, the NanoCT belongs to the category of geometry-based techniques, as opposed to optics-based approaches (Chapter 4). Each of these fundamentally different concepts comes with their own specific set of benefits and drawbacks which will be discussed in the following.
To this day, optics-based approaches still lead the field in terms of spatial resolution ($\delta_x \approx 15\,\mathrm{nm}$) [Chao, 2005]. On the downside, all optics-based systems share two main flaws: the respective optics components reduce the X-ray flux more or less drastically and the finite DOF limits the imaging FOV in beam direction. Furthermore, many X-ray optics, such as FZP and Bragg magnifiers, are very selective regarding the energy of the incident X-ray beam. Using the polychromatic X-ray spectrum of a laboratory X-ray source, this further diminishes the efficiency of the imaging system. Moreover, compound lenses and KB mirrors have very long focal lengths which renders them

impractical for laboratory applications. These characteristic properties tie most X-ray optics-based devices to the high brilliance of synchrotron sources. Synchrotron facilities, however, require a large amount of space, financial resources and are not very accessible compared to laboratory systems.
From all X-ray optics-based microscopes, FZP systems have been implemented with most success into laboratory environments. For instance, the Xradia Ultra from Zeiss promises resolutions even below 50 nm. However, FZP-based laboratory devices entail very long acquisition times, have a rather limited DOF which depends on the resolution limit of the FZP and the fabrication process of FZPs becomes increasingly difficult towards higher X-ray energies [Withers, 2007].

In contrast to that, cone-beam geometry-based systems, such as the NanoCT, have an infinite DOF, and allow for a seamless adjustment of the magnification, which grants these setups a high versatility concerning sample sizes. This versatility of the NanoCT was demonstrated in both the study of the sea cucumber specimen *L. cf. minuta* in Chapter 8, where the relatively large sample with dimensions of around 1 mm × 0.5 mm × 0.5 mm was measured in its entirety, and in the multiscale 3D histology study in Chapter 9, where numerous tissue specimens were studied with different diameters from 150 µm to 1 mm. Compared to that, the previously mentioned Xradia Ultra from Zeiss only offers a maximum FOV of 65 µm. Beyond that, the NanoCT uses the entire energy bandwidth of the available X-ray spectrum for imaging and generally faces less limitations in terms of X-ray energy. The ultimate resolution limit of such systems is given by the X-ray source spot. Fine X-ray source spots, however, always come at the expense of X-ray flux. A true disadvantage of cone-beam systems is the small distance between X-ray source and sample which leaves only little room for additional equipment such as environmental sample chambers.
An example for a commercial cone-beam geometry X-ray microscope is the Skyscan 2214 from Bruker. Here, the technical specifications advertise resolutions down to 500 nm. These resolutions, though, have only been shown for projection images and are not necessarily equivalent to the resolution in the reconstructed volume data. Compared to that, projection images of the NanoCT have achieved resolutions below 200 nm [Müller, 2017].

10.2 Results of this Work

The two main pillars this work is built on are the advancement of the NanoCT system and the exploration of novel fields of application. The advancement of the NanoCT includes characterisations of the system and the optimisation of processes related to software and acquisition routines (Chapter 5 - 7). Applications were further developed in the field of zoology with special focus on correlative microscopy (Chapter 8), and in the field of 3D histology with respect to pathological alterations in human tissues (Chapter 9).

10.2.1 Advancements of the NanoCT

In the process of advancing the NanoCT, the image processing routine was improved (Chapter 5.3), characterisation measurements were carried out (Chapter 6), and comparative analyses were performed regarding propagation-based phase effects in NanoCT data of unstained and X-ray stained samples (Chapter 7).

An integral part of the NanoCT framework is the image processing routine (Chapter 5.3), since it substantially contributes to determining the quality of the resulting volume data. In order to cope with mechanical instabilities, a more stable alternative to the cross-correlation-based projection alignment algorithm based on [Hehn, 2019] was integrated into the NanoCT image processing work-flow to be applied on the data in Chapter 8 and Chapter 9. This novel alignment routine not only allows for optimising detector shifts from the ppp but all parameters of the setup geometry, such as tilt angles of the rotation axis or source-sample distances. During the application of the novel alignment routine it was experienced that the pre-processing of the projection images has an immense influence on the outcome of the projection alignment.
As already mentioned in [Müller, 2019], one major drawback of the original image processing work-flow was the routine for deblurring and phase retrieval, which took over 24 h and was associated with producing a vast amount of excess data. The successful integration of a new deblurring method based on the approach of Gureyev et al. [Gureyev, 2004] allowed for replacing the time-intensive iterative RL-deconvolution by a fast and simple sum operation. Combined with a parallel implementation of the phase retrieval, the previously tedious process which took many hours is now carried out in a matter of seconds.

For optimising the quality of future NanoCT data, Chapter 6 presented results from various experiments characterising the setup. While these experiments largely differed and ranged from quantisations of the electron spot size in the NanoTube, over spectral measurements to imaging of an absorption phantom, they all investigated effects from modifying the acceleration voltage. In these studies, the resolution and the CNR were

used as quality criteria.
The empirical findings and theoretical considerations suggest a number of positive effects for a reduced acceleration voltage down to 30 kV: beyond reducing the minimum achievable X-ray spot size at a constant target current, smaller acceleration voltages contribute to a relative gain in CNR particularly in soft-tissue samples and to a reduction of cupping artefacts in strongly absorbing materials. The experiments were inconclusive though regarding the influence of the acceleration voltage on the X-ray flux. Due to the very thin tungsten X-ray target of the NanoTube ($d \approx 500\,\mathrm{nm}$), larger acceleration voltages are not necessarily associated with higher X-ray flux at a constant target current. Furthermore, a change of the acceleration voltage causes a different X-ray spectrum to be perceived by the sample, while resulting in a very similar spectrum detected by the Pilatus.

In the image formation process of the NanoCT, both X-ray staining and propagation-based phase contrast play an important role. To gain a better grasp on these effects in the NanoCT data, unstained and X-ray eosin stained soft-tissue specimens were analysed with the NanoCT (Chapter 7).
It was striking that propagation-based phase contrast alone without any X-ray staining revealed a considerable amount of information on the tissue structure of CPD samples. While the results indicated that the X-ray eosin stain had a noticeable influence on the resulting soft-tissue contrast, this influence was significantly smaller than previously assumed based on microCT data of X-ray eosin-stained wet murine renal tissue [Busse, 2019]. Nevertheless, it clearly changed the way the tissue morphology was visualised in the NanoCT data and added an additional layer of information by highlighting specific structures.
Investigating the propagation-based phase effects more closely, it was observed that the propagation distance and the X-ray source spot size directly impact the strength of the edge enhancement. The enhancement of the soft-tissue contrast gained from these effects, however, strongly depends on the applied filtering strength of Paganin's phase retrieval.

To conclude, beyond contributing to a more stable and efficient image processing routine, these results complement the fundamental ground-work on which future NanoCT projects may thrive on.

10.2.2 Applications

In previous work, two main fields of application for the NanoCT have emerged: zoology and 3D histology [Müller, 2018; Busse, 2018b; Müller, 2017; Gross, 2019]. In the course of this work, methods were further developed and new research projects were established in these fields.

The potential of the NanoCT for zoological research to study tiny animals has been demonstrated on CPD samples [Müller, 2017; Gross, 2019]. For many zoological studies with correlative microscopy, resin-embedding of samples is a prerequisite. The usefulness of the NanoCT for correlative microscopy particularly with TEM and ss-LM was proven through imaging of two different resin-embedded zoological specimens (*L.* cf. *minuta*, *R.* cf. *eliator*) (Chapter 8). The resulting NanoCT data were co-registered and compared with ss-LM volumes generated from the same specimen of *L.* cf. *minuta*. Throughout this project, the challenges arising from measuring a resin-embedded sample with very high resolutions were particularly interesting. The resin-embedding significantly dampened propagation-based phase effects and reduced the contrast enhancement from phase retrieval. The larger size of the sample due to the surrounding resin made it more difficult to reach high magnifications in the NanoCT. Finally, most edge features appeared less pronounced due to the resin-embedding which complicated the projection alignment prior to FBP reconstruction. This inspired the development of the novel sparsity-based projection alignment routine (Chapter 5.3).

In the field of 3D histology, a method combining the NanoCT with the X-ray eosin stain which had been introduced and tested on murine renal tissue [Busse, 2018b] was translated to human tissues (Chapter 9).
The main challenge in this project was to rethink several strategies. In the previous study [Busse, 2018b] with murine renal tissue, rather small tissue samples were investigated with the NanoCT ($\leqslant 400\,\mu m$). Structures in human renal tissue are in general significantly larger. For instance, a human glomerulus has a size of approximately $150\,\mu m$. A glomerulus in a mouse kidney has a diameter of around $50\,\mu m$.[2] Hence, to properly account for the morphology of human tissue, mostly larger tissue specimens with diameters in the range of $[400\,\mu m; 2\,mm]$ were analysed.
Thereby, the precise 3D morphology for diverse pathologies of human renal tissue and further organs including skin and lung were visualised. Moreover, correlative multiscale 3D imaging was demonstrated by coupling microCT with the NanoCT. These results illustrated the immense versatility of both the NanoCT and the X-ray eosin stain. The actual medical benefit of 3D imaging with sub-cellular resolutions though still remains to be explored.

[2]This size was estimated based on the NanoCT data of a human glomerulus in Fig. 7.1 and the NanoCT data of murine renal tissue in Fig. 7.4.

10.3 Outlook

Here, the most important ideas for further optimising the NanoCT are presented, as well as potential future research projects. For more details the reader is encouraged to consult the outlook sections of the previous chapters.

Recently a new NanoTube version was integrated into the NanoCT including a new focusing software which caused a reduced image quality in the newly acquired data. While there is a large variety of potential error sources, the artefacts in the reconstructed volumes of the new NanoCT data point towards issues regarding the setup geometry. According to several stability measurements, external vibrations from the surrounding environment could be excluded as origin of the problem. One of the most probable causes for such issues are instabilities of the X-ray source spot position or size. Furthermore, traction forces from the cables of the piezo sample alignment stages are known to lead to positional shifts of the sample during a tomography scan.
To get a better impression of these issues, one approach is to measure the CNR phantom from Chapter 6. As its geometry is known and simple, it can help to deduce which geometry parameters cause the difficulties from such data sets. A different approach to address this problem are stability measurements of the NanoTube X-ray source spot position and size over time by measuring a resolution pattern at a constant sample and detector position.

As soon as the NanoCT again provides high-quality data, the findings from Chapter 6 and Chapter 7 can be used to further advance the system and its associated processes. In an attempt to further explore optimum imaging parameters, the acceleration voltage was investigated (Chapter 6). Clearly smaller electron spots were achieved on the X-ray target for smaller acceleration voltages. In theory, this should lead to smaller X-ray source spots as well. This, however, still requires empirical verification. This can be done by a quantitative study of the X-ray source spot for specific electron spot sizes on the X-ray target for different acceleration voltages (60 kV vs. 40 kV or 30 kV). By simultaneously recording both the target current and the resulting X-ray flux on the detector these measurements would also clarify what influence the acceleration voltage has on the resulting X-ray flux.
In the future, such a study would enable to estimate the resolution in a NanoCT data set based on the electron spot size. This would proof particularly valuable for further projects in 3D histology and zoology. Due to the intricate internal structures of the previously imaged specimens, only a qualitative evaluation of the image resolution was possible in the NanoCT data. This was illustrated by the case of *L.* cf. *minuta* (Chapter 8). Since the resolution is the central parameter in the field of microscopy, a quantitative estimation on the resolution in the projection images, comparable to the

Rayleigh criterion in full-field light microscopy, would be immensely helpful.
Moreover, previous work [Müller, 2019] found that a detector threshold of $(6-8)$keV might be favourable for an improved image PSF. These assumptions also require further experiments for confirmation.
After defining the optimum imaging parameters, with respect to the acceleration voltage and the detector threshold, comparative analyses between the old parameter values and the modified values can be performed assessing NanoCT data of a typical soft-tissue sample.

The experiments on propagation-based phase contrast and X-ray staining in the NanoCT yielded a number of interesting findings (Chapter 7). It can be expected that continuing this study with a larger diversity of tissue types and X-ray stains will prove valuable to provide a platform for comparing different stains.
For future research on novel X-ray staining routines for the NanoCT, it is thus highly recommended to take a reference NanoCT scan of unstained tissue as a standard procedure in the development process.

During the projects for zoology (Chapter 8) and 3D histology (Chapter 9), some of the upcoming ideas regarding future work were rather similar, despite being motivated by different fields of research.
One tool, which was used in every project with the NanoCT was X-ray staining. Since the field of X-ray staining is relatively young compared to that of histological staining, there is still a lot of room for growing the library of available X-ray stains. In particular, more X-ray stains with a selective binding behaviour are needed for highlighting functional entities inside of tissue.
Furthermore, more research on combining multiple staining routines for one sample should be conducted. During the studies of diseased human renal tissue in Chapter 9, it became clear that the X-ray eosin stain helps to visualise most but not all relevant structures. For instance, the cell nuclei, which are not reproduced with the X-ray eosin stain, are crucial for defining the grade of a tumour and for identifying inflammatory cells in tissue. Unifying the previously introduced X-ray haematein stain [Müller, 2018] which specifically highlights cell nuclei with the X-ray eosin stain may allow for histological analyses similar to the haematein-eosin stain in conventional histology. While first attempts demonstrated that this is no trivial task, it holds great potential to sustainably increase the appeal of 3D X-ray histology and to create highly-relevant applications for innovative energy-resolved imaging techniques such as spectral X-ray microscopy.
Moreover, a large variety of stains could be tested for future applications with the NanoCT. Osmium tetroxide did not provide adequate contrasts in the NanoCT data for *R.* cf. *eliator*. Other promising X-ray stains which are frequently used in zoology are

PTA, uranylacetate, and ruthenium red [Sombke, 2015; Metscher, 2009; Jahn, 2018]. Furthermore, the X-ray eosin stain is very promising to be tested on zoological samples, based on the previous results achieved with histology specimens. Vice-versa, the above-mentioned stains which are established in zoology could be applied to histology specimens in return.

As the results from Chapter 8 show, the NanoCT is very useful for correlative approaches with other microscopy techniques. While no actual correlation between NanoCT and TEM data has been performed yet, coupling the NanoCT with TEM may prove as a valid alternative to various CLEM approaches.
For 3D histology, such an approach could turn out particularly useful with respect to studying glomerulopathies. TEM is a popular tool in conventional histology when it comes to the analysis of pathological alterations of the glomerular membranes and podocytes. For such a project, however, a collaboration with one of the few glomerulopathy specialists is indispensable.
For sectioning-based microscopy methods, the NanoCT data may serve as a valuable reference for the original sample proportions. Moreover, for FIB-SEM, the NanoCT could provide an overview over a sample and define VOIs for further higher resolution scans.

Despite Chapter 8 showing the feasibility of visualising resin-embedded samples with the NanoCT, CPD samples are considerably easier to handle and generally lead to better results. However, up until now, the process of CPD on a sample prevented any subsequent measurements with other imaging methods, such as performed in 2D histology, and is not suitable for all types of samples (bone, cartilage). Hence, there are still some improvements needed with respect to compatibility of CPD samples with histology and other microscopy methods. In order to achieve this goal, experiments on rehydration of CPD samples and subsequent paraffin or resin embedding need to be pursued.

In Chapter 9, beside an extensive study on diseased human renal tissue, some preliminary NanoCT data of human skin and lung tissue were presented. The next step regarding the study of lung and skin, is to consult pathologists for an expert analysis of the visualised structures.
The NanoCT data of human renal tissue was capable of reproducing most of the 3D tissue architecture precisely. Thereby, the true gain of 3D imaging for diagnostics was, however, not discovered. In order to reach a higher impact for medicine, explicit questions where 3D imaging is largely beneficial for pathological diagnostics are to be defined first. One of these questions can then be addressed in a study featuring a statistically relevant number of cases.

Beside the previously described ideas, there is an increasing number of offers for future collaborative projects. These projects span a wide variety of fields from analyses of

nematode inclusions in amber for the Swedish Museum of Natural History over 3D imaging of mould hyphae for process systems engineering to zoological studies of snail specimens, the tun stage in tardigrades or the slime glands in Onychophorans.

Beyond the results presented in this work, the long list of future projects with the NanoCT highlights its potential, its versatility and its immense value for future research. While the question remains regarding the value of X-ray nanotomography for medical purposes, I believe that research microscopy facilities, such as ScopeM[3] at the ETH Zürich, may truly benefit from an imaging device like the NanoCT as an additional tool to further complete their range of available microscopy techniques.

[3]Scientific Center for Optical and Electron Microscopy

Supporting Information

A.1 Tomography Parameters

Here, the most important tomography parameters are explained and the respective values used in this work are presented in Table A.1, Table A.2 and Table A.3.

NanoTube Parameters

For all NanoCT results presented in Chapter 8 and 9, the NanoTube was operated at an acceleration voltage of U_{acc}= 60 kV and at the maximum available emission current I_0 = 100 µA. In Chapter 6, different U_{acc}-values are explored. The NanoTube was focused to achieve an optimum spot size stability whereby fluctuations of the optimum focus current value were kept within a defined tolerance value of $\Delta I_{foc,opt} \leqslant 0.3$ mA (Table A.1).

Parameter	U_{acc} [kV]	I_0 [µA]	$\Delta I_{foc,max}$ [mA]
Value	60	100	0.3

Table A.1: **NanoTube Parameters.** U_{acc}: acceleration voltage. I_0: emission current at the cathode. $\Delta I_{foc,max}$: maximum acceptable fluctuation of the optimum focus current over time.

Pilatus Parameters

The detector threshold E_{low} throughout this work was generally set to the minimum value of 2.7 keV to maximise the detected X-ray flux. This is, however, associated with stronger charge-sharing effects and a larger detector PSF. For more information on this subject the reader is referred to Müller et al. [Müller, 2019].

Another relevant aspect regarding tomography with the Pilatus detector, are the unresponsive gaps between the detector modules. For a detector which is perfectly aligned to the optical axis, the detector gaps cause a dark ring in the axial slices of the re-

constructed volume. In the acquisition routine used in this work, these ring artefacts are avoided via a random, horizontal typewriter shift. In this technique, the detector is moved horizontally from its central position using a random shift of N_{tw} in pixel: $|N_{\mathrm{tw}}| \leqslant 40\,\mathrm{pixel}$ (Table A.2). Another approach to address this problem, is to introduce a constant horizontal detector offset from the optical axis. However, in case of the NanoCT, the typewriter approach is superior.

Parameter	E_{low} [keV]	$\lvert N_{\mathrm{tw}}\rvert_{\mathrm{max}}$ [pixel]
Value	2.7	40

Table A.2: **Pilatus Parameters.** E_{low}: low energy threshold of the Pilatus. $N_{\mathrm{tw,max}}$: maximum value of the typewriter shift.

General Acquisition Parameters

The values of the following parameters are displayed in Table A.3.

Number of Projection Images: For a tomography, a series of projection images is recorded over an angular range of 360°. To avoid angular under-sampling of the sinogram, the Nyquist sampling criterion defines a minimum number of projections N_{proj}:

$$N_{\mathrm{proj}} = \frac{\pi}{2} N_{\mathrm{FOV}}, \tag{A.1}$$

with N_{FOV} the number of sampling points in each projection [Natterer, 1986; Russo, 2017]. In the NanoCT, this is the number of pixels in the horizontal, effective FOV of the detector. We assume this value as $N_{\mathrm{FOV}} \approx 1000$, since the detector provides 1475 pixels in the horizontal plane with 1000 effectively used pixels and 475 pixels considered as surplus to compensate for instabilities during acquisition. This gives us a minimum number of projection images of $N_{\mathrm{proj}} \geqslant 1,571$. In the NanoCT data, included in this work, a projection number of $N_{\mathrm{proj}} = 1,599$ was chosen.

Number of Flat-Field Images: Apart from the projection images with the sample in the FOV, a number of empty images without the sample ($N_{\mathrm{ff}} = 81$), so-called flat-field images, was taken in the beginning of a NanoCT scan. With such flat-field images, the projection images can be corrected for fluctuations of the detector pixel response and for the intensity distribution of the X-ray beam. In some other acquisition routines, flat-field images are taken after every N-th projection image (with $N \in \mathbb{N}$). This, however, entails moving the sample out of the FOV which may introduce deviations in

the sample position throughout the acquisition and, thus, cause severe inconsistencies in the tomography data.

Exposure Time: The exposure times for each of the projection and flat-field images lie in the range of $(1-8)$s for the NanoCT data presented in this thesis. As the X-ray flux quadratically decreases for increasing detector distances, the exposure time must be also increased quadratically to ensure the same SNR. For longer exposure times, however, effects from mechanical instabilities and source spot drifts are much more severe. Therefore, the exposure time value t_{exp} should be always chosen to be as short as possible and as long as necessary.

Source-Axis Distance and Source-Detector Distance: When adjusting the desired magnification, always the minimum possible d_{sa}-value, and d_{sd}-value should be selected. By minimising the source-detector distance, the exposure time can be reduced considerably.

Field of View, Effective Voxel Size and Sample Size: The cone-beam geometry of the NanoCT generates a strong connection between the FOV of a data set and the effective voxel size v_{eff}.

Furthermore, the algorithms which perform the projection alignment for CT reconstruction require strong, distinct edges. These so-called alignment algorithms are crucial to correct for motion blurring to generate high-quality high-resolution data. The higher the magnification, the more important these routines become. Since most measured samples in the NanoCT consist of soft-tissue and rather low-absorbing materials, the most distinct edges can be found at the interface of the sample to air. As a result, a successful projection alignment requires the sample to completely lie in the imaged FOV. This represents the NanoCT's biggest weakness: small voxel sizes cannot be reached for large samples.

At the beginning of a new project, it is advisable to assess whether it is more important to obtain a small v_{eff}-value or to investigate a large sample. In general, when first investigating a new sample, it is beneficial to acquire a set of successive tomography scans using the same parameters, but varying the source-detector distances and thus exploring different magnifications. It can be clearly observed throughout the results presented in this work that a large variety of v_{eff}-values and FOVs was chosen to answer the respective scientific question. Thereby, the voxel sizes ranged from v_{eff} 210 nm to 1.4 µm.

Parameter	N_{proj}	N_{ff}	t_{exp} [s]	d_{sa} [mm]	d_{sd} [mm]	v_{eff} [µm]
Value	1,599	81	1-8	0.7-2.0	200-900	0.21-1.40

Table A.3: **General Acquisition Parameters.** N_{proj}: number of acquired projections over an angular range of 360°. N_{ff}: number of recorded flat-field images. t_{exp}: exposure time for one projection image. d_{sa}: source-axis distance. d_{sd}: source-detector distance. v_{eff}: effective voxel size.

A.2 Complex Refractive Index of Relevant Materials

Here, the attenuation and the phase coefficient from the complex refractive index (Eq. 3.9, Eq. 3.11) are plotted for different materials over the typical energy range of the NanoTube spectrum for $U_{\text{acc}} = 60\,\text{kV}$ (energy $\in [5\,\text{keV}; 60\,\text{keV}]$).

The values presented in Fig. A.1 and Fig. A.2 were retrieved from Xraylib according to [Schoonjans, 2011]. For soft tissue and cortical bone the compound data was used according to the ICRP (International Commission on Radiological Protection).

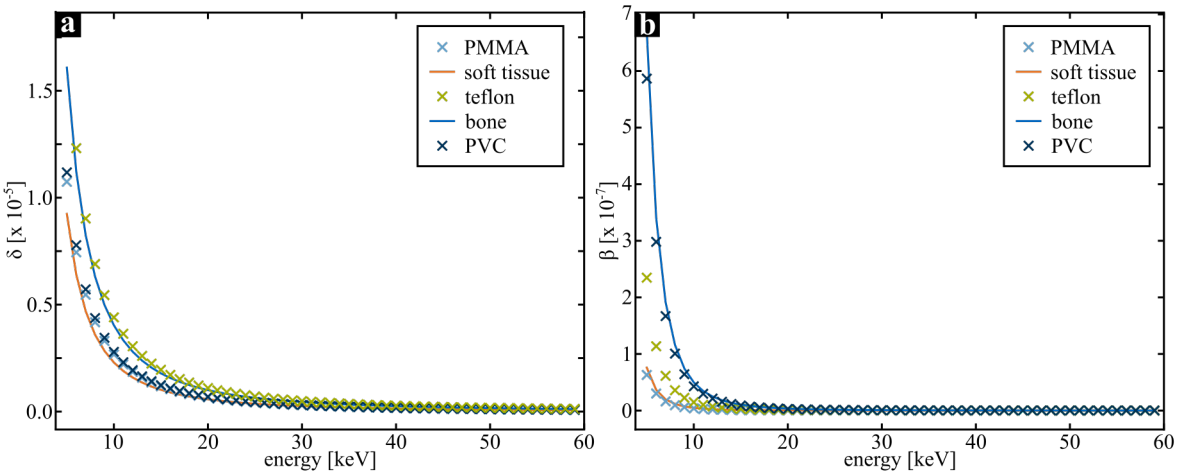

Figure A.1: **Phase and Attenuation Coefficient of the CNR Phantom over the Energy Range of the NanoTube Spectrum.** (a) Phase coefficient δ. (b) Attenuation coefficient β. The coefficients are plotted for bone and soft tissue and for the CNR phantom materials in Chapter 6.

For determining the complex refractive index of superglue for Fig. A.2, the density was obtained from the available technical data sheet of the two different liquid superglues used throughout this work. The first superglue was from Pattex (Henkel, Germany): $\rho_{\text{pattex}} = 1.05\,\text{g/cm}^3$. The other superglue was from Weicon (Germany): $\rho_{\text{weicon}} =$

1.07 g/cm^3. For cyanoacrylate, the main compoment in superglue, two variants were found regarding its chemical composition: C5H5NO2, C6H7NO2. Both densities and both composition variants were investigated. Thereby, the differences between the variants were negligible concerning the coefficients of the refractive index in the relevant energy interval. For the sake of clarity, Fig A.2 only shows the values for a density of $\rho_{\text{pattex}} = 1.05\,\text{g/cm}^3$ and a chemical composition of (C5H5NO2).

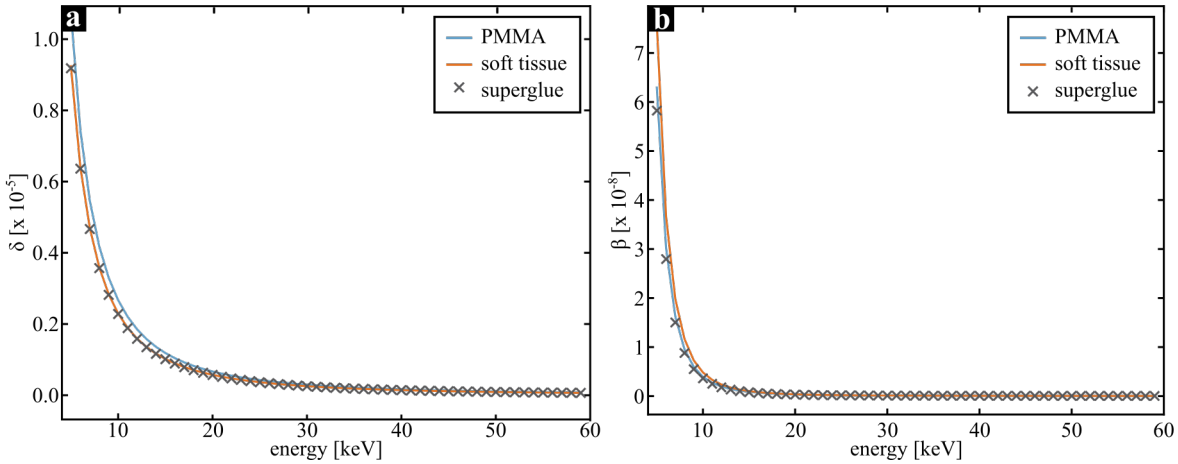

Figure A.2: **Phase and Attenuation Coefficient of Superglue over the Energy Range of the NanoTube Spectrum.** (a) Phase coefficient δ. (b) Attenuation coefficient β. For superglue, a chemical composition of (C5H5NO2) was assumed and a density of 1.05 g/cm^3.

A.3 Influence of a Diffuser on the Beam Coherence in the NanoCT

To eliminate propagation-based phase effects, an attempt was made to destroy the coherence of the X-ray beam with a diffuser. In Fig. A.3 and Fig. A.4, NanoCT data of murine spleen tissue are displayed, of which some were acquired using a rotating diffuser in the FOV of the X-ray beam.

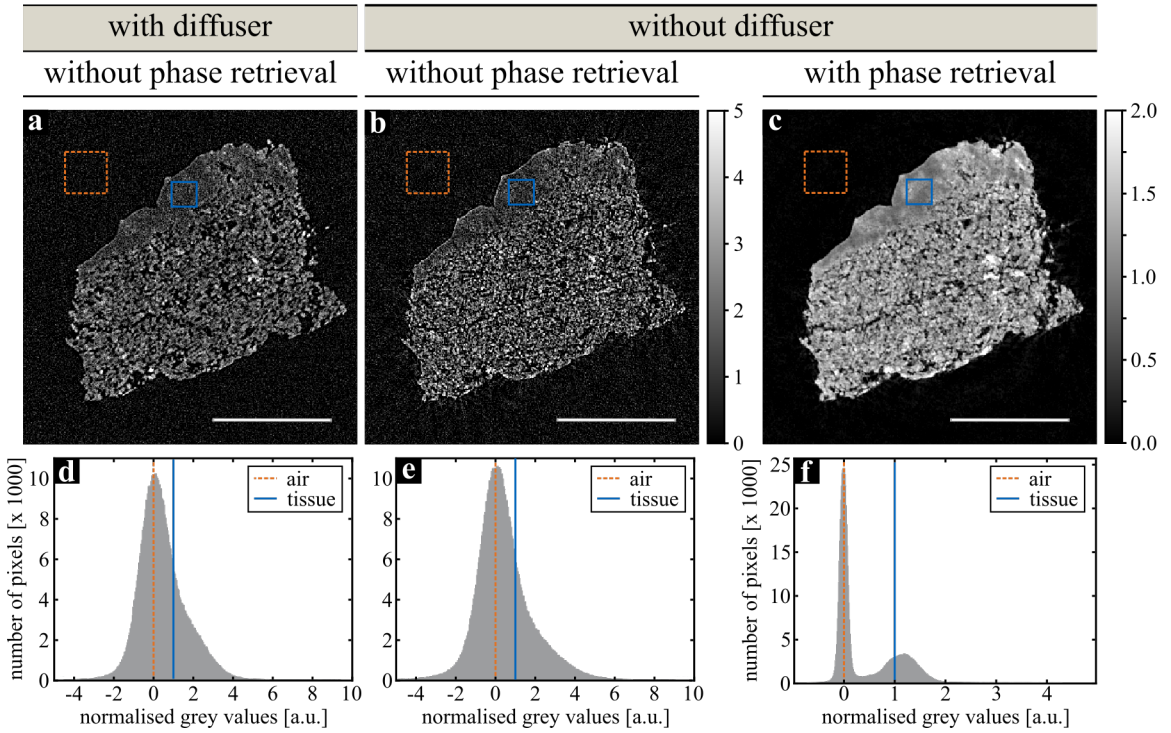

Figure A.3: **NanoCT Slices of Murine Spleen Tissue Stained with X-ray Eosin with and without Diffuser.** (a) Slice through a NanoCT data set acquired with diffuser. (b) Slice through a NanoCT data set acquired without diffuser. (c) The same NanoCT slice as in (b) but with Paganin's phase retrieval. The NanoCT slices were normalised to the mean grey value of air (orange ROI), which was set to zero, and the mean grey value of superglue (blue ROI), which was set to one. The same grey value range was chosen for the NanoCT slices in (a), (b). (d) - (f) Histograms of the respective grey value distribution in image (a) - (c). $v_{\text{eff}} \approx 350\,\text{nm}$. Scalebars: 100 µm.

In neither the NanoCT slices, nor the corresponding histograms in Fig. A.3 a significant difference is observed between the NanoCT data acquired with and without diffuser. The data in Fig. A.4 further support these findings.

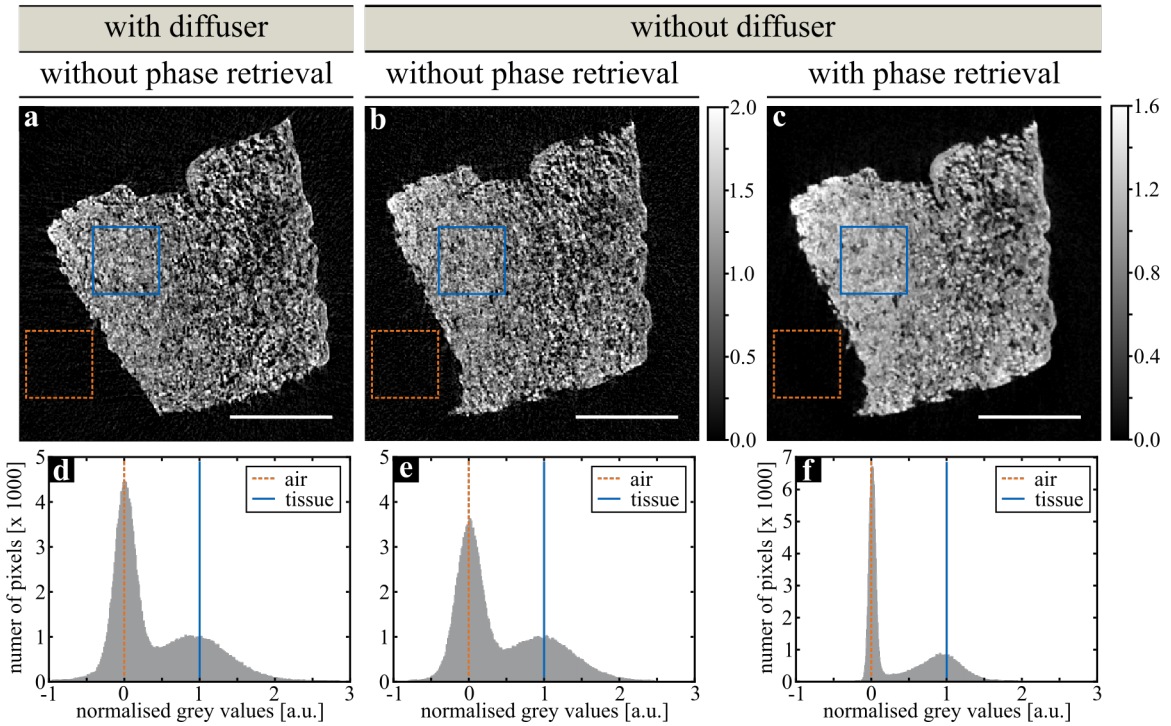

Figure A.4: **NanoCT Slices of Murine Spleen Tissue Stained with Gd-Haematein with and without Diffuser.** (a) Slice through a NanoCT data set acquired with diffuser. (b) Slice through a NanoCT data set acquired without diffuser. (c) The same NanoCT slice as in (b) but with Paganin's phase retrieval. The NanoCT slices were normalised to the mean grey value of air (orange ROI), which was set to zero, and the mean grey value of soft tissue (blue ROI), which was set to one. The same grey value range was chosen for the NanoCT slices in (a), (b). (d) - (f) Histograms of the respective grey value distribution in image (a) - (c). $v_{\text{eff}} \approx 650\,\text{nm}$. Scalebars: 100 µm.

Tissue Specimens and Sample Preparation: The murine spleen tissue specimens were obtained according to the descriptions regarding murine organ tissue in the methods section of Chapter 7.
For the NanoCT data in Fig. A.3, the murine spleen tissue was stained according to the X-ray eosin protocol, which is described in the methods section of Chapter 7. The murine spleen tissue presented in Fig. A.4 was processed with the Gd-haematein staining protocol, as described in [Müller, 2019]. All tissue specimens were then dehydrated in an ethanol series with a subsequent CPD. The samples were then mounted with a liquid superglue from Weicon (Germany) to a plastic pin.

NanoCT Acquisition, Image Processing and Data Analysis For the acquisition of the NanoCT data presented in Fig. A.3 and Fig. A.4, 1,599 projections were recorded over a rotation angle range of 360° with $U_{acc} = 60\,kV$ and a detector threshold of 2.7 keV. The remaining acquisition parameters are listed in Table A.4.

Figure		A.3		A.4	
Panels		a, d	b, c, e, f	a, d	b, c, e, f
diffuser		yes	no	yes	no
v_{eff}	[nm]	350	350	650	650
d_{sa}	[mm]	0.85	0.85	0.85	0.85
d_{sd}	[mm]	420	420	225	225
r_e	[nm]	270	270	300	270
t_{exp}	[s]	5	5	6	6
$t_{acq,tot}$	[h]	4	4	4.5	4.5

Table A.4: **NanoCT Acquisition Parameters for Investigating Propagation-Based Phase Contrast.** Legend: d_{sa}: distance of the source spot from the tomography axis, d_{sd}: distance of the detector from the source, t_{exp}: exposure time for one projection image, r_e: electron spot radius ($0.5 \cdot$FWHM) on the X-ray target prior to acquisition, $t_{acq,tot}$: total acquisition time for the NanoCT volume.

The diffuser was designed from a thin piece of sand paper, which was mounted on a conventional PC ventilator with the ventilation fins removed. For the NanoCT scans with diffuser (Table A.4), the rotating sandpaper was positioned in the FOV of the X-ray beam.

The recorded NanoCT projections were further processed and reconstructed according to the work-flow presented in Section 5.3. For projection alignment, the cross-correlation based approach was used. Paganin's phase retrieval was applied to the

NanoCT data shown in Fig. A.3c and Fig. A.4c. On the NanoCT data of this section, no deblurring was performed.

For the images in Fig. A.3a-c and Fig. A.4a-c, corresponding NanoCT slices were retrieved in both data sets. The final images were then normalised to air as zero (orange ROI) and tissue or superglue as one (blue ROI). The respective histograms were subsequently calculated from the slices shown in Fig. A.3a-c and Fig. A.4a-c.

Scientific Contributions The experimental study was devised by Julia Herzen, Madleen Busse and Simone Ferstl. The staining of the tissue shown in Fig. A.3 and Fig. A.4 was performed by Benedikt Wach. The acquisition, the image processing and the data analysis as well as the generation of the final figures was performed by Simone Ferstl.

Bibliography

[Albers, 2018] Albers, J. *et al.* X-ray-Based 3D Virtual Histology—Adding the Next Dimension to Histological Analysis. *Molecular Imaging and Biology* **20,** 732–741 (2018) (Cited on pages 2, 203).

[Als-Nielsen, 2011] Als-Nielsen, J. & McMorrow, D. *Elements of Modern X-ray Physics* Volume 2 (Wiley and Sons, 2011) (Cited on pages 1, 2, 5, 10, 15, 21–29, 31, 35, 39, 41, 167).

[Andreasen, 1992] Andreasen, A., Drewes, A. M., Assentoft, J. E. & Larsen, N. E. Computer-assisted alignment of standard serial sections without use of artificial landmarks. A practical approach to the utilization of incomplete information in 3-D reconstruction of the hippocampal region. *Journal of Neuroscience Methods* **45,** 199–207 (1992) (Cited on pages 2, 167).

[Bárcena, 2009] Bárcena, M. & Koster, A. J. Electron tomography in life science. *Seminars in Cell & Developmental Biology* **20,** 920–930 (2009) (Cited on pages 2, 203).

[Bech, 2008] Bech, M. *et al.* X-ray imaging with the PILATUS 100k detector. *Applied Radiation and Isotopes* **66,** 474–478 (2008) (Cited on page 58).

[Becher, 1909] Becher, S. Über die "Hörbläschen" der Leptosynapta bergensis. Ein Beitrag zur Kenntnis der statischen Organe. *Biologisches Zentralblatt* **29,** 413–425 (1909) (Cited on page 149).

[Becher, 1906] Becher, S. Über Synapta minuta n. sp., eine brutpflegende Synaptide der Nordsee, und über die contractilen Rosetten der Holothurien. *Zoologischer Anzeiger* **30,** 505–509 (1906) (Cited on page 147).

[Birnbacher, 2016] Birnbacher, L. *et al.* Experimental Realisation of High-sensitivity Laboratory X-ray Grating-based Phase-contrast Computed Tomography. *Scientific Reports* **6,** 1–8 (2016) (Cited on pages 3, 167).

[Boettinger, 1979] Boettinger, W. J., Burdette, H. E. & Kuriyama, M. X-ray magnifier. *Review of Scientific Instruments* **50,** 26–30 (1979) (Cited on pages 3, 39).

[Born, 1980] Born, M. & Wolf, E. *Principles of Optics* 6th ed. (Pergamon Press, Oxford, 1980) (Cited on page 26).

[Bradley, 2016] Bradley, R. S. & Withers, P. J. Correlative multiscale tomography of biological materials. *MRS Bulletin* **41,** 549–556 (2016) (Cited on page 145).

[Braverman, 1986] Braverman, M. S. & Braverman, I. M. Three-dimensional reconstructions of objects from serial sections using a microcomputer graphics system. *Journal of Investigative Dermatology* **86,** 290–294 (1986) (Cited on pages 2, 167).

[Brenzinger, 2013] Brenzinger, B., Haszprunar, G. & Schrödl, M. At the limits of a successful body plan - 3D microanatomy, histology and evolution of Helminthope (Mollusca: Heterobranchia: Rhodopemorpha), the most worm-like gastropod. *Frontiers in Zoology* **10,** 37 (2013) (Cited on page 1).

[Bronnikov, 2002] Bronnikov, A. V. Theory of quantitative phase-contrast computed tomography. *Journal of the Optical Society of America A* **19,** 472 (2002) (Cited on page 82).

[Buddenbrock, 1912] Buddenbrock, W. v. Über die Funktion der Statozysten im Sande grabender Meerestiere (Arenicola und Synapta). *Biologisches Zentralblatt* **32,** 564–585 (1912) (Cited on page 147).

[Burnett, 2014] Burnett, T. L. *et al.* Correlative tomography. *Scientific Reports* **4,** 1–6 (2014) (Cited on page 2).

[Burvall, 2011] Burvall, A., Lundström, U., Takman, P. A. C., Larsson, D. H. & Hertz, H. M. Phase retrieval in X-ray phase-contrast imaging suitable for tomography. *Optics Express* **19,** 10359 (2011) (Cited on page 82).

[Bushong, 2014] Bushong, E. A. *et al.* X-Ray Microscopy as an Approach to Increasing Accuracy and Efficiency of Serial Block-Face Imaging for Correlated Light and Electron Microscopy of Biological Specimens. *Microscopy and Microanalysis* **29,** 231–238 (2014) (Cited on pages 2, 145).

[Busse, 2020] Busse, M., Marciniszyn, J. P., Ferstl, S., Kimm Melanie A. and Pfeiffer, F. & Gulder, T. 3D-Non-Destructive Imaging through Heavy Metal-Eosin Salt Contrast Agents. *Chemistry – A European Journal* **27,** 4561–4566 (2020) (Cited on page 195).

[Busse, 2018a] Busse, M., Müller, M., Kimm, M. A. & Pfeiffer, F. Bismuth-Oxo-Clusters for Soft-Tissue Staining. *Microscopy and Microanalysis* **24,** 368–369 (2018) (Cited on pages 83, 195).

[Busse, 2019] Busse, M. *et al.* 3D Imaging of Soft-Tissue Samples using an X-ray Specific Staining Method and Nanoscopic Computed Tomography. *JoVE,* e60251 (2019) (Cited on page 207).

[Busse, 2018b] Busse, M. *et al.* Three-dimensional virtual histology enabled through cytoplasm-specific X-ray stain for microscopic and nanoscopic computed tomography. *Proceedings of the National Academy of Sciences* **115,** 2293–2298 (2018) (Cited on pages 4, 119, 125, 135, 140, 141, 167, 168, 192, 198, 199, 207, 208).

[Buzug, 2008] Buzug, T. M. *Computed Tomography* (Springer Verlag, 2008) (Cited on pages 14, 35, 37).

[Campbell, 2017] Campbell, J. E. & L., A. R. *International Trauma Life Support for Emergency Care Providers, Global Edition* 8th ed. (Pearson Education Limited, 2017) (Cited on page 176).

[Caplan, 2011] Caplan, J., Niethammer, M., Taylor, R. M. & Czymmek, K. J. The power of correlative microscopy: Multi-modal, multi-scale, multi-dimensional. *Current Opinion in Structural Biology* **21,** 686–693 (2011) (Cited on pages 1, 145).

[Cerroni, 2016] Cerroni, L., Garbe, C. & Metze, D. *Histopathologie der Haut* (eds Cerroni, L., Garbe, C., Metze, D., Kutzner, H. & Kerl, H.) (Springer Berlin Heidelberg, Berlin, Heidelberg, 2016) (Cited on pages 186–189, 201).

[Chao, 2005] Chao, W., Harteneck, B. D., Liddle, J. A., Anderson, E. H. & Attwood, D. T. Soft X-ray microscopy at a spatial resolution better than 15 nm. *Nature* **435,** 1210–1213 (2005) (Cited on pages 2, 3, 38, 39, 42, 43, 167, 204).

[Clark, 1907] Clark, H. L. The apodous holothurians. A monograph of the Synaptidae and Molpadiidae. *Smithsonian Contributions to Knowledge* **35,** 1–13 (1907) (Cited on page 147).

[Clœtens, 1999] Clœtens, P. *et al.* Holotomography: Quantitative phase tomography with micrometer resolution using hard synchrotron radiation x-rays. *Applied Physics Letters* **75,** 2912 (1999) (Cited on pages 3, 26, 41, 121).

[Clœtens, 1999] Clœtens, P. *Contribution to Phase-Contrast Imaging, Reconstruction and Tomography with Hard Synchrotron Radiation* PhD thesis (Vrije Universiteit Brussel, 1999) (Cited on page 140).

[DAgati, 2005] D'Agati, V., Jennette, J. C. & Silva, F. G. *Non-neoplastic kidney diseases* 1st ed. (eds West King, D., Sobin, L. H., Stocker, J. T. & Wagner, B.) (American Registry of Pathology, 2005) (Cited on pages 1, 167, 170–172, 174).

[DAgati, 2011] D'Agati, V. D., Kaskel, F. J. & Falk, R. J. Focal Segmental Glomerulosclerosis. *The New England Journal of Medicine* **365,** 2398–2411 (2011) (Cited on pages 171, 176, 177).

[Demtröder, 2009] Demtröder, W. *Experimentalphysik 2 - Elektrizität und Optik* 5th ed. (Springer Berlin Heidelberg, Berlin, Heidelberg, 2009) (Cited on page 39).

[Denk, 2004] Denk, W. & Horstmann, H. Serial block-face scanning electron microscopy to reconstruct three-dimensional tissue nanostructure. *PLoS Biology* **2,** 1901–1909 (2004) (Cited on pages 2, 167).

[Dittmann, 2018] Dittmann, J. Cone Beam Geometry Calibration for Micro Computed Tomography Systems using Arbitrary Fiducial Markers and the Relation Between Projection Matrices and Real Space Geometry, 1–23. eprint: 1808.03337 (2018) (Cited on page 62).

[Egerton, 2005] Egerton, R. *Physical Principles of Electron Microscopy - An Introduction to TEM, SEM and AEM* Chapter 2 (Springer US, 2005) (Cited on pages 5, 11, 12).

[Ehlers, 1997] Ehlers, U. Ultrastructure of the statocysts in the apodous sea cucumber Leptosynapta inhaerens (Holothuroidea, Echinodermata). *Acta Zoologica* **78,** 61–68 (1997) (Cited on page 147).

[Ehn, 2017] Ehn, S. *Photon-counting hybrid-pixel detectors for spectral X-ray imaging applications* PhD thesis (Technical University of Munich, 2017) (Cited on pages 55, 56).

[Fahrmeir, 2016] Fahrmeir, L., Heumann, C., Künstler, R., Pigeot, I. & Tutz, G. *Statistik. Der Weg zur Datenanalyse* (Springer Spektrum, Berlin, Heidelberg, 2016) (Cited on page 113).

[Ferstl, 2020a] Ferstl, S. *et al.* Revealing the Microscopic Structure of Human Renal Cell Carcinoma in Three Dimensions. *IEEE Transactions on Medical Imaging* **39,** 1494–1500 (2020) (Cited on pages 4, 38, 119, 141, 168, 169, 182, 183, 185, 191, 192, 198–200).

[Ferstl, 2015] Ferstl, S. *Implementation and Optimisation of an Automatic Focusing Routine Specified to a Nanofocus X-ray Source Prototype* Masters Thesis (TU Munich, 2015) (Cited on pages 7, 10, 11, 14, 16, 48, 51, 53).

[Ferstl, 2018] Ferstl, S. *et al.* Laboratory-based X-ray NanoCT Explores Morphology of a Zebrafish Embryo. *Microscopy and Microanalysis* **24,** 184–185 (2018) (Cited on pages 4, 146).

[Ferstl, 2019] Ferstl, S. *et al.* Nanoscopic X-ray tomography for correlative microscopy of a small meiofaunal sea-cucumber. *Scientific Reports* (2019) (Cited on pages 4, 44, 79, 80, 147, 148, 150, 151, 153, 155, 163, 165, 167).

[Ferstl, 2020b] Ferstl, S. *et al.* Targeted multiscale investigation of human tissue in three dimensions. *submitted* (2020) (Cited on pages 4, 119, 141, 169, 170, 173–176, 178, 180, 192, 198–200).

[Forman, 2014] Forman, D. *et al. Cancer incidence in five continents, vol. X* tech. rep. (International Association of Cancer Registries, World Health Organization, 2014), 105. eprint: `arXiv:1011.1669v3` (Cited on page 181).

[Gabner, 2020] Gabner, S., Böck, P., Fink, D., Glösmann, M. & Handschuh, S. The visible skeleton 2.0: phenotyping of cartilage and bone in fixed vertebrate embryos and foetuses based on X-ray microCT. *Development* **147,** dev187633 (2020) (Cited on page 161).

[Garini, 2005] Garini, Y., Vermolen, B. J. & Young, I. T. From micro to nano: Recent advances in high-resolution microscopy. *Current Opinion in Biotechnology* **16,** 3–12 (2005) (Cited on page 1).

[Giepmans, 2008] Giepmans, B. N. Bridging fluorescence microscopy and electron microscopy. *Histochemistry and Cell Biology* **130,** 211–217 (2008) (Cited on pages 1, 145, 204).

[Goldstein, 2018] Goldstein, J. I. *et al. Scanning Electron Microscopy and X-Ray Microanalysis* 4th ed., VII–XIV (Springer Verlag, 2018) (Cited on pages 2, 5, 12, 13, 17, 48, 92).

[Gross, 2005] Gross, J. L. *et al.* Diabetic Nephropathy: Diagnosis, Prevention, and Treatment. *Diabetes Care* **28,** 164–176 (2005) (Cited on page 170).

[Gross, 2019] Gross, V. *et al.* X-ray imaging of a water bear offers a new look at tardigrade internal anatomy. *Zoological Letters* **5,** 14 (2019) (Cited on pages 20, 145, 146, 207, 208).

[Guizar-Sicairos, 2015] Guizar-Sicairos, M. *et al.* Quantitative interior x-ray nanotomography by a hybrid imaging technique. *Optica* **2,** 259 (2015) (Cited on page 78).

[Gureyev, 2004] Gureyev, T. E., Stevenson, A. W., Ya.I. Nesterets & Wilkins, S. W. Image deblurring by means of defocus. *Optics Communications* **240,** 81–88 (2004) (Cited on pages 84, 206).

[Gureyev, 2017] Gureyev, T. E., Nesterets, Y. I., Kozlov, A., Paganin, D. M. & Quiney, H. M. On the "unreasonable" effectiveness of transport of intensity imaging and optical deconvolution. *Journal of the Optical Society of America A* **34,** 2251 (2017) (Cited on page 90).

[Gürsoy, 2017] Gürsoy, D. *et al.* Rapid alignment of nanotomography data using joint iterative reconstruction and reprojection. *Scientific Reports* **7,** 1–12 (2017) (Cited on page 78).

[Hajj, 2010] Hajj, P. *et al.* Prevalence of Renal Cell Carcinoma in Patients With Autosomal Dominant Polycystic Kidney Disease and Chronic Renal Failure. *Urology* **74,** 752–753 (2010) (Cited on page 171).

[Handschuh, 2013] Handschuh, S., Baeumler, N., Schwaha, T. & Ruthensteiner, B. A correlative approach for combining microCT, light and transmission electron microscopy in a single 3D scenario. *Frontiers in Zoology* **10,** 1–16 (2013) (Cited on pages 1, 2, 20, 145, 158).

[Hawkes, 2018] Hawkes, P. & Kasper, E. in *Principles of Electron Optics (Second Edition)* (eds Hawkes, P. & Kasper, E.) 2nd ed., 1157–1170 (Academic Press, 2018) (Cited on page 9).

[Hehn, 2019] Hehn, L., Tilley, S., Pfeiffer, F. & Stayman, J. W. Blind deconvolution in model-based iterative reconstruction for CT using a normalized sparsity measure. *Physics in Medicine and Biology* **64** (2019) (Cited on pages 78, 177, 206).

[Hell, 1994] Hell, S. W. & Wichmann, J. Breaking the diffraction resolution limit by stimulated emission: stimulated-emission-depletion fluorescence microscopy. *Opt. Lett.* **19,** 780–782 (1994) (Cited on page 1).

[Hendee, 2003] Hendee, W. R., Ritenour, E. R. & Hoffmann, K. R. *Medical Imaging Physics* Fourth Edi. **4,** 730 (2003) (Cited on page 11).

[Hignette, 2005] Hignette, O., Cloetens, P., Rostaing, G., Bernard, P. & Morawe, C. Efficient sub 100 nm focusing of hard x rays. *Review of Scientific Instruments* **76** (2005) (Cited on pages 3, 41).

[Hossler, 2001] Hossler, F. E. & Douglas, J. E. Vascular Corrosion Casting: Review of Advantages and Limitations in the Application of Some Simple Quantitative Methods. *Microscopy and Microanalysis* **7,** 253–264 (2001) (Cited on page 2).

[Humphries, 1990] Humphries, S. J. *Charged Particle Beams* (John Wiley & Sons, New York, 1990) (Cited on pages 7, 9).

[Ishikawa, 1993] Ishikawa, I. & Kovacs, G. High incidence of papillary renal cell tumours in patients on chronic haemodialysis. *Histopathology* **22,** 135–140 (1993) (Cited on page 171).

[Jahn, 2018] Jahn, H. *et al.* Evaluation of contrasting techniques for X-ray imaging of velvet worms (Onychophora). *Journal of Microscopy* **270,** 343–358 (2018) (Cited on pages 2, 161, 211).

[Jans, 1989] Jans, D. & Jangoux, M. Functional morphology of vibratile urnae in the synaptid holothurid Leptosynapta inhaerens (Echinodermata). *Zoomorphology* **109,** 165–171 (1989) (Cited on page 147).

[Kak, 1988] Kak, A. C. & Slaney, M. *Principles of Computerized Tomographic Imaging* (IEEE Press, 1988) (Cited on page 37).

[Keller, 2012] Keller, P. J. & Dodt, H. U. Light sheet microscopy of living or cleared specimens. *Current Opinion in Neurobiology* **22,** 138–143 (2012) (Cited on pages 2, 203).

[Keller, 2008] Keller, P. J., Schmidt, A. D., Wittbrodt, J. & Stelzer, E. H. Reconstruction of Zebrafish Early Embryonic Development by Scanned Light Sheet Microscopy. *Science* **322,** 1065–1069 (2008) (Cited on page 203).

[Kerr, 2001] Kerr, A. M. Phylogeny of the Apodan Holothurians (Echinodermata) inferred from morphology. *Zoological Journal of the Linnean Society* **133,** 53–62 (2001) (Cited on page 147).

[Kirkpatrick, 1948] Kirkpatrick, P. & Baez, A. V. Formation of Optical Images by X-Rays. *J. Opt. Soc. Am.* **38,** 766–774 (1948) (Cited on pages 3, 39).

[Kirz, 1995] Kirz, J., Jacobsen, C. & Howells, M. Soft X-ray microscopes and their biological applications. *Quarterly Reviews of Biophysics* **28,** 33–130 (1995) (Cited on page 2).

[Klein, 1929] Klein, O. & Nishina, Y. Über die Streuung von Strahlung durch freie Elektronen nach der neuen relativistischen Quantendynamik von Dirac. *Zeitschrift für Physik* **52,** 853–868 (1929) (Cited on page 23).

[Knott, 2008] Knott, G., Marchman, H., Wall, D. & Lich, B. Serial Section Scanning Electron Microscopy of Adult Brain Tissue Using Focused Ion Beam Milling. *Journal of Neuroscience* **28,** 2959–2964 (2008) (Cited on pages 2, 167).

[Koch, 1998] Koch, A., Raven, C., Spanne, P. & Snigirev, A. X-ray imaging with submicrometer resolution employing transparent luminescent screens. *J. Opt. Soc. Am. A* **15,** 1940–1951 (1998) (Cited on page 44).

[Kraft, 2009] Kraft, P. *et al.* Performance of single-photon-counting PILATUS detector modules. *Journal of Synchrotron Radiation* **16,** 368–375 (2009) (Cited on page 58).

[Kremer, 2015] Kremer, A. *et al.* Developing 3D SEM in a broad biological context. *Journal of Microscopy* **259,** 80–96 (2015) (Cited on page 203).

[Krieger, 2009] Krieger, H. *Grundlagen der Strahlungsphysik und des Strahlenschutzes* 3rd editio (Vieweg and Teubner, 2009) (Cited on pages 11–13, 21, 22).

[Lai, 2015] Lai, W. L. *et al.* Membranous nephropathy: A review on the pathogenesis, diagnosis, and treatment. *Journal of the Formosan Medical Association* **114,** 102–111 (2015) (Cited on page 171).

[Lavery, 2014] Lavery, L. L., Gelb, J., Merkle, A. P. & Steinbach, A. X-Ray Microscopy for Hierarchical Multi-Scale Materials. *Microscopy Today* **22,** 16–21 (2014) (Cited on page 145).

[Lengeler, 1999] Lengeler, B. *et al.* A microscope for hard x rays based on parabolic compound refractive lenses. *Applied Physics Letters* **74,** 3924–3926 (1999) (Cited on pages 3, 39, 41).

[Li, 2013] Li, X. *et al.* Electron counting and beam-induced motion correction enable near-atomic-resolution single-particle cryo-EM. *Nature Methods* **10,** 584–590 (2013) (Cited on page 203).

[Lloyd, 1987] Lloyd, C. W. The Plant Cytoskeleton: The Impact of Fluorescence Microscopy. *Annual Review of Plant Physiology* **38,** 119–137 (1987) (Cited on page 1).

[Lucas, 2012] Lucas, M. S., Günthert, M., Gasser, P., Lucas, F. & Wepf, R. Bridging Microscopes: 3D Correlative Light and Scanning Electron Microscopy of Complex Biological Structures. *Methods in Cell Biology* **111,** 325–356 (2012) (Cited on page 1).

[Lucy, 1974] Lucy, L. B. An iterative technique for the rectification of observed distributions. *The Astronomical Journal* **79,** 745–754 (1974) (Cited on page 84).

[Massin, 2005] Massin, C., Appeltans, W., Van Hoey, G., Vincx, M. & Degraer, S. Leptosynapta minuta (Becher, 1906)(Echinodermata, Holothuroidea), a new record for Belgian marine waters. *Belgian Journal of Zoology* **135,** 83–86 (2005) (Cited on page 147).

[Mayo, 2007] Mayo, S., Miller, P., Gao, D. & Sheffield-Parker, J. Software image alignment for X-ray microtomography with submicrometre resolution using a SEM-based X-ray microscope. *Journal of Microscopy* **228,** 257–263 (2007) (Cited on page 78).

[Mayo, 2002] Mayo, S. C. *et al.* Quantitative X-ray projection microscopy: phase-contrast and multi-spectral imaging. *Journal of Microscopy* **207,** 79–96 (2002) (Cited on pages 44, 45).

[Mayo, 2005] Mayo, S., Miller, P., Sheffield-Parker, J., Gureyev, T. & Wilkins, S. *Attainment of¡ 60 nm Resolution in Phase-Contrast X-ray Microscopy using an add-on to an SEM* in *Proceedings of the 8th International Conference on X-ray Microscopy* (2005), 343–345 (Cited on page 45).

[McInnes, 2005] McInnes, E. Artefacts in histopathology. *Comparative Clinical Pathology* **13,** 100–108 (2005) (Cited on pages 2, 158, 167).

[Merchan-Pérez, 2009] Merchan-Pérez, A. Counting synapses using FIB/SEM microscopy: a true revolution for ultrastructural volume reconstruction. *Frontiers in Neuroanatomy* **3,** 1–14 (2009) (Cited on pages 2, 167).

[Meschede, 2015] Meschede, D. *Gerthsen Physik* (Springer, Berlin, Heidelberg, 2015) (Cited on page 9).

[Metscher, 2009] Metscher, B. D. Micro CT for comparative morphology: Simple staining methods allow high-contrast 3D imaging of diverse non-mineralized animal tissues. *BMC Physiology* **9,** 11 (2009) (Cited on pages 2, 161, 167, 211).

[Miller, 2017] Miller, A. K. *et al.* Molecular phylogeny of extant Holothuroidea (Echinodermata). *Molecular Phylogenetics and Evolution* **111,** 110–131 (2017) (Cited on page 147).

[Modregger, 2006] Modregger, P., Lübbert, D., Schäfer, P. & Köhler, R. Magnified x-ray phase imaging using asymmetric Bragg reflection: Experiment and theory. *Physical Review B* **74,** 054107 (2006) (Cited on page 41).

[Modregger, 2007] Modregger, P., Lübbert, D., Schäfer, P. & Köhler, R. Spatial resolution in Bragg-magnified X-ray images as determined by Fourier analysis. *physica status solidi (a)* **204,** 2746–2752 (2007) (Cited on page 41).

[Motzer, 1996] Motzer, R. J., Bander, N. H. & Nanus, D. M. Renal-Cell Carcinoma. *Medical Progress* **335,** 865–875 (1996) (Cited on pages 181, 183).

[Muglia, 2015] Muglia, V. F. & Prando, A. Renal cell carcinoma: histological classification and correlation with imaging findings. *Radiologia Brasileira* **48,** 166–174 (2015) (Cited on page 181).

[Müller, 2019] Müller, M. *Laboratory-Based X-ray NanoCT for Biological Imaging* PhD thesis (Technical University of Munich, 2019) (Cited on pages 55, 57, 58, 90, 109, 119, 125, 146, 206, 210, 213, 220).

[Müller, 2017] Müller, M. *et al.* Myoanatomy of the velvet worm leg revealed by laboratory-based nanofocus X-ray source tomography. *Proceedings of the National Academy of Sciences* **114,** 12378–12383 (2017) (Cited on pages 3, 4, 20, 45, 85, 146, 193, 205, 207, 208).

[Müller, 2018] Müller, M. *et al.* Nucleus-specific X-ray stain for 3D virtual histology. *Scientific Reports* **8,** 1–10 (2018) (Cited on pages 4, 167, 195, 207, 210).

[Natterer, 1986] Natterer, F. *The Mathematics of Computerized Tomography* 1st ed. (Vieweg+Teubner Verlag, Wiesbaden, 1986) (Cited on page 214).

[Nelder, 1964] Nelder, J., Mead, R., Nelder, B. J. a. & Mead, R. A simplex method for function minimization. *Computer Journal* **7,** 308–313 (1964) (Cited on page 53).

[Ng, 1983] Ng, W. L., Chan, K. W. & Ma, L. A scanning electron microscope study of isolated glomeruli in glomerulonephritis. *Pathology* **15,** 139–146 (1983) (Cited on page 177).

[Ojeda, 1991] Ojeda, J. L. & Icardo, J. M. A scanning electron microscope study of the neck segment of the rabbit nephron. *Anatomy and Embryology* **184,** 605–610 (1991) (Cited on page 1).

[Ong, 1998] Ong, K., Phang, J. & Thong, J. A Robust Focusing and Astigmatism Correction Method for the Scanning Electron Microscope–Part III: An Improved Technique. *Scanning* **19,** 553–563 (1998) (Cited on page 10).

[Orloff, 2008] Orloff, J. *Handbook of Charged Particle Optics* 2nd (CRC Press, 2008) (Cited on pages 6, 7, 10).

[Paganin, 2002] Paganin, D., Mayo, S. C., Gureyev, T. E., Miller, P. R. & Wilkins, S. W. Simultaneous phase and amplitude extraction from a single defocused image of a homogeneous object. *Journal of Microscopy* **206,** 33–40 (2002) (Cited on pages 3, 44, 82, 90, 174).

[Parkinson, 2012] Parkinson, D. Y., Knoechel, C., Yang, C., Larabell, C. A. & Le Gros, M. A. Automatic alignment and reconstruction of images for soft X-ray tomography. *Journal of Structural Biology* **177,** 259–266 (2012) (Cited on page 78).

[Patel, 2009] Patel, V. *et al.* Self-calibration of a cone-beam micro-CT system. *Medical physics* **36,** 48–58 (2009) (Cited on page 77).

[Patton, 2014a] Patton, K. T. & Thibodeau, G. A. (Mosby, 2014) (Cited on page 186).

[Patton, 2014b] Patton, K. T. & Thibodeau, G. A. *Mosby's Handbook of Anatomy and Physiology.* (Mosby, 2014) (Cited on pages 130, 187).

[Pfeiffer, 2006] Pfeiffer, F., Weitkamp, T., Bunk, O. & David, C. Phase retrieval and differential phase-contrast imaging with low-brilliance X-ray sources. *Nature Physics* **2,** 258–261 (2006) (Cited on pages 3, 25, 26).

[Richardson, 1972] Richardson, W. Bayesian-based iterative method of image restoration. *Journal of the Optical Society of America* **62,** 55–59 (1972) (Cited on page 84).

[Rini, 2009] Rini, B. I., Campbell, S. C. & Escudier, B. Renal cell carcinoma. *The Lancet* **373,** 1119–1132 (2009) (Cited on pages 181, 184).

[Rudnaya, 2012] Rudnaya, M. E., ter Morsche, H. G., Maubach, J. M. L. & Mattheij, R. M. M. A Derivative-Based Fast Autofocus Method in Electron Microscopy. *Journal of Mathematical Imaging and Vision* **44,** 38–51 (2012) (Cited on page 53).

[Rudnaya, 2010] Rudnaya, M., Mattheij, R. & Maubach, J. Evaluating sharpness functions for automated scanning electron microscopy. *Journal of Microscopy* **240,** 38–49 (2010) (Cited on page 51).

[Russo, 2017] Russo, P. *Handbook of X-ray Imaging* (ed Russo, P.) (CRC Press, 2017) (Cited on pages 22, 30, 31, 35, 39–42, 55, 56, 89, 90, 104, 214).

[Ruthensteiner, 2008] Ruthensteiner, B. & Heß, M. Embedding 3D models of biological specimens in PDF publications. *Microscopy Research and Technique* **71,** 778–786 (2008) (Cited on pages 145, 165).

[Salamon, 2008] Salamon, M., Hanke, R., Krüger, P., Uhlmann, N. & Voland, V. Realization of a computed tomography setup to achieve resolutions below 1 μm. *Nuclear Instruments and Methods in Physics Research, Section A: Accelerators, Spectrometers, Detectors and Associated Equipment* **591,** 50–53 (2008) (Cited on page 3).

[Salvat, 2006] Salvat, F., Fernández-Vera, J. M. & Sempau, J. *PENELOPE-2006: A code system for Monte Carlo simulation of electron and photon transport* `http://pypenelope.sourceforge.net/` (Cited on page 115).

[Schneider, 2012] Schneider, G., Guttmann, P., Rehbein, S., Werner, S. & Follath, R. Cryo X-ray microscope with flat sample geometry for correlative fluorescence and nanoscale tomographic imaging. *Journal of Structural Biology* **177,** 212–223 (2012) (Cited on pages 2, 145).

[Schoonjans, 2011] Schoonjans, T. *et al.* The xraylib library for X-ray–matter interactions. Recent developments. *Spectrochimica Acta Part B: Atomic Spectroscopy* **66,** 776–784 (2011) (Cited on pages 21, 135, 216).

[Schroer, 2002] Schroer, C. G. *et al.* Nanotomography based on hard x-ray microscopy with refractive lenses. *Applied Physics Letters* **81,** 1527–1529 (2002) (Cited on page 41).

[Schwaha, 2012] Schwaha, T. & Wanninger, A. Myoanatomy and serotonergic nervous system of plumatellid and fredericellid phylactolaemata (Lophotrochozoa, Ectoprocta). *Journal of Morphology* **273,** 57–67 (2012) (Cited on page 1).

[Schwarz, 2007] Schwarz, A., Vatandaslar, S., Merkel, S. & Haller, H. Renal cell carcinoma in transplant recipients with acquired cystic kidney disease. *Clinical Journal of the American Society of Nephrology* **2,** 750–756 (2007) (Cited on page 171).

[Sedlacek, 1996] Sedlacek, M. *Electron physics of vacuum and gaseous devices* (John Wiley & Sons, New York, 1996) (Cited on page 8).

[Seibert, 2005] Seibert, J. A. & Boone, J. M. X-ray imaging physics for nuclear medicine technologists. Part 2: X-ray interactions and image formation. *Journal of Nuclear Medicine Technology* **33,** 3–18 (2005) (Cited on page 20).

[Smith, 2014] Smith, E. A. *et al.* Quantitatively imaging chromosomes by correlated cryo-fluorescence and soft x-ray tomographies. *Biophysical Journal* **107,** 1988–1996 (2014) (Cited on page 145).

[Snigirev, 1996] Snigirev, A., Kohn, V., Snigireva, I. & Lengeler, B. A compound refractive lens for focusing high-energy X-rays. *Nature* **384,** 49–51 (1996) (Cited on page 40).

[Sombke, 2015] Sombke, A., Lipke, E., Michalik, P., Uhl, G. & Harzsch, S. Potential and limitations of X-Ray micro-computed tomography in arthropod neuroanatomy: A methodological and comparative survey. *Journal of Comparative Neurology* **523,** 1281–1295. eprint: `arXiv:1011.1669v3` (2015) (Cited on pages 2, 145, 161, 211).

[Stricker, 1985] Stricker, S. A. The ultrastructure and formation of the calcareous ossicles in the body wall of the sea cucumber Leptosynapta clarki (Echinodermata, Holothuroida). *Zoomorphology* **105,** 209–222 (1985) (Cited on page 147).

[Suvarna, 2013] *Bancroft's Theory and Practice of Histological Techniques* 7th ed. (eds Suvarna, K. S., Layton, C. & Bancroft, J. D.) (2013) (Cited on pages 1, 167, 186, 204).

[Tervaert, 2010] Tervaert, T. W. C. *et al.* Pathologic Classification of Diabetic Nephropathy. *Journal of the American Society of Nephrology* **21,** 556–563 (2010) (Cited on pages 170, 176).

[Titze, 2016] Titze, B. & Genoud, C. Volume scanning electron microscopy for imaging biological ultrastructure. *Biology of the Cell* **108,** 307–323 (2016) (Cited on page 161).

[Tkachuk, 2009] Tkachuk, A. *et al.* X-ray computed tomography in Zernike phase-contrast mode at 8 keV with 50-nm resolution using Cu rotating anode X-ray source. *Zeitschrift für Kristallographie - Crystalline Materials* **222,** 650–655 (2009) (Cited on page 43).

[Tomashefski, 2008] *Dail and Hammar's Pulmonary Pathology* (eds Tomashefski, J. F., Cagle, P. T., Farver, C. F. & Fraire, A. E.) (Springer New York, New York, NY, 2008) (Cited on pages 187, 190, 201).

[Töpperwien, 2018a] Töpperwien, M., Doeppner, T. R., Zechmeister, B., Bähr, M. & Salditt, T. Multiscale x-ray phase-contrast tomography in a mouse model of transient focal cerebral ischemia. *Biomedical Optics Express* **10,** 92 (2018) (Cited on page 2).

[Töpperwien, 2018b] Töpperwien, M., van der Meer, F., Stadelmann, C. & Salditt, T. Three-dimensional virtual histology of human cerebellum by X-ray phase-contrast tomography. *Proceedings of the National Academy of Sciences* **115,** 6940–6945 (2018) (Cited on pages 3, 167).

[Tuohimaa, 2008] Tuohimaa, T. *Liquid-Jet-Target Microfocus X-Ray Sources : Electron Guns , Optics and Phase-Contrast Imaging* (2008) (Cited on pages 5, 7, 10, 12, 14–17).

[Umkehrer, 2019] Umkehrer, S. *et al.* Optimization of in vivo murine X-ray dark-field computed tomography. *Review of Scientific Instruments* **90** (2019) (Cited on page 3).

[Vandenspiegella, 1998] Vandenspiegella, D., Geronnez-Lecomte, A. & Jangoux, M. Ultrastructure of the Ciliated Cups of a Synaptid Holothuroid , Leptosynapta galliennei (Echinodermata). *Invertebrate Biology* **117,** 253–260 (1998) (Cited on page 147).

[vHelden, 2010] Van Helden, A., Dupré, S. & van Gent, R. *The Origins of the Telescope (History of Science and Scholarship in the Netherlands)* (Amsterdam University Press, 2010) (Cited on page 1).

[Von Smekal, 2004] Von Smekal, L., Kachelrieß, M., Stepina, E. & Kalender, W. A. Geometric misalignment and calibration in cone-beam tomography. *Medical Physics* **31,** 3242–3266 (2004) (Cited on page 62).

[Wagner, 2011] Wagner, R., Van Loo, D., Hossler, F. & Czymmek, K. High-Resolution Imaging of Kidney Vascular Corrosion Casts with Nano-CT. *Microscopy and Microanalysis* **17,** 215–219 (2011) (Cited on page 2).

[Walton, 2015] Walton, L. A. *et al.* Morphological characterisation of unstained and intact tissue micro-architecture by X-ray computed micro- and nano-tomography. *Scientific Reports* **5,** 1–14 (2015) (Cited on pages 2, 145).

[Weitkamp, 2010] Weitkamp, T. *et al.* Parallel-beam imaging at the ESRF beamline ID19: Current status and plans for the future. *AIP Conference Proceedings* **1234,** 83–86 (2010) (Cited on page 44).

[Weitkamp, 2004] Weitkamp, T. *XWFP: an x-ray wavefront propagation software package for the IDL computer language* in *SPIE Proceedings* (ed Sanchez del Rio, M.) (2004), 181–189 (Cited on page 28).

[Weninger, 1998] Weninger, W. J., Meng, S., Streicher, J. & Müller, G. B. A new episcopic method for rapid 3-D reconstruction: Applications in anatomy and embryology. *Anatomy and Embryology* **197,** 341–348 (1998) (Cited on pages 2, 167).

[Wilkins, 1996] Wilkins, S. W., Gureyev, T. E., Gao, D., Pogany, A. & Stevenson, A. W. Phase-contrast imaging using polychromatic hard X-rays. *Nature* **384,** 335–338 (1996) (Cited on pages 24, 26).

[Williams, 1996] Williams, D. B. & Carter, C. B. *The Transmission Electron Microscope* 3–17 (Springer US, Boston, MA, 1996) (Cited on page 1).

[Withers, 2007] Withers, P. J. X-ray nanotomography. *Materials Today* **10,** 26–34 (2007) (Cited on pages 2, 3, 17, 38–45, 90, 205).

[Worster, 1969] Worster, J. The brightness of electron beams. *Journal of Physics D: Applied Physics* **2,** 457–462 (1969) (Cited on page 8).

[Youn, 2010] Youn, H. S., Yin, G. C., Andrews, J. C. & Pianetta, P. Condenser optics in the X-ray microscope. *AIP Conference Proceedings* **1365,** 345–348 (2010) (Cited on page 42).

[Zdora, 2020] Zdora, M.-C. *et al.* X-ray phase imaging with the unified modulated pattern analysis of near-field speckles at a laboratory source. *Applied Optics* **59,** 2270 (2020) (Cited on page 3).

List of Figures

List of Tables

List of Acronyms and Symbols

LaB_6 lanthanum hexaboride. 7, 48, 104

U_{acc} acceleration voltage. 6, 8, 11, 15–17, 48, 57, 89–115, 118, 119, 136, 137, 200, 202, 205, 208, 212

U_g grid voltage. 48–50, 91, 111, 113

v_{eff} effective edge length of a cubic voxel. 58, 60, 62, 71, 75–80, 83, 85, 86, 114, 118, 119, 121, 122, 127, 137, 139, 142, 144–149, 151–153, 159, 160, 166, 168–173, 175, 177, 178, 180, 183–185, 187, 192, 194, 207, 208, 210–212

L.* cf. *minuta *Leptosynapta* cf. *minuta*. 141–145, 152, 154–157, 159–162, 199

R.* cf. *eliator *Rissoella* cf. *eliator*. 142, 143, 153, 157, 159, 162

ASIC application specific integrated circuit. 54, 55

CCD charge-coupled device. 44, 55

CdTe cadmium telluride. 58

CLEM correlative light and electron microscopy. 1, 158, 203

CNR contrast-to-noise ratio. 81, 87–90, 97–101, 103–107, 109, 110, 113–115, 142, 148, 149, 156, 157, 162, 200, 202, 208

CPD critical-point drying. 68, 117, 122, 123, 127, 132, 138, 142, 157, 165, 189, 191, 193, 203, 211

CT computed tomography. 2, 61, 73, 86, 87, 141, 155

DOF depth of field. 38–44, 198, 199

EM electron microscopy. 1, 2, 163

FBP filtered back projection. 37, 74, 76–80, 83, 188, 193

FIB focused ion beam. 2, 158, 203

FOV field of view. 3, 12, 38, 40, 54, 60, 62, 64, 67, 69–71, 73–75, 77, 113, 133, 135, 159, 160, 191, 194, 198, 206, 207, 210, 212

FT Fourier transform. 35, 36

FWHM full width half maximum. 52, 53, 91, 92, 97, 105, 111, 139, 159, 194, 212

FZP Fresnel zone plate. 3, 42, 43, 198

KB Kirkpatrick-Baez. 3, 41, 198

LM light microscopy. 1, 2, 141, 146, 148, 150–153, 155–157, 159, 161–163, 165, 166, 187, 189

microCT microscopic computed tomography with resolutions down to 1 µm. 3, 62, 141, 142, 154, 164–169, 171, 187, 188, 190, 192, 193, 201

NA numerical aperture. 38–40, 150, 160, 194

nanoCT nanoscopic computed tomography with resolutions below 1 µm. 3

PMMA poly-methyl methacrylate. 97, 98, 100, 101, 105, 113, 114, 132, 135, 203

ppp projection principle point. 61–64, 67, 68, 70, 199

PSF point-spread function. 51, 56, 59, 84, 87–89, 91, 106, 107, 150, 191, 200, 202, 205

PTA phospho-tungstic acid. 2, 142, 157, 203

PVC polyvinyl chloride. 97–101, 105, 113, 114

QE quantum efficiency. 56–59

RCC renal cell carcinoma. 176, 178, 179, 186, 188, 192

RL Richardson-Lucy. 84, 200

ROI region of interest. 50, 52, 53, 76, 77, 79, 80, 121, 123, 124, 126–130, 139, 140, 148, 149, 162, 167, 168, 210–212

SBF serial block-face. 2

SEM scanning electron microscopy. 1, 2, 45, 51, 157, 158, 203

SNR signal-to-noise ratio. 55, 56, 59, 71, 207

ss serial-sectioning. 2

ss-LM serial-sectioning light microscopy. 2, 141, 142, 145–151, 154–157, 160–162, 197, 198, 201

STED stimulated emission depletion. 1

STORM stochastic optical reconstruction microscopy. 1

TEM transmission electron microscopy. 1, 2, 141, 142, 144, 152, 154, 155, 157, 158, 165, 172, 189, 191, 201, 203

TIE transport of intensity equation. 29, 117, 119, 132

VOI volume of interest. 71, 97–100, 114, 115, 142, 145, 148, 154, 158, 167–169, 187, 191, 193, 203

Publications and Scientific Presentations

In the following, all peer-reviewed publications as first author and as co-author, as well as scientific presentations are listed.

Publications as First Author

Ferstl, S.[†], Busse, M.[†], Kimm, M. A., Hehn, L., Steiger, K., Allner, S., Müller, M., Drecoll, E., Bürkner, T., Dierolf, M., Gleich, B., Weichert, W. & Pfeiffer, F. Targeted multi-scale and non-destructive investigation of human renal tissue in three dimensions. *submitted* (2020).

Ferstl, S.[†], Schwaha, T.[†], Ruthensteiner, B., Hehn, L., Allner, S., Müller, M., Dierolf, M., Achterhold, K., & Pfeiffer, F. Nanoscopic X-ray tomography for correlative microscopy of a small meiofaunal sea-cucumber. *Scientific Reports* **10**, 1 (2020).

Ferstl, S.[†], Busse, M.[†], Müller, M., Kimm, M. A., Drecoll, E., Bürkner, T., Allner, S., Dierolf, M., Pfeiffer, D., Rummeny, E. J., Weichert, W., & Pfeiffer, F. Revealing the Microscopic Structure of Human Renal Cell Carcinoma in Three Dimensions. *IEEE Transactions on Medical Imaging* **39**, 1494-1500 (2020).

Ferstl, S., Metscher, B., Müller, M., Allner, S., Dierolf, M., Busse, M., Achterhold, K., Gleich, B. & Pfeiffer, F. Laboratory-based X-ray NanoCT Explores Morphology of a Zebrafish Embryo. *Microscopy and Microanalysis* **24**, 184-185 (2018).

[†]: shared first authorship

Publications as Co-author

Busse, M., **Ferstl, S.** & Pfeiffer, F. Capturing three-dimensional cell structure with X-ray tomography. *Research Outreach* **118** (2020).[1]

Busse, M., Marciniszyn, J. P., **Ferstl, S.**, Kimm, M. A., Pfeiffer, F., & Gulder, T. 3D-Non-Destructive Imaging through Heavy Metal-Eosin Salt Contrast Agents. *Chemistry - A European Journal* **27**, 4561-4566 (2020).

Gross, V.[†], Müller, M.[†], Hehn, L., **Ferstl, S.**, Allner, S., Dierolf, M., Achterhold, K., Mayer, G., & Pfeiffer, F. X-ray imaging of a water bear offers a new look at tardigrade internal anatomy. *Zoological Letters* **5**, 14 (2019).

Busse, M., Müller, M., Kimm, M. A., **Ferstl, S.**, Allner, S., Achterhold, K., Herzen, J. & Pfeiffer, F. 3D Imaging of Soft-Tissue Samples using an X-ray Specific Staining Method and Nanoscopic Computed Tomography. *JoVE* **152**, e60251 (2019).

Müller, M.[†], Kimm, M.A.[†], Ferstl, S., Allner, S., Achterhold, K., Herzen, J., Pfeiffer, F. & Busse, M. Nucleus-specific X-ray stain for 3D virtual histology. *Scientific Reports* **8**, 1-10 (2018).

Busse, M.[†], Müller, M.[†], Kimm, M. A., **Ferstl, S.**, Allner, S., Achterhold, K., Herzen, J. & Pfeiffer, F. Three-dimensional virtual histology enabled through cytoplasm-specific X-ray stain for microscopic and nanoscopic computed tomography. *PNAS* **115**, 2293-2298 (2018).

Müller, M., de Sena Oliveira, I., Allner, S., **Ferstl, S.**, Bidola, P. Mechlem, K., Fehringer, A., Hehn, L., Dierolf, M., Achterhold, K., Gleich, B., Hammel, J. U., Jahn, H., Mayer, G. & Pfeiffer, F. Myoanatomy of the velvet worm leg revealed by laboratory-based nanofocus X-ray source tomography. *PNAS* **114**, 12378-12383 (2017).

Müller, M., Allner, S., Ferstl, S., Dierolf, M., Tuohimaa T. & Pfeiffer, F. Lab-based x-ray nanoCT imaging. *Proceedings of SPIE* **10132**, 101320L (2017).

[1]: This publication has not undergone a peer-review process.
[†]: shared first authorship

Oral Presentations

Staining-based Nanoscopic X-ray Tomography for Soft-Tissue Imaging
International Conference on Tomography of Materials & Structures (ICTMS). Cairns, Australia, July 2019

Nanoscopic X-ray Tomography with Photon Counting Detectors for Biological Applications
International Symposium on Photon Counting Technologies & Applications. Munich, Germany, July 2019

NanoCT - 3D Microscopy with a high-resolution X-ray CT
Invited Talk, Department of Zoology, University of Vienna. Vienna, Austria, December 2018

The NanoCT setup - Laboratory based high-resolution X-ray imaging
International Conference on X-ray Microscopy (XRM). Saskatoon, Canada, August 2018

Poster Presentations

X-ray NanoCT Imaging - Visualization of the Muscular Structures of an Onychophoran Limb
International Conference on Tomography of Materials & Structures (ICTMS). Lund, Sweden, June 2017

Acknowledgements

This work was only possible with the help of many people. I would like to thank...

... Franz Pfeiffer for giving me the opportunity to work on this PhD topic and for fostering this unique environment that is the chair of E17. His lecture on Biomedical Physics was so intriguing that I ditched my BMW scholarship to stay at the university instead. There was not a single day of regret.
Furthermore, I want to thank him for the trust and freedom to develop and follow my own ideas. I also want to thank him for his support to participate at the ICTMS and the XRM conferences, but especially the Microscopy Winterschool at the ETH Zürich. Each of these visits provided me with invaluable experiences and insights and served as inspiration for various projects during my research.

... Madleen Busse for supporting me to become the researcher I am today. For not only being my colleague, but also my mentor and my friend, for always having my back. I especially want to thank her, for giving me new impulses to evolve professionally and personally and to nourish my strengths and talents. I believe, with her empathy, her courage and her love for her family, she has keyed her own style of leadership and is a true role-model for modern women today.

... Martin Dierolf whom I deeply respect for his kind personality and his sheer infinite knowledge on...well...pretty much everything?! I want to thank him for always helping me, whenever I reached a dead end and had no clue how to fix the NanoCT. I also want to thank him for being pretty much the best paper and thesis corrector there ever will be. I hope he will be able to further grow as a researcher to explore his full potential and receive the appreciation he deserves.

... Lorenz Hehn. It was an immense pleasure working with him and getting the NanoCT image processing to the next level.

... Sebastian Allner for developing the image processing script of the NanoCT in the first place and for always helping everybody with anything.

... Bernhard Ruthensteiner and Thomas Schwaha, for their team spirit, the enjoy-

able and interesting meetings, their competence not only in the field of zoology but also in the field of imaging and of course the Weaner Schmäh. I want to further thank them for their immense support during the correlative microscopy project and during my application for the Werner-Meyer-Ilse Memorial Award. I was able to learn a lot about zoological research during our project.

... Melanie Kimm for all her insights, input and for the invaluable support to more than only our 3D X-ray histology projects.

... Wilko Weichert for his commitment and support during the 3D X-ray histology projects and during my application for the Werner Meyer-Ilse Memorial Award, despite his busy schedule.

... Bastian Brenzinger for the great cooperation, and for contributing the anatomy of the marine snail without asking anything in return. I hope there will be fruitful projects with the group and him in the future.

... Mark Müller for being the best master's student supervisor, I could have wished for.

... David Paganin, for his inspiring talks, for his infectious passion for physics, and for reminding me what physics research is all about.

... Andrew Kingston, for the fruitful discussions on conferences, for sharing his knowledge and thus being a great example of what the international scientific community should really be like. I am especially grateful for him inspiring me to implement Gureyev's deblurring into the NanoCT image processing routine.

... Bernhard Gleich for being the knight in shining armour and rescuing the NanoCT more than once.

... Silja Flenner, and Fei Yang for the interesting discussions and the fun times at the ICTMS 2020.

... the organisers and the tutors at the Zurich Microscopy Winter School for an educational, fascinating workshop which inspired the outline of the correlative microscopy paper.

... Klaus Achterhold, Veronica Bodek and especially Nelly De Leiris for always supporting me and the rest of the group with all administration struggles.

... all the people involved in developing and maintaining the IT-infrastructure, especially Eldorado and Quarth, which I will sorely miss.

... the entire group of E17 for creating this welcoming, fun and creative atmosphere: Pidassa, Christoph and Stefan for the enjoyable table-kicker matches, Lisa for the great conversations during tea time and the fun times during Italian class and Tabata, Kathi who would have been a more than capable successor at the NanoCT, and last but not least the rest of the Schnitzel-Club.

... the people who have proof-read chapters of my thesis: Lisa Heck, Melanie Kimm, Thomas Schwaha, Bernhard Ruthensteiner, Lorenz Hehn, Eva Prexl, and particularly Madleen Busse, Katharina Scheidt and Martin Dierolf.

... Tanja and Kathrin. I never expected to find my best (girl-)friends during my physics studies. It was great fun surviving analysis with Prof. Castrigiano, theoretical physics and any Tupperware-related incidents together.

... my sister Christina, for being not only the best sister, but also my best friend.

... my love Philip, for accepting and loving me for who I am with all my quirks and flaws and for always bringing a spark of light into my life with his brilliant sense of humour and for deeply caring for his friends, family, his Simone and his Jabbas.

Finally I want to thank my parents, who have always done everything in their ability to keep us safe. I want to particularly thank my father, who taught me so much about nature, craftsmanship and life in general.